Micromechanical modelling of ductile damage: from Single crystals to Polycrystals

by

Manjunath Dakshinamurthy

A dissertation submitted by in partial fulfillment of the requirements for the degree of Doctor of Philosophy in

Mechanical Engineering and Industrial Organization

Universidad Carlos III de Madrid

Advisor:

Guadalupe Vadillo

July 2022

The research leading to the results reported in this doctoral thesis has received funding from the European Union's Horizon2020 Programme (Excellent Science, Marie Skłodowska-Curie Actions) under REA grant agreement 675602 (Project OUTCOME).

Abstract

For more than six decades, improving the strength and ductility of industrially important materials has been in the focus of research. Besides economic reasons, safety issues have driven research and development in this field. For the purpose of safety, it is imperative to understand the failure behaviour of ductile materials, as ductile materials are commonly used in protective structures. It is well known that major failure mode for ductile materials is through void nucleation, growth and void coalescence. In structural ductile materials voids nucleate at inclusions and second-phase particles by decohesion of the particle–matrix interface or by particle cracking. The presence of voids can have drastic implications at the macroscopic level including strong material softening and incipient fracture.

Significant efforts have been made over the years to describe the plastic behavior of isotropic and anisotropic ductile materials. Numerous investigations, in the last decades, have been dedicated to the study of ductile failure, leading to a deeper knowledge on the factors influencing the ductile process. This doctoral thesis contributes to the understanding of the key role played by material anisotropy and stress state on the growth of voids in single crystals, bi-crystals and polycrystals using numerical and experimental methods.

Using a numerical approach, void growth and morphology evolution in fcc single crystals and bi-crystals are investigated using crystal plasticity finite element method. For that purpose, representative volume element of single crystals and bi-crystals are considered in the analysis. Fully periodic boundary conditions are prescribed in the representative volume element and macroscopic stress triaxiality and Lode parameter are kept constant during the whole deformation process. Simulations are performed to study the implications of triaxiality, Lode parameter and crystallographic orientation on slip mechanism, hardening and hence void evolution. In the bi-crystal case, a void at the grain boundary is considered in the analysis. Grain boundary is assumed initially perpendicular/coaxial with the straight sides of the cell. Three different pairs of crystal orientations characterized as hard-hard, soft-soft and soft-hard has been employed for modelling the mechanical response of the bi-crystal. The impact of void presence and its growth on the heterogeneity of lattice rotation and resulting grain fragmentation in neighbouring areas is analysed and discussed.

On the other hand and using an experimental approach, void growth behaviour in pure Aluminium polycrystals with pre-drilled holes are investigated in this work. By varying the hole diameter and position of the holes, three different types of specimens are defined and considered for investigation. Using in-situ tensile test coupled with scanning electron microscope, uni axial tensile tests are performed at constant low strain rate. The specimens are analysed with the help of EBSD, DIC and high resolution SEM images. Interrelation between hole diameter,

distance between holes, local orientation of the grains and grain size on void growth and final failure of the material are analysed and discussed

Keywords: Crystal plasticity, single crystals, bi-crystals, polycrystals, finite element calculations, stress triaxiality, Lode parameter, anisotropy, porosity, SEM, In-Situ tensile test.

Acknowledgements

This work is the result of my time as a doctoral candidate at the Nonlinear Solid Mechanics group of the department of Continuum Mechanics and Structural Analysis in the University Carlos III of Madrid. First and foremost I truly want to thank Professor José A. Rodríguez-Martínez for providing me an opportunity to be part of Project OUTCOME. It has been a great honor to be part of this project, working with talented people from around the world, as well as an extremely fun experience.

I would like to express acknowledgment to my supervisor Professor Guadalupe Vadillo for her invaluable guidance, kind help and encouragement during the course of my doctoral thesis. The work written here is the result of many hours of exciting discussions and it would not have been possible without her support.

My sincere gratitude to Professor Katarzyna Kowalczyk-Gajewska (Institute of Fundamental Technological Research Polish Academy of Sciences). Chapter 5 is the work that has been done in very close collaboration with her. I would also like to thank Professor Shmuel Osovski (Technion, Israel). I had the pleasure to work with him during my 12-weeks stay at Technion. I appreciate his help in performing experiments in SEM. Chapter 6 presented in this work has been done in collaboration with him. I owe my deepest gratitude to both of them for their constant support in completion of this thesis.

I would like to express my gratitude to Prof. Daniel Rittel (Technion, Israel) and Prof. Sébastien Mercier (University of Lorraine, France) for hosting my research stays in their labs and for giving access to their computer clusters.

I would like to acknowledge the fruitful discussions i had with Dr.Christophe Czarnota and Dr. Álvaro Vaz-Romero. I am also grateful to Laura Fajardo who made my life easier in the administrative matters. Always ready to help, she has been an essential support during all these years.

I would also like to thank my colleagues Komi Espoir N'souglo with whom I have spent my daily life, Kokouvi Gbetchi, Juan Carlos Nieto Fuentes, Irfan Habeeb, Manoj Subramani, Essossinam Simlissi, Stylianos Tsopanidis and Pilar Fernandez Pison. Thanks for having shared all these fun moments with you.

I would like to thank Guadalupe Vadillo and my Dear Boss José A. Rodríguez-Martínez for all the help outside academics. You made my life very comfortable and easy during my stay in Madrid. Thank you for being my friends and family. `Gracias..`

Finally, I would like to express my heartfelt thanks to my mother, father and brother, who have always encouraged me to pursue my dreams and have made me happy everywhere i have been. Thanks to those i did not mention!

Published and submitted content

- Manjunath Dakshinamurthy, Katarzyna Kowalczyk-Gajewska, and Guadalupe Vadillo. Influence of crystallographic orientation on the void growth at the grain boundaries in bi-crystals. International Journal of Solids and Structures 212 (2021): 61-79. DOI:10.1016/j.ijsolstr.2020.11.035. This publication is entirely included in Chapter 5, Sections 2.2.3.2 and 2.2.3.3, and Appendix D of this thesis. The material from this source included in this thesis is not singled out with typographic means and references.

- Navab Hosseini, Juan Carlos Nieto-Fuentes, Manjunath Dakshinamurthy, Jose Antonio Rodríguez-Martínez and Guadalupe Vadillo. The effect of material orientation on void growth. International Journal of Plasticity 148 (2022):103149. DOI:10.1016/j.ijplas.2021.103149. This publication is partially included in Appendix D of this thesis. The material from this source included in this thesis is not singled out with typographic means and references.

Table of Contents

List of Tables

List of Figures

Part I

General introduction and basic concepts of crystal plasticity

1

General introduction

With the focus on reducing carbon emission, resulting environmental guidelines has become a top priority for automobile and space industry. This has resulted in a more stringent requirement for improved fuel economy and emission. Weight reduction is the most effective way for achieving fuel economy, hence a new trend in automobile and aerospace industry is to use lighter materials, without compromising the strength and durability of the components. Due to a favourable strength-to-density ratio, which could be translated into fuel economy and efficiency, light weight materials (i.e. aluminum and its alloys) are increasingly used in the automotive, aviation and space industries for the fabrication of skins and other structural elements. However, compared to denser metals (i.e. steel), the use of light weight materials has been restricted by its poor ductility at room temperature and spot weld difficulties. Additionally light weight materials are prone to ductile failure by accumulation and evolution of microscopic voids. The complete potential of these light weight materials can be unleashed only by thoroughly understanding its ductile and failure behaviour.

The main reason for ductile damage of metals are nucleation, growth and coalescence of micro-voids. The first studies of void behavior of ductile metals studies date back to 1960 with the work of Rogers (1960), Beachem (1963) and Gurland and Plateau (1963). Numerical insights into studying of voids were pioneered by McClintock (1968) and Rice and Tracey (1969). For next five decades, numerous work has been performed by various researchers in order to understand void growth and coalescence in ductile metals. This problem is analyzed via experimental, analytical and numerical approach considering both isotropic and anisotropic material modeling. Some of these works provide a general background to this doctoral thesis.

1.1 Research background and objectives

Studying the origin and behaviour of voids in different materials has been a major topic of interest in the last six decades by virtue of its importance to understand its effects on the material failure. Voids are observed in many materials, ranging from metals (Rogers, 1960), biological tissues (Pishchalnikov et al., 2003) to polymers (Gent and Lindley, 1959; Huang

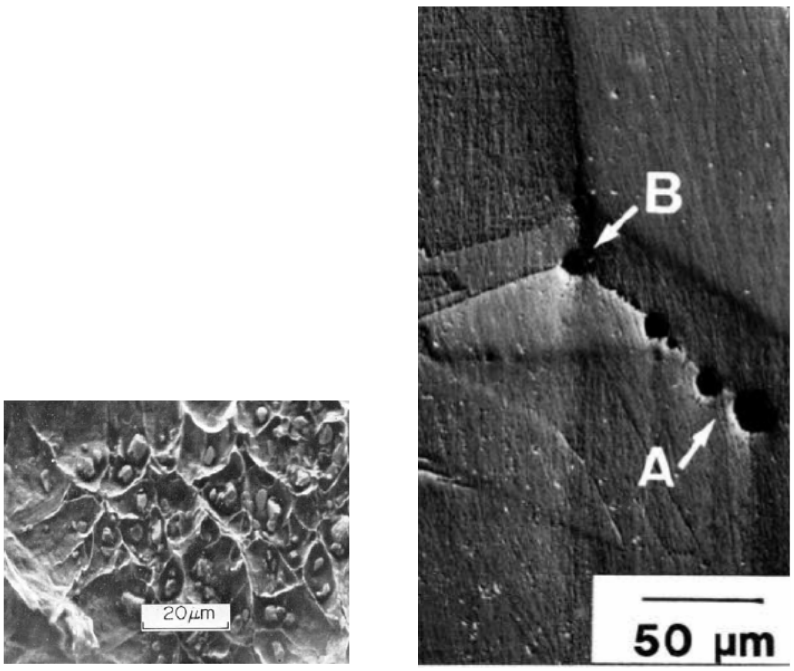

(a) (b)

Figure 1.1: *Illustration of various void nucleation sites: (a) Void growth within an inclusion colony in quenched and tempered steel (Hancock and Mackenzie, 1976); (b) Nucleation of spherical voids at grain boundary and grain boundary triple point (Meyers et al., 1986)*

and Kinloch, 1992). It was observed by (Bauer and Wilsdorf, 1974) that even pure materials develop voids in order to accommodate the applied deformation.

The main reason for ductile damage of metals are nucleation, growth and coalescence of micro-voids as reported by Rogers (1960); Gurland and Plateau (1963); Beachem (1963). A theoretical study of growth of cylindrical voids in an ideally plastic material (i.e., without hardening) has been performed by McClintock (1968). Similar investigation has been performed by Rice and Tracey (1969) to determine the relationship between the growth of an initially spherical void and the stress triaxiality. Significance of void interaction under plane strain condition has been reported by Needleman (1972). To study the effect of porosity on deformation and fracture behaviour of titanium alloys Bourcier et al. (1986) performed experimental and analytical studies. To understand size effect on void growth, Liu et al. (2003) performed analytical studies by extending the work of Rice and Tracey. Li and Steinmann (2006) unveiled the effect of void size and shape on deformation behaviour of a material containing micro-voids, by performing studies on different type of spheroidal voids in an axisymmetric spheroidal unit cell.

Numerical studies on plane strain void cells under uni-axial deformation were studied by Andersson (1977). Tvergaard (1979) extended this study by using an elastic-plastic solid matrix and studied the effect of micro-voids during ductile failure of the material. Li and Howard (1983) and Chen et al. (1983) performed finite element analysis on an elasto-plastic matrix containing a spherical void to understand void growth and ductile failure behaviour. Koplik and Needleman (1988) presented a numerical solution to predict the influence of an

array of voids in an axisymmetric cell model. Similarly Hom and McMeeking (1989) performed 3D finite element analysis to investigate void evolution in a cell with a cubic array of voids. Further and in order to understand void size effect Tvergaard and Needleman (1997) used a non local damage model. Using plane strain analysis Tvergaard and Hutchinson (2002) studied the behaviour of voids located ahead of a crack tip, whereas Tvergaard and Niordson (2004) performed axisymmetric non local elastic-plastic analysis. The effect of secondary void population on ductile fracture is studied by Hütter et al. (2014) and Zybell et al. (2014) under plane strain condition.

1.1.1 Void growth in single crystal and polycrystals

It is well known that void nucleation in polycrystalline ductile materials occurs mainly at second-phase particles by interfacial decohesion or particle fracture (Puttick, 1959). As showed by Hull and Rimmer (1959), grain boundary and triple points acts as preferred locations for void nucleation as seen in figure 1.1. In single crystals, void nucleation may take place by irradiation or quenching or by clustering of vacancies produced during plastic deformation as noted by (Cawthorne and Fulton, 1967). For polycrystals the process of void nucleation, growth and coalescence is different to single crystals as reported by Bauer and Wilsdorf (1974); Lyles Jr and Wilsdorf (1975). Voids nucleated at grain boundaries, cracking of second phase or clustering of vacancies are generally micron or submicron-sized (Goods and Brown, 1983; Thompson, 1987). Nemat-Nasser and Hori (1987) studied void growth or collapse in a crystalline solid undergoing large deformation. Using 2D plane strain formulation with an idealized two slip system configuration O'regan et al. (1997) performed crystal plasticity based studies to investigate micro-void growth and coalescence in single crystals. Similarly Orsini and Zikry (2001) performed 3D crystal plasticity based analysis to understand void growth and interaction in copper single crystal plates. By using dislocation based crystal plasticity theory, Ohashi (2005) studied spherical micro-void growth in single crystals. Li and Guo (2002) performed FE based study to investigate the void growth and coalescence at the interface in a bi-material system. Crystal plasticity based finite element simulation on two dimensional unit cell with one and two voids has been studied by (Kysar et al., 2005; Potirniche et al., 2006a). Liu et al. (2007a) investigated the effect of crystal orientation on void growth and coalescence in face centered cubic (FCC) single crystals. To understand micro-void growth under biaxial loading Huang et al. (2007) used discrete dislocation dynamics based theory. Similarly Segurado and Llorca (2009) performed discrete dislocation dynamics based simulations in 2D framework to understand void size effect in single crystals. By performing 3D crystal plasticity simulations, Yerra et al. (2010a) investigated void growth and coalescence in body centered cubic (BCC) single crystals. They reported that void growth rate depends strongly on the initial orientation of the crystal and also proposed a model to predict the onset of void coalescence. Liu et al. (2012) investigated void coalescence in a single crystal and bi-crystal using 3D crystal plasticity framework. Carroll et al. (2013) performed experimental statistical analysis of stress projection factors in BCC tantalum and reported that Schmid factors are suitable for room temperature. Tensile

deformation in tantalum as long as grain neighbor effects are accounted for. Hosokawa et al. (2013) studied the onset of void coalescence in uniaxial tension by continuous X-ray tomography. Similarly Landron et al. (2013) investigated void coalescence in a dual phase steel using X-ray tomography. Both studies suggested that the coalescence models developed by Thomason (1985) and later extended by Pardoen and Hutchinson (2000) provide accurate predictions of coalescence strain. Srivastava and Needleman (2013) and Srivastava and Needleman (2015a) studied void growth in creeping single crystals and showed the effect of inter-ligament distance between voids on void shape evolution. Kysar and Gan (2005) studied the deformation state around a cylindrical void in a single crystal matrix using anisotropic slip line theory. Nemcko et al. (2016) studied the effect of void volume fraction on void growth and linkage in commercially pure magnesium by using X-ray micro-tomography and reported that there is a critical strain required to initiate fracture in these boundaries. Pushkareva et al. (2016) studied void growth in commercially pure titanium using X-ray tomography and crystal plasticity based simulations. They observed that void growth depends on grain orientation more than inter void spacing and material strength. In the work of Asim et al. (2017) numerical studies has been performed by using both local and non-local crystal plasticity constitutive models, providing insights into the relationship between void growth, initial porosity, initial void size, plastic anisotropy and local/non local size effects.

Within this context, this doctoral thesis aims at providing new insights into void growth in single crystals and bi-crystals using numerical finite element calculations with controlled loading conditions following up with experimental studies of void growth in polycrystals.

1.2 Contents and original contributions

The main contents and original contributions of this thesis are detailed here. First, we present in Chapter 2 in **Part I**, based on the textbook by Roters et al. (2011), the fundamental concepts and equations of nonlinear solid mechanics and crystal plasticity, essential to understand the problems addressed. Then, the main contributions of this investigation are reported in **Parts II and III** of this manuscript.

Part II composed of Chapters 3, 4 and 5 is dedicated to the **Numerical modelling of void growth in single crystals and bi-crystals**:

- In **Chapter 3**, based on the crystal plasticity model described in Chapter 2, we have performed 3D unit cell finite element calculations to address the role of anisotropy, stress triaxiality and Lode parameter on the response of FCC single crystals without voids. Six different crystal orientations and three different Lode parameters are studied in this chapter. Results obtained provide important and relevant conclusions to be used for studying porous single crystals and bi-crystals.

- In **Chapter 4**, we have performed 3D unit cell finite element calculations for porous FCC single crystals, following the approach used in Chapter 3. In this chapter we studied the role of crystal anisotropy and stress state on void evolution. We have used four

different crystal orientations, four different stress triaxiality values and three different Lode parameters. The outcome of this study gave insight into factors affecting void growth in porous single crystals.

- In **Chapter 5**, based on a published paper (Dakshinamurthy et al., 2021), void growth and morphology evolution in FCC bi-crystals are investigated using crystal plasticity finite element method. For that purpose, representative volume element of bi-crystals with a void at the grain boundary is considered. Three different pairs of crystal orientations characterized as hard-hard, soft-soft and soft-hard has been employed for modelling the mechanical response of the bi-crystal. Simulations are performed to study the implications of triaxiality, Lode parameter and crystallographic orientation on slip mechanism, hardening and hence void evolution. The impact of void presence and its growth on the heterogeneity of lattice rotation and resulting grain fragmentation in neighbouring areas is also analysed and discussed.

Part III is composed of Chapter 6, that is dedicated to **Experimental investigation of void growth in metallic sheets containing holes**:

- In **Chapter 6**, we performed uniaxial in-situ tensile tests, coupled with scanning electron microscope to study the void growth behaviour in pure Aluminium tensile specimens with pre-drilled holes. By varying the hole diameter, distance between the holes and arrangement of holes, three different types of specimens were considered. With the help of EBSD, DIC and high resolution SEM images, the relationship between local microstructure and void growth are analysed and discussed.

- Finally, some conclusions about the work presented are provided in Chapter 7, where some ideas for future work are also discussed.

2

Micromechanical Modelling Framework

Contents

This chapter summarizes the fundamental concepts and equations necessary for building constitutive models for crystal plasticity (CP) simulations at different length scales. All the numerical simulations presented in this work are based on a crystal plasticity model built via the Finite Element solver ABAQUS using a user subroutine UMAT. The contents of this chapter are primarily based on the textbook by Roters et al. (2011). We start by introduction of continuum mechanics in section 2.1. Later and in section 2.2 the mechanical behaviour of the body under consideration is described based on a crystal plasticity model that is formulated in a continuum mechanics framework.

2.1 Continuum Mechanics

Continuum mechanics is a combination of mathematical principles common to all media, that generally ignores size and shape of materials and frequency of atomic vibrations. Continuum mechanics considers that the field values of a body are equal to the averaged values of each particle in time. By making this assumption we can express the field variables as continuous functions in both space and time. Continuum mechanics is used to describe the flow behaviour of a body under prescribed boundary conditions like displacement, traction or temperature. In continuum mechanics and in order to find a legitimate solution for describing the behaviour of a material, conditions of compatibility between strains and displacements, equations of equilibrium (static or dynamic), and stress–strain relations or material constitutive law has to be fulfilled.

In subsection 2.1.1, we present different configurations of a body under load boundary conditions. Later on and with the help of these configurations, stress measure and strain measure are derived in subsection 2.1.1.4 and subsection 2.1.1.7 respectively. Further in subsection 2.1.2 condition for compatibility is presented. Similarly equilibrium condition is discussed in subsection 2.1.3. The constitutive model used in this work is presented in section 2.2.

2.1.1 Kinematics

A correct definition of bodies and configuration is necessary to model materials in different frames. Let body $\mathscr{B}$ be a composition of multiple number of material points. The body occupies the region $\mathscr{B}_0$ in reference configuration and $\mathscr{B}_t$ in current or deformed configuration. Vector $\mathbf{x}$, where $\mathbf{x} \in \mathscr{B}_0$ defines the material point in reference configuration and vector $\mathscr{X}$ where, $\mathscr{X} \in \mathscr{B}_t$ in deformed configuration as shown in figure 2.1. There are many coordinate system basis available to define each configuration. In this work Cartesian coordinate system is used as a common coordinate system for both reference and current configuration. This helps in skipping explicit notation for each configuration.

Deformation of a body can be described either in reference or current configuration. In general there are two different description for representing deformation of a body: Lagrangian and Eulerian description. In Lagrangian description each particle belongs to the current spatial location. In Eulerian description the spatial location itself belongs to the particle. In general

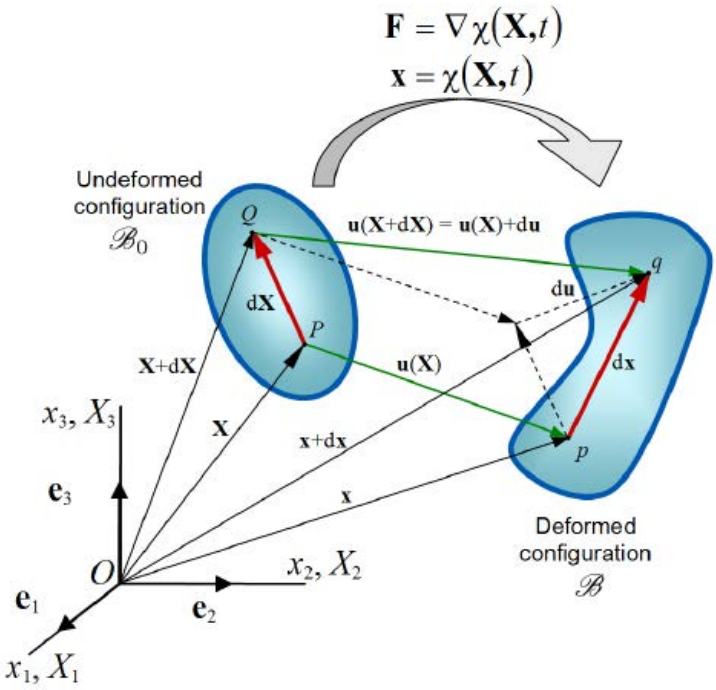

Figure 2.1: *Configurations of a continuum body. $\mathscr{B}_0$ is the space occupied by the undeformed body. Mapping $\mathscr{X}(\mathbf{X}, \mathbf{t})$ maps it to the deformed configuration $\mathscr{B}$. Figure adopted from Roters et al. (2011)*

and in solid mechanics, it is convenient to use Lagrangian description. Therefore it is necessary to introduce a deformation map that can connect points in reference configuration to points in current configuration.

2.1.1.1 Displacement field

For a material body occupying the space $\mathscr{B}_0$ at time t_0, if there is a change in the configuration of the body by a motion $\mathscr{X}(t)$, then it occupies the space $\mathscr{B}_t$ at time t. During this motion we observe a change in position of material points from $\mathscr{X}$ to $\mathbf{x}$. The displacement vector can be denoted by equation 2.1

$$\mathbf{u}(\mathbf{x}, t) = \mathbf{X}(\mathbf{x}, t) - \mathbf{x} \tag{2.1}$$

Displacement vector is function of $\mathbf{x}$ and t that maps material points between current and reference configuration.

2.1.1.2 Deformation gradient

Like displacement vector, deformation gradient tensor maps all elements $\mathbf{dX}$ radiating from $\mathbf{X}$ in the reference configuration as they deform to $\mathbf{dx}$ in deformed configuration. The inverse of deformation gradient maps a vector from deformed configuration to reference configuration. It is denoted by $\mathbf{F}$ and is a second order tensor. Taking into account the relations:

$$\mathbf{x} + d\mathbf{x} = \mathbf{x}(\mathbf{X}) + \frac{\partial \mathbf{x}}{\partial \mathbf{X}} d\mathbf{X} + ... \tag{2.2}$$

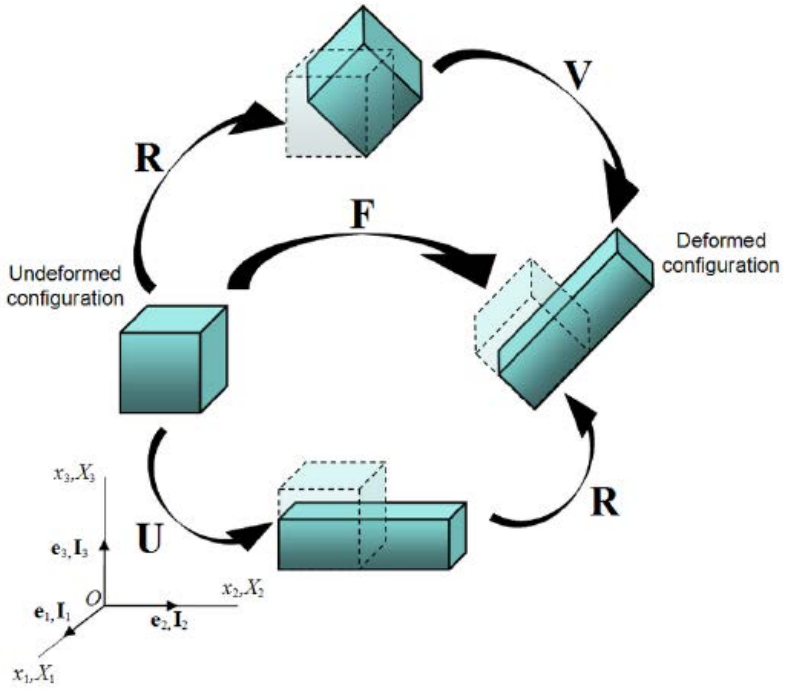

Figure 2.2: *A schematic showing decomposition of deformation into pure rotation followed by pure stretch or pure stretch followed by pure rotation. Figure adopted from Roters et al. (2011)*

$$d\mathbf{x} = \frac{\partial \mathbf{x}}{\partial \mathbf{X}} d\mathbf{X} \tag{2.3}$$

by using equations 2.1 and 2.3, the deformation gradient can be obtained as:

$$\mathbf{F} = \frac{d\mathbf{x}}{d\mathbf{X}} = \nabla \ \mathscr{X} = \mathbf{I} + \frac{\partial \mathbf{u}}{\partial \mathbf{X}} \tag{2.4}$$

where $\frac{\partial \mathbf{u}}{\partial \mathbf{X}}$ is defined as displacement gradient and $\mathbf{I}$ is the second order unit tensor.

Similarly, the inverse of deformation gradient is given by equation 2.5:

$$\mathbf{F}^{-1} = \frac{d\mathbf{X}}{d\mathbf{x}} = \nabla \ \mathscr{X}^{-1} \tag{2.5}$$

The determinant of deformation gradient is called Jacobian J and it gives the measure of volume change associated with deformation. If dV and dV_0 are volumes before and after deformation then J is given by equation 2.6.

$$J = \frac{dV}{dV_0} = det\mathbf{F} \tag{2.6}$$

2.1.1.3 Polar decomposition of the deformation gradient

The deformation gradient $\mathbf{F}$ can be decomposed to a pure rotation and stretch, which is commonly termed as polar decomposition. Depending on which one of transformation comes first, the polar decomposition can be applied in two ways as follows (see figure 2.2):

$$\mathbf{F} = \mathbf{RU} = \mathbf{VR} \tag{2.7}$$

where $\mathbf{R}$ is an orthogonal tensor, and $\mathbf{U}$ and $\mathbf{V}$ are symmetric right and left stretch tensor respectively. It should be noted that rotation component does not contribute to shape change of the body, hence will have zero contribution to strain as should be discussed later. Stretch component contribute only to shape change and hence strain. With the help of polar decomposition we can validate particular strain measures.

2.1.1.4 Measure of strain

Apart from deformation gradient, deformation of the body can also be expressed in terms of displacement gradient $\frac{\partial \mathbf{u}}{\partial \mathbf{X}}$ as shown by equation 2.8:

$$\mathbf{F} = \frac{\partial \mathbf{x}}{\partial \mathbf{X}} = \frac{\partial (\mathbf{X} + \mathbf{u})}{\partial \mathbf{X}} = \mathbf{I} + \frac{\partial \mathbf{u}}{\partial \mathbf{X}} \tag{2.8}$$

By definition, a strain tensor is a tensor describing the locations of two points of a body after deformation with respect to their location before deformation. The length of the deformed element can be expressed as (Eq. 2.9):

$$d\mathbf{x}^T.d\mathbf{x} = (\mathbf{F}.d\mathbf{X})^T\ (\mathbf{F}.d\mathbf{X}) = d\mathbf{X}^T.(\mathbf{F}^T\mathbf{F}).\ d\mathbf{X} \tag{2.9}$$

Subsequently the change in the length of the element can written as (Eq. 2.10):

$$d\mathbf{x}^T.d\mathbf{x} - d\mathbf{X}^T.d\mathbf{X} = d\mathbf{X}^T.(2\mathbf{E}_0).d\mathbf{X} \tag{2.10}$$

where $\mathbf{E}_0 = \frac{1}{2}(\mathbf{F}^T\mathbf{F} - \mathbf{I}) = \frac{1}{2}(\mathbf{C} - \mathbf{I})$ is the Green-Lagrange strain tensor. Since it depends only on the right Cauchy-Green deformation tensor $\mathbf{C} = \mathbf{F}^T\mathbf{F}$, $\mathbf{E}_0$ is defined completely in the reference configuration.

Similarly:

$$d\mathbf{x}^T.d\mathbf{x} - d\mathbf{X}^T.d\mathbf{X} = d\mathbf{x}^T.(2\mathbf{E}_t).d\mathbf{x} \tag{2.11}$$

where $\mathbf{E}_t = \frac{1}{2}(\mathbf{I} - \mathbf{F}^{-T}\mathbf{F}^{-1}) = \frac{1}{2}(\mathbf{I} - \mathbf{C}^{-1})$ is the Almansi strain tensor defined in the current configuration. Both Green-Lagrange and Almansi strain tensors are applicable to finite strain framework.

For small strain formulation Green-Lagrange and Almansi strains can be linearized to obtain the strain tensor called Cauchy strain tensor ε, given by equation 2.12 in Einstein convection:

$$\varepsilon_{ij} = \frac{1}{2}(\mathbf{u}_{i,j} + \mathbf{u}_{j,i}) \tag{2.12}$$

whereas in index notation it is given by equation 2.13:

$$\varepsilon = \frac{1}{2}(\nabla \mathbf{u} + \nabla \mathbf{u}^T) \tag{2.13}$$

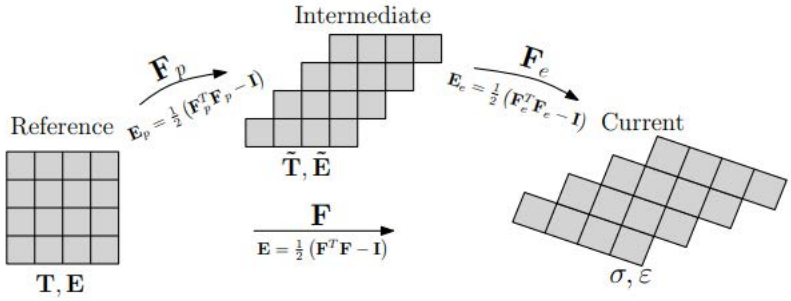

Figure 2.3: *Multiplicative decomposition of the total deformation gradient* $\boldsymbol{F}$*. The plastic deformation gradient* $\mathbf{F}_p$ *relates the reference and plastic intermediate configuration. Finally* $\mathbf{F}_e$ *maps to the current configuration. Figure recreated from Roters et al. (2011)*

2.1.1.5 Velocity gradient

It is known that material points in reference configuration do not move with time, where as material points in current configuration move at velocity $\mathbf{v}$. This velocity can be calculated using displacement vector ($\mathbf{u}$) of a material point:

$$\mathbf{v} = \frac{d}{dt}\mathbf{u} = \dot{\mathbf{u}} = \dot{\mathbf{x}} - \dot{\mathbf{X}} = \dot{\mathbf{x}} \tag{2.14}$$

Relative motion of two material points in current configuration can be obtained by taking spatial gradient of material velocity field. This is termed as velocity gradient and is given by

$$\mathbf{L} = \frac{\partial \mathbf{v}}{\partial \mathbf{x}} = \nabla\ \mathbf{v} \tag{2.15}$$

and is related to deformation as:

$$\mathbf{L}d\mathbf{x} = \frac{\partial \mathbf{v}}{\partial \mathbf{x}}d\mathbf{x} = \frac{d}{dt}\mathbf{F}d\mathbf{X} = \dot{\mathbf{F}}d\mathbf{X} = \dot{\mathbf{F}}\mathbf{F}^{-1}d\mathbf{x} \tag{2.16}$$

From Eq. 2.16, we obtain the relationship between velocity gradient and deformation gradient:

$$\mathbf{L} = \dot{\mathbf{F}}\mathbf{F}^{-1} \tag{2.17}$$

The velocity gradient $\mathbf{L}$ can be divided into a symmetric part $\mathbf{D}$ and a skew-symmetric part $\mathbf{W}$ which are termed as stretch rate tensor and spin tensor respectively:

$$\mathbf{L} = \mathbf{L}_{sym} + \mathbf{L}_{skew} = \frac{1}{2}(\mathbf{L} + \mathbf{L}^T) + \frac{1}{2}(\mathbf{L} - \mathbf{L}^T) = \mathbf{D} + \mathbf{W} \tag{2.18}$$

2.1.1.6 Multiplicative decomposition of deformation

The path of material point $\mathscr{X}$ in a body $\mathscr{B} \in \mathscr{R}^3$ takes to reach the current configuration $\mathbf{x} = \mathscr{X}(\mathbf{X})$, which depends mainly on material behaviour. In small strain framework, we use additive decomposition of total strain (ε) as $\varepsilon = \varepsilon_e + \varepsilon_p$, where ε_e is elastic strain and ε_p is inelastic or plastic strain. Inelastic strains has many contributions from crystal be-

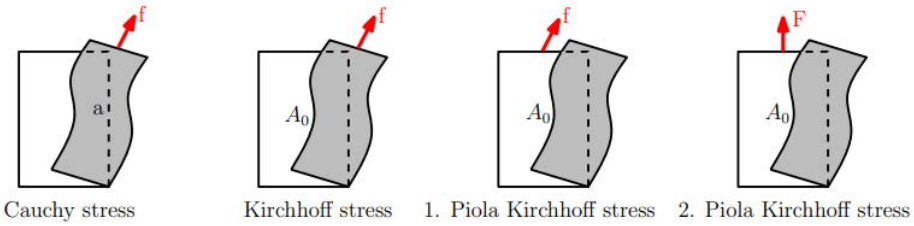

Figure 2.4: *Graphical interpretation of Cauchy, first Piola Kirchhoff and second Piola Kirchhoff stresses. Reference configuration is defined as white rectangle, while current configuration is defined as deformed grey area. Figure recreated from Roters et al. (2011)*

haviours like dislocation glide, phase transformation, twinning, etc. In this work we will focus on dislocation glide as major inelastic strain contributor. Since in this work we are using large strain formulation for modelling material behavior, more focus will be laid on that. In large strain formulation, multiplicative decomposition of deformation gradient is used as shown in equation 2.19:

$$\mathbf{F} = \mathbf{F}_e \mathbf{F}_p \tag{2.19}$$

where $\mathbf{F}_e$ is the elastic part of deformation gradient. $\mathbf{F}_e$ helps in mapping material points from intermediate configuration to current configuration. $\mathbf{F}_p$ is the plastic part of deformation gradient, which maps material point from reference configuration to an imaginary intermediate configuration as shown in figure 2.3. As mentioned earlier, in this work only dislocation glide will contribute to plastic deformation. The intermediate configuration posses the same lattice orientation as reference configuration. Velocity gradient can be obtained in terms of deformation gradient by additive decomposition of total velocity gradient as shown in equation 2.20:

$$\mathbf{L} = \dot{\mathbf{F}}\mathbf{F}^{-1} = \frac{\partial \mathbf{F}_e \mathbf{F}_p}{\partial \mathbf{t}} {\mathbf{F}_p}^{-1} {\mathbf{F}_e}^{-1} \tag{2.20}$$

2.1.1.7 Measure of stress

Stress is defined as the force per acting area on the material. As there are different measures for strains in different configurations, measure for stresses are also different depending on configuration in which force and area are defined as shown in figure 2.4.

$$Stress = \lim_{\triangle A \to 0} \frac{\triangle F}{\triangle A} \tag{2.21}$$

If we consider both forces and area in current configuration, then we have Cauchy stress $\boldsymbol{\sigma}$. This is also called true stress and is a second order tensor defined by the equation:

$$\boldsymbol{\sigma} = \lim_{\triangle A \to 0} \frac{\triangle f}{\triangle A} \tag{2.22}$$

Another definition of stress is the first Piola Kirchhoff stress $\mathbf{P}$, in which force is defined in current configuration, whereas area is defined in the reference configuration. This stress is again a second order tensor which is not essentially a symmetric tensor:

$$\mathbf{P} = \lim_{\triangle A_0 \to 0} \frac{\triangle f}{\triangle A_0} \tag{2.23}$$

If both force and area are defined in reference configuration then the stress is called Second Piola Kirchhoff stress. This tensor is a symmetric second order tensor given by equation 2.24:

$$\mathbf{S} = \lim_{\triangle A_0 \to 0} \frac{\triangle F}{\triangle A_0} \tag{2.24}$$

A schematic illustration of these three stress measures are given in figure 2.4. These three stress measures are related to each other by equation 2.25:

$$\boldsymbol{\sigma} = \frac{1}{J}\mathbf{P}\mathbf{F}^T = \frac{1}{J}\mathbf{F}\mathbf{S}\mathbf{F}^T \tag{2.25}$$

In plastic intermediate configuration, the second Piola Kirchhoff stress $\mathbf{S}$ is related to Mandel stress $\mathbf{T}$ by the equation 2.26:

$$\mathbf{T} = \mathbf{F}_e{}^T\mathbf{F}_e\mathbf{S} \tag{2.26}$$

2.1.2 Compatibility conditions

Certain mathematical conditions are necessary to ensure that a continuum body does not develop gaps or overlaps and not violate basic assumption of continuous medium. A body is called a compatible body if it deforms without developing gaps or overlaps. Compatibility conditions determine whether a particular deformation is permissible. In large strain formulation, a body is said compatible if strain field originates from a curl free deformation gradient $\boldsymbol{\nabla} \times \mathbf{F} = 0$ i.e., curl $\mathbf{F}= 0$

2.1.3 Boundary value problem and static equilibrium

In this work boundary value problem addresses a system of coupled mechanical partial differential equations. This involves solving partial differential equation of static mechanical equilibrium.

For a system in static equilibrium, no forces acting on the body can force parts of it to change their position. If the components of Cauchy stress tensor in every material point satisfies the condition $\sigma_{ji,i} = 0$ then the body is in static equilibrium. In large strain formulation similar condition is given by $\boldsymbol{\nabla} \cdot \mathbf{P} = 0$.

2.2 Elasto-plastic behaviour in crystalline materials

2.2.1 Introduction

In crystalline materials, the properties of the material are directly related to the underlying crystalline structure. For crystalline materials, atoms are arranged in a periodic array over large atomic distances.

Metals normally have relatively simple crystalline structures, i.e., a small group of atoms form a repetitive pattern which can be conveniently divided into small entities known as unit cells. A unit cell is chosen to represent the symmetry of the crystal structure. Therefore, a unit cell is a basic building block of the crystal structure.

Three relatively simple crystal structures are found for most of the metals: Face Centered Cubic (FCC) unit cells, Body Centered Cubic (BCC) unit cells and Hexagonal Close Packed (HCP) unit cells. Unit cell structures determine some of the properties of metals. For example, FCC structures are more likely to be ductile than BCC or HCP.

The crystal structure found for many metals has a unit cell of cubic geometry, with atoms located at each corner and centers of all the cube faces. This structure is called Face Centered Cubic (FCC) crystal structure. Some of the commonly used metals like aluminum, copper, gold and silver have FCC crystal structure. Figure 2.5 shows a model for the FCC unit cell, where the small circles represent the atom centers.

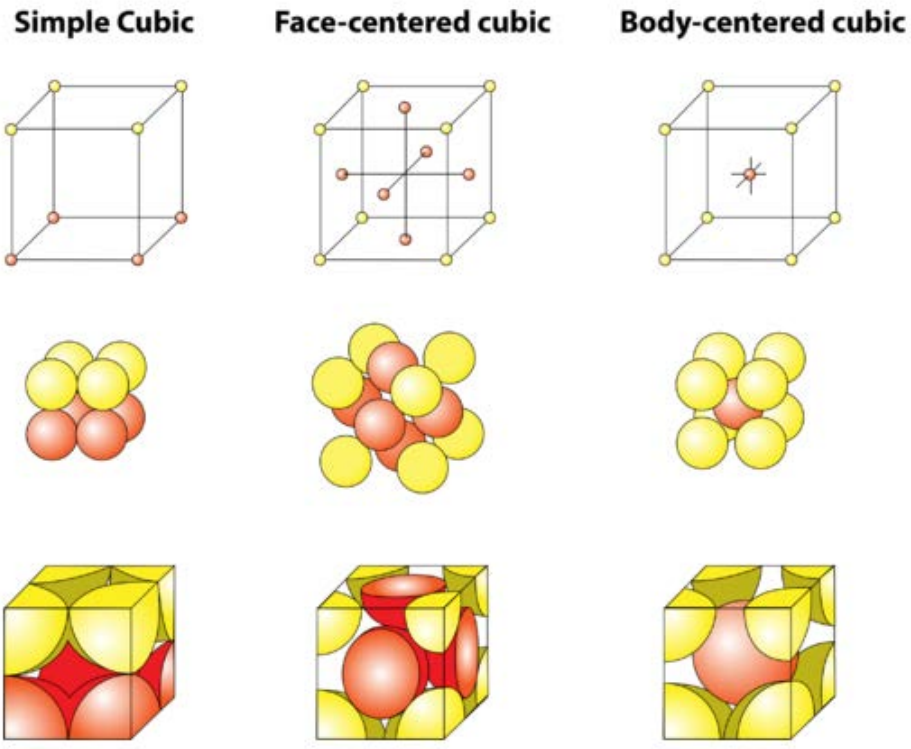

Figure 2.5: *Crystal structure for metals that has cubic geometry unit cell*

Body Centered Cubic (BCC) crystal structures also has cubic unit cells with atoms located at all eight corners and a single atom located at the center of cube. Figure 2.5 shows

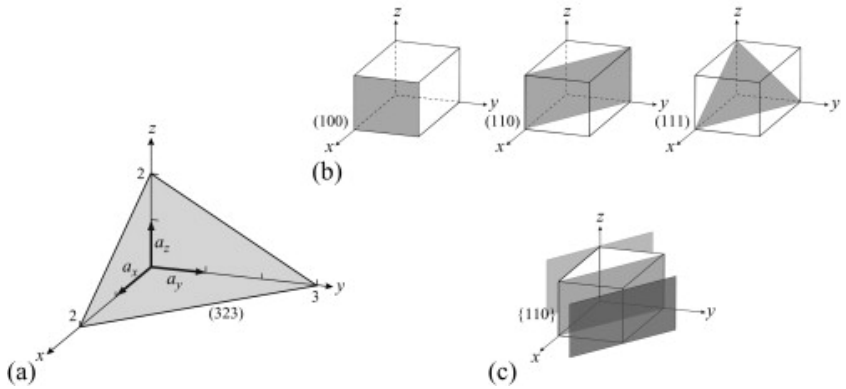

Figure 2.6: *Pictorial representation of different crystal planes in a cubic unit cell*

the crystal structure of BCC unit cells. Some of the metals that exhibit BCC structure are chromium, iron or tungsten.

Apart from cubic symmetry, some metals also exhibit non cubic symmetry, like hexagonal symmetry. These structures are termed as Hexagonal Close Packed (HCP) structures. The top and bottom faces of the hexagonal unit cell consists of six atoms that form regular hexagons and surround a single atom located in the center. Another plane that provides three additional atoms to the unit cell is situated between the top and the bottom planes. Hexagonal Close Packed (HCP) metals include titanium, zirconium and magnesium.

For understanding crystalline materials, it becomes necessary to specify a particular point, a crystallographic direction and a crystallographic plane of atoms. A crystallographic direction is defined as a line between two points, or a vector. Basically three indices are used for representing the projections of the vector. They are characterized by enclosing the indices in square brackets [uvw]. u, v, w are integers corresponding to the projections of the vector along x, y and z axes respectively. Commonly used directions in cubic crystallographic system are [100], [110] and [111].

Crystallographic planes are also defined in a similar manner, with the unit cell as the basis. Crystallographic planes are specified by three Miller indices as (hkl). Plane examples in a cubic crystallographic system are (100), (110) and (111) and are drawn in a FCC unit cell as shown in figure 2.6. Any two planes parallel to each other are equivalent and have identical indices.

Single crystal materials are characterized by a periodic and repeated arrangement of cells extended throughout the entirety of the specimen without interruption. All unit cells interlock in the same way and have the same orientation. Similarly polycrystalline materials are composed of collections of many small single crystals or grains. These grains have random crystallographic orientations and exists some atomic mismatch within the region where two grains meet. This area is called grain boundary.

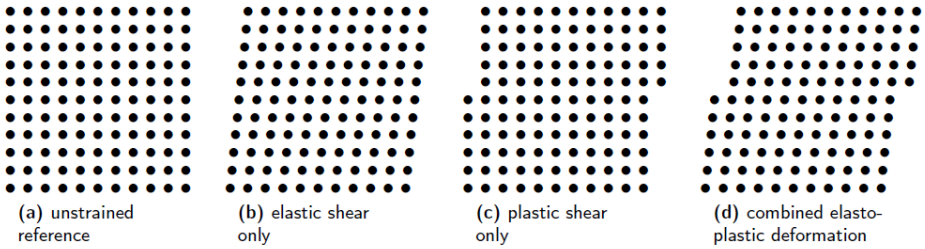

Figure 2.7: *Elastic and plastic deformation in a cell. Figure adopted from Roters et al. (2011)*

2.2.2 Elastic and plastic deformation of crystals

In a crystal lattice, the atoms are arranged in the three dimensions and the atoms are held together by atomic bonding. Deformation of crystal lattices, because of the changes in the positions of atoms, are crucial for understanding the behavior of systems defined on larger length scales. Continuum mechanics are very useful for describing elastic and plastic effects on the mesoscopic and/or macroscopic scales.

2.2.2.1 Elastic deformation

When a definite force is applied on a crystal lattice, the atoms start moving around. When the atoms in a crystal lattice are forcefully displaced without changing their neighbouring atoms, we say the crystal has deformed elastically. In stress free configuration, the atoms are pulled back to its original position because of the bonding between atoms.

2.2.2.2 Plastic deformation

If the movement of atoms is high exceeding a threshold limit of atomic bonding, then the atoms cannot come back to its original position and a permanent deformation is generated. Plastic deformation takes place by a process of slip on certain crystal planes under the action of a shear stress. The lowest stress to displace the atoms permanently from its original position is called as yield stress. Figure 2.7 shows a scheme of different types of deformation (elastic, plastic and elasto-plastic). Normally plastic deformation relaxes stress in the system by allowing the crystal shape change in stress free configuration.

Theoretically, the stress needed to deform plastically a perfect crystalline structure is much higher than the measured force. The existence of dislocations, twinning and transformation mechanisms produces plastic deformation of crystals at stresses well below the theoretical shear strength of a perfect crystal.

2.2.2.3 Dislocations

Dislocations are defined as 1D line of defects in the lattice that can move under shear stress. Plastic deformation occurs when atoms start moving by forming new bonds and breaking old bonds. Less energy is required to break a single bond as compared to the energy required to break all bonds on the entire plane of atoms at once. Dislocations are said to be carriers of plastic deformation as they contribute to crystalline material deformation.

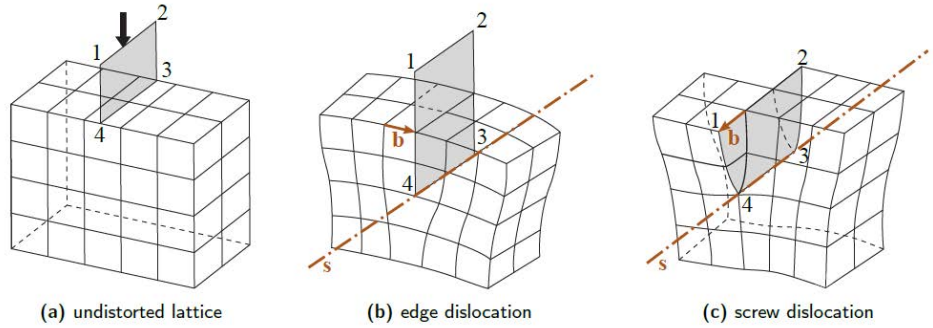

Figure 2.8: *Undistorted lattice compared to a lattice with an edge and screw dislocation. Figure adopted from Roters et al. (2011)*

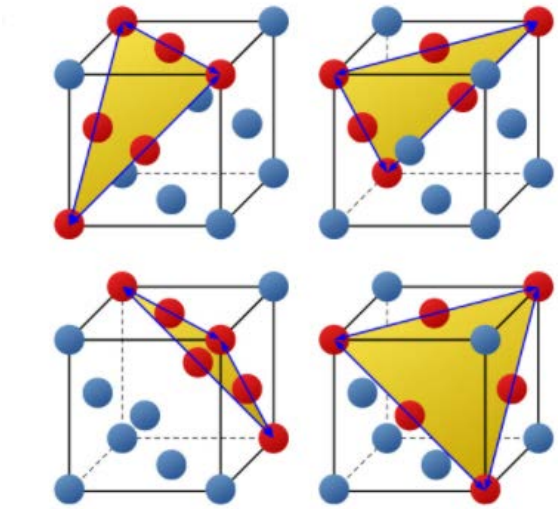

Figure 2.9: *Representation of* {111} *family of slip planes in an FCC single crystal unit cell.Figure adopted from Roters et al. (2011)*

Dislocations are characterized by two vectors namely tangential vector and burger vector. Tangential vector (**s**) describes the line of dislocation, whereas burger vector (**b**), describes the length and direction of dislocation. Based on these two vectors (**s** and **b**) dislocations are distinguished into two types, edge dislocation and screw dislocation as shown in figure 2.8.

1. Edge dislocation: in edge dislocation, burger vector is perpendicular to the line direction as shown in figure 2.8. This dislocation will create an additional (in-plane) layer of atoms due to asymmetrical nature of edge dislocation. The stress field around edge dislocation is complex.

2. Screw dislocation: in screw dislocation, burger vector is parallel to the line of dislocation. By cutting the plane through the crystal and slipping one side by a lattice vector, we can construct a screw dislocation as shown in figure 2.8. Stress field around screw dislocation is simpler compared to edge dislocation.

In a crystalline structure, dislocation movement is restricted only to certain paths. The path of dislocation movement constitute a slip system. Each slip system contains a slip plane

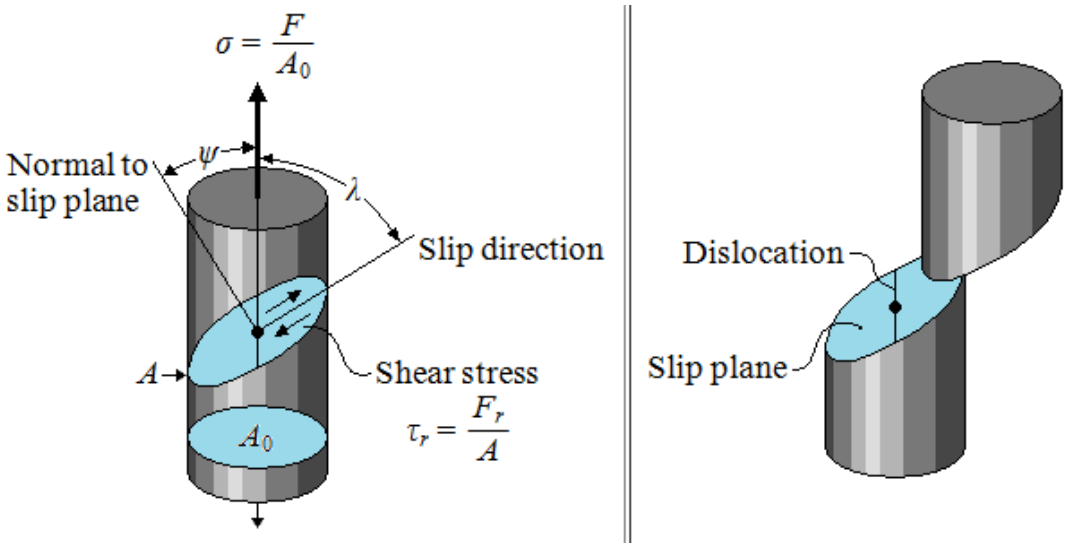

Figure 2.10: *Schmid factor: Resolved shear stress on slip plane and movement of dislocation on slip plane. Figure adopted from Roters et al. (2011)*

and a slip direction. A slip plane is a plane with the closest package of atoms and a slip direction is a densely packed direction within a slip plane. Minimum energy is required for the movement of dislocations in the slip system, hence it is always preferred for dislocation movement. Normally, edge dislocations slips only in a single plane whereas screw dislocations may slip in the direction of any plane. Depending on the structure of a crystal, different densely packed planes are available. For FCC crystal structure, planes are {111} (the notation {111} in curly brackets is used for all the family of planes that are equivalent to (111) by the symmetry of the lattice) and densely packed direction is <110> (the family of crystal directions that are equivalent to the direction [110] is notated as <110>) . For FCC crystal structure there are 12 slip systems and four 111 planes as shown in figure 2.9. Within each plane there are three independent <110> directions as shown in table 2.1:

Table 2.1: *Slip systems* $\{\widetilde{\mathbf{m}}^{\alpha}, \widetilde{\mathbf{n}}^{\alpha}\}$ *of the FCC crystal structure*

α	$\widetilde{\mathbf{n}}_{\alpha}$	$\widetilde{\mathbf{m}}_{\alpha}$	α	$\widetilde{\mathbf{n}}_{\alpha}$	$\widetilde{\mathbf{m}}_{\alpha}$
1	(111)	$[\bar{1}01]$	7	$(\bar{1}11)$	$[0\bar{1}1]$
2	(111)	$[0\bar{1}1]$	8	$(\bar{1}11)$	[101]
3	(111)	$(1\bar{1}0]$	9	$(\bar{1}11)$	[110]
4	$(1\bar{1}1)$	$[\bar{1}01]$	10	$(11\bar{1})$	$[\bar{1}10]$
5	$(1\bar{1}1)$	[011]	11	$(11\bar{1})$	[101]
6	$(1\bar{1}1)$	[110]	12	$(11\bar{1})$	[011]

2.2.2.4 Slip activity in single crystals

Slip system activity arises from the movement of edge, screw, or mixed dislocations in response to shear stresses applied along a slip plane and a slip direction. Even though an applied stress may be pure tensile/compressive, shear components exists along a slip plane that is other than perpendicular or parallel to the stress axis. These are termed as resolved shear stresses.

The magnitude of resolved shear stress depends not only on the applied stress, but also on the orientation of both slip plane and slip direction as shown in figure 2.10. It can be shown that for a applied stress σ, the resolved shear stress τ_R can be written as

$$\tau_R = \sigma \; cos\Psi \; cos\lambda \tag{2.27}$$

where Ψ represents the angle between the tensile axis and the slip-plane normal, and λ the angle between the slip direction and the tensile axis. The quantity $cos\Psi \; cos\lambda$ is called the Schmid factor.

It is well known that a single crystal has a number of different slip systems that can be operative at the same time. Therefore, the resolved shear stress normally differs for each one because of the relative orientation of each axis to the stress is different.

In response to the applied tensile or compressive stress, slip in a single crystal commences on the most favorable oriented slip system when the resolved shear stress reaches a critical value, termed critical resolved shear stress. Critical resolved shear stress (τ_{crss}) represents the minimum shear stress required to initiate slip, and is a property of the material that determines when yielding occurs. Single crystals starts yielding when $\tau_R = \tau_{crss}$. The magnitude of the applied stress required to initiate yielding (σ_y) is given by equation 2.28 when $\sigma = \sigma_y$ and $cos\Psi \; cos\lambda = (cos\Psi \; cos\lambda)_{max}$.

$$\sigma_y = \frac{\tau_{crss}}{(cos\Psi \; cos\lambda)_{max}} \tag{2.28}$$

During deformation of crystals, the dislocations accumulate, interact with one another and serve as pinning points or obstacles that significantly impede their motion. Because dislocation motion is hindered, plastic deformation cannot occur at normal stresses. On this basis, an increase in dislocation density leads to an increase in the yield strength of the material and the subsequent decrease in ductility. The resistance to dislocation-formation manifests as material strengthening or work hardening.

2.2.3 Large strain elastoplastic model

In this point the proposed constitutive model used in this work is presented. First main results of kinematics problem are given followed by a summary of the constitutive equations.

2.2.3.1 Kinematics

The kinematics for elasto-plastic crystal behavior is defined within the finite deformation framework. According to this framework, the deformation gradient tensor is written as the product of the elastic and plastic part as discussed in section 2.1.1.6:

$$\mathbf{F} = \mathbf{F}_e\mathbf{F}_p \tag{2.29}$$

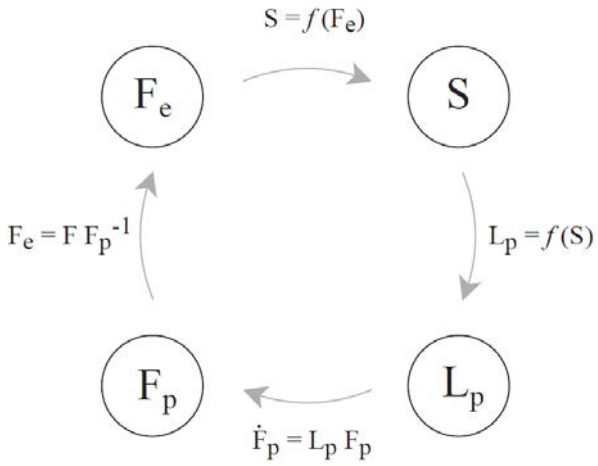

Figure 2.11: *Generalised elasto-viscoplastic calculation loop. Figure adopted from Roters et al. (2011)*

Based on the multiplicative decomposition of deformation gradient $\mathbf{F}$, we can derive velocity gradient $\mathbf{L}$. $\mathbf{L}$ is decomposed additively into elastic $\mathbf{L}_e$ and plastic $\mathbf{L}_p$ velocity gradients as given by equation 2.30:

$$\mathbf{L} = \mathbf{L}_e + \mathbf{L}_p = \mathbf{F}_e \mathbf{F}_e{}^{-1} + \mathbf{L}_p \tag{2.30}$$

Plastic velocity gradient $\mathbf{L}_p$ depends on the underlying microstructure, represented by variable ζ and stress state $\mathbf{S}$ as shown in equation 2.31:

$$\mathbf{L}_p = \mathbf{f}(\mathbf{S}, \zeta) \tag{2.31}$$

where ζ depends on the kind of plasticity model used and $\mathbf{S}$ is the second Piola Kirchhoff stress given by equation 2.32:

$$\mathbf{S} = \frac{\mathbb{C}}{2}(\mathbf{F_e}{}^T \mathbf{F_e} - \mathbf{I}) \tag{2.32}$$

being $\mathbb{C}$ the elastic IVth order stiffness tensor.

The rate of plastic deformation $\dot{\mathbf{F}}_p$ is defined as:

$$\dot{\mathbf{F}}_p = \mathbf{L}_p \mathbf{F}_p \tag{2.33}$$

The set of nonlinear equations previously presented needs to be solved iteratively, as all the parameters are dependent on each other. The idea of the iterative process is to start by guessing any one of the component and find the remaining components by following the loop as shown in figure 2.11, until predicted values converges for given guessed values.

2.2.3.2 Constitutive model for an FCC single crystal

In this work, it is assumed that the plastic deformation occurs by dislocation glide on slip systems, therefore the evolution of the plastic part follows the equation

$$\dot{\mathbf{F}}^{\mathrm{p}} = \left(\sum_{\alpha=1}^{N^{\mathrm{S}}} \dot{\gamma}_\alpha \widetilde{\mathbf{M}}_\alpha \right) \mathbf{F}^{\mathrm{p}} , \quad \widetilde{\mathbf{M}}_\alpha = \widetilde{\mathbf{m}}_\alpha \otimes \widetilde{\mathbf{n}}_\alpha \tag{2.34}$$

$\widetilde{\mathbf{M}}_\alpha$ being a Schmid tensor where the slip directions $\widetilde{\mathbf{m}}_\alpha$ and planes $\widetilde{\mathbf{n}}_\alpha$ are specified in the intermediate configuration. It should be noted that the plastic deformation described by Eq.2.34 is volume preserving, $\det \mathbf{F}^{\mathrm{p}} = 1$, since $\widetilde{\mathbf{m}}_\alpha \cdot \widetilde{\mathbf{n}}_\alpha = 0$. The current orientation of crystallographic directions and planes can be found using the elastic part of the deformation gradient as follows

$$\mathbf{n}(t)_\alpha = (\mathbf{F}^{\mathrm{e}T})^{-1} \widetilde{\mathbf{n}}_\alpha , \quad \mathbf{m}(t)_\alpha = \mathbf{F}^{\mathrm{e}} \widetilde{\mathbf{m}}_\alpha . \tag{2.35}$$

Because the face centred cubic (fcc) crystal structure is considered in the study, the dislocations glide happens on the $\{111\}$ planes in $\langle 110 \rangle$ directions. For the $N^{\mathrm{S}} = 12$ slip systems, the slip planes and directions are listed in Table 2.1.

The shear rate $\dot{\gamma}_\alpha$ on a given slip system α is related the stress state by the phenomenological visco-plastic type power law (Asaro and Needleman, 1985)

$$\dot{\gamma}_\alpha = \dot{\gamma}_0 \left| \frac{\tau_\alpha}{\hat{\tau}_\alpha} \right|^{p_1} \operatorname{sign}(\tau_\alpha). \tag{2.36}$$

with the resolved shear stress

$$\tau_\alpha = \widetilde{\mathbf{T}} \cdot \widetilde{\mathbf{M}}_\alpha \tag{2.37}$$

where the parameter $\dot{\gamma}_0$ is the reference shear rate, p_1 is the inverse of the strain rate sensitivity parameter and $\widetilde{\mathbf{T}}$ is the Mandel stress. When the elastic strains are small as compared to the inelastic ones, the Mandel stress can be approximated by the IInd Piola-Kirchhoff stress pushed forward to the intermediate configuration $\widetilde{\mathbf{S}}$, namely:

$$\widetilde{\mathbf{T}} = \underbrace{(\mathbf{F}^{\mathrm{e}T} \mathbf{F}^{\mathrm{e}})}_{\approx \mathbf{I}} \widetilde{\mathbf{S}} \approx \mathbf{F}^{\mathrm{p}} \mathbf{S} \mathbf{F}^{\mathrm{p}T} \tag{2.38}$$

The stress tensor $\widetilde{\mathbf{S}}$ is calculated with help of the hyperelastic law assuming the Kirchhoff-type function of free energy density per unit volume in the reference configuration

$$\widetilde{\mathbf{S}} = \frac{\partial \Psi}{\partial \mathbf{E}^{\mathrm{e}}} = \mathbb{C} \cdot \mathbf{E}^{\mathrm{e}} \quad \text{where} \quad \mathbf{E}^{\mathrm{e}} = \left[\frac{1}{2} \left(\mathbf{F}^{\mathrm{e}T} \mathbf{F}^{\mathrm{e}} - \mathbf{I} \right) \right] \tag{2.39}$$

with $\mathbb{C}$ the elastic IVth order stiffness tensor.

The critical resolved shear stress $\hat{\tau}_\alpha$, obeys the following evolution rule (Kalidindi et al., 1992)

$$\dot{\hat{\tau}}_\alpha = h_0 \sum_{\beta=1}^{N^S} q_{\alpha\beta} \left(1 - \frac{\hat{\tau}_\beta}{\hat{\tau}_s}\right)^{p_2} |\dot{\gamma}_\beta| \tag{2.40}$$

where h_0 is the initial hardening rate, $\hat{\tau}_s$ the saturation resistance, p_2 the hardening exponent and $q_{\alpha\beta}$ the cross hardening coefficient matrix. The model parameters for elasticity and plasticity used in Chapters 3, 4 and 5 are given in Table 2.2.

The constitutive equations mentioned above are implemented into a user subroutine UMAT in ABAQUS/Standard (2019). The implementation of the crystal plasticity model follows the time integration procedure with the consistent material tangent operator presented by Meissonnier et al. (2001) and is described in detail in appendix B and C. In particular, the evolution equation (2.34) is integrated using the expansion of tensor exponent into the Taylor series.

$$\mathbf{F}^p = \exp\left(\sum_{\alpha=1}^{N^S} \Delta\gamma_\alpha \widetilde{\mathbf{M}}_\alpha\right) \mathbf{F}^{p0} \approx \left(\mathbf{I} + \sum_{\alpha=1}^{N^S} \Delta\gamma_\alpha \widetilde{\mathbf{M}}_\alpha\right) \mathbf{F}^{p0} \tag{2.41}$$

Table 2.2: *Material parameters for crystal plasticity model (Han et al., 2013; Kalidindi et al., 1992)*

Parameter	**Notation**	**Value**
Reference shear rate	$\dot{\gamma}_0$ (s^{-1})	0.001
Inverse of strain rate sensitivity	p_1	20
Initial critical resolved shear stress	$\hat{\tau}_0$ (MPa)	20
Initial strain hardening modulus	h_0 (MPa)	180
Saturated critical resolved shear stress	$\hat{\tau}_s$ (MPa)	117
Strain hardening exponent	p_2	2.25
Self-hardening coefficient	$q_{\alpha\beta}$ ($\alpha = \beta$)	1
Latent hardening coefficient	$q_{\alpha\beta}$ ($\alpha \neq \beta$)	1.4
Elastic constants		
	c_{11} (GPa)	199
	c_{12} (GPa)	136
	c_{44} (GPa)	105

2.2.3.3 Measure of macroscopic stresses and strains in this work

Following a general homogenization approach, the definition of equivalent stresses and strains considered in this work is as shown by the equations below. Macroscopic Cauchy stress σ_{ij} components are related to the microscopic Cauchy stresses $\bar{\sigma}_{ij}$ through the relations:

$$\sigma_{ij} = \frac{1}{V_{cell}} \int_{V_{cell}} \bar{\sigma}_{ij} \, dV_{cell} \tag{2.42}$$

where V_{cell} denotes the volume of cell. The definition of macroscopic equivalent stress σ_{eqv}, triaxiality T and Lode parameter L are given by:

$$\sigma_{eqv} = \sqrt{\frac{3}{2}\,\sigma'_{ij}\sigma'_{ij}}; \quad T = \frac{\sigma_h}{\sigma_{eqv}}; \quad L = \frac{2\sigma_2 - \sigma_1 - \sigma_3}{\sigma_1 - \sigma_3} \tag{2.43}$$

with

$$\sigma'_{ij} = \sigma_{ij} - \sigma_h \delta_{ij}; \qquad \sigma_h = \frac{\sigma_{ii}}{3} \tag{2.44}$$

and σ_1, σ_2 and σ_3 the principal macroscopic true stress components. Following Srivastava and Needleman (2015b), an equivalent strain is calculated based on the following numerical volume average of local logarithmic strain $\bar{\varepsilon}_{ij}$, namely:

$$\langle \varepsilon_{ij} \rangle = \frac{1}{V_{matrix}} \int_{V_{matrix}} \bar{\varepsilon}_{ij} dV_{matrix} \tag{2.45}$$

where V_{matrix} denotes the volume of the cell excluding the void. It must be stressed that, in general, this volume averaged value $\langle \varepsilon_{ij} \rangle$ is not equal to the macroscopic logarithmic strain as long as deformation is non-uniform. The definition of the equivalent strain is then proposed as follows:

$$\varepsilon_{eqv} = \sqrt{\frac{2}{3}\,\langle \varepsilon'_{ij} \rangle\,\langle \varepsilon'_{ij} \rangle} \quad \text{where} \quad \langle \varepsilon'_{ij} \rangle = \langle \varepsilon_{ij} \rangle - \varepsilon_h \delta_{ij}\,; \quad \varepsilon_h = \frac{\langle \varepsilon_{ii} \rangle}{3} \tag{2.46}$$

This value is used only for the purpose of graphical presentation of results and remains common through out this thesis.

Part II

Crystal plasticity modelling of void growth in single crystals and bi-crystals

3

Numerical study of single crystals without voids: effect of Orientation

Contents

3.1 Introduction

In the previous section, a brief overview of important aspects of crystalline plasticity, constitutive equations and its implementation in the continuum framework has been given. In this section, our attention is focused on how micromechanical features included in continuum analysis of large strain plasticity of single crystals reproduces slip phenomenons, crystal rotation and texture.

It is well known that in single crystals, the yield stress for uni-axial tension varies depending on the loading direction (Asaro, 1983) as shown in figure 3.1. For the purpose of understanding the single crystal response considering more complex loading conditions, 6 different orientations are analyzed in this chapter. For each of these orientations numerical tests are performed at different triaxialities and Lode parameters considering a representative unit cell. Based on the obtained results, the orientations will be categorized as soft and hard orientations. The obtained results will act as a road map for our future studies of porous single crystals and bi-crystals.

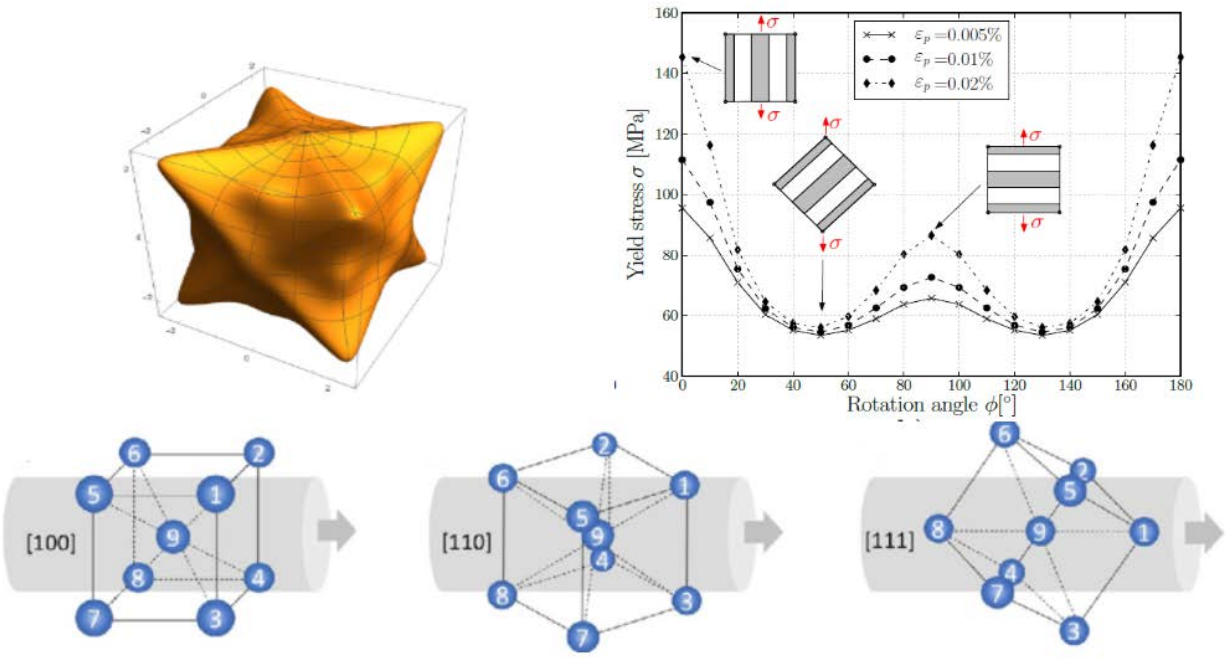

Figure 3.1: *Critical yield stress for uniaxial tension in different direction along crystal axis for a FCC unit cell single crystal.*

Orientations in terms of miller indices and respective Euler angles used in this section are given in table 3.1. Orientations in terms of miller indices represents the direction cosines in crystal coordinate system. Orientation in the matrix is constructed by using the direction cosines. First row represents miller index parallel to specimen X direction and last row represents miller index parallel to specimen Z direction. In orientation 1 and as example, specimen cell X axis is parallel to [100] and Z axis is parallel to [001]. The method used for calculating

Euler angles from miller indices is well documented and a brief explanation is given considering some examples in Appendix E.

Table 3.1: *Orientation of single crystal matrix for different RVE's in terms of Euler angles. The Euler angles are defined with respect to global axis(X,Y,Z)*

RVE	**Bunge euler angles (°)** (ϕ_1, Φ, ϕ_2)	**Crystallographic orientation on global coordinates X-Z**
O1	(0,0,0)	[100] -[001]
O2	(0,45,0)	[100] -[011]
O3	(45,0,0)	[110] -[001]
O4	(45,54.73,0)	$[1\bar{1}0]$ -[111]
O5	(0,45,54.73)	[111] -$[1\bar{1}0]$
O6	(45,35.26,90)	$[1\bar{1}1]$ -$[\bar{1}12]$

3.2 Representative volume element

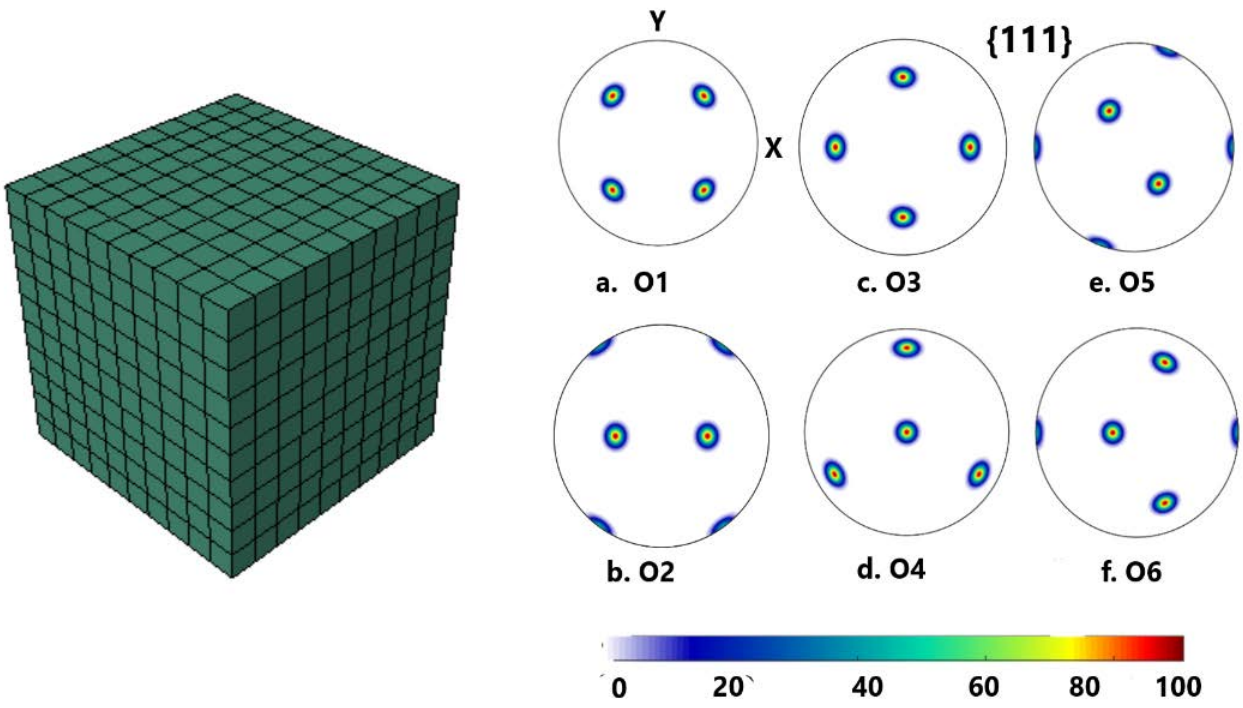

Figure 3.2: *Cell used for studying the behavior of the single crystal.Pole figures representing the initial orientations studied in this work.*

For studying the effect of orientation in a single crystal, the representative volume element used in this work consist of a cubic cell as shown in figure 3.2. The complete cell is discretized into 1000 C3D8R elements. Initially, the unit cell is aligned such that the edges of the unit cell are parallel to the global XYZ axes. The notation adopted here denotes each orientation by the crystallographic directions, aligned with the main loading direction. The main loading direction is parallel to the X axis and the secondary loading direction is parallel to Z or Y

axis depending on the selected Lode parameter. A dimensionless equivalent strain rate $\dot{\epsilon}_0/\ \dot{\gamma}_0$ in the range $(100 - 150)$ is ensured in all simulations.

As previously mentioned, six crystallographic orientations are used in this study. Orientations are given in terms of the Bunge Euler angles and crystallographic planes parallel to each loading direction are as shown in table 3.1. Pole figures for the orientations considered are shown in figure 3.2. For simplicity, each 6 orientations will be henceforth called O1 - O6 as shown in table 3.1. The material of the unit cell is modelled as a single crystal using the rate dependent crystal plasticity constitutive relations discussed in section 2.2.3.2. Material parameters are given in table 2.2. The plastic parameters of the material analyzed in this work correspond to annealed OFHC copper (Kalidindi et al., 1992). Three dimensional finite element calculations are carried out on the cell under different loading conditions. Different triaxiality and Lode parameters are applied to the cell following the method developed in Appendix D. Periodic boundary conditions, as explained in Appendix D are applied to the cell.

3.3 Results and discussion

3.3.1 Effect of orientation on stress strain curve

The effect of the orientation on the response of a single crystal is analyzed in this section. Results in the form of stress strain curves and deformed cell shape are presented for each of the 6 orientations studied.

Figure 3.3a shows the $\sigma_{eqv} - \epsilon_{eqv}$ relation for different Lode parameters on the single crystal cell. As it is well known that there is no effects of hydrostatic components of stress tensor on the Schmid criterion, only one triaxiality is considered in this case ($T = 1/3$). For a given triaxiality, the response of the single crystal is characterized by the value of the yield stress. The orientation is considered harder for a given Lode parameter if the yield stress curve is higher, and softer is the yield stress curve is lower. As shown in the figure, for O1, the value of the yield stress is higher for $L = -1, 1$ and lower for $L = 0$. We can therefore say that O1 orientation has a harder response for $L = 1, -1$ and a softer response for $L = 0$.

For orientation 2 (O2), specimen cell X axis is parallel to [100] and Z axis is parallel to [011]. Figure 3.3b shows the $\sigma_{eqv} - \epsilon_{eqv}$ relation for different Lode parameters. As seen in the figure, the equivalent yield stress is higher for $L = -1$, closely followed by $L = 1$ and lower for $L = 0$. For O2, we can say that $L = -1, 1$ gives harder response if compared to $L = 0$.

Orientation 3 (O3) is similar to O2, but here specimen X axis is parallel to [110] and [001] is parallel to specimen Z axis (opposite to O2). The response of the single crystal cell for different Lode parameters is as shown in figure 3.3c. For $L = 1$, we obtain the hardest response, followed by $L = -1$ and softer response for $L = 0$. The response of O2 and O3 for $L = 1$ and $L = -1$ are completely opposite to each other, i.e., the response of O2 for $L = 1$ is the same as the response of O3 for $L = -1$. Similarly, the response of O2 for $L = -1$ is the same as $L = 1$ for O3. The response of O2 and O3 is the same for $L = 0$.

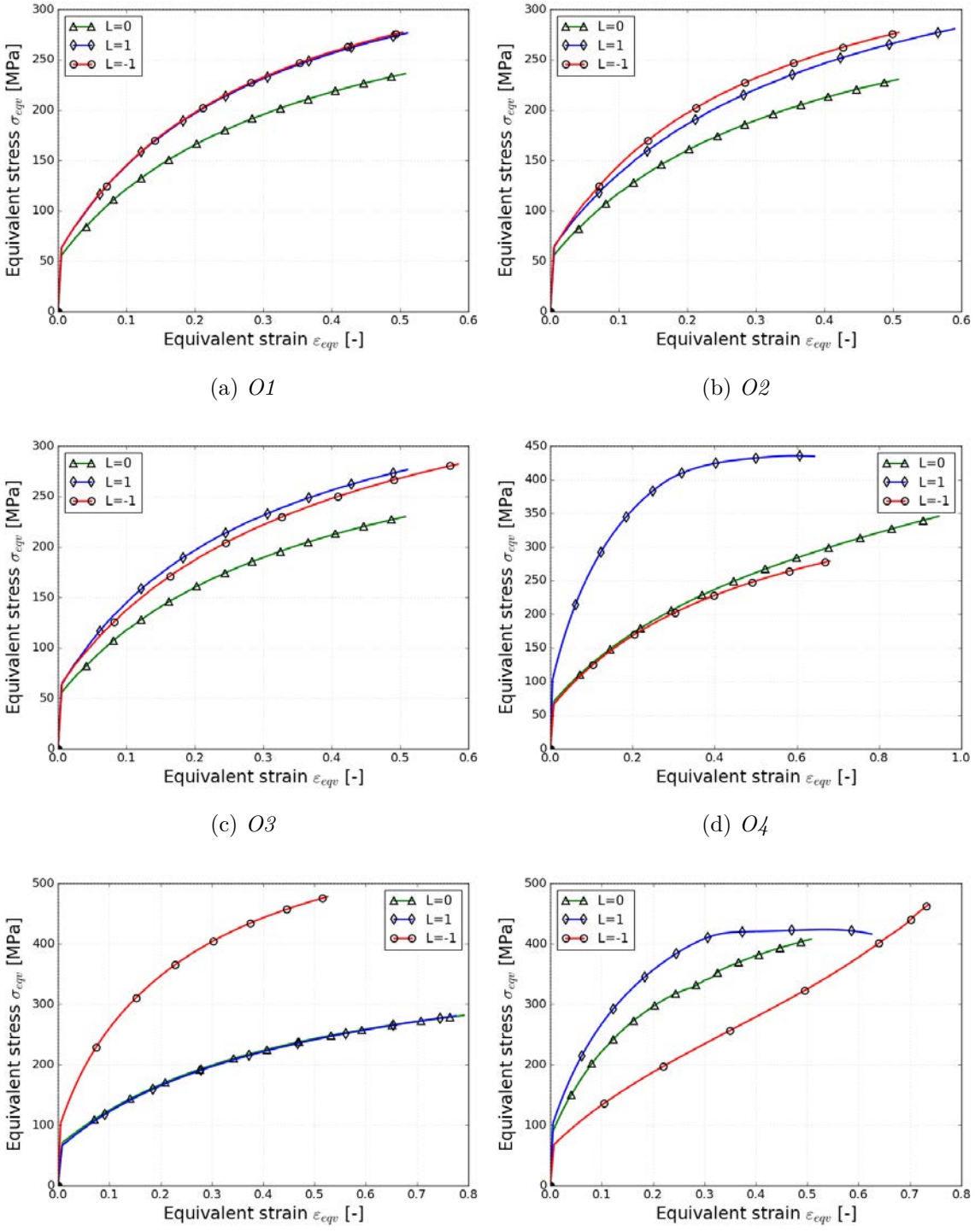

(a) *O1* (b) *O2*

(c) *O3* (d) *O4*

(e) *O5* (f) *O6*

Figure 3.3: *Equivalent stress - Equivalent strain for single crystals at different Lode parameters and crystal orientations.*

For orientation 4 (O4), specimen cell X direction is parallel to [110] and Z direction is parallel to [111]. Coordinate planes normal to $< 111 >$ crystallographic orientation does not posses any symmetry as in the case of $< 100 >, < 110 >$, and periodic boundary conditions will allow the cell to deform along non principal directions. As we can see from figure 3.3d, the

response of the cell for $L = 1$ is harder and for $L = -1, 0$ is softer. $L = -1$ has slightly higher equivalent yield stress compared to $L = 0$.

For O5, specimen X direction is parallel to [111] and Z direction is parallel to [011]. As in the case of O4, there is no crystal symmetry along <111> and periodic boundary conditions applied along the faces will allow the cell to deform along non principal directions. Figure 3.3e shows the response of the cell considering different Lode values. $L = -1$ produces the hardest response followed by $L = 0$ and softer response is observed for $L = 1$. The response of O4 and O5 are opposite to each other for $L = 1$ and $L = -1$. Orientation O4 at $L = 1$ has the same response as orientation O5 for $L = -1$. Similarly orientation O4 at $L = -1$ has the same response as orientation O5 at $L = 1$.

For O6, [-112] is parallel to X direction and [1-11] is parallel to Z direction. As shown in figure 3.3f the plot of $\sigma_{eqv} - \epsilon_{eqv}$ shows the difference in the yield stress behavior for all 3 Lode parameters. $L = 1$ gives the hardest response followed by $L = 0$ and $L = -1$ gives the softest response.

3.3.2 Effect of orientation on deformed cell shape

When the loading is applied along a specific crystallographic direction, single crystals exhibit specific deformation modes. For O1 and when triaxiality and Lode parameter are prescribed in the cell following the method developed in Appendix D, the cell deforms only along the principal loading axes. This is because of the crystal symmetry, i.e., reflection planes normal to $< 100 >$. Single crystals with O1 orientation gives an isotropic response. By using the definition of $\mathbf{L}_p$ it is observed that non diagonal components of $\mathbf{L}_p$ are zero and hence we observe deformation only along the principal directions. From the deformed cell, we can see that crystal undergoes uniform expansion/contraction along the faces of the cell and the cell shape remains a rectangular prism during the whole deformation process. The deformed cell shapes for O2 and O3 looks similar to the case of O1, because of the crystal symmetry along $< 110 >$.

For O4, O5 and O6, because of the orientation of the single crystal, we observe some non-zero off-diagonal terms in $\mathbf{L}_p$. Due to $\mathbf{L}_p$ non diagonal terms, we observe non principal deformation of cell accommodating rotations. Because of periodic boundary conditions applied in the external surfaces of the cell, the cell is allowed to move freely in non principal directions. By allowing shear deformations in the cell, we make sure that non principal stresses are zero, hence triaxiality and Lode parameters and the response of the cell remains completely homogeneous. Depending on the orientation, we observe different off diagonal component values for O4, O5 and O6.

For O4, as we can see from figure 3.4, the cell for different Lode parameters deform in directions other than principal directions, i.e., cell has shearing deformation. For O5 and O6 orientations, the cell deformation behaviour is similar to O4. For brevity these figures are not presented in this thesis.

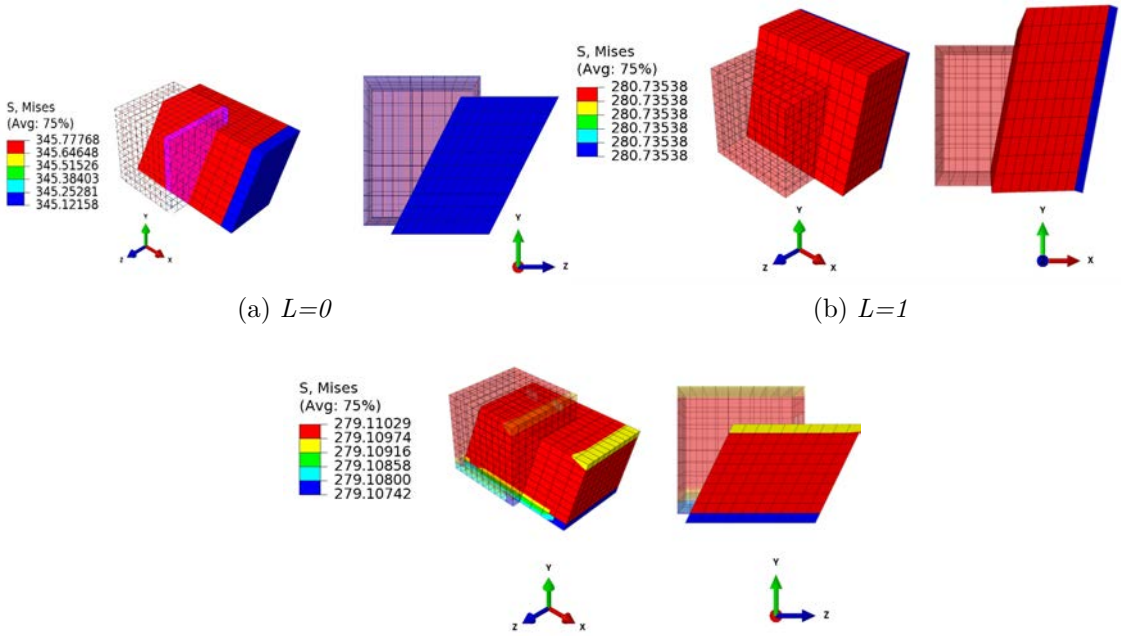

(a) *L=0* (b) *L=1*

(c) *L=-1*

Figure 3.4: *Deformed cell shapes for O4 orientations at different Lode parameters at* $\varepsilon_{eqv} = 0.6\%$.

3.4 Summary and conclusions

The main purpose of the study in this section is to categorize crystals based on their orientation for a given loading condition as soft and hard crystals. In order to simplify the observations, new plots of stress strain curves $\sigma_{eqv} - \epsilon_{eqv}$ are presented in figures 3.5. Here we have commonized the plots based on Lode parameters, so that we can compare all orientations in the same figure. Stress-strain curves for different orientations are represented for $L = -1$, 0 and 1. This will help us to clearly define hard and soft orientation for a given Lode value.

In figure 3.5, different colours represents different orientations: blue for O1, green for O2, red for O3, cyan for O4, magenta for O5 and black for O6. For $L = -1$, as shown in figure 3.5a, O5 and O6 orientations produces the hardest response, followed by O4 orientation and softer response is observed for O1, O2 and O3. For $L = 1$, as shown in figure 3.5b, O4 orientation produces the hardest response, followed by O5 orientation, afterwards by O6 orientation and softer response is observed for O1, O2 and O3 orientations. Similarly, for $L = 0$, as shown in figure 3.5c the hardest response is obtained for O4 orientation, followed by O5 and O6 orientation respectively and the softest response is observed for O1, O2, O3.

In this section, we analyzed the effect of Lode parameter on each orientation and for a given orientation and Lode parameter, we observed a hard and soft response of the single crystal. It is clear from the figures that for anisotropic orientations O4, O5, O6, we observe harder response as compared to O1, O2, O3, which produces softer response irrespective of Lode parameter.

Based on these results, in the following sections we will consider only four orientations instead of the six orientations presented here, two hard orientations and two soft orientations,

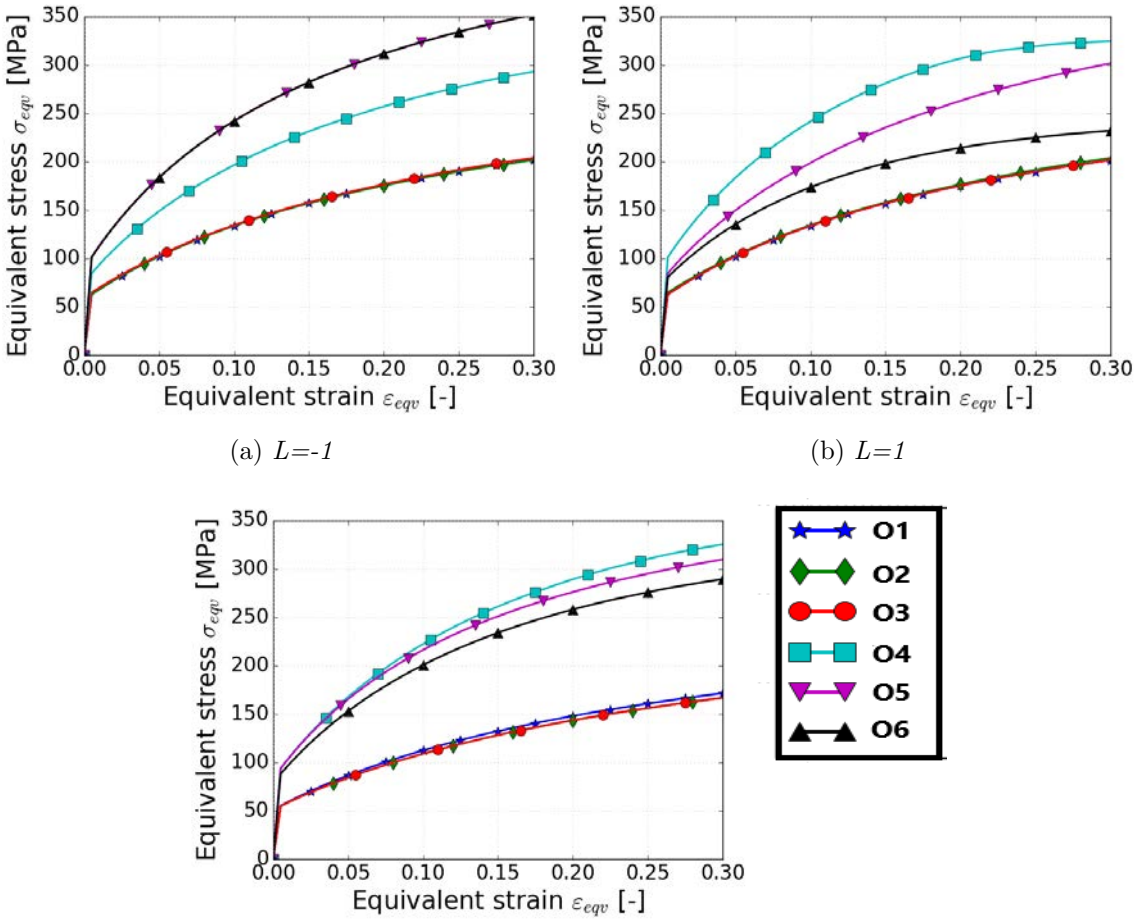

(a) *L=-1*

(b) *L=1*

(c) *L=0*

Figure 3.5: *Equivalent stress - Equivalent strain for single crystals for different Lode parameters and different crystal orientations. The presented curves are the same for all triaxiality values considered.*

to characterize the soft and hard crystal behavior irrespective of the Lode parameter and triaxiality value analized. For hard orientations we will select O4 and O6 orientations, whereas for soft orientations we will select O1 and O2 orientations. Based on the observation of deformed cell shapes, it is important to clear that, and in order to allow cells to deform freely in shear directions, that simulations performed in future sections will be subjected to periodic boundary conditions irrespective of the crystal orientation considered.

In future chapters, we will use the results and observations from this section as a base to understand the effect of orientation, triaxiality and Lode parameter on void and cell behavior in single crystals and bi-crystals with a void inside.

4

Numerical study of void growth in porous single crystals

Contents

4.1 Introduction

The prediction of damage and fracture in ductile materials is essential to ensure structural integrity and failure mitigation in several advanced engineering applications such as high-speed machining (Chen et al., 2011), projectile penetration (Nahshon and Hutchinson, 2008), ballistic impact on armor steels (McDonald et al., 2019) or crack propagation (Besson, 2010a) among others.

Ductile fracture in structural materials has been subject of many studies over the past decades and is known to occur by void nucleation, growth and final coalescence of voids. The voids in the ductile material either pre-exists toda2014true or nucleate at material inclusions due to de-cohesion of the matrix–particle interface or particle cracking (Maire et al., 2011; Segurado and LLorca, 2005).

During the past decades, numerous micromechanics based models have been developed to capture the evolution of ductile damage (Gurson, 1977a; Tvergaard, 1981; Tvergaard and Needleman, 1984; Duva and Hutchinson, 1984; Gologanu et al., 1997, 2001). All the above mentioned models concern matrix materials with isotropic behavior.

Rolled plates, extruded profiles, and other formed structural components typically exhibit plastic anisotropy as reported in several experimental studies (Benzerga et al., 2004a; Fourmeau et al., 2013a; Khadyko et al., 2014). Important efforts have been also made over the years to describe the plastic behavior of anisotropic ductile materials considering orthotropic matrix material obeying the Hill (1948) anisotropic yield criterion (Benzerga et al., 2004a,b; Monchiet et al., 2008; Morin et al., 2015) or using continuum crystal plasticity models (Orsini and Zikry, 2001; Potirniche et al., 2006b; Liu et al., 2007b; Yerra et al., 2010a; Han et al., 2013; Lebensohn and Cazacu, 2012).

Finite element void cell computations have been widely used to investigate the behaviour of porous ductile solids (Koplik and Needleman, 1988; Tvergaard, 1982, 1990; Worswick and Pick, 1990). Following the unit cell approach, several studies have already been performed to address void growth in single crystals using classical crystal plasticity constitutive models within a rate dependent formulation (see Srivastava and Needleman (2013, 2015b); Yerra et al. (2010a)). Further Segurado and Llorca (2009) performed discrete dislocation simulations in order to treat explicitly the interaction between dislocations, crystal orientation and void growth in a more physical way. Most of these works have given a detailed view of the behaviour of the voids in both isotropic and anisotropic matrix.

For isotropic materials, the effect of triaxiality and Lode parameter can be analyzed in 3D cell simulations under prescribed loading conditions where the principal directions of the loading are aligned with the axes of the cell and the void. However, for anisotropic matrix materials, the response of the cell also depends on the orientation of the anisotropy axes. Recently, Dæhli et al. (2017) performed 3D unit-cell analyses imposing the external stress state of the cubic cell (macroscopic triaxiality and Lode parameter) and considering that the matrix material is governed by the anisotropic yield criterion Yld2004-18p (Barlat et al., 2005). The material

orthotropy directions were imposed to be collinear with the prescribed loading conditions and with the edges of the cell. Later, Hosseini et al. (2022) devised a novel strategy to perform unit cell calculations with a matrix material modeled using the macroscopic Yld2004-18 anisotropic yield criterion with prescribed misalignment between loading and material axes and, at the same time, macroscopic stress triaxiality and Lode parameter controlled to be constant during loading.

The main objective in this section is to investigate the effect of triaxiality, Lode parameter and crystal orientation on void growth. This analysis will be achieved using 3D finite element calculations considering periodic boundary conditions and constant (prescribed) values of stress triaxiality and Lode parameters. Material orthotropy directions will be collinear with the prescribed loading conditions. FCC single crystal will be described with the constitutive relations given in section 2.2.3.2. Material parameters are given in table 2.2. The obtained results from this work will be used for comparison with results of bi-crystals which will be presented in next chapter 5.

4.2 Representative volume element

Three dimensional finite element calculations are carried out to model the response of voids under different triaxial loading conditions (different triaxiality and Lode parameters) and different matrix orientations using a 3D cubic cell model. The 3D cubic cell contains a spherical void with initial radius R_0 at its center. The initial volume of the cubic cell is $V_0^{cell} = L_0^3$ and the initial volume of the spherical void $V^{void} = (4/3)\pi R_0^3$ so that the initial void volume fraction, defined as the ratio between the initial volume of the void and the initial volume of the cell, is $f_0 = V_0^{void}/V_0^{cell} = 4\pi R_0^3/3L_0^3 = 0.0044$. Cross-section of the cell with the void is as shown in figure 4.1. For controlling triaxiality and Lode parameter values, the procedure described in appendix D is followed. For both symmetric and non symmetric orientations, fully periodic boundary conditions are applied to the cell as described in appendix D.

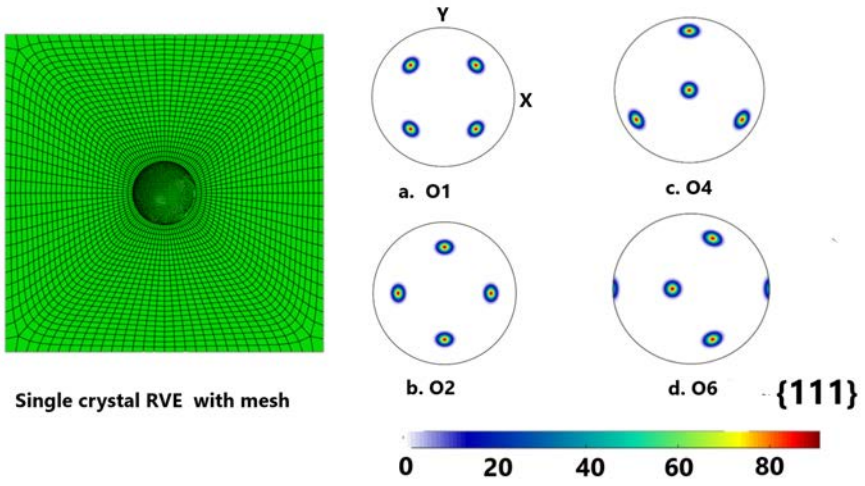

Figure 4.1: *Cell containing a initially spherical void at its center and pole figures representing the initial orientations studied in this section.*

The unit cell considered here has been meshed using ABAQUS/CAE environment with reduced integration first order brick elements designated as C3D8R. The effect of mesh on the response of the cell was analized. Four different meshes were created for the cell, basically adding more number of elements around the void. Evolution of void volume fraction and stress strain response were used as criterion for selecting mesh size. Finally a mesh with 86000 elements is considered as optimal choice with respect to convergence and simulation time. It should be noted that special care has been taken to keep most of the elements in the cell to be cubical.

Initially, the unit cell is aligned such that the edges of the unit cell are parallel to the global XYZ axes. The notation adopted here denotes each orientation by the crystallographic directions, aligned with the main loading direction. The main loading direction is parallel to the X axis and the secondary loading direction is parallel to Z or Y axis depending on the selected Lode parameter. A dimensionless equivalent strain rate $\dot{\epsilon}_0/\ \dot{\gamma}_0$ in the range $(100-150)$ is ensured in all simulations.

For studying the response of porous single crystals for different loading conditions, we have chosen 4 values of triaxiality ($T = 0,\ 1/3,\ 2/3,\ 1$) and 3 values of Lode parameters ($L = 1,\ 0,\ -1$). Some of the combinations of triaxiality and Lode parameters analyzed corresponds to general loading scenarios used in experiments and simple loading conditions, like $T = 1/3$, $L = -1$ (uniaxial tension), $T = 2/3,\ \ L = 1$ (biaxial tension) and $T = 0,\ \ L = 0$ (pure shear stress).

Four different orientations are considered for studying porous single crystal response: two soft orientations (O1 and O2) and two hard orientations (O4 and 06) following the observations made from the study of single crystals without voids. The initial pole figures of the orientations considered here are shown in figure 4.1.

For O1 and O2 orientations, there exist a crystal reflection symmetry about the coordinate planes normal to <100> and <110>. The cell faces remain straight during deformation and determine the current volume of the cell is straight forward. The volume of the void can be calculated ad the difference between the volume of the cell and the volume of the matrix (current sum of the volume of all the elements in the cell).

For non symmetric orientations (O4, O6), the initially straight sides of the unit cell (along which fully periodic conditions are applied) becomes curved during deformation process and is not straight forward to calculate the current volume of cell. In order to overcome this problem, a different approach is adopted for calculating the volume of the void. The 3D (X, Y, Z) coordinates of all the nodes on the surface of the void (initially spherical) is extracted from the finite element calculations for all the time steps. By using these coordinates, void volume is calculated at each time increment with the help of convex hull algorithms as described in appendix F. With this approach, we can directly calculate the volume of the void at any given point in the simulations.

4.3 Results and discussion

In this section, results of porous single crystals for orientations O1, O2, O4, O6 are presented for different triaxialities and Lode parameters.

For O1 orientation, void growth and void shape evolution remain symmetric in all 3 principal directions. Figure 4.2a shows the normalized void volume fraction (f/f_0)-equivalent strain (ε_{eqv}) evolution for Lode $= -1$. In this figure different colours represents different triaxialities. Black colour represents $T = 1$, red colour represents $T = 2/3$, blue colour represents $T = 1/3$ and green colour represents $T = 0$. As seen in the figure, void volume fraction increases monotonically for $T = 1$ and $T = 2/3$. For $T = 1$ void volume fraction increases almost 6 times the initial void volume fraction (f_0) at ε_{eqv}=0.8, whereas for $T = 2/3$, void volume fraction increases 3 times f_0 at $\varepsilon_{eqv} = 0.8$. For $T = 1/3$, void volume fraction increases slightly above the initial void volume fraction and is negligible if compared to $T = 1$ and 2/3. For $T = 0$, void volume fraction decreases below f_0 but we do not observe void collapse at any value of equivalent strain.

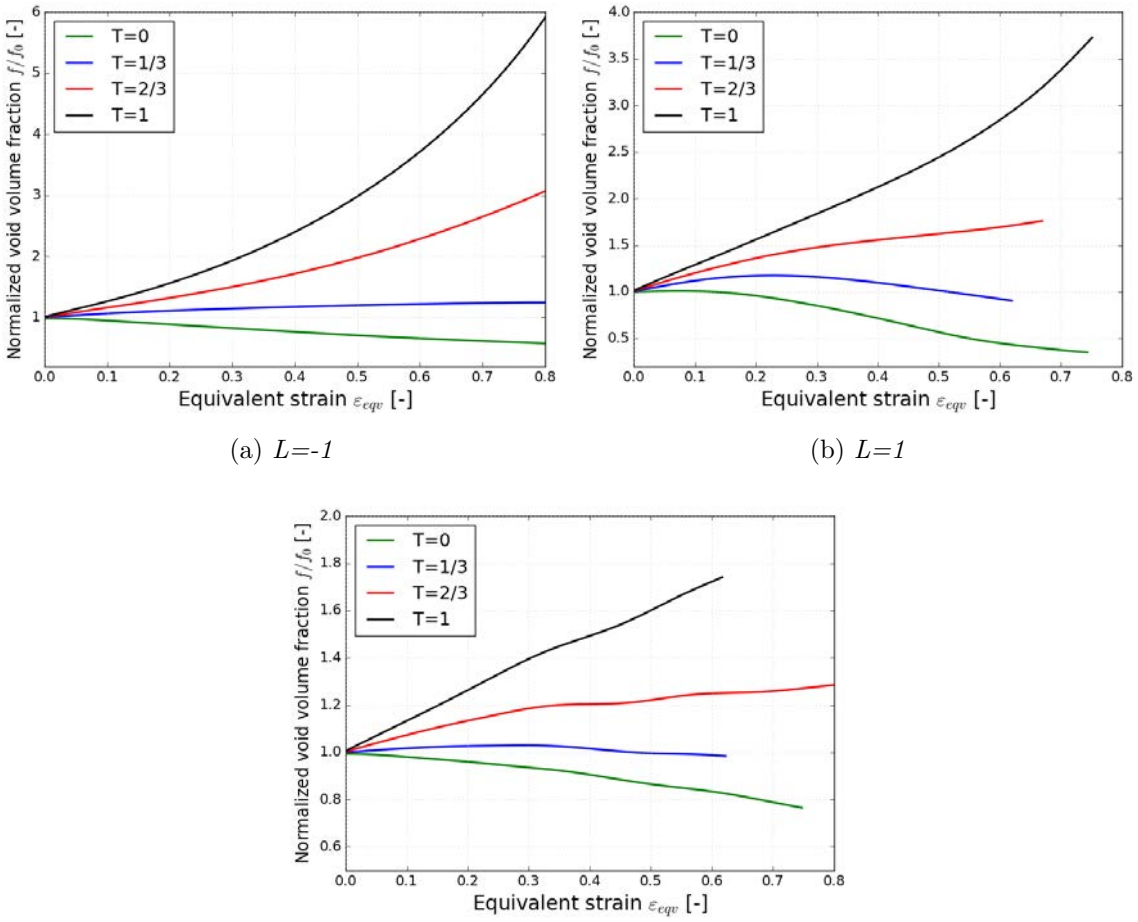

(a) *L=-1*

(b) *L=1*

(c) *L=0*

Figure 4.2: *Normalized void volume fraction -Equivalent strain evolution for O1 orientation at different triaxialities and Lode parameters.*

For $L = 1$ and as shown in Fig. 4.2b, we observe void growth for $T = 1$ and $T = 2/3$. However, void growth is less significant if compared to $L = -1$ case. For $T = 1$, void volume fraction grows almost four times the initial void volume fraction for $\varepsilon_{eqv} \approx 0.8$ and for $T = 2/3$, void volume fraction growth is 1.5 times the initial void volume fraction at $\varepsilon_{eqv} \approx 0.4$. For $T = 1/3$, even we observe small void growth in the initial stages of deformation, void volume fraction starts dropping in the later stages and for $\varepsilon_{eqv} > 0.5$, void volume drops below f_0. For $T = 0$, void volume fraction starts dropping below f_0 from the initial stages of deformation and larger drop is observed as compared to $L = -1$ case. Void volume fraction becomes less than half f_0 at $\varepsilon_{eqv} = 0.6$.

Similarly, for $L = 0$, void growth is observed for $T = 1$ and $T = 2/3$ (see Fig.4.2c). For $T = 1$, void volume fraction grows almost 1.8 the initial void volume fraction when $\varepsilon_{eqv} = 0.6$, whereas for $T = 2/3$, void volume fraction growth is 1.2 times the initial void volume fraction for $\varepsilon_{eqv} = 0.6$. For $T = 1/3$, 0 we observe void volume fraction dropping below the initial void volume fraction. As $L = 1$ and $L = -1$ cases, for $T = 1/3, 0$ we do not observe void collapse.

For O1 orientation, for $T = 1$ and $T = 2/3$ and among all the Lode parameters considered, void volume fraction growth is higher for $L = -1$, followed by $L = 1$ and lower in $L = 0$ case. For $T = 1/3$ and $T = 0$, void volume fraction decrease is more significant for $L = 1$, followed by $L = -1$ and less significant in $L = 0$ case. The trends observed for O1 shows that void growth is favourable for $L = -1$ and void shrinkage is favourable for $L = 1$ case.

For O2 orientation, we have crystal symmetry along <110>. As O1 orientation, O2 orientation is considered in this work as soft orientation. Normalized void volume fraction-equivalent strain evolution for different triaxialities and Lode parameters are analyzed in Figs. 4.3. In Fig.4.3a and for $L = -1$, a significant increase in void volume fraction is observed for high values of triaxiality. For $T = 1$, void volume fraction grows six times the initial void volume fraction when $\varepsilon_{eqv} = 0.8$. For $T = 2/3$, void volume fraction grows three times f_0 when $\varepsilon_{eqv} = 0.8$. For low triaxialities like $T = 1/3$, we observe a small amount of void volume fraction growth, whereas for $T = 0$ negative void volume fraction growth is observed as shown in figure 4.3a.

The trend of higher void growth at high triaxiality and lesser void growth at low triaxiality is also observed for $L = 1$ in Fig.4.3b and $L = 0$ in Fig.4.3c. However, for both $L = 1$ and $L = 0$ values, the total void volume fraction growth is very low if compared to $L = -1$. For $L = 1,\ 0$, the void volume fraction for $T = 1$ and $T = 2/3$ is below 1.3 times the initial void volume fraction when $\varepsilon_{eqv} = 0.6$. For $T = 1/3$ and $T = 0$, a negligible change in void volume fraction is observed. The effect of Lode parameter is more evident for O2 orientation if compared to O1 orientation.

For O4 orientation, unlike O1 and O2 orientations, we do not have any crystal symmetry. Because of the anisotropic nature of the matrix orientation and the applied periodic boundary conditions, the cell undergoes shear deformations. This behavior majorly influences on the way void shape evolves and the rate at which void evolves.

As shown in figure 4.4a, for O4 and $L = -1$ and as previously observed for O1 and O2 orientations, void volume fraction increases for high triaxiality values ($T = 1,\ 2/3$) and

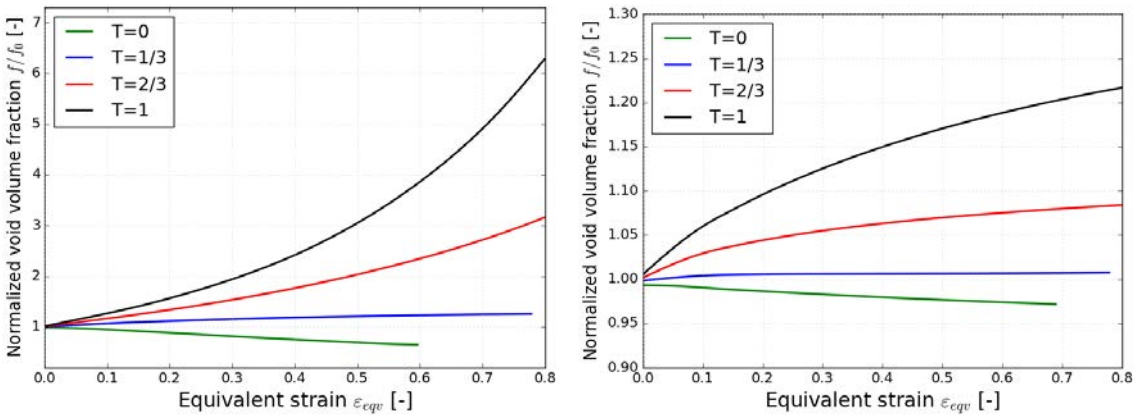

(a) *L=-1* (b) *L=1*

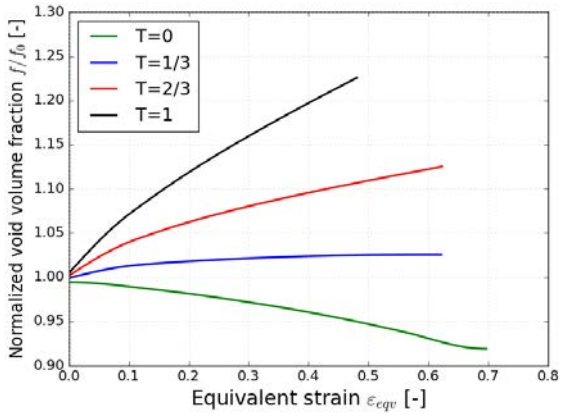

(c) *L=0*

Figure 4.3: *Normalized void volume fraction- Equivalent strain evolution for O2 orientation at different triaxialities and Lode parameters.*

void volume fraction decreases below the initial void volume fraction for low triaxiality values ($T = 1/3,\ 0$). For $T = 1$, void volume fraction grows almost 5 times the initial void volume fraction at ε_{eqv}=0.6. For $T = 2/3$, void volume fraction grows nearly two times the initial void volume fraction at ε_{eqv}=0.8. For triaxiality $T = 1/3$, void volume fraction growth is observed initially (till $\varepsilon_{eqv} = 0.2$), but during the later stages of deformation, void volume fraction starts dropping and it drops below f_0 at $\varepsilon_{eqv} = 0.45$. For $T = 0$, void volume fraction starts dropping below the initial void volume fraction from the early stages of deformation, and void volume fraction reduces to half the initial void volume fraction when $\varepsilon_{eqv} = 0.65$.

Figure 4.4b shows the response of the cell when the matrix has O4 orientation and Lode parameter $L = 1$. For $T = 1$, void volume fraction grows almost 4 times f_0 at $\varepsilon_{eqv} = 0.8$, whereas for $T = 2/3$, void volume fraction grows initially till $\varepsilon_{eqv} = 0.2$, but starts dropping in the later stages of deformation and void volume fraction decreases below the initial void volume fraction for $\varepsilon_{eqv} = 0.6$. For $T = 2/3$, the behaviour of void volume fraction evolution at $L = 1$ is different from $L = -1$. For $L = -1$ we see void volume fraction increasing from the whole deformation history, whereas for $L = 1$ we see void volume fraction decreasing during the later stages of deformation ($\varepsilon_{eqv} > 0.2$). For $T = 1/3,\ 0$, we see void volume fraction decreasing

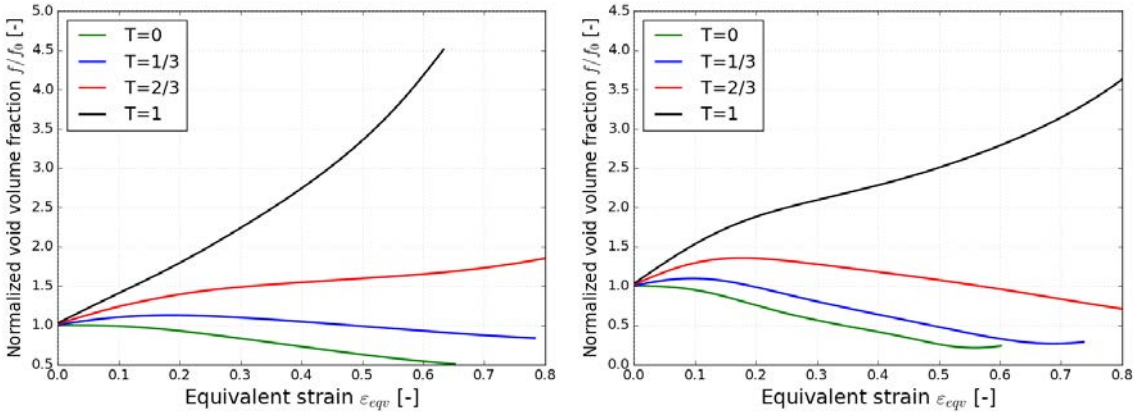

(a) *L=-1* (b) *L=1*

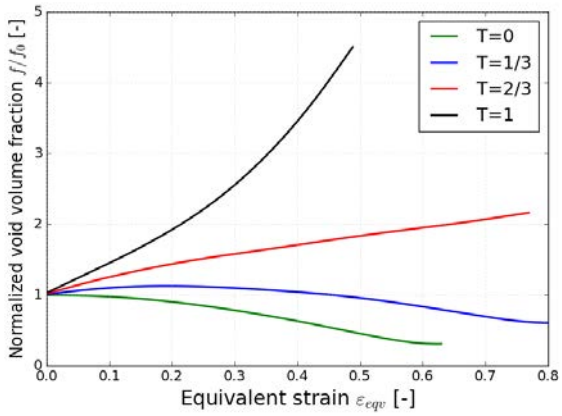

(c) *L=0*

Figure 4.4: *Normalized void volume fraction- Equivalent strain evolution for O4 orientation at different triaxialities and Lode parameters.*

below the initial void volume fraction from the early stages of deformation. For $T = 1/3$, void volume fraction increases initially till $\varepsilon_{eqv} = 0.1$, but starts dropping below the initial void volume fraction and we observe void collapse for $\varepsilon_{eqv} \approx 0.7$. Void is considered collapsed when the surface of the void comes in contact and simulation is stopped at this point. For $T = 0$, void volume fraction drops below the initial void volume fraction from the beginning and void collapses at $\varepsilon_{eqv} = 0.6$.

Figure 4.4c shows the response of the cell considering O4 orientation and $L = 0$. For $T = 1$, void volume fraction grows almost 5 times the initial void volume fraction at $\varepsilon_{eqv} = 0.5$ and void volume fraction growth rate is higher if compared to $L = -1, 1$ cases. For $T = 2/3$, void volume fraction grows almost twice the initial void volume fraction at $\varepsilon_{eqv} = 0.5$, and the rate of void volume fraction growth is higher than $L = -1, 1$ cases. For low triaxialities ($T = 1/3, 0$), void volume fraction drops below the initial void volume and we observe void collapse.

For O4 orientation, the analyzed results show that the Lode parameter affects the response of the void for all triaxiality values considered. For high triaxialities, void volume fraction

growth is faster for $L = 0$, followed by $L = -1$ and least for $L = 1$ case. For low triaxiality values, void volume fraction drops bellow f_0 and void collapses for $L = 1$ and $L = 0$ cases.

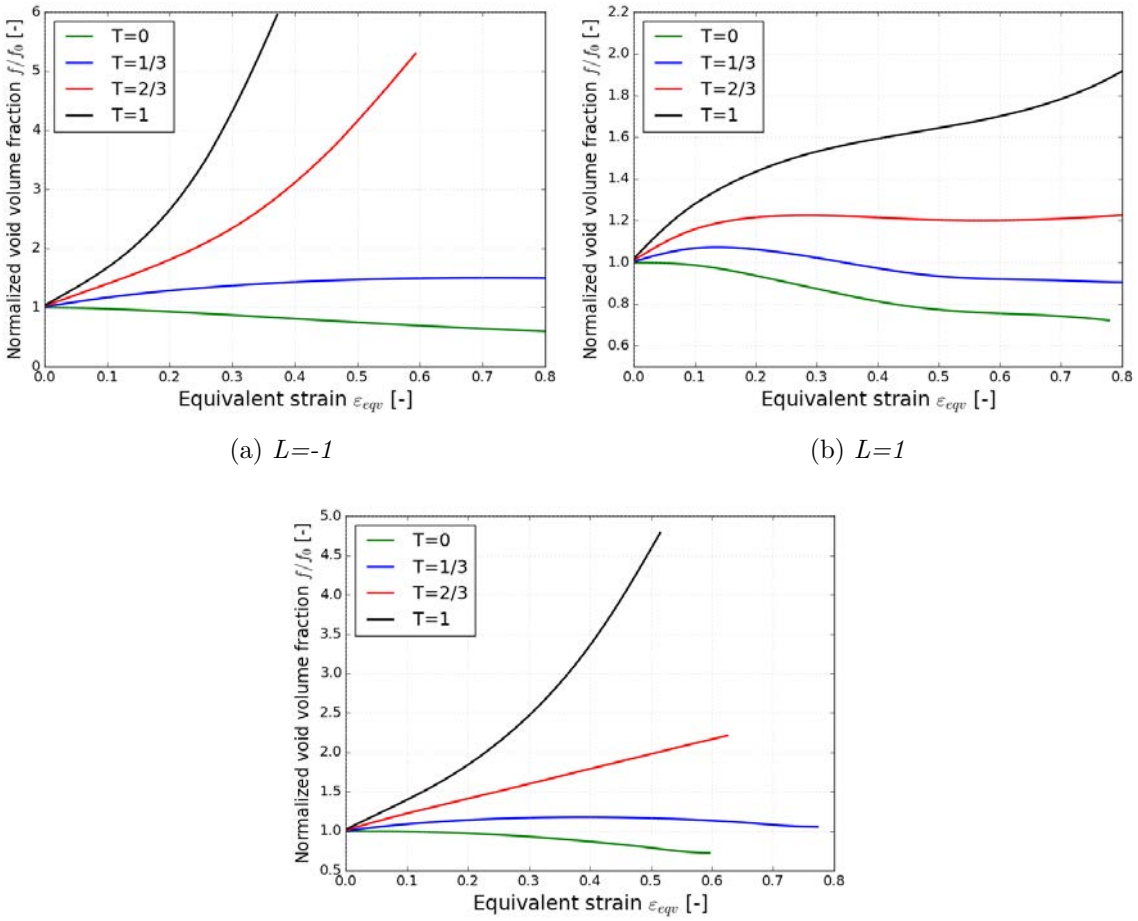

(a) *L=-1*

(b) *L=1*

(c) *L=0*

Figure 4.5: *Normalized void volume fraction- Equivalent strain evolution for O6 orientation at different triaxialities and Lode parameters.*

For O6 orientation and because of the anisotropy of the matrix, the cell deforms with shear components. Figure 4.5a shows the response of the cell with O6 orientation for Lode parameter $L = -1$. For $T = 1$ and as seen in the figure, void volume fraction grows almost six times the initial void volume fraction at $\varepsilon_{eqv} = 0.35$ and f grows at a very high rate. For $T = 2/3$, void volume fraction grows almost 5 times the initial void volume fraction at $\varepsilon_{eqv} \approx 0.6$ with a growth rate that is slower than $T = 1$ case. For $T = 1/3$, void volume fraction grows initially, but at later stages of deformation ($\varepsilon_{eqv} = 0.5$), void volume fraction growth saturates. For $T = 0$, void volume fraction decreases below the initial void volume fraction and even in this case, after the initial drop of f, void volume fraction growth saturates and we do not observe void collapse.

For $L = 1$ and as shown in Fig 4.5b void volume fraction grows almost 2 times the initial void volume fraction for $T = 1$ and $\varepsilon_{eqv} = 0.8$. For $T = 2/3$, void volume fraction grows at low rate initially, and after $\varepsilon_{eqv} = 0.3$ void volume fraction growth saturates. For $T = 1/3$, 0 void void volume fraction decreases below the initial void volume fraction (from $\varepsilon_{eq} = 0.35$

at $T = 1/3$ and from $\varepsilon_{eq} = 0$ at $T = 0$) and after the initial drop in void volume fraction, f saturates and we do not observe void collapse.

Figure 4.5c shows the response of the cell for O6 orientation and Lode parameter $L = 0$. For $T = 1$, void volume fraction increases almost five times the initial void volume fraction at $\varepsilon_{eq} = 0.5$. For $T = 2/3$, void volume fraction grows more than two times the initial void volume fraction at $\varepsilon_{eq} = 0.6$. For $T = 1/3$, void volume fraction grows initially, and for $\varepsilon_{eqv} > 0.2$ void volume fraction decreases. For $T = 0$ and during the initial stages of deformation, there is neither void growth nor decrease in void volume fraction, as void volume doesn't change until $\varepsilon_{eqv} = 0.2$. For higher strains ($\varepsilon_{eqv} > 0.2$) void volume fraction decreases below the initial void volume fraction, and no void collapse is observed.

As shown in Figs. 4.5 and for O6 orientation, at high triaxiality values ($T = 1,\ 2/3$) void volume fraction growth rate is higher for $L = -1$, followed by $L = 0$ and least for $L = 1$ case. For low triaxiality values ($T = 1/3$ and $T = 0$), void volume fraction evolution is very similar for $L = -1$, $L = 1$ and $L = 0$ cases.

Previous results clearly show that void volume fraction growth is dependent on both triaxiality and Lode parameter values. In Figs. 4.6, 4.7 and 4.8 we will compare the influence of orientation on void volume fraction growth at different triaxialities for a prescribed Lode parameter values. The results analyzed now are the same as the previous ones, but represented in a different way to interpret the effect of orientation better.

In Figs. 4.6 results for O1, O2, O4 and O6 orientations are presented for $T = 1,\ 2/3,\ 1/3,\ 0$ and Lode parameter $L = -1$. Different colours represents different orientations. Black color represents O6, red color represents O4, blue color represents O2 and green color represents O1. Figure 4.6a shows void volume fraction-equivalent strain evolution for different orientations at $T = 1$. The magnitude of void volume fraction growth reached in the simulations (close to 6 times the initial void volume fraction) is almost the same for all the orientations considered, but the rate at which void volume fraction grows is higher for O6 (maximum growth at $\varepsilon_{eqv} = 0.35$), followed by O4, O2 and least for O1 orientation (with a growth of 6 times the initial void volume fraction at $\varepsilon_{eqv} = 0.8$). The difference in void volume fraction growth rate for O1, O2, O4 is small if compared to O6.

Figure 4.6b shows void volume fraction-equivalent strain evolution for $T = 2/3$. As shown in the figure, the amount of void volume fraction growth in O6 is higher if compared to other orientations. Compared to O6, a lower void volume fraction growth is observed by O1 and O2 orientations which has nearly the same void volume fraction evolution. Least void volume fraction growth is observed for O4 orientation.

For $T = 1/3$ and as shown in figure 4.6c the amount of void volume fraction growth and the rate of void volume fraction growth is higher for O6 orientation if compared to other orientations. For O4 orientation, void volume fraction growth is observed during the initial stages of deformation at a rate higher than O1 and O2 orientations. However, as the deformation proceeds, we observe void volume fraction dropping below the initial void volume fraction. For O1 and O2 orientations, void volume fraction growth is almost the same.

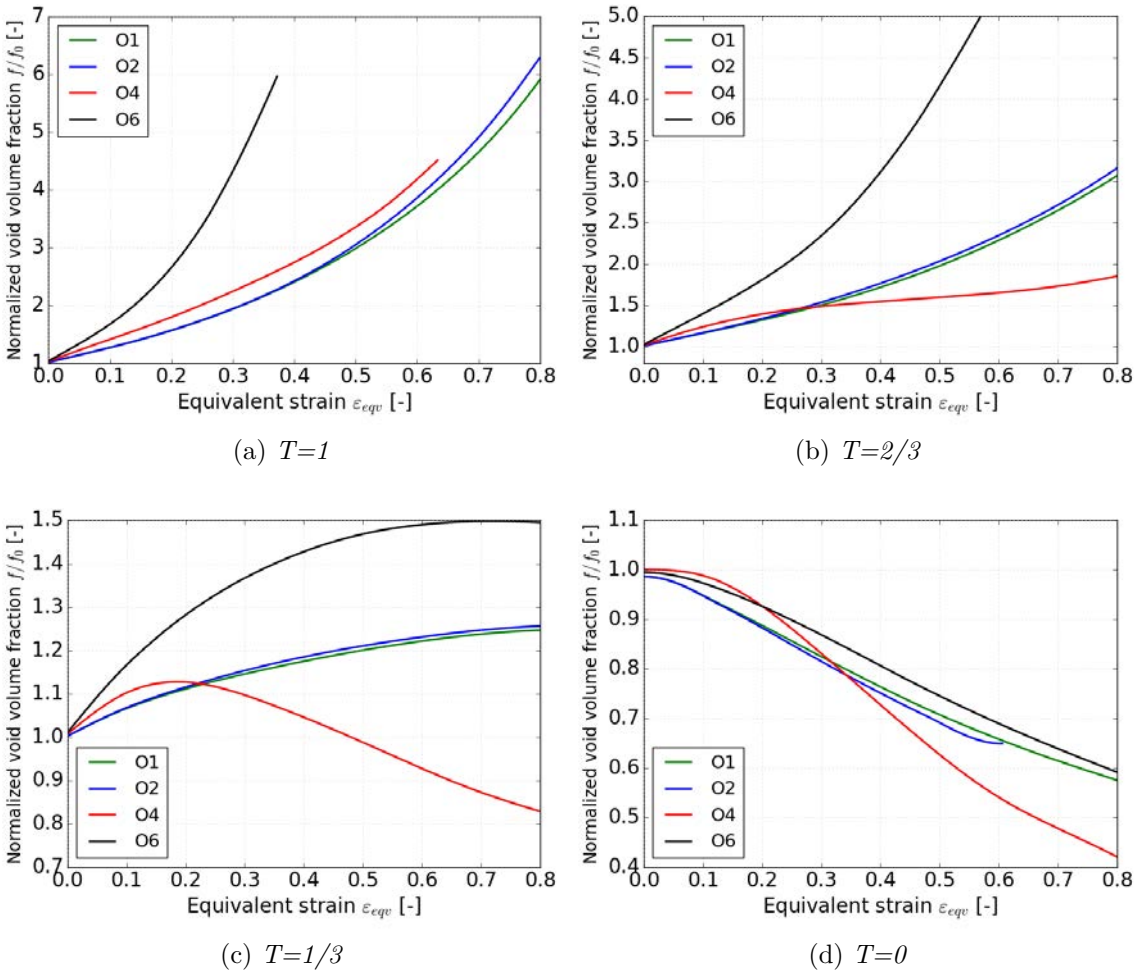

(a) *T=1* (b) *T=2/3*

(c) *T=1/3* (d) *T=0*

Figure 4.6: *Normalized void volume fraction-Equivalent strain evolution for different orientations at* $L = -1$ *and* $T = 1,\ 2/3,\ 1/3$ *and* 0.

As shown in figure 4.6d for $T = 0$ and from the initial stages of deformation, void volume fraction decreases below f_0 for all orientations. At the initial values of ε_{eqv}, the rate at which void volume fraction decreases is higher for O1 and O2 orientations followed by O6 and O4 orientations respectivelly. However, as the deformation progresses and for $\varepsilon_{eqv} > 0.1$ void volume fraction for O4 orientation decreases faster than O1, O2 and O6 orientations.

The surface of the void comes in contact earlier for O2 orientation and simulations are stopped at this point, whereas for O4 orientation, void volume fraction decreases further below f_0 and reduces to almost $0.4f_0$. Until $\varepsilon_{eqv} \approx 0.6$, the rate of decrease of void volume fraction is smaller for O6 orientation if compared with the other orientations considered. For O6 orientation, the value of void volume fraction is $f = 0.6f_0$ for $\varepsilon_{eqv} = 0.8$.

Figure 4.7 shows void volume fraction evolution for Lode parameter $L = 1$ considering various triaxialities ($T = 1,\ 2/3,\ 1/3,\ 0$). At $T = 1$, the amount of void volume fraction growth is higher for O1 and O4, followed by O6 and least for O2 orientation as shown in figure 4.7a. Void growth is higher for O4 orientation until $\varepsilon_{eqv} = 0.55$. For further deformation, the rate of void volume fraction growth increases for O1 orientation and dominates over O4. Void volume fraction growth rate is lower for O2, as void grows slowly from the beginning till the end.

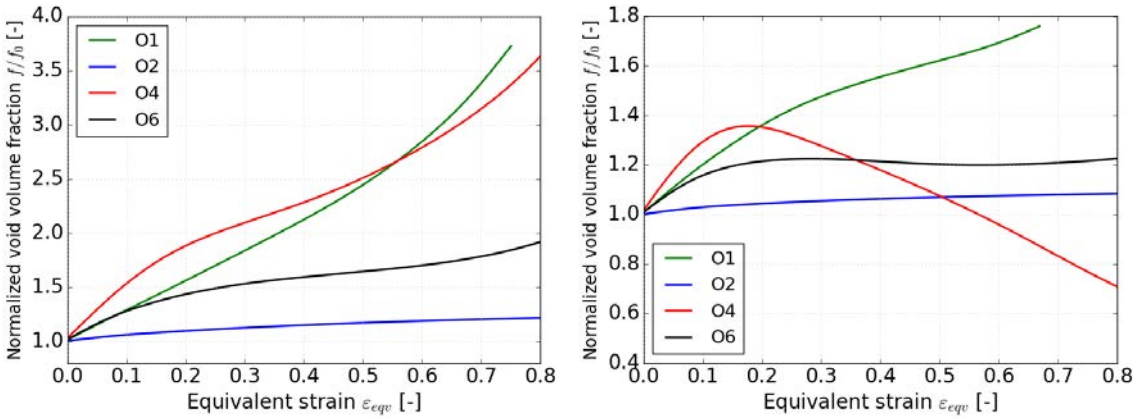

(a) *T=1* (b) *T=2/3*

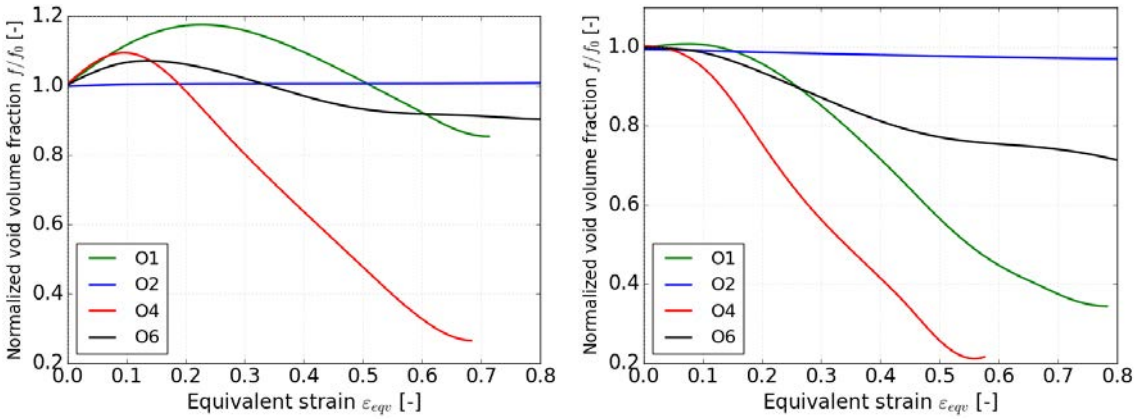

(c) *T=1/3* (d) *T=0*

Figure 4.7: *Normalized void volume fraction-Equivalent strain evolution for different orientations at* $L = 1$ *and* $T = 1,\ 2/3,\ 1/3,\ 0$.

For $T = 2/3$, as shown in figure 4.7b, void volume fraction growth is observed for O1 and O2 orientation. For O4 orientation, void growth is observed only in the initial stages of deformation. For O4 and during later stages of deformation, void volume fraction starts decreasing and drops below the initial void volume fraction. The rate of void growth is higher for O4 orientation until $\varepsilon_{eqv} = 0.18$ is reached. For higher strains void growth rate is higher for O1 orientation, followed by O2 and least in O6 and O4 case.

At $T = 1/3$ and for O1, O4, O6 orientations, void volume fraction growth is observed initially, but during later stages of deformation, void volume fraction starts dropping below the initial void volume fraction, as shown in figure 4.7c. Void volume fraction starts dropping earlier for O4 orientation, followed by O6 orientation and finally in O1 orientation case. Void volume fraction decrease is higher for O4 orientation as void volume nearly becomes zero, whereas for O6 orientation, after dropping below the initial void volume fraction, growth saturates as we do not see any change in void volume. For O2 orientation, void volume fraction remains constant throughout the whole simulation.

At $T = 0$, void volume fraction decreases for all the orientations considered. Void volume fraction drops faster for O4, followed by O1, O6 and least for O2 case as shown in figure 4.7d.

The amount of void volume fraction drop is higher for O4 orientation as void volume fraction almost reduces to zero and we observe void collapse. As in the case of $T = 1/3$, void volume fraction for O2 orientation doesn't change appreciably and we observe a saturation in void volume fraction.

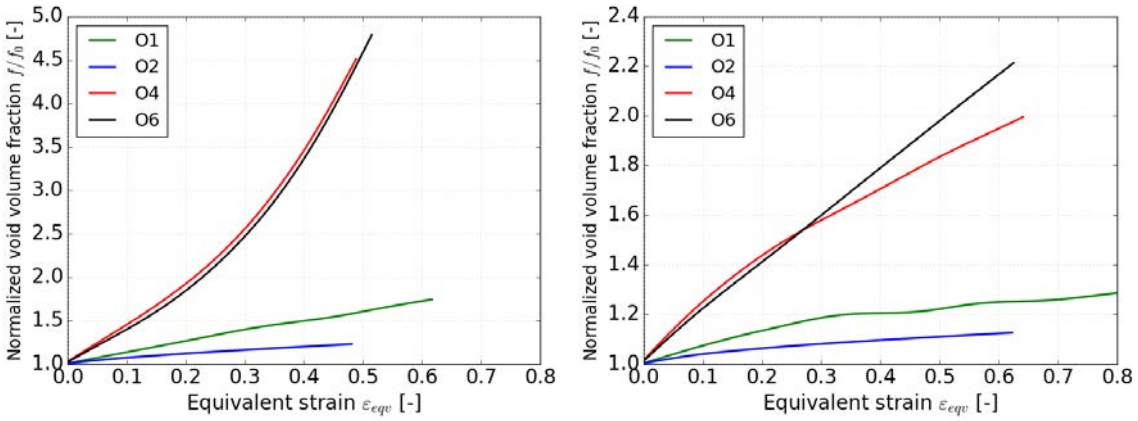

(a) *T=1* (b) *T=2/3*

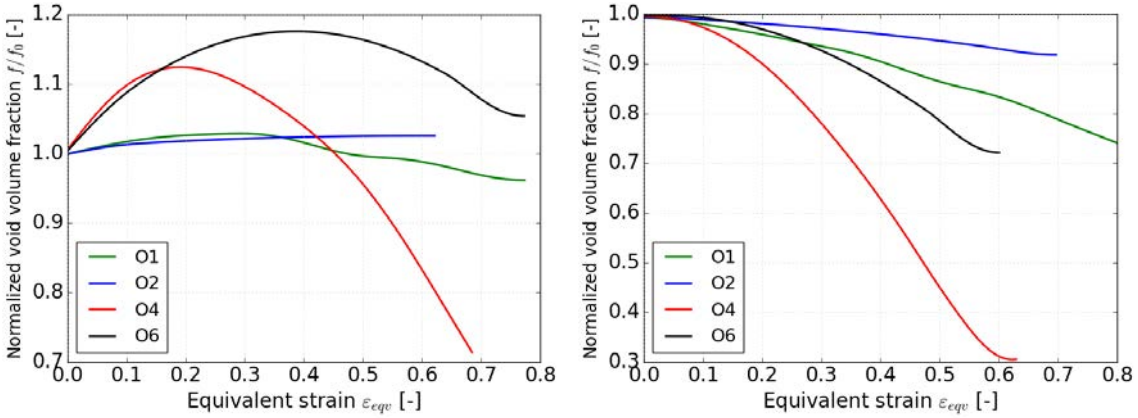

(c) *T=1/3* (d) *T=0*

Figure 4.8: *Normalized void volume fraction-Equivalent strain evolution for different orientations at* $L = 0$ *and* $T = 1,\ 2/3,\ 1/3,\ 0$

At $L = 0$, the evolution of void volume fraction for $T = 1$ and different orientations are shown in figure 4.8a. As observed in the figure, the amount of void volume fraction growth and the rate of void volume fraction growth is higher for O4 and O6 orientations, and both orientations behave similarly throughout the whole simulation. O1 follows O4 and O6 in the amount of void volume fraction growth. Least void volume fraction growth is observed for O2 orientation.

Similarly for $T = 2/3$, void volume fraction growth rate and the amount of void volume fraction growth is higher for O4 and O6 orientation, followed by O1 and O2 orientation as shown in figure 4.8b.

For $T = 1/3$, void volume fraction growth is observed during the initial stages of deformation for O4 and O6 orientation. During the initial stages of deformation, the amount of void volume fraction and void volume fraction growth rate is higher for O4 orientation, followed

by O6 orientation and least for O1 and O2 orientations. After the initial growth, we observe void volume fraction decreasing for O1, O4 and O6 orientations. For O1 and O4 orientation void volume fraction decreases below f_0 as shown in figure 4.8c. Void volume fraction drop is higher for O4 orientation, followed by O6 orientation. Even though we observe a decrease in void volume fraction for O6 orientation, f never drops below f_0.

For $T = 0$, void volume fraction drops below the initial void volume fraction for all the orientations as shown in figure 4.8d. The amount of void volume fraction drop is higher for O4 orientation, followed by O6 orientation and lower for O2 orientation. Void surfaces comes in contact earlier for O6 orientation and later for O4 orientation, even though void volume fraction for O4 drops well below O6 orientation. This can be attributed to the effect of secondary orientation and rotation of the cell because of the matrix anisotropy.

For all Lode parameters considered and among all orientations, the general tendency for void volume fraction growth is higher for O6 orientation at high triaxialities, whereas the tendency for void collapse is higher for O4 orientation at low triaxialities.

4.4 Summary and conclusions

3D finite element calculations are carried out in this chapter with the aim of analysing the response of voids in FCC single crystals. The effect of crystal orientation on void evolution is analyzed for different orientations using representative cells subjected to different loading conditions. Unit cells consisting of cubic cells with a initial spherical void with $f_0 = 0.0044$ are considered. Fully periodic boundary conditions with controlled triaxiality and Lode parameter are applied to the cells. Four different orientations are studied: O1, O2, O4 and O6. Out of these four orientations, two are soft orientations (O1, O2) and two hard orientations (O4, O6). Four different triaxialities ($T = 0,\ 1,\ 1/3,\ 2/3$) and three Lode parameters ($L = 0,\ 1,\ -1$) are prescribed in the cells with a strictly specified orientation of loading directions with respect to the initial crystal orientation, and a dimensionless equivalent strain rate $\dot{\epsilon}_0/\ \dot{\gamma}_0$ in the range $(100 - 150)$.

For any given orientation and triaxiality, void volume fraction growth is higher for Lode parameter $L = -1$, followed by $L = 0$ and finally by $L = 1$. For a given orientation, void volume fraction growth is always higher for $L = -1$ and $T = 1$ case and least void volume fraction growth is observed for $L = 1$ and $T = 0$ case.

At $L = -1$ void volume fraction growth is higher for O6 orientation followed by O4 orientation and lower void volume fraction growth is observed for O1 and O2 orientations. Similar behaviour is observed for $L = 0$. However, for $L = 1$ we observe higher void volume fraction growth for O4 orientation, followed by O1 orientation and lower void volume fraction growth is observed for O2 and O6 orientations.

The obtained results show that irrespective of the orientation and Lode parameter considered, void volume fraction growth is always higher for higher triaxialities ($T = 1,\ 2/3$). For lower triaxialities ($T = 1/3,\ 0$) void growth is always lesser and in some cases and as deforma-

tion proceeds we observe void volume fraction bellow f_0 and void collapse. This behavior (slow porosity growth for low and moderate triaxiality level and fast porosity growth for high triaxiality level) is well known and has been reported previously for FCC crystals by Srivastava and Needleman (2013) and Yerra et al. (2010a). Similarly, at low and moderate triaxiality levels, Lode parameter has a significant influence on void behaviour.

In general void volume fraction growth is higher for harder orientations (O6 and O4) if compared to soft orientations (O1 and O2). This trend is attributed to the behavior of the anisotropic matrix. These results are used for comparison with bi-crystal results which will be discussed in detail in next chapter 5.

5

Numerical study of void growth at the grain boundaries in bi-crystals

Contents

5.1 Introduction

One of the common challenges to overcome when using advanced metals and alloys in engineering applications is their insufficient ductility (Fourmeau et al., 2013b; Basu et al., 2017). Strengthening of materials is usually achieved by introduction of precipitates, second phase particles or new grain boundaries while at the same time these additions are possible sites of damage/fracture initiation (Yerra et al., 2010b). Predominant mechanisms of ductile failure in polycrystaline metals are nucleation, growth and coalescence of micro-voids (small scale voids) (Benzerga and Besson, 2001). Accounting for these mechanisms in modelling, a family of macroscopic approximations were proposed, namely prominent models like Gurson-types models (Gurson, 1977b; Tvergaard and Needleman, 1984), their extension in later works by taking into account many aspects such as void shape, size, volume fraction and distribution of voids, as well as distinct features of the constitutive model of a virgin material such as strain and kinematic hardening, viscoplasticity and plastic anisotropy. For respective contributions see extensive review by Besson (2010b). Such type of approach was also used to formulate the micro-scale Gurson-type yield condition for single crystal (Han et al., 2013; Paux et al., 2015). In the case of Han et al. (2013) such condition is the result of micromechanical analysis based on variational estimates due to de Botton and Ponte Castañeda (1995). Note that, there are number of papers in which such variational approach is directly applied to estimate the yield surface of single crystal with voids (Mbiakop et al., 2015; Song and Castañeda, 2017).

On the micro-scale, two failure modes have been found to be operational in parallel: cleavage and dimple fracture (Papaefthymiou et al., 2006). Studies of Kadkhodapour et al. (2011a,b); Lani et al. (2007); Furnémont et al. (2007) have reported different types of damage mechanisms based on their experimental work with the help of SEM and light optical microscopy. By experimental observations, nucleation of voids is related to the fracture and decohesion of second phase particles or other precipitates. The next steps in understanding the failure process are intergranular fracture along high angle boundary (HAB) and microvoid-induced transgranular fracture. For example, such observations have been made for aluminium alloys AA7XXX subjected to the solution treatment along the processing route, which resulted in partial recrystallization (Dorward and Beerntsen, 1995; Deshpande et al., 1998). For such alloys it was observed that precipitates are often grouped along HABs which promotes intergranular fracture along them. Importance of HAB as a possible location of void growth has been also confirmed by molecular dynamics simulations (Bringa et al., 2010). Additionally, as seen in Morere et al. (2000), concentration of precipitates is also observed along subgrain boundaries, characterized by a low misorientation angle, together with associated intersubgranular failure. It is also worth to note that the effect of crystal orientation and the grain boundary was observed under shock loading conditions for copper bi-crystal by Perez-Bergquist et al. (2011). They observed formation of voids both at the grain boundary and within each crystal, with the number and shape of voids highly dependent on the crystallographic orientation. Although

this type of loading is beyond the scope of this paper, these experiments confirm the role of crystal anisotropy and grain boundaries in the failure of crystalline material.

Although there is quite a lot numerical studies of single crystals with voids, (O'Regan et al., 1997; Potirniche et al., 2006b; Yerra et al., 2010b; Srivastava and Needleman, 2015b; Selvarajou et al., 2019) very few numerical studies have been dedicated to the studies on void in bi-crystals. One can mention earlier works by Liu et al. (2009) in which the fcc bi-crystal under uniaxial tension was investigated to assess the effect of boundary inclination and the crystallographic orientation and misorientation on the void growth and the plastic deformation distribution around the voids. Liu et al. (2007b, 2010) studied mechanisms of coalescence of voids located at adjacent grains in bi-crystal unit cell using finite element calculations. Recently, Jeong et al. (2018) considered the unit cells with a void inside a grain, at a grain boundary and at a triple junction. The effect of crystal orientation on the flow strength and growth rate of the void was discussed under prescribed boundary conditions for constant stress triaxialities. Even though studies mentioned above shed light on the behaviour of void at boundary on bi-crystals, there are still open questions, like the effect of neighbouring grain orientation on void shape, the effect of stress state on void growth or void collapse behaviour among others.

Appreciating the important role of a grain boundary on void behaviour, as noted by Deshpande et al. (1998); Bringa et al. (2010); Morere et al. (2000), the main purpose of the current work is to study the factors affecting void growth and morphology evolution in bi-crystals, such as stress triaxiality and Lode parameter and the relative orientation between grains, focusing specifically on voids originating in high angle grain boundaries. The response of bi-crystals containing a void at the grain boundary are also compared with the response of a single crystal with a void.

5.2 Representative volume element

Three dimensional finite element calculations are carried out to model the response of voids, located at the grain boundary of a bi-crystal, under triaxial loading conditions using a unit cell model. The unit cell is modelled as an fcc single crystal with the 12 potentially active slip systems taken to be $\{111\}\langle 110\rangle$ (table 2.1). Finite element analyses are carried out using a rate dependent crystal plasticity constitutive relation in the large deformation framework given in section 2.2.3.2. Material parameters used for calculations are given in Table 2.2. The plastic parameters of the material analyzed in this work correspond to annealed OFHC copper (Kalidindi et al., 1992).

For bi-crystals with a void, figure 5.1 shows FE mesh and the 3 RVEs used in the present study with their respective initial pole figures. The projection of misorientation axis is also marked in the pole figure. Representative unit cells used for studying the behaviour of a void in bi-crystal cases consists of a cube with a void at the center, divided into two equal parts, each half having half spherical void with $f_0 = 0.0022$, as shown in figure 5.1. The initial void volume fraction is selected to be small, so that we can study the void shape changes and its

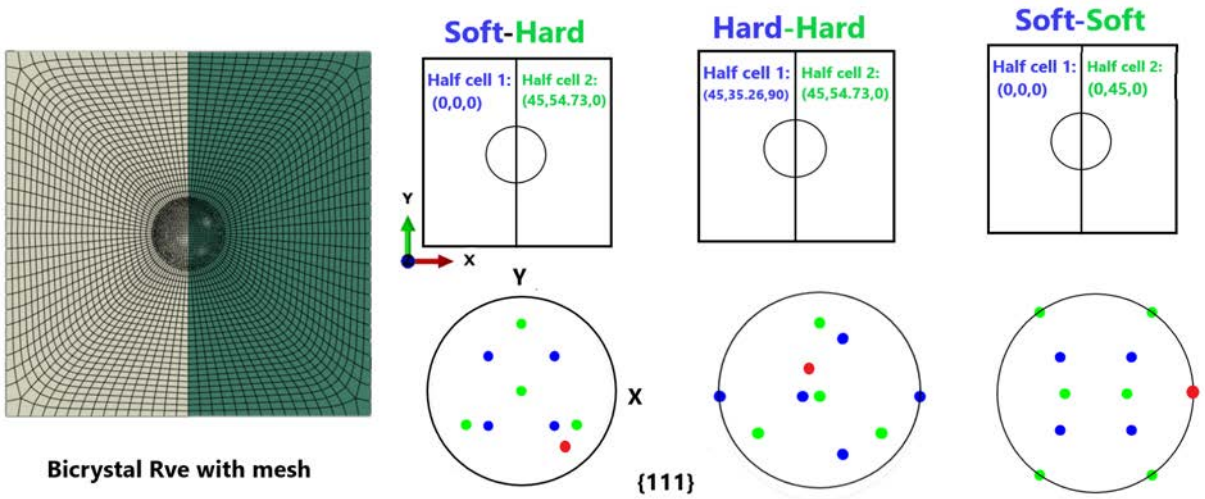

Figure 5.1: *Different bi-crystal RVEs and respective pole figures representing the orientations used for studying the effect of matrix orientation on the void behaviour. Blue colour represents orientations in half cell 1, green colour represents orientation in half cell 2 and red colour represents the projection of misorientation axis*

evolution at large deformations. Void volume fraction is calculated as $f_0 = V_{void}/V_{cell}$, where V_{cell} is the initial volume of the cell and V_{void} is the initial volume of the void. The complete matrix-void zone is discretized into 90000 C3D8R elements. Finite element mesh and number of elements in the mesh are the same as for the single crystal case. Depending on the cases to be studied, different crystallographic orientations are assigned to each half of the bi-crystal matrix.

Initially, unit cells are aligned such that the edges of the unit cell are parallel to the global XYZ axes. In the case of the bi-crystal cell, interface (grain boundary) between the two halves of the unit cell is perpendicular to the global X axis. The notation adopted here denotes each orientation by the crystallographic directions, aligned with the main loading direction. The main loading direction is parallel to the X axis and the secondary loading direction is parallel to Z or Y axis depending on the selected Lode parameter. From the study presented in the chapter of single crystals without voids, we categorized the crystal orientations into hard and soft orientations. For a given Lode parameter, the orientation with higher values of equivalent stress are considered as hard orientations and orientations with lower values of equivalent stress are considered as soft orientations. In reference to classical crystal plasticity studies, it can be said that soft (resp. hard) orientations are such which have high (resp. low) Schmid-like factor under given loading conditions.

In this chapter four values of stress triaxiality ($T = 0,\ 1/3,\ 2/3,\ 1$) and three values of Lode parameter ($L = 0,\ \ 1,\ -1$) with fully periodic boundary conditions (as explained in Appendix D) are considered. Some of the combinations of triaxiality and Lode parameters analyzed corresponds to general loading scenarios used in experiments and simple loading conditions, like $T = 1/3,\ \ L = -1$ (uniaxial tension), $T = 2/3,\ \ L = 1$ (biaxial tension) and $T = 0,\ \ L = 0$ (pure shear stress). Since anisotropic material model is assumed in each case

orientation of principal stress axes is explicitly specified with respect to material anisotropy axes. It should be underlined that in the considered examples dependence of the void growth on the Lode parameter cannot be studied separately from the effect of plastic anisotropy. Finally, as our material model is rate dependent, a value of $\dot{\varepsilon}_{eqv}/\dot{\gamma}_0$ in the range $(100 - 150)$ is also assured in all the simulations performed in this work.

5.3 Results and Discussion

Analytical studies on the void growth in an anisotropic rigid-plastic matrix described by the quadratic criterion performed by Benzerga and Besson (2001) for spherical voids, and continued by Keralavarma and Benzerga (2010) and Keralavarma et al. (2020) for ellipsoidal voids, revealed that this growth is governed by the formula:

$$\frac{\dot{f}}{f(1-f)} \sim \frac{3}{h}\frac{1}{\tilde{\sigma}^2_{eq}(\mathbf{N})}\sinh\left(\frac{3}{h}\frac{\sigma_m}{\sigma_1}\right) \tag{5.1}$$

in which $\tilde{\sigma}_{eq}(\mathbf{N})$ depends on the matrix plastic anisotropy, changing with the loading directions $\mathbf{N}$ with respect to the main anisotropy axes, σ_m is the mean stress, σ_1 the yield stress in the selected direction, while h is the so-called net anisotropy invariant calculated as a single value for a given material. Accordingly an exponential void growth is affected by the triaxiality T and h, while stress direction $\mathbf{N}$ modifies mainly the proportionality coefficient through $\tilde{\sigma}^2_{eq}$. In analogy to this study Paux et al. (2015) proposed an approximate condition for the voided single crystal described by the non-quadratic regularized Schmid law, bearing mathematical similarities with the power-law rate-dependent model studied here. Authors have assessed the coefficient $\kappa \sim 1/h$ as equal to 0.506 for the fcc crystals, so it can be assumed as constant here. Therefore, qualitatively, mainly the dependencies on triaxiality and the plastic anisotropy are expected to be observed in the present analysis. Nevertheless, as it will be shown, they are additionally modified by the fact that the void is located at the bi-crystal boundary and not in the homogeneous matrix. At this moment such additional dependencies can be analyzed only numerically.

In this section results from different numerical simulations are presented. We will focus on the joint effect of stress state (T, L) and matrix crystallographic orientations (i.e. material anisotropy) on void volume fraction evolution and void morphology. We will compare results from single crystals with bi-crystals and results from different bi-crystal RVEs. In this work results of single crystal are used as reference values to compare with bi-crystals. Calculations of single crystals with voids are performed for four different crystallographic orientations O1, O2, O4, O6, 3 Lode parameters ($L = -1,\ 0,\ 1$) and 4 values of triaxialities ($T = 0,\ 1/3,\ 2/3,\ 1$). Based on the previous studies on the void growth in fcc single crystals (Srivastava and Needleman, 2015b) at this low moderate and high triaxiality level, porosity growth is expected to be rather slow, void shape change significant and Lode parameter to have an important influence on void behavior in this respect. It should be added that for the advanced regime of the

considered processes the changing shape of a void and a unit cell may additionally affect the dependencies observed in the calculations (Keralavarma and Benzerga, 2010)

5.3.1 Void growth in a bi-crystal

For studying the effect of grain orientation on the void growth in bi-crystals, three different representative volume elements (RVE) representing three different microstructures are created. The difference between each RVE are the crystallographic orientation assigned to the matrix of each half cell. Different orientations are assigned for half cell 1 and half cell 2, such that three different bi-crystal RVEs are formed. The orientations sets for the simulations of bi-crystals are selected from the cell calculations of single crystals without voids for different Lode parameters. By using the hard and soft orientations data, three different RVEs of bi-crystals representing; 1.soft-soft; 2. hard-hard; 3. soft-hard are created.

Orientations used for soft-soft RVE are O1 and O2 for half cell 1 and half cell 2, respectively. Similarly for hard-hard RVE, orientations used are O6 and O4 for half cell 1 and half cell 2, respectively. For soft-hard case, the orientations considered are O1 and O4 for half cell 1 and half cell 2. It can be verified that for all three cases the grain boundary between two halves of bi-crystal is a high angle boundary. The misorientation angle and misorientation axis specified by the common crystallographic direction of two orientations is for soft-hard 56.6° and $\langle 0.590, -0.769, 0.245\rangle$, for hard-hard is 35.6° and $\langle 0.598, 0.800, 0.046\rangle$, while for soft-soft is 45° and $\langle 100\rangle$. Note that for soft-soft bi-crystal the grain boundary is a twist boundary for which its unit normal is coaxial with misorientation axis. In the remaining two cases these two vectors are inclined with respect to each other.

For bi-crystals without voids, figs. 5.2a and 5.2b represent equivalent stress- equivalent strain curves for soft-hard orientation when different Lode parameter values ($L = -1$ and $L = 1$) are prescribed in the whole cell. Green lines represent stress-strain relations for (soft) half cell 1 and red lines represent stress strain relation for (hard) half cell 2. Blue lines represent stress -strain curves when the whole bi-crystal is considered. The presented curves are the same for any triaxiality value. For comparison purposes, equivalent strain is calculated in all the cases considering the volume of the whole cell. Note that due to imposed periodic boundary condition analyzed bicrystal without a void represent the behaviour of the laminate with alternating layers with O1 (soft) and O4 (hard) crystallographic orientation. Thus the predicted stress and strain fields within each half cell are uniform, however, considerably different from each other and from the overall behaviour. For $L = 1$, fig. 5.2c presents stress-strain curves for soft-soft orientation. For $L = -1$, fig. 5.2d shows stress-strain relations for the hard-hard case. For $L = -1$ and $L = 0$, for the soft-soft bi-crystal case, stress-strain curves overlaps for both half cells and the full cell. For $L = 1$ and $L = 0$, stress-strain curves for hard-hard bi-crystal are similar as for $L = -1$. These last cases are not shown in the document for the sake of brevity.

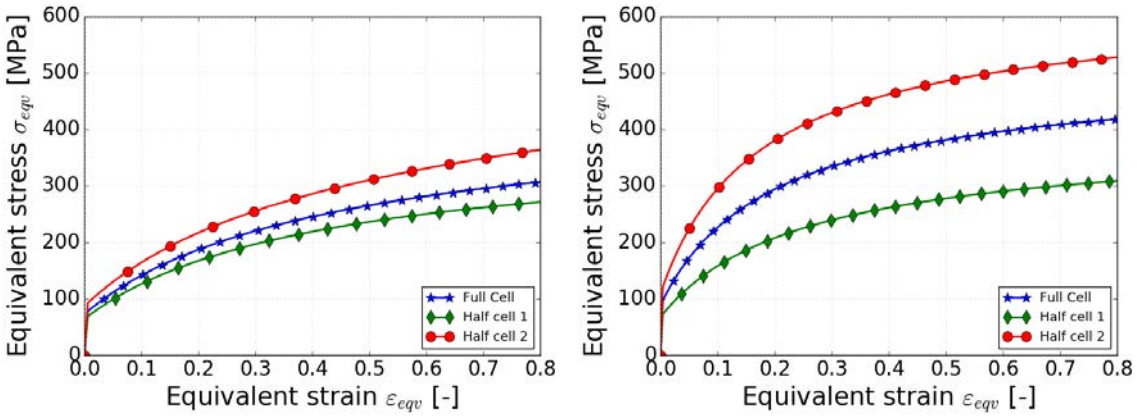

(a) *Soft-hard bi-crystal, L=-1* (b) *Soft-hard bi-crystal, L=1*

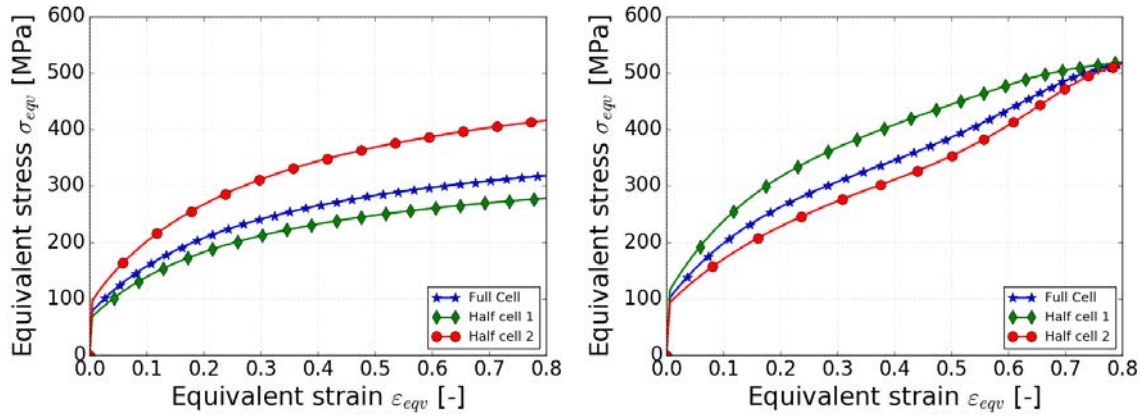

(c) *Soft-soft bi-crystal, L=1* (d) *Hard-hard bi-crystal, L=-1*

Figure 5.2: *Equivalent stress - equivalent strain in half cell 1, half cell 2 and the whole bi-crystal without void for soft-hard, soft-soft and hard-hard orientation for different Lode parameters. The presented curves are the same when any value of triaxiality is prescribed in the whole cell.*

5.3.1.1 Void growth in a soft-soft bi-crystal.

First we will present some results related to soft-soft bi-crystal RVE. This RVE has O1 orientation for half cell 1 and O2 orientation for half cell 2. Evolution of void volume fraction f with respect to the equivalent strain ε_{eqv} for Lode parameter $L = -1$ is shown in figure 5.3a for different triaxialities (T). Continuous lines represent void volume fraction evolution in half cell 1 and dotted lines in half cell 2 and different colours represents different triaxiality values. For triaxility $T = 1$, $T = 2/3$ and $T = 1/3$, we can see that void volume fraction f increases with ε_{eqv} in both half cell 1 and half cell 2, whereas for triaxiality $T = 0$, void volume fraction decreases below f_0 in both half cell 1 and half cell 2. This behaviour of void volume decreasing below f_0 was also observed for porous single crystal by Srivastava and Needleman (2015b). In the case of low triaxialities, simulations are terminated when the outer surface of the voids comes in contact with each other. In general void grows faster at high and moderate triaxialities ($T = 1, 2/3$) compared to low triaxialities ($T = 1/3, 0$). This trend has been previously observed by Srivastava and Needleman (2015b); Yerra et al. (2010b), Srivastava and Needleman (2013) for porous single crystals. Comparing void volume fraction evolution between the two half cells,

we observe that difference in void volume evolution between two half cells is hardly noticeable. This results from the fact that for this case direction X of major stress $\sigma_1 \neq \sigma_2 = \sigma_3$ coincides with the same crystallographic direction [001] in both half cells.

As seen from figure 5.3b, for Lode parameter $L = 1$, void grows slower than for $L = -1$ (note that the vertical axis of both figures has different scale). We can see differences in void growth behaviour of half cell 1 and half cell 2 for all triaxialities considered. In this case direction Z of a minor stress $\sigma_3 \neq \sigma_1 = \sigma_2$ varies between both half cells (see table 2.1). As seen in Fig. 5.2c the stress response in two half cells is then different, so the level of equivalent stress in half cell 1 is lower than in half cell 2. Following relation (Eq. 5.1), void grows faster in half cell 1 (continuous lines) compared with void growth in half cell 2 (dotted lines) at high and moderate triaxialities ($T = 1, 2/3$). However, at low triaxialities ($T = 0, 1/3$) void volume in half cell 1 decreases faster as compared to void in half cell 2. To find a source of such behaviour the local triaxialities have been calculated for the Cauchy stress averaged over each half cell separately. It has been found that the local triaxiality in half cell 1 for the case $T = 0$ is negative and equal to -0.2, while for half cell 2 it is higher and equal to 0.23. Similarly, respective values for the case $T = 1/3$ are 0.22 and 0.44, correspondingly. For the remaining cases local triaxialities per half cell are approximately equal to the macroscopic ones. All the values are collected in the table 5.3.

For Lode parameter $L = 0$, the behaviour of the void in both half cell 1 and half cell 2 are similar to the case of Lode parameter $L = 1$, hence plot of $f - \varepsilon_{eqv}$ is not presented. Among the Lode parameters considered, void growth rate is in general higher for Lode parameter $L = -1$, followed by $L = 0$ and $L = 1$.

5.3.1.2 Void growth in a hard-hard bi-crystal.

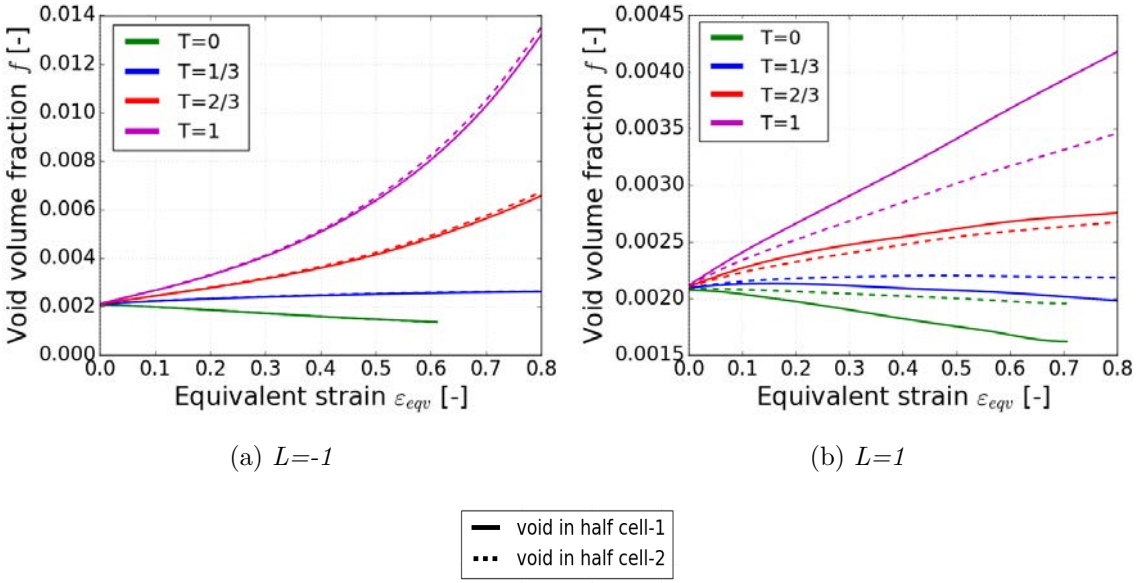

(a) *L=-1* (b) *L=1*

Figure 5.3: *Void volume evolution at different stress triaxialities and Lode parameters for the soft-soft bi-crystal. Matrix orientation of half cell 1 is O1 and half cell 2 is O2.*

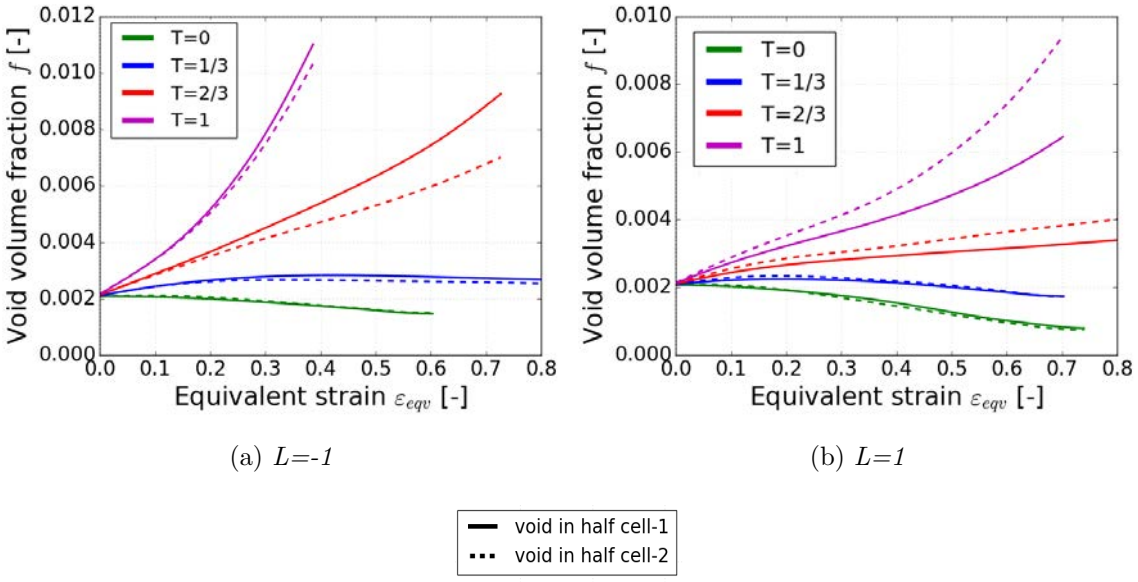

(a) *L=-1* (b) *L=1*

Figure 5.4: *Void volume evolution at different stress triaxialities and Lode parameters for the hard-hard bi-crystal. Matrix orientation of half cell 1 is O6 and half cell 2 is O4.*

For hard-hard bi-crystal RVE, half cell 1 has orientation O6 and half cell 2 has orientation O4. Similarly to previous comparison, void volume fraction evolution for different Lode parameters and triaxialities are plotted in figures 5.4.

For Lode parameter $L = -1$, void growth in half cell 1 is quite similar to void growth in half cell 2 for triaxiality ($T = 0, 1/3, 1$). For triaxiality $T = 2/3$, we observe a different void growth behaviour in both half cells. Void in half cell 1 grows faster compared with void in half cell 2.

For Lode parameter $L = 1$, we can see distinction in void growth between half cell 1 and half cell 2 at high and moderate triaxialities ($T = 1, 2/3$), as void in half cell 2 grows faster than void in half cell 1. For the remaining triaxialities ($T = 0,\ 1/3$), there is no significant difference in the void growth in two half cells. Similarly to the soft-soft bicrystal, when calculating local triaxilities per each half cell it has been found that the local triaxilities in half cell 2 are higher than in half cell 1.

For $L = 0$, the difference in void growth in half cell 1 and half cell 2 is small. Void in half cell 1 grows faster than void in half cell 2. Plots are not presented for $L = 0$ for brevity. As in the case of soft-soft bi-crystal RVE, void growth rate is higher for Lode parameter $L = -1$, followed by $L = 0$ and finally by $L = 1$.

5.3.1.3 Void growth in a soft-hard bi-crystal.

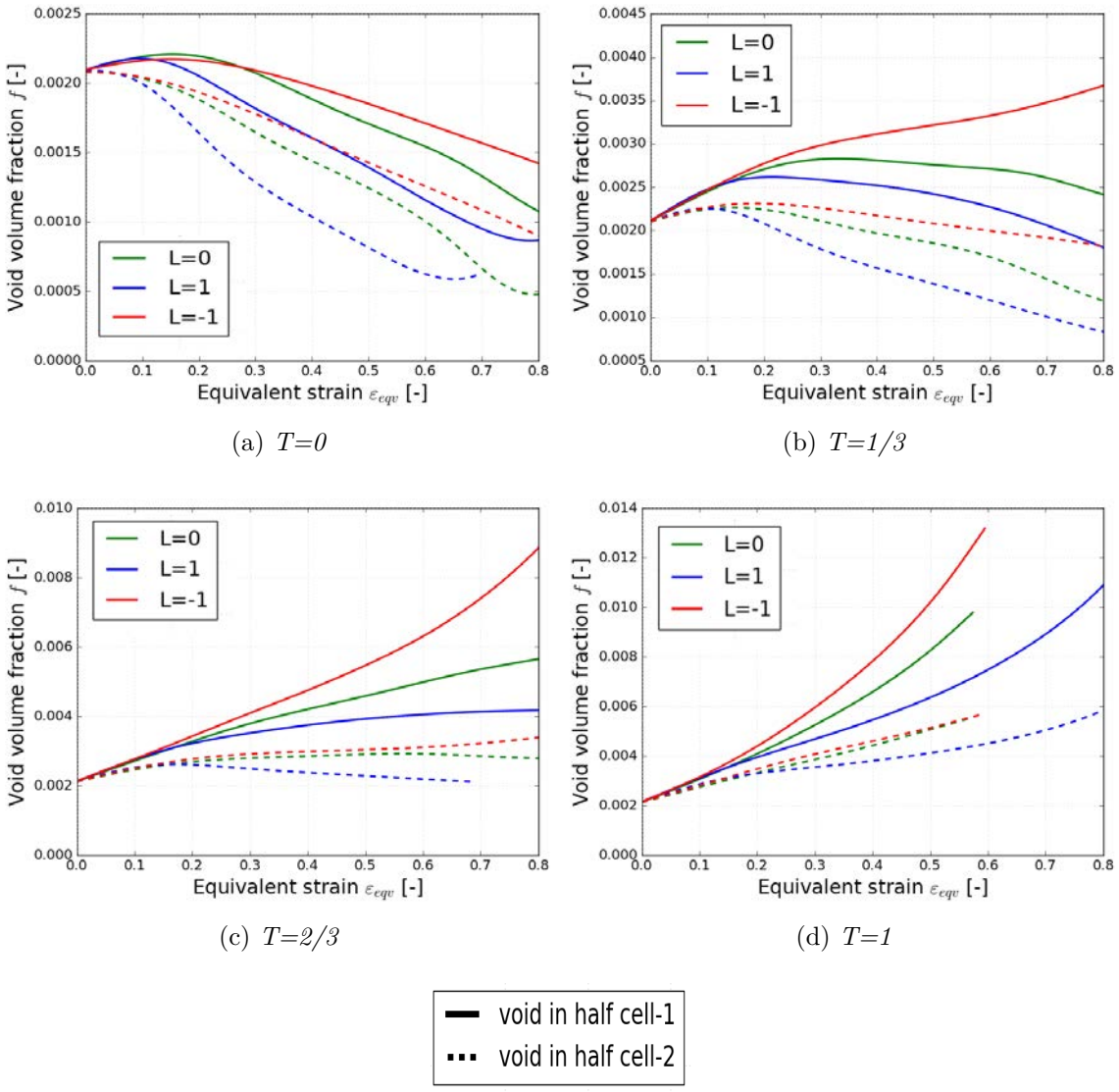

(a) *T=0* (b) *T=1/3*

(c) *T=2/3* (d) *T=1*

Figure 5.5: *Void volume evolution at different stress triaxialities and Lode parameters for the soft-hard bi-crystal. Matrix orientation of half cell 1 is O1 and in half cell 2 is O4.*

For soft-hard bi-crystals, half cell 1 has orientation O1 (soft) and half cell 2 has orientation O4 (hard). Evolution of f versus ε_{eqv} for half cell 1 and half cell 2 for different values of T and L are given in figures 5.5. The way results are presented in figures 5.5 are different as in previous sections to clearly show the changes occurring at low triaxialities ($T = 0, 1/3$), as the amount of void growth is small compared to high and moderate triaxialities ($T = 1, 2/3$).

For $T = 0$, as we can see from figure 5.5a, void volume fraction in both half cell 1 and half cell 2 decreases below the initial void volume fraction f_0. For half cell 1, void volume fraction increases slightly in the early stages of deformation, but starts dropping as deformation progresses, whereas void volume fraction f in half cell 2 drops faster than f in half cell 1 for all Lode parameters. Among the 3 Lode parameters considered, void volume fraction drops faster for $L = 1$, followed by $L = 0$ and least for $L = -1$ in both half cells.

Considering $T = 1/3$, as shown in figure 5.5b, at $L = -1$, we can see that the volume of the void in half cell 1 increases, whereas in half cell 2, void volume fraction grows slightly up until $\varepsilon_{eqv} = 0.2$, but later on the void volume fraction decreases. For $L = 0$, void volume fraction in half cell 1 increases up to $\varepsilon_{eqv} = 0.3$, but for ε_{eqv} greater than 0.3 it starts decreasing, and during the final stages of deformation, void volume decreases below the initial value $f_0 = 0.0022$. For void in half cell 2 even though we see a slight increase in f until $\varepsilon_{eqv} = 0.2$, at higher ε_{eqv} void volume starts decreasing below f_0. For $L = 1$, void in half cell 1 and void in half cell 2 behaves similarly to the case of $L = 0$.

The behaviour of the void in half cell 1 is similar for both triaxialities $T = 2/3, 1$, as shown in figures 5.5c and 5.5d as we observe void growth. For void in half cell 2, we observe void growth for $T = 1$ and $L = -1, 0, 1$, but for $T = 2/3$ void growth is very small and gradually during the course of deformation, we observe void growth saturation (i.e. no change in f) for $L = 0$ and $L = -1$. For $T = 2/3, 1$, void in half cell 1 grows faster than void in half cell 2 irrespective of Lode parameters. In general void grows faster for $L = -1$, followed by $L = 0$ and $L = 1$.

The difference in the behaviour of the void in both half cells are significant. For high and moderate triaxialities, the effect of Lode parameter is more prominent for void in half cell 1 (soft) compared to void in half cell 2 (hard). For all triaxialities and Lode parameters values considered, f always grows faster (or shrinks slower) in half cell 1 (soft orientation) compared with half cell 2 (hard orientation). This general trend is following the formula (Eq. 5.1) since the level of equivalent stress is much higher in the half cell 2 than in half cell 1, as seen in Figs. 5.2a,5.2b. Additionally, when calculating the average triaxialities per each half cell we have found almost two times higher values in half cell 1 (soft) than in half cell 2 (hard). The values are included in table 5.2.

5.3.2 Deformed Void shape in a bi-crystal

In this section, we will present results on the influence of matrix orientation and stress state on void shapes and accumulated shear distribution $\gamma = \sum_\alpha \int_0^t |\dot{\gamma}^\alpha| \, dt$ on void shape evolution in different bi-crystal RVEs.

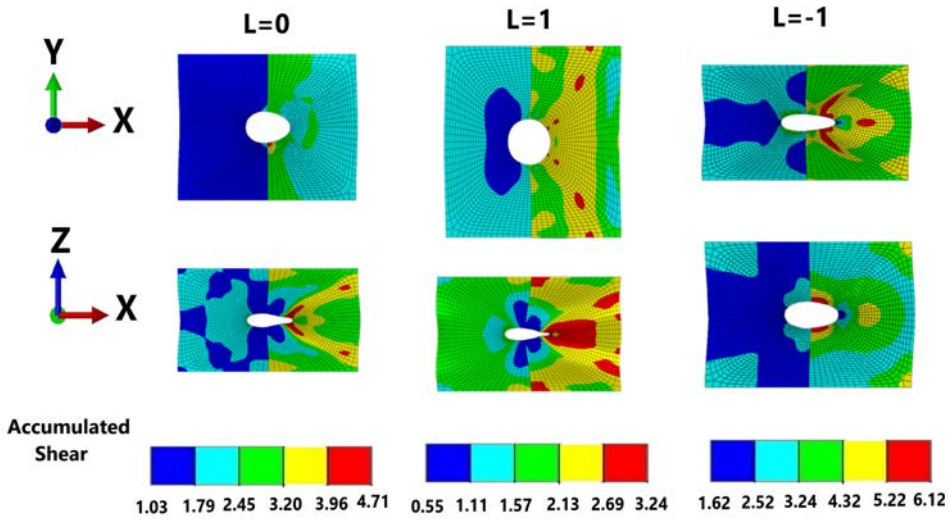

(a) *T=0*

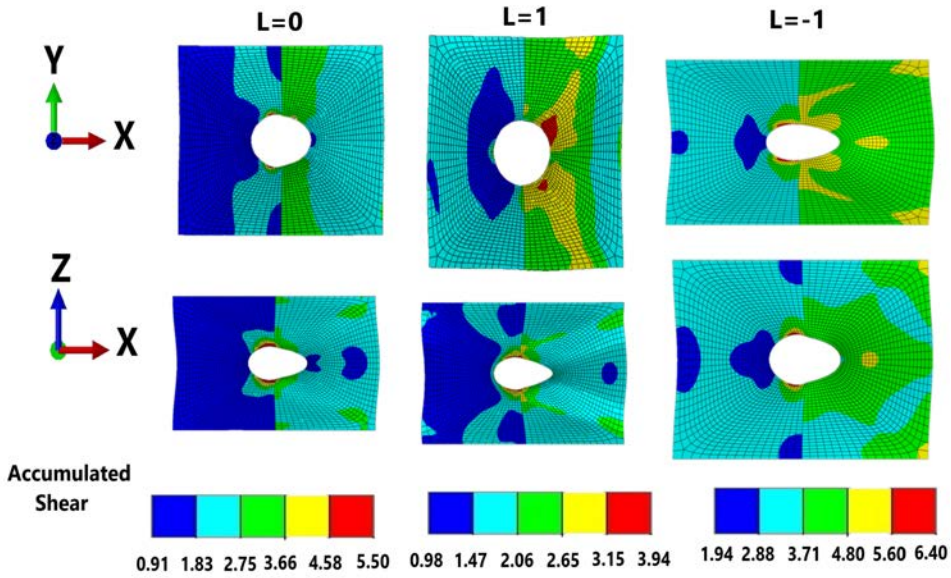

(b) *T=1*

Figure 5.6: *Deformed void shape and distribution of accumulated shear γ for soft-hard bi-crystal at stress triaxiality $T = 0, 1$ and equivalent strain $\varepsilon_{eqv} = 0.45$ for $L = 0, 1, -1$.*

5.3.2.1 Deformed void shape in a soft-hard bi-crystal

For soft-hard bi-crystal, at triaxiality $T = 0$, figure 5.6a shows the cross section of the deformed cell in two different planes (XY and XZ) at $\varepsilon_{eqv} = 0.45$ and the contours showing distribution of the accumulated shear γ for Lode parameters $L = 0, 1, -1$. As can be clearly seen from the plots, the distribution of γ and void shape in half cell 1 and half cell 2 are different for all the Lode parameters considered. For $L = 0$, the deformed cross-section of the cell along XY plane shows the void evolving into an ellipsoid on both half cells with the major axis of ellipsoid along X axis (direction of the maximum applied stress). Looking at deformed cross section along XZ plane, we see the void in half cell 2 flattening into an elliptical crack like shape, with its major axis along X axis and the crack like surface arising from collapsing

of void located away from the grain boundary, whereas void shape in half cell 1 is an oblate ellipsoid. The accumulated shear values are higher in half cell 2 compared with half cell 1 and the highest values of the accumulated shear is observed near the collapsed void surface in half cell 2, with a maximum value of 4.71.

From the deformed cell cross-section along XY axis, for $L = 1$, we see the void shape in both half cell 1 and half cell 2 to be circular at $\varepsilon_{eqv} = 0.45$. As in the case of $L = 0$, the void in half cell 2 collapses into a crack in XZ plane, with its tip along X axis and away from the grain boundary, whereas for void in half cell 1, the void evolves into an oblate ellipsoid. The value of the accumulated shear is higher in half cell 2 as compared to half cell 1 with a maximum value of 3.24.

For $L = -1$, the void shape in both half cell 1 and half cell 2 are very similar, and void evolves into an ellipsoid with the major axis along X. At $\varepsilon_{eqv} = 0.45$, we do not see void collapsing, but at higher strains void tend to collapse in both half cell 1 and half cell 2. Unlike $L = 0, 1$, for $L = -1$, void tends to collapse along Y axis and void radius evolves in the order $R_x > R_z > R_y$. Similar to the cases of $L = 0, 1$, the values of accumulated shear is higher in half cell 2. For the 3 Lode parameters analysed, the values of accumulated shear is higher for $L = -1$, followed by $L = 0$ and least by $L = 1$.

Similar analysis has been performed for $T = 1$ at Lode parameters $L = 0, 1, -1$ as shown in figure 5.6b. As we discuss previously from figure 5.5d, at $T = 1$ void growth is observed for all Lode parameters and the shape of the voids in both half cell 1 and half cell 2 are ellipsoid in all the cases, but there is a clear difference in the amount of growth within each half cell, as well as the void growth along each principal loading direction. Void radius is different along each direction and can be characterized as follows: for $\varepsilon_{eqv} = 0.45$ and for $L = 0$, void radius is of the order $R_x > R_y > R_z$ and for $L = 1$, order is $R_x = R_y > R_z$. Finally for $L = -1$ void radius is of order $R_x > R_z > R_y$. Accumulated shear values are higher in half cell 2 compared to half cell 1 and the value of the accumulated shear is higher for $L = -1$, followed by $L = 0$ and least in $L = 1$.

5.3.2.2 Deformed void shape in a hard-hard bi-crystal

In this section we will study void shape and accumulated shear distribution γ in the hard-hard bi-crystal, where the matrix orientation for half cell 1 is O6 and for half cell 2 is O4. Figure 5.7 shows the cross section of the deformed cell in XY and XZ planes, for $L = 0, 1, -1$ and $T = 0$ when $\varepsilon_{eqv} = 0.45$. For a hard-hard bi-crystal, we observe that the whole cell is deforming in such a way that it bends around the grain boundary. Such behaviour is understood when observing deformation of a respective bicrystal without a void for which in addition to axial deformation also shearing in opposite directions in two half cells is found. This shearing in XZ plane is also seen in Fig. 5.7. This is because of the anisotropic nature of the cell and the incompatibility between both half cells when hard-hard crystals comes in contact. This deformation behaviour of the cell has a huge influence on the way the void shape evolves. For $L = 0$, void shows elliptical shape with the major axis along X axis of the cell on both XY and

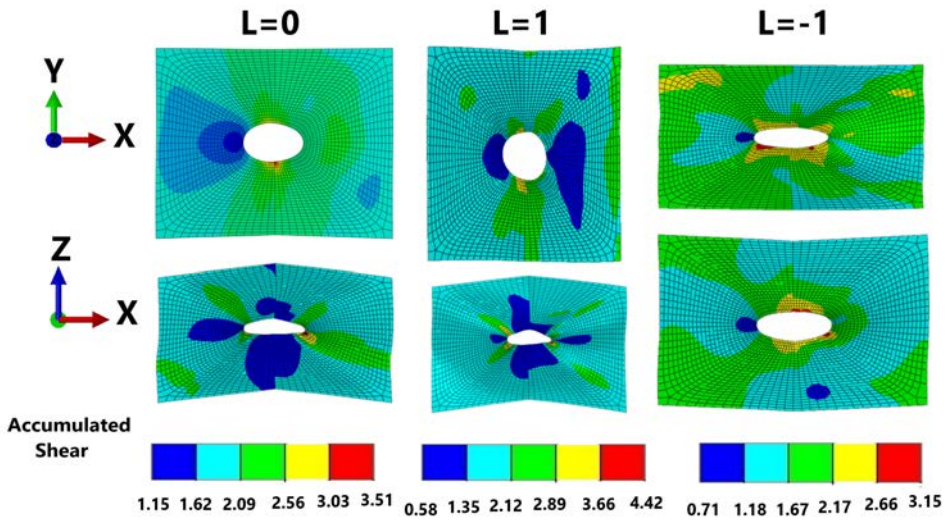

Figure 5.7: *Deformed void shape and distribution of accumulated shear γ for a hard-hard bi-crystal at stress triaxiality $T = 0$ and equivalent strain $\varepsilon_{eqv} = 0.45$ for $L = 0, 1, -1$*

XZ plane. Void shape is not symmetric along X axis of the cell and void radius along Z axis is higher in the upper part of the cell compared to the lower part along the grain boundary. The trend for void collapsing is clearly evident from the shape of the void. Void tends to collapse in half cell 2 faster than in half cell 1.

Similarly, for $L = 1$ and along XY plane, we observe void shape being circular and along XZ plane void shape is irregular and it is unsymmetrical along X axis. Similar to the case of $L = 0$, void radius on the upper part of the cell in Z axis is higher than void radius in the lower part of the cell and void growth is observed along X and Y axis, whereas void collapse along Z axis. Finally for $L = -1$, void shape is elliptical in both half cells and in both XY and XZ planes. Void radius evolution is of the order $R_x > R_z > R_y$ and void tend to collapse along Y axis.

The location of the maximum value of accumulated shear is close to the void in half cell 2 for all 3 Lode parameters considered, and away from void we observe a homogeneous distribution of accumulated shear and similar values in both half cell 1 and half cell 2. At $\varepsilon_{eqv} = 0.45$ and $T = 0$, the maximum γ is found in $L = 1$ and has the value 4.42.

For $T = 1$ (results not shown here) and all Lode parameters considered, we observe elliptical void shapes in both XY and XZ planes. Void shape is similar in both half cells and the accumulated shear distribution is similar to the case $T = 0$.

5.3.3 Effect of neighbouring grain orientation

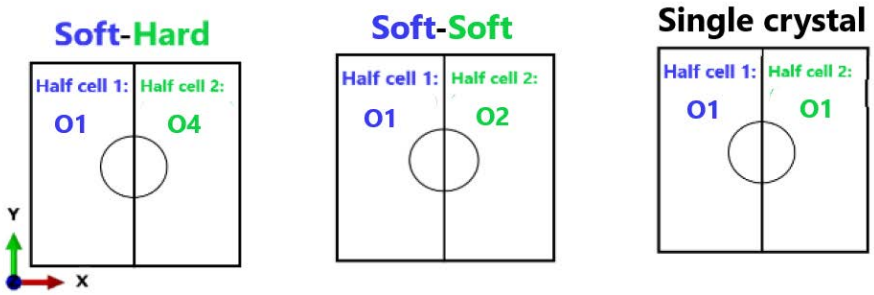

(a) *soft-hard, soft-soft and single crystal with orientation O1*

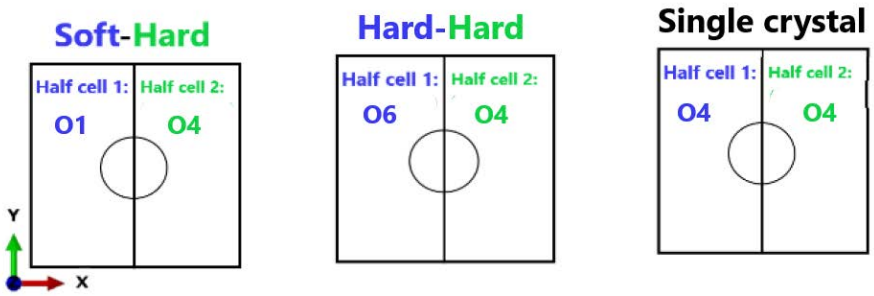

(b) *soft-hard, hard-hard and single crystal with orientation 04*

Figure 5.8: *Soft-hard, soft-soft, hard-hard bi-crystal and single crystal RVEs used for studying the effect of neighbouring grain orientation on the void behaviour. Blue colour represents orientations in half cell 1 and green colour represents orientation in half cell 2.*

In this section, three different comparisons are made to study the effect of neighbouring grain orientation on void growth, 1. a matrix with hard orientation neighbour, 2. a matrix with soft orientation neighbour, and 3. neighbour grain with the same orientation (i.e., single crystal). For that end, first we will compare void evolution in half cell 1 of the soft-hard bi-crystal and soft-soft bi-crystal. As shown in figure 5.8a, soft-hard bi-crystal and soft-soft bi-crystal has the same orientation for half cell 1 i.e., O1, but orientation of half cell 2 in soft-soft bi-crystal and soft-hard bi-crystal is different. Second, we will show results of void evolution in half cell 2 of hard-hard bi-crystal and soft-hard bi-crystal. For hard-hard bi-crystal and soft-hard bi-crystal orientation of half cell 2 is the same (i.e., O4 orientation), but orientation of half cell 1 in hard-hard bi-crystal and in soft-hard bi-crystal is different (see figure.5.8b).

Similarly, void behaviour is compared between half cell in a bi-crystal and half cell in a single crystal. The orientation of the single crystal is the same as half cell in the bi-crystal. For the case of the soft-hard bi-crystal, void in half cell 1 is compared with void in single crystal with the same orientation, i.e., O1, whereas for void in half cell 2 comparison is made with void in single crystal with the same orientation i.e., O4. By comparing the void behaviour in these cases, we can better understand the effect of neighbouring grain orientation on void behaviour and its morphology.

5.3.3.1 Void growth in soft-hard, soft-soft bi-crystals and single crystal

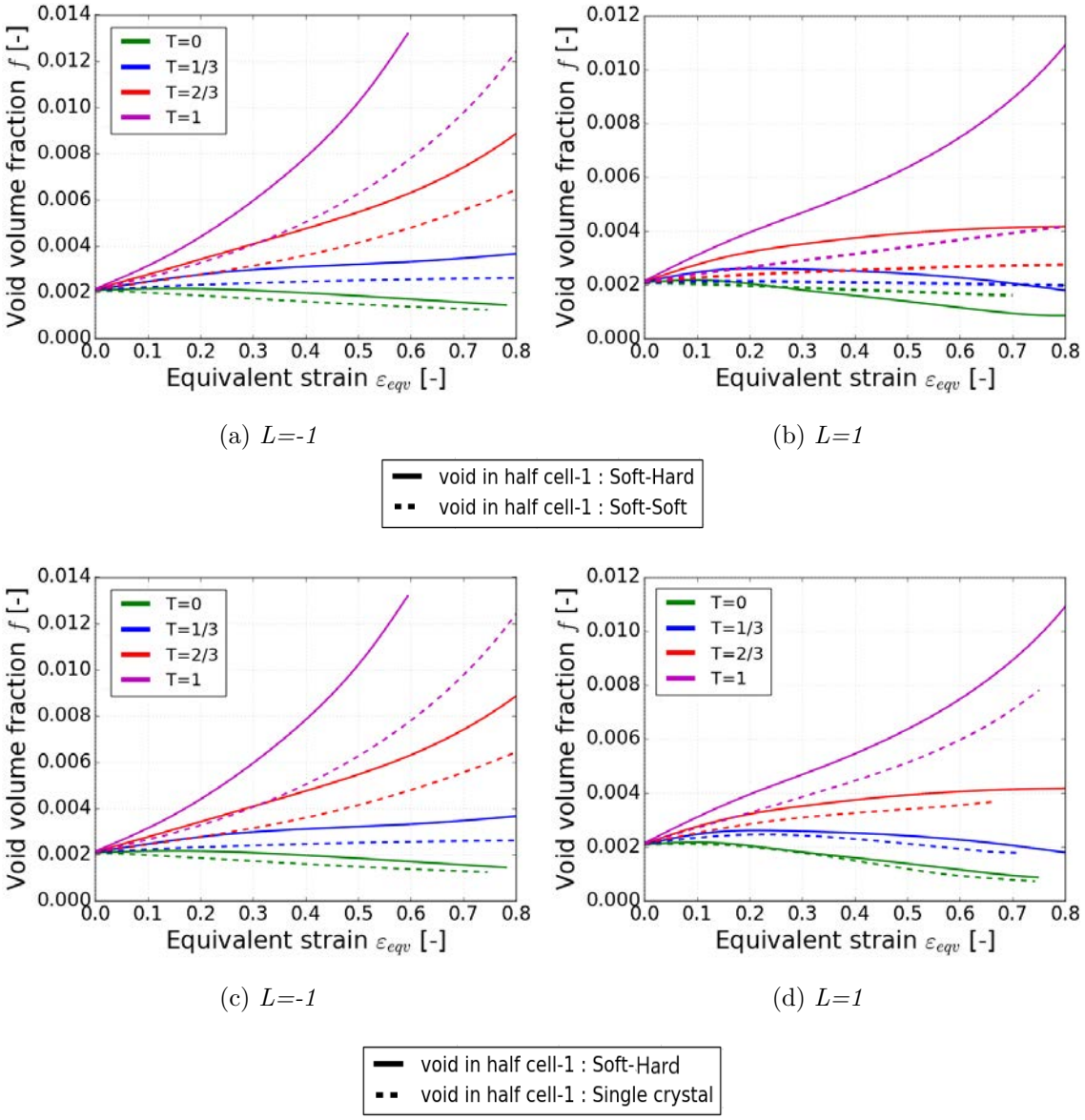

(a) *L=-1* (b) *L=1*

(c) *L=-1* (d) *L=1*

Figure 5.9: *Comparison of void volume fraction-equivalent strain evolution for half cell 1 in soft-hard, soft-soft bi-crystals and in a single crystal with the same orientation as half cell 1 at different stress triaxialities* $T = 0, 1/3, 2/3, 1$ *and Lode parameters* $L = 1, -1$.

In the case of soft-hard bi-crystal, soft-soft bi-crystal and single crystal, we will compare the effect of hard, soft and identical neighbouring matrix, respectively, on the void evolution in a soft matrix (half cell 1 is always O1 orientation). Figures 5.9 show void volume fraction-equivalent strain at different triaxialities and Lode parameters $L = -1, 1$. Figures 5.9a and 5.9b shows void volume evolution in half cell 1 for soft-soft and soft-hard bi-crystals. Figures 5.9c and 5.9d show void evolution in half cell 1 of soft-hard bi-crystal and of a single crystal. Single crystal calculations are performed for the full cell, but for comparison with bi-crystals, only half of the cell is taken into account.

For Lode parameter $L = -1$, void in half cell 1 of soft-hard bi-crystal (continuous lines) grows faster than in soft-soft bi-crystal (dotted lines) for triaxialities $T = 1,\ 2/3$ as shown in figure 5.9a. For triaxiality $T = 1/3$, void volume fraction in soft-hard bi-crystal increases slowly, whereas for soft-soft bi-crystal, void stops growing (i.e. void volume saturates after initial growth). For triaxiality $T = 0$, void volume fraction in both bi-crystals drop below f_0 from the beginning, and void in soft-soft bi-crystal drops faster than in soft-hard bi-crystal.

For $L = 1$ and $T = 1,\ 2/3$, as we can see from figure 5.9b, void in half cell 1 of soft-hard bi-crystal grows faster than void of soft-soft bi-crystal and the difference in void volume evolution between both bi-crystals is smaller compared to $L = -1$. For $T = 1/3$, the amount of void growth in both bi-crystals is very less and void volume fraction in soft-hard bi-crystal is higher than in soft-soft bi-crystal. For $T = 0$, void volume in both bi-crystals drops below the initial volume f_0, dropping faster in soft-soft bi-crystal than in soft-hard bi-crystal.

Void evolution in half cell 1 for soft-hard bi-crystal and single crystal is presented in figures 5.9c, 5.9d. For $L = -1$ and for all triaxialities considered, void growth in half cell 1 in a soft-hard bi-crystal is higher than void growth in a single crystal. Interestingly, for $L = -1$, if we compare the void volume evolution of single crystal with half cell 1 of soft-soft bi-crystal shown previously in figure 5.9a, we observe that the response of the void is the same for both cases at all triaxialities considered. This is explained by the same reason as almost the same response in two half cells seen in Fig. 5.3a.

For $L = 1$ and $T = 1$ we observe that void growth in half cell 1 of soft-hard bi-crystal is much higher than void growth in a single crystal. For $T = 2/3,\ 1/3$, void growth in half cell 1 of soft-hard bi-crystal is higher than the single crystal case, but the difference in value of f is not as big as for $T = 1$. For $T = 0$, void volume fraction decreases below f_0 for both cases and void in half cell 1 of soft-hard bi-crystal drops slightly faster than void in single crystal. For $L = 1$ void behaviour in half cell 1 of soft-soft bi-crystal is closer to the void behaviour of the single crystal case.

The observed variation in the void growth for O1 orientation placed in these 3 different configurations for a given Lode parameter can be correlated with the hierarchy of an average triaxiality in the corresponding half cell 1 demonstrated in table 5.2 and 5.3. Note that for a single crystal case its value is equal to the imposed triaxiality.

5.3.3.2 Void growth in soft-hard, hard-hard bi-crystals and single crystal

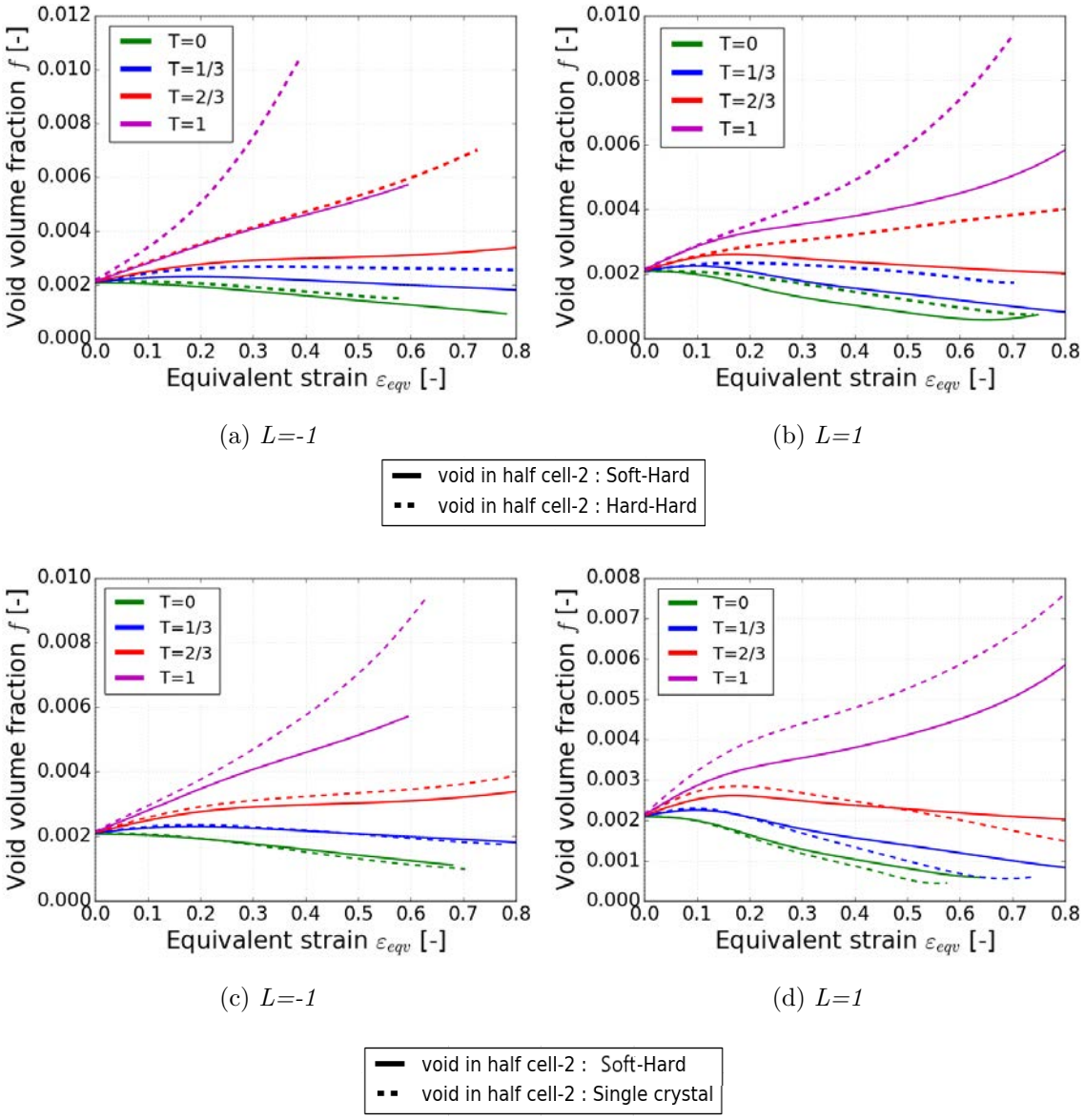

(a) *L=-1* (b) *L=1*

(c) *L=-1* (d) *L=1*

Figure 5.10: *Comparison of void volume evolution-equivalent strain for half cell 2 in soft-hard, hard-hard bi-crystals and and single crystal with the same orientation as half cell 2 at different stress triaxialities* $T = 0, 1/3, 2/3, 1$ *and Lode parameters* $L = 1, -1$.

In this section, the behaviour of the void in half cell 2 of a soft-hard bi-crystal is compared with the behaviour of the void in half cell 2 of hard-hard bi-crystal and single crystal with O4 orientation. The effect of a softer, harder and identical neighbouring matrix on the evolution of a void located in a hard matrix (half cell 2 is always O4 orientation) is compared and discussed.

Figures 5.10a and 5.10b show void volume fraction evolution with equivalent strain for voids of half cell 2 in a soft-hard (continuous lines) and in a hard-hard bi-crystal (dotted lines). For Lode parameter $L = -1$, void volume fraction in half cell 2 of a hard-hard bi-crystal grows faster than half cell 2 in a soft-hard bi-crystal for triaxialities $T = 1, 2/3, 1/3$. The difference in void volume fraction evolution of both bi-crystals is less remarkable for $T = 1/3$ than for

$T = 2/3,\ 1$. For $T = 0$, void volume fraction for both bi-crystals drop below initial void volume fraction f_0 and void volume fraction of half cell 2 in soft-hard bi-crystal drops faster than half cell 2 in hard-hard bi-crystal. As we can see from the figure, void grows faster when the half cell has hard neighbour compared to soft neighbour.

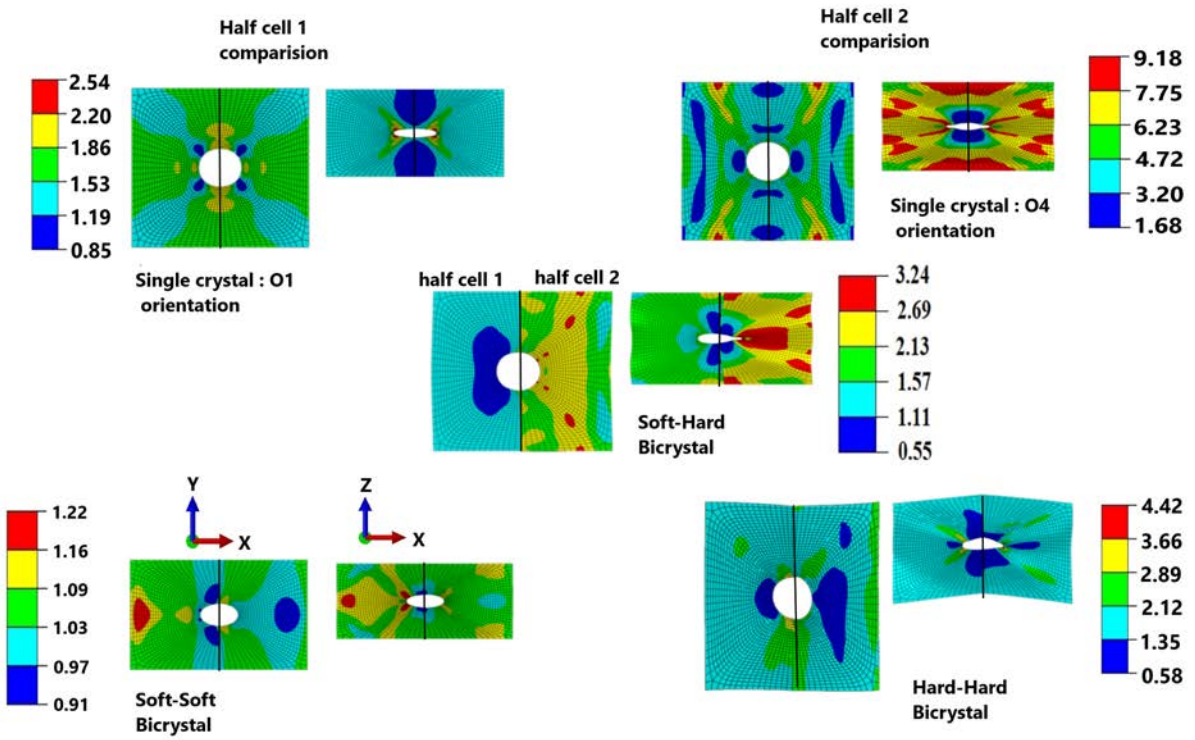

Figure 5.11: *Cross section showing deformed void shape and accumulated shear γ for a (soft) single crystal, a (hard) single crystal, soft-hard bi-crystal, soft-soft bi-crystal and hard-hard bi-crystal for $T = 0$, $L = 1$ and $\varepsilon_{eqv} = 0.45$. The soft orientation in half cell 1 is always O1 and the hard orientation in half cell 2 is always O4 for configurations containing soft or hard component, respectively (see figure 5.8a and 5.8b).*

Figure 5.10b shows void volume fraction evolution for Lode parameter $L = 1$. For $T = 1$, void volume fraction in both bi-crystals initially increases at the same rate, but at $\varepsilon_{eqv} > 0.15$ void volume in a hard-hard bi-crystal increases faster than in a soft-hard bi-crystal. For $T = 2/3$, we observe contrasting void behaviour in both bi-crystals: as f of a hard-hard bi-crystal gradually increases at constant rate, f of a soft-hard bi-crystal start decreasing below initial void volume fraction f_0. For $T = 1/3$ and $T = 0$, void volume fraction decreases in both bi-crystals below initial void volume fraction f_0, dropping faster in half cell 2 of a soft-hard bi-crystal than in a hard-hard bi-crystal.

Similarly, figures 5.10c and 5.10d show comparisons of half cell 2 void evolution for soft-hard bi-crystal (continuous lines) and for a single crystal with the same orientation as half cell 2 (dotted lines). Single crystal calculations are performed considering the full cell, but for comparison with bi-crystals, only the behaviour of half cell is considered. For $L = -1$ and comparing soft-hard bi-crystal with a (hard) single crystal, we observe that, at $T = 1,\ 2/3$, void growth in the single crystal is higher than in the soft-hard bi-crystal. At $T = 1/3,\ 0$, void

evolution f in the soft-hard bi-crystal is very similar to the single crystal case. For $L = 1$ and at $T = 1$, void growth in the single crystal is higher than in the soft-hard bi-crystal. For $T = 2/3$, we observe void growing in different way compared to other cases, as void volume fraction in both soft-hard bi-crystal and single crystal increases initially, but starts decreasing during final stages of deformation and void in single crystal drops faster than in soft-hard bi-crystal. For $T = 1/3, 0$ void volume decreases below initial void volume fraction for both cases and void volume fraction in single crystal drops faster than void in soft-hard bi-crystal.

Overall, for $L = -1$, 1 and at $T = 1$, void growth is higher in a hard-hard bi-crystal, followed by a (hard) single crystal and finally by a soft-hard bi-crystal. For $T = 1$ and $L = -1$, void evolution growing faster for orientation O4 than orientation O1 were also found by Ling et al. (2016) for a voided single crystal. At $T = 2/3$, f is higher in a hard-hard bi-crystal and the void behaviour of a soft-hard and a (hard) single crystal has similar trend. At $T = 1/3, 0$, void volume fraction decreases faster in a single crystal, followed by a soft-hard bi-crystal and finally by a hard-hard bi-crystal. The tendency for void collapse is higher in the single crystal case. For all triaxialities tested, the behaviour of the hard-hard bi-crystal is in general closer to the response of the single crystal case.

The calculated average triaxialities per each half cell included in table 5.1 and 5.2 conform with the exposed tendencies. An additional role in shaping the void evolution is played by the specific deformation of a unit cell in the case of the hard-hard bi-crystal as demonstrated in the next section.

5.3.4 Effect of neighbouring grain orientation on the deformed void shape.

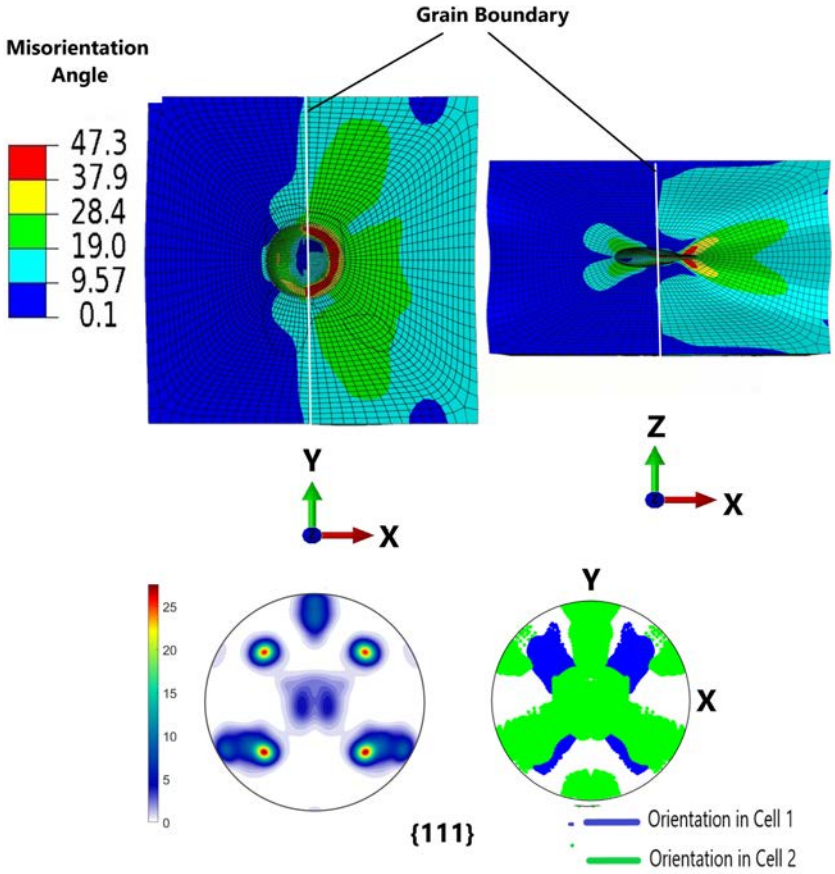

Figure 5.12: *Distribution of misorientation angle with respect to the initial orientation for soft-hard bi-crystal for* $T = 0$, $L = 1$ *and equivalent strain* 0.45*, Pole figures 111 at the bottom present the spread of the current crystal orientations for each Gauss point in the cell (pole figure on the left is a density plot, pole figure on the right-discrete point plot.*

It is clearly evident from the results presented in the previous section that void growth is affected by neighbouring grain orientation and, depending on the Lode parameter and triaxiality values, the behaviour of the void is either closer to a single crystal or its respective bi-crystal counterpart. In this section, the effect of neighbouring grain orientation on the void shape is presented and discussed. As in the previous section, the cases that are going to be compared are:

1. Void in half cell 1 in a soft-hard bi-crystal, void in half cell 1 in a soft-soft bi-crystal and in a single crystal with the same orientation as half cell 1 (O1).

2. Void in half cell 2 in a soft-hard bi-crystal, void in half cell 2 in a hard-hard bi-crystal and in a single crystal with the same orientation as half cell 2 (O4).

As noted by Srivastava and Needleman (2013), Srivastava and Needleman (2015b), changes in void shape in a initially spherical void are more significant at low triaxialities than

at moderate or high triaxiality values. We now focus on studying the influence of neighbouring grain orientation on the deformed void shape. We choose to present only one case here, i.e., triaxiality value $T = 0$ and $L = 1$ as a representative example. Deformed void shapes are compared in different RVEs at $\varepsilon_{eq} = 0.45$.

Fig. 5.11 shows the deformed void shape in single crystals with O1 and O4 orientation respectively, soft-soft, soft-hard and hard-hard bi-crystals. By comparing deformed void shape in half cell 1 (left-half) in a soft-hard bi-crystal and in a single crystal with O1 orientation, we observe that void in half cell 1 is ellipsoidal in both RVEs at both XY and XZ planes, with void radius in order $R_x \approx R_y > R_z$. In the soft-soft bi-crystal case, we observe that void within half cell 1 is also ellipsoidal but the order of void radius is $R_x > R_y > R_z$. In a soft-hard bi-crystal void shape in half cell 2 (right-half) is quite similar to the void shape in a single crystal with O4 orientation in both XY and XZ planes. As we see from figure 5.11 for the aforementioned RVEs, void tends to collapse into a "crack like" shape along X direction, and void radius for both RVEs are in order $R_x \approx R_y > R_z$. For a hard-hard bi-crystal, void evolves into irregular shape before collapsing along XZ plane, but void collapse occurs at rate slower than for single crystal. By comparing accumulated shear in half cell 1 among soft-hard, soft-soft and single crystal RVE, the maximum value of accumulated shear is observed in single crystal with O1 orientation (soft orientation) in the vicinity of the void in XZ plane. Similarly comparing accumulated shear in half cell 2 among soft-hard, hard-hard and single crystal RVE, the maximum value of γ is obtained in single crystal with O4 orientation (hard orientation) in XZ plane. Overall, for $T = 0$, $L = 1$ and at $\varepsilon_{eq} = 0.45$, γ values are higher in (hard) single crystal, followed by hard-hard bi-crystal, soft-hard bi-crystal, (soft) single crystal and finally soft-soft bi-crystal.

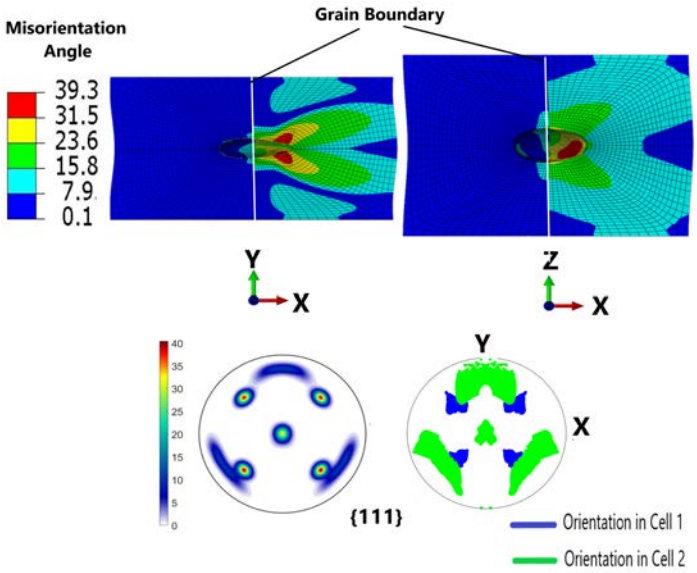

Figure 5.13: *Distribution of misorientation angle with respect to the initial orientation for soft-hard bi-crystal for* $T = 0$, $L = -1$ *and equivalent strain* 0.45. *Pole figures (111) at the bottom present the spread of the current crystal orientations for each Gauss point in the cell (pole figure on the left is a density plot, pole figure on the right-discrete point plot.)*

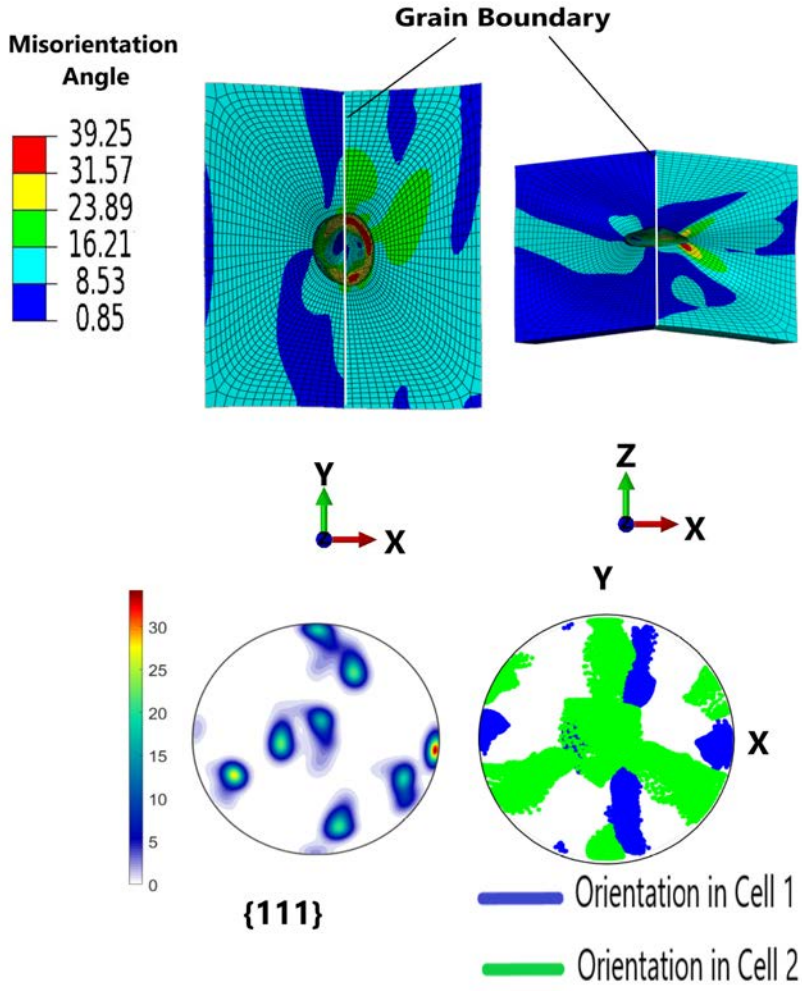

Figure 5.14: *Distribution of misorientation angle with respect to the initial orientation for hard-hard bi-crystal for* $T = 0$, $L = 1$ *and equivalent strain* 0.45*, Pole figures 111 at the bottom present the spread of the current crystal orientations for each Gauss point in the cell (pole figure on the left is a density plot, pole figure on the right-discrete point plot.)*

Figure 5.12, presents the influence of void on the heterogeneity of lattice rotation in the soft-hard bi-crystal, at $T = 0$ and $L = 1$. Let us stress that initially all elements within each half cell have the same orientation. While for a bi-crystal without a void, lattice rotates uniformly within each half cell (results are confirmed by calculations, but not presented here for brevity), strong variation is observed when the voids are present at the grain boundary. What is not obvious at first is that heterogeneity is more pronounced within hard half cell as initially homogeneous orientation in half cell is fragmented into two distinct orientations after deformation, as visible in the left pole figure. This is probably caused by the fact that different set of slip systems are operating in the top and bottom part of the half cell and the lattice is rotating in opposite directions in these two parts. Note that the largest misorientation angle ($> 45^o$) is observed close to the void boundary, where the void is distorted most. Figure 5.13 presents analogical results for the same bi-crystal but for $L = -1$ and $T = 0$. Here, also the larger misorientation angles are found in the hard half cell. Note that in both cases observed, differences in misorientation angles between elements belonging to the hard half cell are often

higher than 15^o, which suggests appearance of new high angle boundaries and possibility of grain refinement. Smaller differences in misorientation angles in two half cells are observed for hard-hard bi-crystal in figure 5.14. Nevertheless, also in this case the presence of void leads to the non-uniform lattice rotation leading to an increase of a lattice curvature.

Table 5.1: *Average local Triaxiality and Lode parameter for each half cell of hard-hard voided bi-crystal*

Applied global T and L	Local T and L (half cell 1)	Local T and L (half cell 2)
$T = 0$, $L = -1$	$T = 0$, $L = -1$	$T = 0$, $L = -0.8$
$T = 0$, $L = 0$	$T = 0$, $L = 0$	$T = 0$, $L = 0$
$T = 0$, $L = 1$	$T = -0.2$, $L = 1$	$T = 0.23$, $L = 1$
$T = 0.33$, $L = -1$	$T = 0.33$, $L = -1$	$T = 0.33$, $L = -1$
$T = 0.33$, $L = 0$	$T = 0.33$, $L = 0$	$T = 0.3$, $L = 0$
$T = 0.33$, $L = 1$	$T = 0.22$, $L = 1$	$T = 0.4$, $L = 1$
$T = 0.66$, $L = -1$	$T = 0.66$, $L = -1$	$T = 0.66$, $L = -1$
$T = 0.66$, $L = 0$	$T = 0.66$, $L = 0$	$T = 0.66$, $L = 0$
$T = 0.66$, $L = 1$	$T = 0.53$, $L = 1$	$T = 0.72$, $L = 1$
$T = 1$, $L = -1$	$T = 1$, $L = -1$	$T = 1$, $L = -0.86$
$T = 1$, $L = 0$	$T = 1$, $L = 0.1$	$T = 1$, $L = -0.1$
$T = 1$, $L = 1$	$T = 1$, $L = 1$	$T = 1$, $L = 1$

Table 5.2: *Average local Triaxiality and Lode parameter for each half cell of soft-hard voided bi-crystal*

Applied global T and L	Local T and L (half cell 1)	Local T and L (half cell 2)
$T = 0$, $L = -1$	$T = 0$, $L = -1$,	$T = 0$, $L = -0.8$
$T = 0$, $L = 0$	$T = 0$, $L = 0$	$T = 0$, $L = 0$
$T = 0$, $L = 1$	$T = 0$, $L = 1$	$T = 0$, $L = 1$
$T = 0.33$, $L = -1$	$T = 0.64$, $L = -1$	$T = 0.14$, $L = -1$
$T = 0.33$, $L = 0$	$T = 0.6$, $L = 0$	$T = 0.3$, $L = 0$
$T = 0.33$, $L = 1$	$T = 0.48$, $L = 1$	$T = 0.22$, $L = 1$
$T = 0.66$, $L = -1$	$T = 0.85$, $L = -1$	$T = 0.5$, $L = -1$
$T = 0.66$, $L = 0$	$T = 1$, $L = 0$	$T = 0.4$, $L = 0$
$T = 0.66$, $L = 1$	$T = 0.86$, $L = 1$	$T = 0.51$, $L = 1$
$T = 1$, $L = -1$	$T = 1.43$, $L = -1$	$T = 0.65$, $L = -0.86$
$T = 1$, $L = 0$	$T = 1.61$, $L = 0.1$	$T = 0.62$, $L = -0.1$
$T = 1$, $L = 1$	$T = 1.3$, $L = 1$	$T = 0.78$, $L = 1$

5.4 Summary and conclusions

Three-dimensional finite element cell calculations are carried out with the aim of analysing the response of voids at the grain boundary of a bi-crystal RVE. The effect of crystal orientation on porosity evolution are studied for three different cases: soft-hard, soft-soft and hard-hard RVEs subjected to different loading conditions. Unit cells consisting of cubic cells divided in two halves with a spherical void at the grain boundary with total void volume fraction in the

Table 5.3: *Average local Triaxiality and Lode parameter for each half cell of soft-soft voided bi-crystal*

Applied global T and L	Local T and L (half cell 1)	Local T and L (half cell 2)
$T = 0$, $L = -1$	$T = 0$, $L = -1$	$T = 0$, $L = -0.8$
$T = 0$, $L = 0$	$T = 0$, $L = 0$	$T = 0$, $L = 0$
$T = 0$, $L = 1$	$T = -0.2$, $L = 1$	$T = 0.23$, $L = 1$
$T = 0.33$, $L = -1$	$T = 0.33$, $L = -1$	$T = 0.33$, $L = -1$
$T = 0.33$, $L = 0$	$T = 0.33$, $L = 0$	$T = 0.3$, $L = 0$
$T = 0.33$, $L = 1$	$T = 0.22$, $L = 1$	$T = 0.4$, $L = 1$
$T = 0.66$, $L = -1$	$T = 0.66$, $L = -1$	$T = 0.66$, $L = -1$
$T = 0.66$, $L = 0$	$T = 0.66$, $L = 0$	$T = 0.66$, $L = 0$
$T = 0.66$, $L = 1$	$T = 0.66$, $L = 1$	$T = 0.66$, $L = 1$
$T = 1$, $L = -1$	$T = 1$, $L = -1$	$T = 1$, $L = -0.86$
$T = 1$, $L = 0$	$T = 1$, $L = -0.11$	$T = 1$, $L = 0.11$
$T = 1$, $L = 1$	$T = 1$, $L = 1$	$T = 1$, $L = 1$

cell $f_0 = 0.0044$ and volume of void in each half cell $f_0 = 0.0022$ are analysed. The responses of bi-crystal RVEs are studied for four stress triaxiality values: $T = 0, 1/3, 2/3, 1$, three Lode parameters $L = -1, 0, 1$ with a strictly specified orientation of loading directions with respect to the initial bi-crystal orientation, and a dimensionless equivalent strain rate $\dot{\varepsilon}_{eqv}/\dot{\gamma}_0$ in the range (100 – 150). For a given Lode parameter, the orientation with higher values of equivalent stress are considered as hard orientations and orientations with lower values of equivalent stress are considered as soft orientations.

The evolution of void volume fraction strongly depends on the overall stress triaxiality and more specifically on the triaxiality for the stress averaged over each half cell for all bi-crystal RVEs considered. When the level of strain increases the Lode value of macroscopic loading importantly modifies this dependencies. Moreover the Lode value has a prominent effect on the evolving shape of void, which especially seen at low triaxialities. Even though all bi-crystal RVEs considered have high angle grain boundaries, significant difference in void growth between the two half cells occurs specially for soft-hard bi-crystal case. The different behaviour of the void evolution in each half cell can be attributed to the difference in the strength (soft-hard) between the two initial orientations (O1 and O4) and the incompatibility between the two half cells. In the soft-hard bi-crystal case, at high triaxialities, void grows faster in softer crystal compared to harder crystal counterpart, whereas at low triaxialities, void tends to collapse faster in harder half cell compared to neighbouring softer crystal. Void growth is higher for higher triaxialities and void growth is faster for $L = -1$, followed by $L = 0$ and $L = 1$.

Void shape evolution in bi-crystals depends on triaxiality, Lode parameter and initial orientation of each grain. At high triaxialities, void tends to evolve into spherical/ ellipsoidal shapes irrespective of Lode parameter and grain orientation. At low triaxialities, void shape is greatly affected by the initial bi-crystal orientation with respect to the assumed loading conditions specified by the Lode parameter as the void tend to evolve into ellipsoidal shapes

for soft-half cells, and into crack like shapes for hard-half cells. Void shape in half cell 2 of soft-hard bi-crystal looks more similar to hard (O4) single crystal, rather than half cell 2 of hard-hard bi-crystal. Void shape in half cell 1 of soft-hard bi-crystal, half cell 1 of soft-soft bi-crystal and soft single crystal looks similar.

If the volume and morphology of voids with the same matrix orientation, but different neighbouring cell orientation are compared we observe that void tend to behave like the single crystal case (same orientation as bi-crystal half cell) if the difference in strength between two half's of the bi-crystal is small, i.e., in the cases soft-soft and hard-hard. When the difference in strength between the two half cells is higher (i.e., soft-hard) void behaviour tend to move away from the respective single crystal behaviour.

At high triaxialities, the profound effect the orientation of the neighbouring grain has on the evolution of the void volume becomes even more important than the orientation of the grain itself. Irrespective of Lode value, for void in half cell 1 of soft-soft, soft-hard bi-crystals and soft (O1) single crystal, void growth is faster in the soft grain when the neighbouring grain has hard orientation. For void in half cell 2 of soft-hard, hard-hard bi-crystal and hard (O4) single crystal, void grows faster in the hard grain if the counterpart has hard orientation.

Slip system activity also depends on triaxiality, Lode parameter and initial crystal orientation and far away from the void becomes similar to a fully dense crystal under the same imposed loading conditions. Depending on crystal orientation we have different Schmid factors, which in turn leads to different slip activity. Higher the value of stress triaxiality, higher will be the amount of slip activity, and hence higher plastic deformation in the matrix around the void, leading to higher void growth. For a soft-hard bi-crystal, at high triaxiality, the maximum value of accumulated shear occurs around the void in the softer part, and away from the void, slip activity in the harder part is higher. At low triaxiality, slip system activity is significantly higher in the harder part and the maximum value of accumulated shear is observed around the void also in the harder part, irrespective of Lode value. Moreover, in soft-hard bi-crystal the heterogeneity of slip activity, especially within the harder crystal increases leading to a non-uniform lattice rotation and consequently grain fragmentation. Slip activities dependence on Lode parameter is clearly evident from our studies. Slip activity is higher for $L = -1$, followed by $L = 0$ and least for $L = 1$, irrespective of triaxiality value. For hard-hard and soft-soft bi-crystals, slip activity away from the void is similar in both half cells and around the void maximum slip activity occurs.

Part III

Experimental work and microstructural investigation

6

Metallic sheets containing holes subjected to uniaxial tension: in-situ observation of hole evolution

Contents

6.1 General introduction

The challenge to predict ductility remains a difficult task even with advancement in numerical modelling and experimental techniques. Ductile process is extensively studied in the literature. It is known that ductile failure consists of three parts: nucleation (Goods and Brown, 1983; Maire et al., 2008), growth (Puttick, 1959; McClintock, 1968; Rice and Tracey, 1969; Gurson, 1977b) and coalescence (Needleman, 1984; Thompson, 1987; Pardoen and Hutchinson, 2000; Gologanu et al., 2001) of voids during plastic deformation. It is esential to include all three stages to have a comprehensive understanding of ductile failure process. The theory containing all three stages of ductile failure is very difficult to derive and is also difficult to asses the validity of the models through experiments. The main reason behind this is the lack of systematic experimental ways for observing and studying void coalescence. Non availability of quantitative experimental results is due to the stochastic nature of fracture, which makes capturing of the coalescence event very difficult. Furthermore, it is challenging to analyse coalescence between few voids, as the number of voids intervening during final failure is normally very high.

To overcome these challenges, different researches adopted a strategy of using fabricated material for experimental studies. For example Buffiere et al. (1999) studied aluminium matrix reinforced with zirconia particles and Gammage et al. (2004) tested aluminium matrix reinforced with alumina sphere particles by controlling the number of reinforced particles, thereby controlling the number of holes being nucleated. Magnusen et al. (1988) developed fabricated model materials with pre-existing holes and studied coalescence event in detail. By positioning the holes in a controlled manner, fixing its size (diameter of hole from 0.8 to 1.2 mm) and number of holes, Magnusen et al. (1988) simplified the microstructure by removing the nucleation problem. Further following the same approach, Weck and Wilkinson (2008) studied void coalescence in Al-Mg alloys by using model materials containing holes of micro dimension. In there study, they compared experimental results with McClintock (1968)'s model for void growth and coalescence. Moreover Nemcko et al. (2016); Nemcko and Wilkinson (2016) studied the significance of local microstructure on void growth and linkage in magnesium.

Studies presented earlier included testing of 2D model materials, with pre-drilled holes in gauge section of thin sheet tensile specimens. Weck et al. (2008); Hosokawa et al. (2012, 2013) studied 3D model materials with voids embedded in the specimens and by using x-ray tomography, they observed void growth and linkage in these model materials.

Investigations involving x-ray tomography, provides a non destructive way studying internal process as they happen. The application of x-ray tomography has been recently used by Maire et al. (2011); Toda et al. (2011); Seo et al. (2015) for studying fracture, predominantly investigating the effect of matrix properties and nucleation of voids. Lhuissier et al. (2013) used x-ray tomography to study the nucleation of cavities and its interaction with particles in wrought AZ31 magnesium alloy. Pushkareva et al. (2016) studied fracture process in

pure titanium. Using model materials with voids in the interior of the samples, they performed x-ray tomography to record void growth in 3D during in-situ straining. They reported that grain orientation plays the most important role on void growth than inter-void spacing and material strength.

In this doctoral thesis, we have used experimental specimens, similar to the ones described in Magnusen et al. (1988) and Weck and Wilkinson (2008), with pre-drilled holes located both within the grains and grain boundaries in a high purity polycrystalline aluminum. The holes are drilled in the gauge section of the samples, oriented at 90° and 45° with respect to the tensile axis with configurations shown in figure 6.1. By varying the hole diameter and position of the holes, three different types of specimens are defined. The influence of local microstructure, hole size, hole distance and hole orientation on void evolution and void interaction will be studied in detail.

6.2 Material and configuration of the samples

The material used to prepare experimental specimens is high purity Aluminum foils (99.9995%). The tensile specimens used in this work are dog bone shaped, with gauge length equal to $12mm$ and gauge width equal to $6mm$ as shown in figure 6.1. The initial thickness of the tensile specimen is $1mm$. Three different specimen configuration are produced with holes of different sizes and patterns:

1. Specimen pattern 1: tensile specimen with hole diameter $\phi = 1mm$ placed along the line of the loading axis.

2. Specimen pattern 2: tensile specimen with hole diameter $\phi = 0.5mm$ placed along the line of the loading axis.

3. Specimen pattern 3: tensile specimen with hole diameter $\phi = 0.5mm$, with angle between adjacent holes and loading axis being close to 45°

For all the three specimen configurations, the base, length, thickness, gauge length and gauge width dimensions are the same (see figure 6.1). Tensile specimen 1 contains five holes with diameter of each hole equal to 1 mm, distance between holes is 1.5 mm and the distance of the center of the holes to the edge is 3 mm. It is important to note that there are more than 0.5 mm of specimen free of holes of each side of the gauge enabling a better control of the samples, by allowing local microstructure to play its part. The holes are placed in the same line as the tensile loading axis.

Specimen 2 contains eight holes with diameter of each hole equal to 0.5 mm. The distance between the center of two consecutive holes is 1 mm and the distance to the edge is 3 mm. The holes are placed in the same line as the tensile loading axis.

Specimen 3 configuration contains 7 holes with diameter of the holes equal to 0.5 mm. The distance between the center of each consecutive hole is 1 mm horizontally and 1 mm

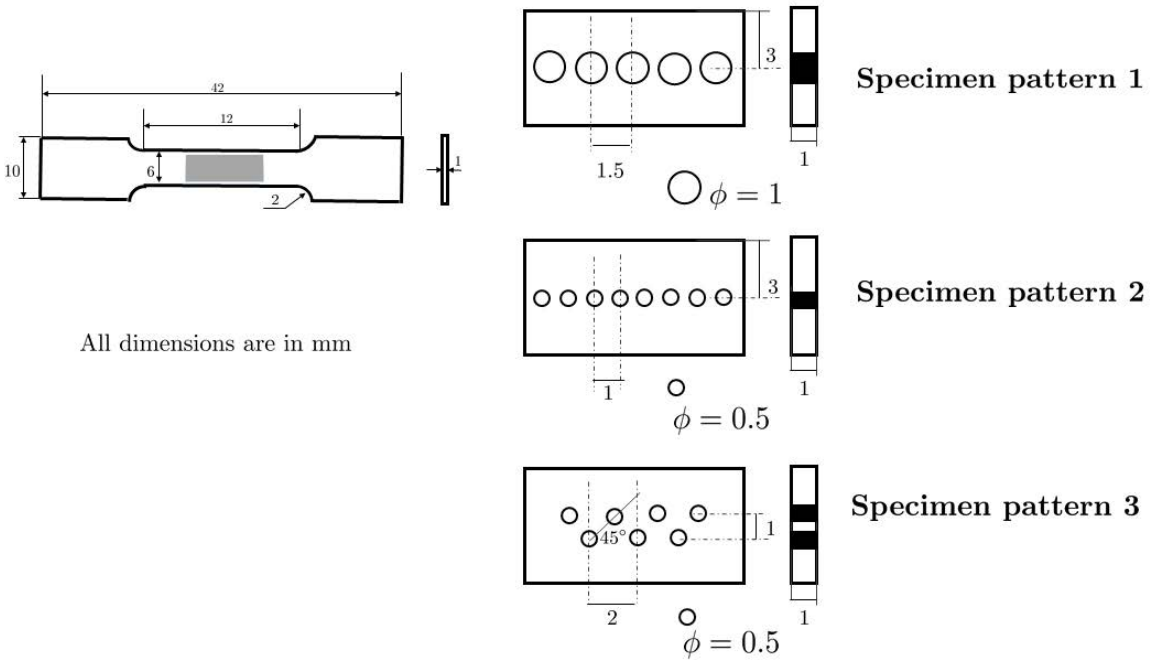

Figure 6.1: *Tensile specimens with 3 different configurations*

vertically. The distance from the edge of the specimen to the line of upper holes is 2 mm. Holes are placed in a pattern that forms an angle of 45° with the loading axis as shown in figure 6.1.

By changing the hole orientation, hole radius and number of holes in the specimens, a systematic comparison is conducted in this work to study the influence of relative position of the holes on failure behaviour. Specifically, by comparing specimen pattern 1 and specimen pattern 2, we will analyze the influence of the initial hole diameter on hole shape evolution, local microstructure evolution and final failure. Similarly, by comparing specimen pattern 2 and specimen pattern 3, we will analyze the influence of angular orientation of hole on hole shape evolution, local microstructure and final failure of the material.

6.3 Experimental procedure

By using the experimental technique, EBSD (Electron Backscatter Diffraction) before the start of tensile testing, orientation in terms of Euler angles in all the grains are obtained. This information will be used for calculating the misorientation between grains, the active slip systems, the Schmid factors in each grain and to predict which slip system is active and how favourable is the grain to deform (hard or soft orientations). The in-situ tensile testing of specimens are performed at room temperature by using tensile stage mounted inside SEM. Tensile testing was carried out within the chamber of a Scanning Electron Microscope (SEM) and high resolution images of specimens was captured during the process of loading at regular intervals. These images acquired at high magnifications reveals slip traces and finer details associated with the microstructure of the polycrystal and its evolution during loading. Additionally using

	Total samples	With EBSD	With DIC
Pattern 1	2	2	-
Pattern 2	1	1	1
Pattern 3	2	2	1

Table 6.1: *Tensile specimens and experimental procedures applied.*

Digital Image Correlation (DIC) during the tensile loading, strain distribution was also monitored in areas close to the holes. Finally by combining the experimentally obtained data and computationally calculated information (like Schmid factors, active slip planes) the effect of the heterogeneous microstructure on deformation behaviour can be analyzed for all the specimens.

6.4 Specimen preparation

In the gauge length of the specimen, various drilled hole configurations were produced by electro discharge machining, for which the holes run through the thickness of the tensile specimen. After making holes in the tensile specimen, the samples are annealed at 200 degrees for 2 hrs to remove residual stresses from the heat affected zones around the holes.

Preparing samples for EBSD process (Electron Backscatter Diffraction) is one of the most important task in any experiment, as the quality of experimental data depends on the smoothness of the surfaces. The surface of the specimens obtained from electro discharge machining are irregular and not smooth. For smoothing the surface, different processes can be used such as mechanical polishing, electro polishing or chemical etching.

The specimens used in this study are made of pure Aluminium. For such soft material, mechanical polishing has to be performed very carefully to minimize the risk of removing too much material in order to prevent significant changes in the thickness of the specimen. For the present study the samples are first mechanically polished with 1200 and 4000 grit silicon carbide papers with de-ionized water. By doing it we ensure that the surfaces of all the specimens are similar, despite their initial condition and previous treatment. This process is followed by smooth polishing with diamond colloidal particles starting from 9 µm grit and followed by 3 µm and 1µm grit. Finally the specimens are electro polished resulting in good surfaces for EBSD technique.

Electron Backscatter Diffraction (EBSD) scans are used to identify the crystal orientation and microstructure of the samples. EBSD scans are able to develop crystal orientation maps scanning the electron beam over the specimen and measuring the diffraction pattern at each point. In the orientation maps, a grain is defined as the region of the sample, where the crystal orientation is the same considering certain orientation angle tolerance. The maps are processed to show the position of all the grains and grain boundaries.

Orientation maps determined by EBSD, as any other experimental technique, are affected by measurement errors. These errors mostly occur due to a bad calibration of the EBSD system. Deviations from the true orientation due to noisy Kikuchi pattern or tolerances of the

indexing algorithm will also induce errors. Errors can be significantly reduced using de-noising techniques (Hielscher et al., 2019).

In this work, the EBSD data are cleaned up using Matlab (MATLAB, 2010) scripts with the help of MTEX (Bachmann et al., 2010). Grain reconstruction is defined as the subdivision of the specimen into regions of similar orientation. The grain reconstruction method that is used in MTEX is based on the definition of high angle grain boundaries, which are assumed at the Mittelsenkrechten between neighbouring measurements, whenever their misorientation angle exceeds a certain threshold. According to this idea grains are regions surrounded by grain boundaries. For grain reconstruction, there are different choices of how to deal with the unindexed regions. In this work, we assign the unindexed pixels into the surrounding grains. Afterwards, orientation of the grain is averaged, such that the misorientation within a grain does not exceed a given tolerance.

After performing EBSD, specimens are prepared for in-situ tensile testing. For the samples where Digital Image Correlation (DIC) is used, see table 6.1, surfaces are coated with diamond particles of size 3 μm-5 μm that provides image contrast enhancement. By measuring the movement of the particles on the surface of the specimen, it is possible to measure the distribution of local strains in the surface of the sample.

For all the specimens, tensile tests are conducted using an in-situ tensile machine of a maximum load cell of 1 kN and mounted within the SEM chamber. The imposed displacement rate to the specimens is constant and has a value of $10 \mu m/s$.

6.5 Tensile Specimen Pattern 1

In this section, results of specimen pattern 1 that contains five holes, with diameter of each hole = 1 mm are going to be presented. The holes are created such that they are inline with the loading axis as shown in figure 6.1. In order to better understand the influence of the local microstructure on the evolution and interaction of holes, two different samples are tested for this pattern. Both specimens are made of the same material, but they are different in terms of local microstructure. For both specimens, EBSD is performed before the tensile testing. In-situ tensile tests are developed and observations related to the evolution of the holes are made using SEM. Finally, results related to both samples are analysed looking at the EBSD maps, the deformation of the holes, the Schmid factors and active slip systems in each grain.

6.5.1 Sample 1

In this section, we will analyze the behaviour of sample 1, subjected to uniaxial tensile loading. With the help of EBSD, we can clearly differentiate between different grains based on their orientation. The orientation of the grains are marked with different colors representing their proximity to different planes (111, 101, 001) of a FCC crystal lattice following the inverse pole figure notation along the z axis [001] as shown in figure 6.2. The grain profiles obtained by EBSD of both front and back face of the sample 1 (flattened geometry representation) are

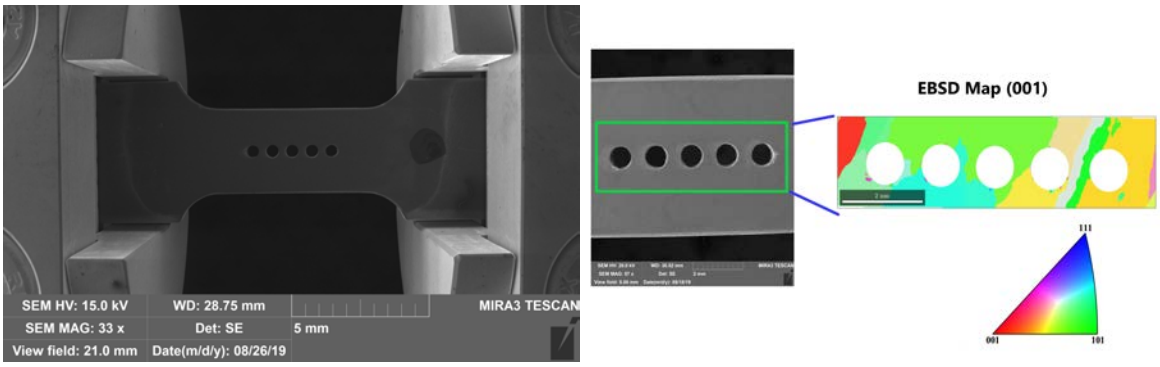

Figure 6.2: *(a) Tensile specimen of sample 1, mounted on tensile machine inside the SEM chamber. (b) Initial EBSD scan of sample 1 (only for the region marked around the holes)*

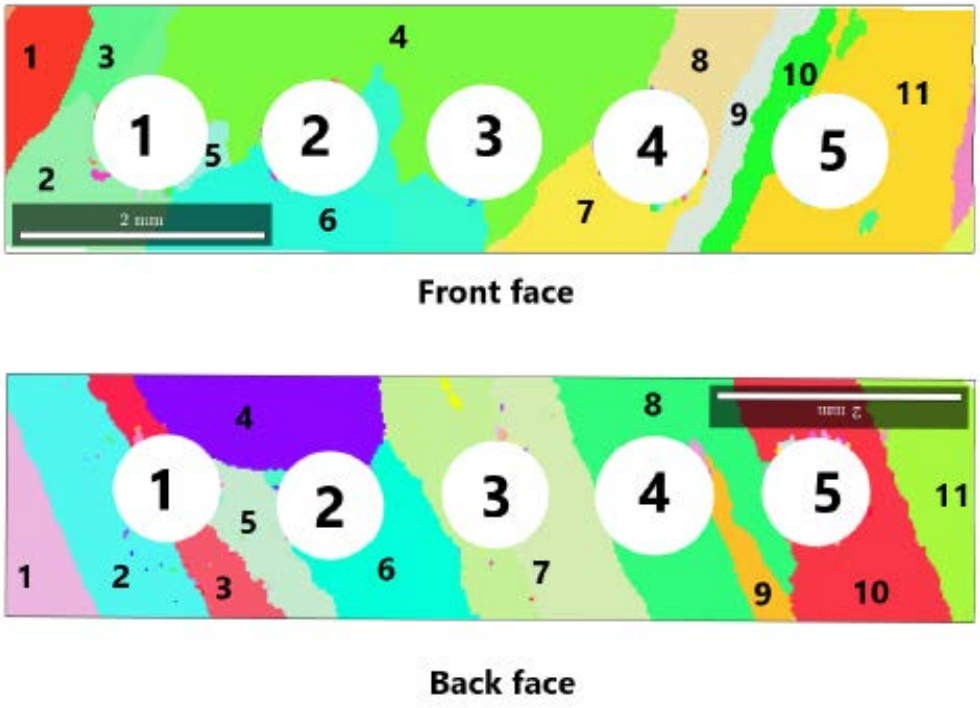

Figure 6.3: *Initial EBSD of the front and back faces of sample 1. Holes and grains are numbered for convenience.*

shown in figure 6.3. To differentiate between the grains and to aid the visualization of the orientations, in this case a 10° misorientation measure is used to illustrate the grain boundary profiles. It can be observed that grains shape and size on both front and back surface are not the same. Orientation distribution is also different, suggesting that grains are not perfectly columnar through the thickness. By looking at the contrast in the size, shape and orientation of each grain on front and back surface, a highly heterogeneous behaviour is expected of the specimen.

In this sample, most of the grains occupy a texture component in the vicinity of the twisted cube orientation (shown as example in figure 6.4). That is, most of the grains align their [0 0 1] directions parallel to the normal surface, and are also slightly rotated about this [0 0 1] axis. This texture provides the possibility to study different kinds of grain boundaries,

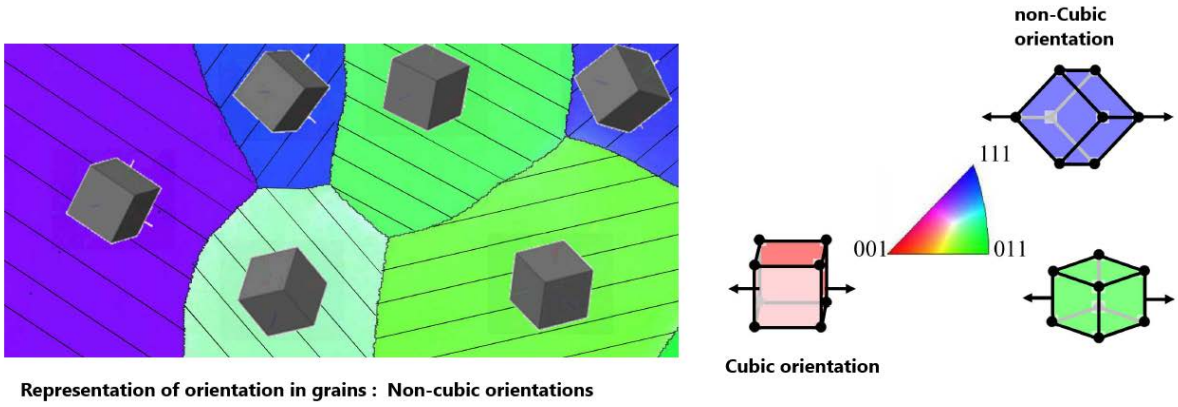

Figure 6.4: *Representation of cubic and non cubic orientation for FCC crystals*

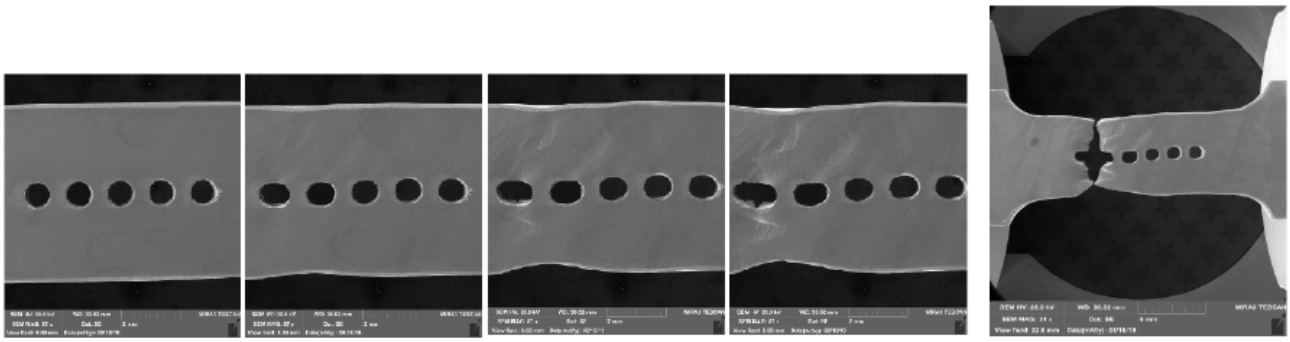

$(a)\ \varepsilon = 0\%$ $(b)\ \varepsilon = 2.26\%$ $(c)\ \varepsilon = 4.04\%$ $(d)\ \varepsilon = 5.0\%$

Figure 6.5: *SEM images of the specimen showing the evolution of slip traces and the growth the of the holes at different global strains* ε_{global} *(equation 6.1)*

taking into account distinctions between slip in cube versus non-cube orientations (figure 6.4 shows the representation for cube and non-cube orientations). It can also be observed that the holes are sharing boundaries with at least 2 grains. Further, by calculating the misorientation between each grain, it is found that most of the grain boundaries are high angle boundaries $(50-60°)$. This makes sample 1 a very interesting specimen for studying the evolution of holes at grain boundaries and for analyzing the effect of grain orientation on hole shape evolution.

6.5.1.1 Hole shape evolution and final failure of the specimen

In this section, results of hole shape evolution during tensile test are presented. Figure 6.5 shows hole shape evolution at different global strains. The images are captured during testing. From these high resolution SEM images the behaviour and growth of each hole and its surroundings in sample 1 can be analysed at different global strains (defined by equation 6.1).

$$\varepsilon_{global} = \frac{\Delta L}{L_0}; \Delta L = \text{total elongation}; \quad L_0 = \text{original length} \tag{6.1}$$

As observed in figure 6.5, hole 1 and hole 2 evolves into an elliptical shape, with major axis of the ellipse being parallel to the horizontal axis of the specimen. The ellipticity of hole

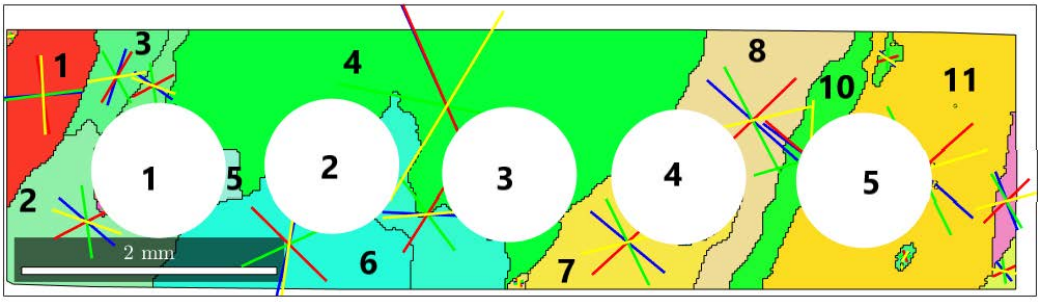

Figure 6.6: *Initial EBSD of the front face of sample 1 considering all possible slip systems. Slip system projections are based on the orientation of each grain.*

2 is in this case less clear than in hole 1. Deformation of hole 2 above and below the major axis is different. Hole growth is lower for the region above the major axis, than for the region below as observed from figure 6.5 at $\varepsilon_{global} = 5.00\%$. This observation can be attributed to the heterogeneity of the material, caused by the presence of multiple grains around hole 2. Hole 2 is sharing boundary with 2 grains (front face) and 3 grains (back face), all of them with different orientations and different Schmid factors and slip system activity as it would be discussed later. The maximum growth is observed in hole 1 and hole 2. Before the final failure, hole 3, 4 and 5 haven't evolved enough to provide a clear evidence of an irregular hole shape, but shows a glimpse of irregularity in its evolved shape. Final failure is observed through hole 1, starting from the bottom surface of the hole and cutting the specimen into two halves. The side of fracture is perpendicular to the loading axis.

In this case, high resolution SEM images of the specimen during loading revels the presence of slip traces as shown in figure 6.5 for $\varepsilon = 2.26$, 4.04 and 5.0%. A slip line is defined as a straight line resulting from the intersection of an active slip plane with the surface of the sample. The slip lines are observed in Scanning Electron Microscopy as steps or white leads on the surface of the specimen.

By analyzing the Scanning Electron Microscopy images of sample 1 given in Fig 6.5, it is observed that the grains surrounding hole 1 and hole 2 have more intensive slip traces than any other grain. Away from hole 1 and hole 2, slip lines does not appear very evidently. By comparing the experimentally observed slip planes with the computed slip traces in each grain, it will be possible to find out the slip system activity around the holes in the specimen. Also, with the help of the computed Schmid factors, we can confirm the likelihood of the slip system activity.

6.5.1.2 Maximum Schmid factors and active slip systems

Based on the orientation of each grain, for a given load, slip system is considered active if it has higher Schmid factor. It is interesting to mention that in uniaxial tension, the ideal cube oriented grain deformed along a <100> direction has eight active slip systems with Schmid factors of 0.41 and four with value 0. For the non cubic orientations, as the ones considered in this case, one or two slip systems will be normally dominant with high Schmid factor values, controlling the deformation process in the grain.

Slip System	Slip Plane	Slip Direction
1	(111)	[01-1]
2	(111)	[-101]
3	(111)	[1-10]
4	(11-1)	[101]
5	(11-1)	[011]
6	(11-1)	[01-1]
7	(-111)	[101]
8	(-111)	[110]
9	(-111)	[-101]
10	(1-11)	[110]
11	(1-11)	[011]
12	(1-11)	[0-1-1]

Table 6.2: *Definition of the slip systems considered. Different colours represents different slip planes with its respective slip directions.*

From the orientation of the grains obtained from EBSD scans, the slip trace directions and Schmid factors can be numerically computed for each grain, assuming uniaxial tension along the loading direction. The slip systems adopted in this work for FCC single crystal are listed in table 6.2. Four different FCC slip planes (each having three slip directions) are considered and marked with different colours: green, yellow, blue and magenta. The computed slip traces of the four slip planes are according to their 111 plane and are shown in table 6.2.

Figure 6.6, shows all the slip planes in each grain on the front surface of the specimen. The planes are represented in different colours following the different colour coding given in table 6.2. Figure 6.7 shows the maximum Schmid factor of each grain and the trace of the slip planes (blue line) in combination with the slip direction (red line) for which the Schmid factor is maximum for $\varepsilon = 2.26\%$. As seen in the figure, numerically calculated active slip lines and experimentally observed slip lines matches well.

Front Surface

Slip System	Grain 2	Grain 3	Grain 4	Grain 5	Grain 6
1	0.23	0.20	-0.20	0.008	0.26
2	-0.27	-0.41	-0.23	-0.019	.063
3	0.044	0.20	0.43	0.010	-0.33
4	0.14	0.39	0.17	0.43	-0.36
5	0.052	0.33	0.16	0.037	-0.08
6	-0.08	-0.05	-0.007	-0.39	0.27
7	-0.33	-0.24	0.22	-0.37	0.48
8	-0.024	-0.21	-0.46	-0.039	-0.14
9	-0.36	-0.46	-0.23	-0.41	0.33
10	0.19	-0.14	-0.39	-0.057	-0.12
11	-0.17	0.139	0.36	0.028	-0.35
12	0.019	-0.009	-0.03	-0.028	-0.48

Back Surface

Grain 2	Grain 3	Grain 4	Grain 5	Grain 6
-0.11	0.24	0.12	-0.13	0.07
-0.17	0.016	-0.02	-0.06	-0.33
0.29	-0.26	-0.10	0.19	0.26
0.18	-0.43	-0.48	-0.11	0.48
0.13	-0.15	-0.28	-0.08	0.33
-0.04	0.27	0.19	0.029	-0.15
0.27	0.47	-0.35	0.40	-0.14
-0.49	-0.17	-0.17	-0.43	-0.34
-0.22	0.29	-0.178	-0.03	-0.48
-0.46	0.04	0.133	-0.29	-0.34
0.25	-0.39	-0.41	0.049	0.26
-0.20	-0.43	-0.27	-0.24	-0.08

Table 6.3: *Schmid factor in each slip system for different grains in the front and back surface of sample 1.*

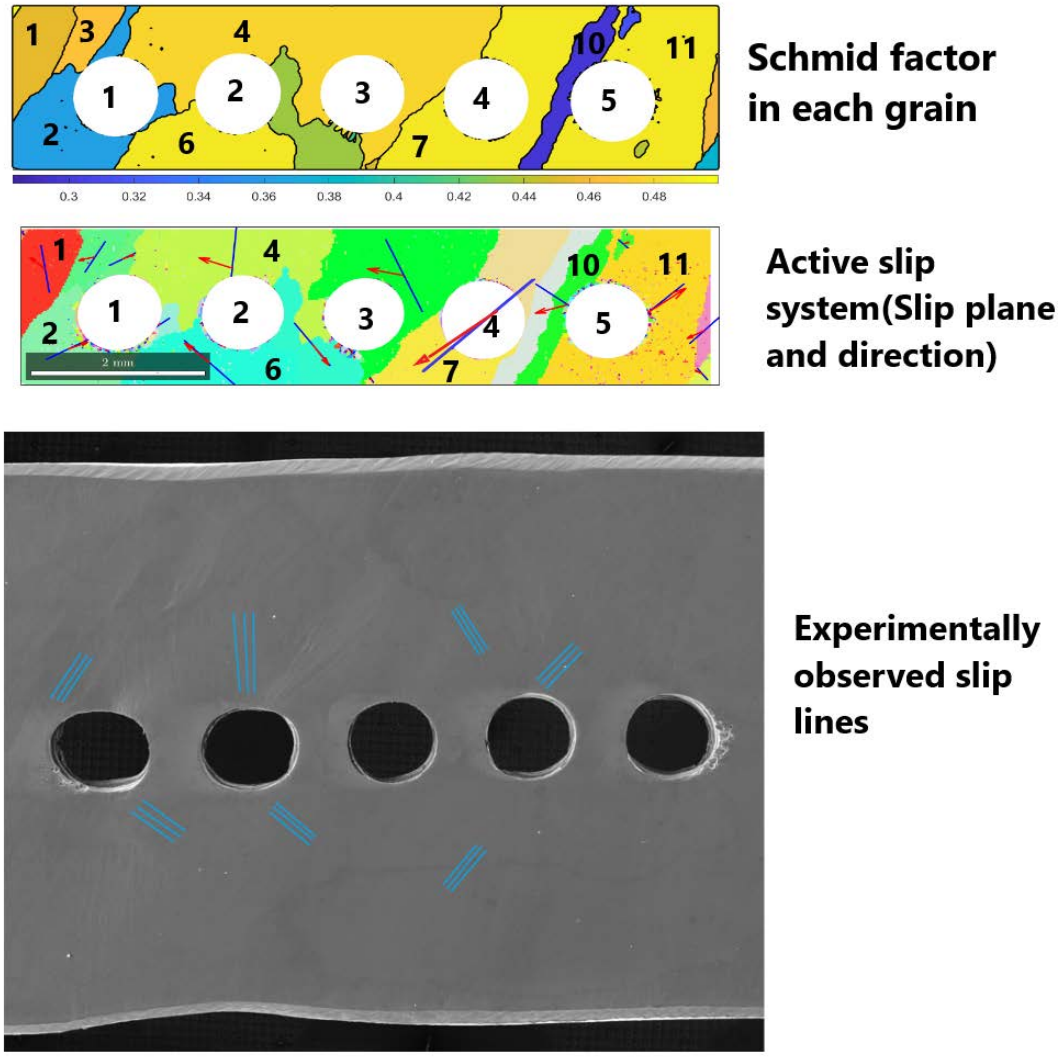

Figure 6.7: *Distribution of the Maximum Schmid factor, numerically computed active slip system and experimentally observed slip lines on the front surface of specimen for* $\varepsilon = 2.26\%$

In order to have a better understanding of slip system activity, table 6.3 presents the Schmid factors corresponding to uniaxial stress for all 12 slip systems inside the grains 2, 3, 4, 5, 6. These grains are placed around holes 1 and 2, and are the ones with higher slip activity. As observed in table 6.3, the difference in the maximum value of Schmid factors for all the grains is significant, indicating that the grains should all have different hardening/softening behaviour. From both the front and back surface of the specimen, most of the grains have a maximum Schmid factor in the range $(0.43 - 0.49)$.

From the front surface, in grain 6, multiple slip systems are active and two slip systems has a Schmid value of 0.48. The slip systems are number 7 and 12. Its trace on the surface is a straight line marked with blue and red colours respectively as shown in figure 6.7, which happens to closely matches the slip lines observed experimentally. Similarly, for grain number 4, multiple slip systems are active with Schmid factors greater than 0.3, but only two slip systems dominates: number 3 and number 8. The maximum Schmid values are equal to 0.43

and 0.46 respectively and are marked by straight lines with blue and red colours. The traces of these 2 slip systems also matches well with the experimentally observed slip planes.

For the back surface of the sample, for the region of interest (area around hole 1 and 2), the values of Schmid factor for grain numbers 2, 3, 4, 5, 6 for all the slip systems are also provided in table 6.3. The grains have similar behaviour as in the front surface. The orientation of each grain is different and the calculated maximum Schmid factor is also different with values ranging from 0.43 to 0.48. Because of the way the specimens were mounted inside the chamber, SEM images could not be acquired for the back surface of the sample.

Based on Schmid factor and slip system activity, it can be said that grain 2 is not favourable for deformation (hard grain), whereas grain 3 and 4 seems to be the most favourable for deformation (soft grains). These contrasting behaviours of grains around hole 1 is responsible for inducing necking and subsequent failure of the specimen.

No major slip bands are observed in the region between two holes and very less or no interaction between holes are found in the specimen. The grain orientation and microstructural heterogeneity is therefore the main cause of promoting failure in the sample.

6.5.2 Sample 2

Similar to the study conducted for sample 1, now we will analyse sample 2, which is similar to sample 1 in terms of number of holes and hole diameter, but different in terms of microstructure. Like sample 1, the grain profiles obtained by EBSD of the front face of sample 2 is given in figure 6.8. The inverse pole figure also is presented in figure 6.8 and shows that most of the grains are oriented in non cubic orientations, therefore heterogeneous grain deformation response is expected similar to sample 1.

Figure 6.9 shows all the possible slip planes in the grains of the front surface of the specimen. Four planes are represented in different colours following the criterion given in table 6.2. As sample 1, holes are named from 1 to 5 and grains from 1 to 12 for convenience and descriptive purpose. As seen in the figure, there are multiples holes (number 2, 3, 4, 5) which are located at grain boundaries, i.e. sharing boundary with at least two grains. Nevertheless, hole 1 is located within a single grain (grain number 2). Similar to previous section, hole shape evolution and slip system analysis are presented for sample 2.

6.5.2.1 Hole shape evolution and final failure of the specimen

Figure 6.10 shows SEM images of the sample during the tensile test. It is observed that hole 1 grows faster compared with the other holes and evolves into a regular elliptical shape. Even though other holes shows growth, it is not as large as hole 1 and also most of the holes tend to evolve into irregular shapes. Final failure occurs in the vicinity of hole 1 at a global strain of $\varepsilon = 5.35\%$.

The deformation of hole number 2 is higher on the left side if compared to the right side, as a consequence of the presence of grain 2 on the left side. Grain 2 is more prone to be deformed (softer) than other grains as we will discuss later. For holes 3 and 4, the deformation

of the upper halves is higher if compared to the lower halves. For hole number 5, which is surrounded by 3 grains, the deformation on the right side is higher if compared to the left side, again because of the presence in that side of the hole of grain number 9 that is a soft grain.

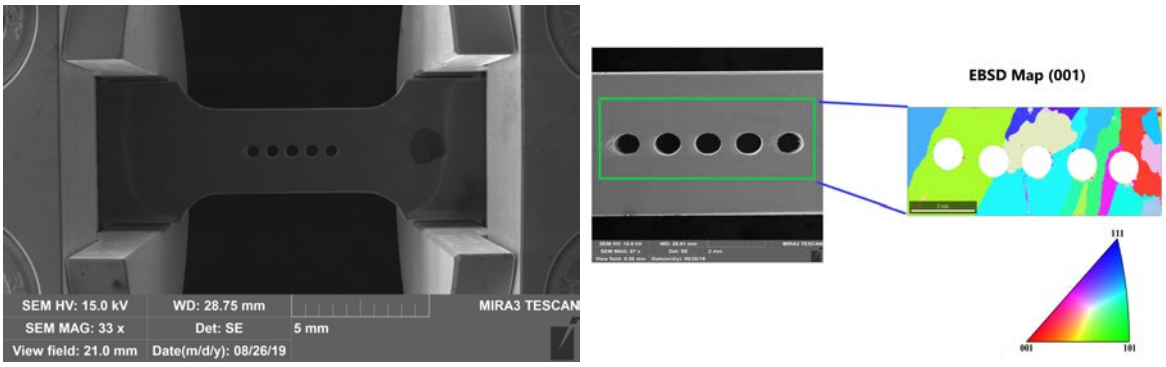

Figure 6.8: *(a) Sample 2 within the SEM chamber. (b) Initial EBSD scan of the front face of sample 2*

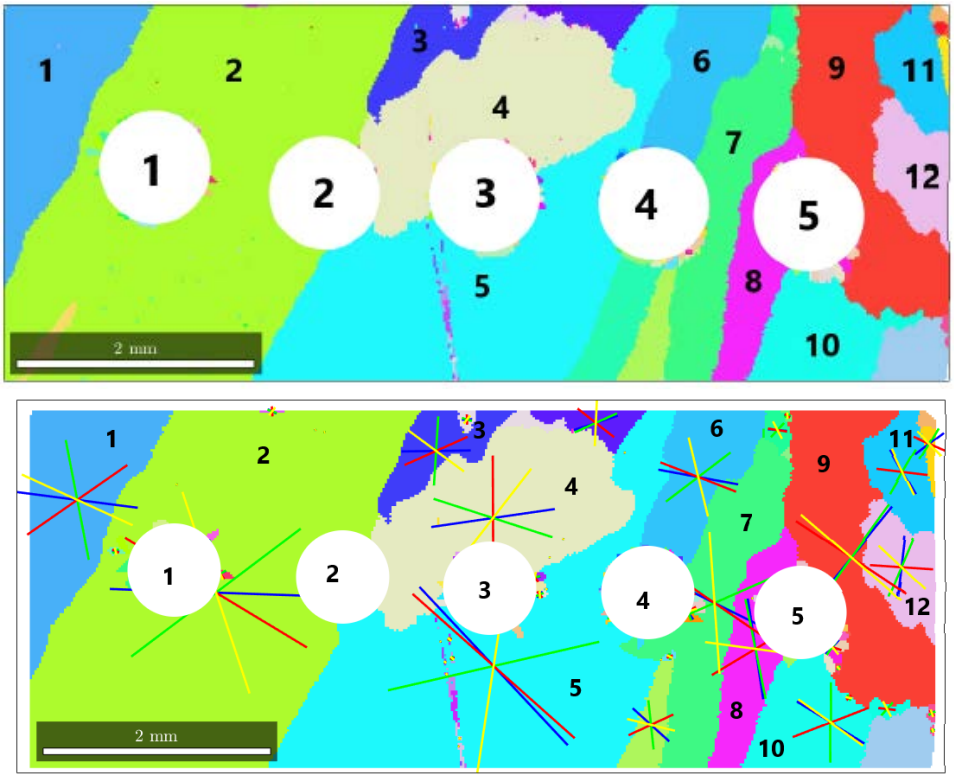

Figure 6.9: *Initial EBSD of the front face of sample 2, considering all possible slip planes. Holes and grains are numbered for convenience.*

6.5.2.2 Maximum Schmid factors and active slip systems

By analyzing figure 6.11, where the map of maximum Schmid factors is given for the front surface of sample 2, we observe that the maximum Schmid values varies from 0.3 to 0.5. The grain where we observe necking before final failure (grain 2) has a maximum Schmid factor close to 0.5. This high value of Schmid factor means that grain 2 is rather favourable to be deformed (soft grain). The maximum Schmid factor of the neighbouring grain is 0.33 (grain

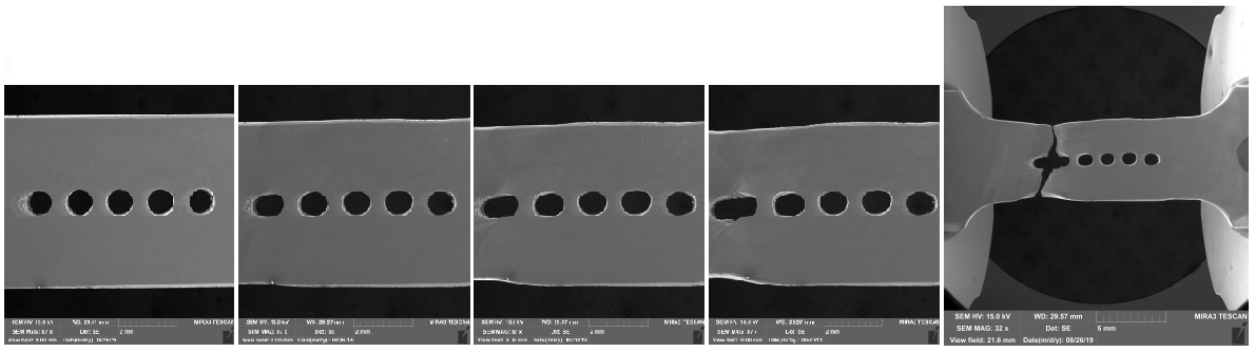

(a) $\varepsilon = 0\%$ (b) $\varepsilon = 2.5\%$ (c) $\varepsilon = 4.2\%$ (d) $\varepsilon = 5.35\%$

Figure 6.10: *SEM images of sample 2 at different overall strains.*

number 5). This low value of Schmid factor means that grain 5 is less favourable to be deformed than grain 2 (harder grain).

Hole 1 grows faster than other holes and is located within a soft grain with a neighbouring grain that has a hard orientation. This soft-hard set of grains creates the optimal conditions for higher deformation of hole 1 compared to the other holes.

Slip band formation (active slip plane and direction) in the front surface of the specimen is numerically calculated and is also given in Fig. 6.11. For the grain containing hole 1, slip trace calculated numerically matches well with experimentally observed slip lines and is along this plane where we observe the final failure of the specimen. The remaining holes (numbers 2, 3, 4 and 5) share boundary with at least 2 grains, each grain having different Schmid factor and slip system activity. This nature (hard-soft) of grains allows them to deform differently and hence holes evolve into irregular shapes.

As in sample 1, no significant slip bands were observed in the region between two holes showing no significant interaction between the holes. As in previous sample, the grain orientation and the grain heterogeneity are the main reason for the failure of the specimen.

6.6 Tensile Specimen Pattern 2

6.6.1 Sample 1

Following a similar approach as the one made for specimen pattern 1, in this section, we will analyse a new specimen pattern. The dimensions of the specimen remain the same as in the previous case, but the hole diameter and the number of holes of the specimen will be different. Apart from EDSD and slip trace analysis and in order to have a better understanding of the configuration, the digital image correlation (DIC) technique will be used to measure local strains on the specimen.

The tensile specimen (pattern 2) has smaller holes that pattern 1, placed in the same line as the tensile loading axis as shown in figure 6.1. The number of holes in this specimen are 8. The distance between holes is equal to 1.0 mm and hole diameter is 0.5 mm. Microstructural

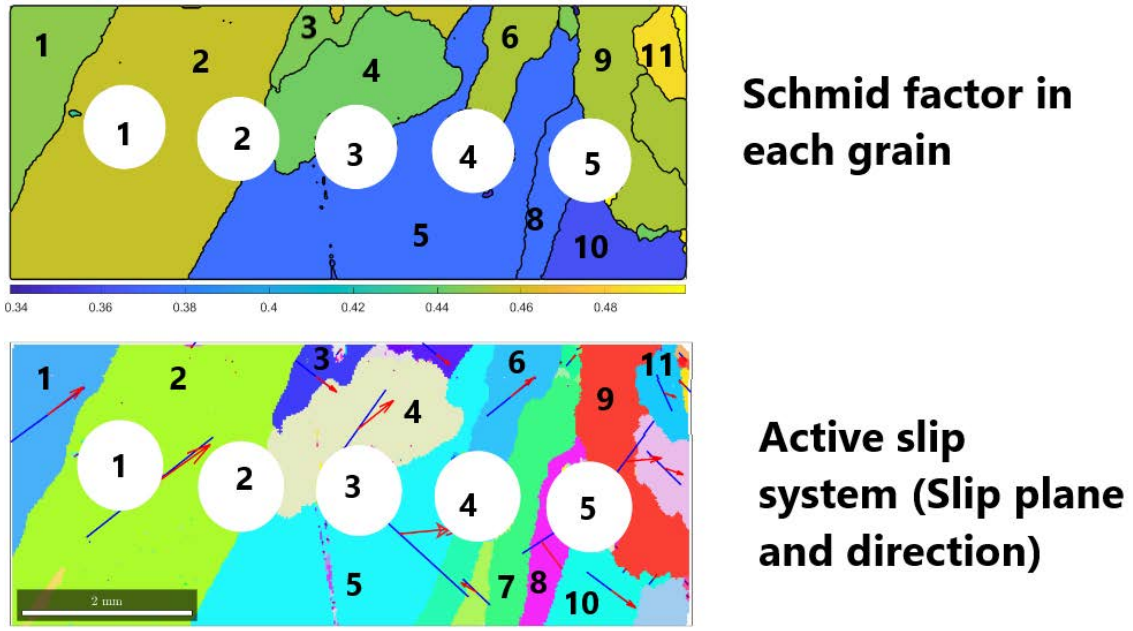

Figure 6.11: *Distribution of the Maximum Schmid factor and active slip system on the front surface of sample 2*

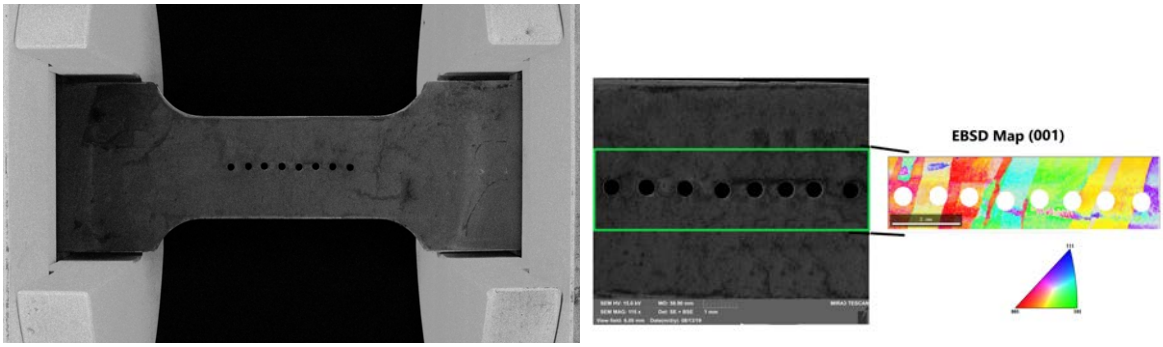

Figure 6.12: *a) Sample of specimen with pattern 2 within the SEM chamber. (b) Initial EBSD scan of the front face of the sample*

behaviour, hole shape evolution and possible interaction between holes will be analyzed for this specimen.

Figure 6.12 shows the undeformed specimen mounted on the tensile stage inside the SEM chamber. EBSD scan was carried out in the front surface of the sample before performing the tensile test experiment. The initial grain orientation map and the inverse pole figure is also presented in figure 6.12. In EBSD image (figure 6.13), holes are marked with numbers from 1 to 8 and grains with numbers from 1 to 7 for identification purpose. As observed from the image, holes 1, 2, 3, 4 and 5 are located on a single grain meanwhile holes 6, 7 and 8 share borders with two or three grains respectively. Grain 1, 2, 3 have perfectly cubic orientations, whereas remaining grains have non cubic orientations.

6.6.1.1 Hole shape evolution and final failure of the specimen

Figure 6.14 shows SEM images at different applied global strains. High resolution SEM images are captured only for the area defined between holes 2-7. As observed in the images,

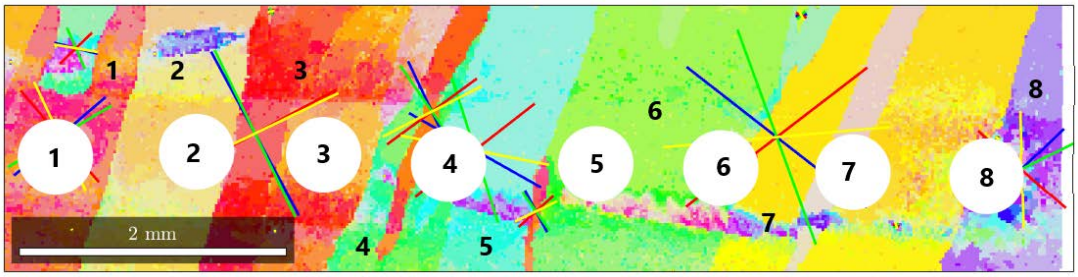

Figure 6.13: *Initial EBSD of the front surface of the sample considering all possible slip planes in the grains. Holes and grains are numbered for convenience.*

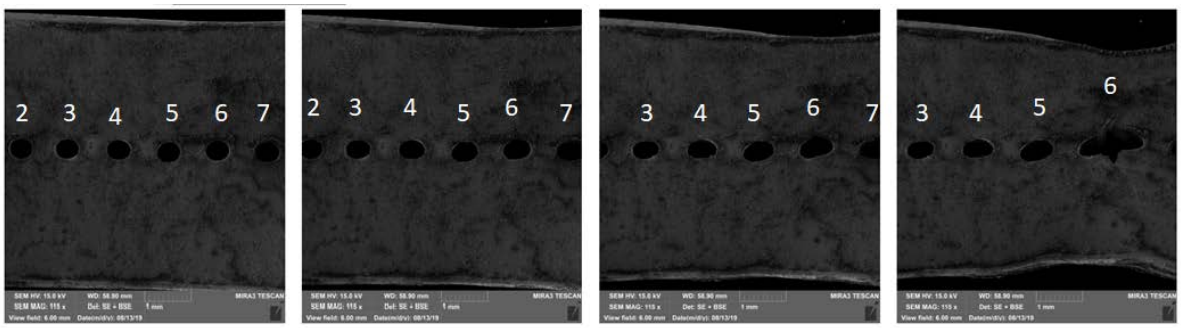

(a) $\varepsilon = 0\%$ b) $\varepsilon = 1.5\%$ c) $\varepsilon = 4.1\%$ d) $\varepsilon = 6.7\%$

Figure 6.14: *SEM images of specimen showing evolution of slip traces and growth of holes at different global strains* ε_{global} *(Eqs. 6.1).*

the magnitude of growth and deformation in each hole is different. As can be seen also in the SEM images, holes 4, 5, 6 and 7 evolve into elliptical shapes and we observe holes 4, 5 and 6 evolving as oblate ellipses with the major axis inclined a certain angle with respect to the loading axis. Holes starts deforming into irregular shapes from global strain of $\varepsilon = 4.1\%$ and finally cracks starts to appear from hole 6 at global strain of $\varepsilon = 6.7\%$, which results in the final failure of the specimen. Apart from the holes 4, 5, 6 and 7, the rest of the holes haven't evolved significantly. Hole 7 is the second most deformed hole, whereas hole 1 is the least deformed hole. Based on this observation analysis related to holes 1, 2, 3 and 8 and surrounded grains are not considered in this study.

6.6.1.2 Maximum Schmid factors and active slip systems

Now we will analyse the slip system activity in each grain surrounding the holes. Unlike previous section, high resolution images of slip lines cannot be obtained from SEM for this specimen because of the Digital Image Correlation particles covering the surface that obscure results. Therefore slip line analysis will be performed for this specimen only based on the numerically calculated slip traces. Figure 6.13 shows all possible slip planes on the different grains in the sample. Slip planes are projected on the initial microstructure of the sample and slip trace formation (active slip plane and active slip direction) are computed for each grain based on the maximum Schmid factor. Figure 6.15 shows the maximum Schmid factor in all of the grains. As seen in the figure, maximum Schmid factor ranges from $0.3 - 0.49$. In figure 6.15,

also active slip plane and active slip direction are represented by lines with colors blue and red respectively.

Focusing on the grains surrounding holes 4, 5 and 6, by looking at the grain structure and orientation, we can interpret the hole shape evolution and deformation behaviour of the sample. Hole 4 is located in grain 5, whereas hole 5 is located in grain 6 and hole 6 is located at the grain boundary of grains 6 and 7. Orientation of grains 5, 6 and 7 are different and hence the slip system activity in each grain is also different. Grains 5, 6 and 7 all have maximum Schmid factor higher than 0.4, but in grain 6 we have a slip system with maximum Schmid factor 0.48, which is more favourable for deformation. As we see from figure 6.14 holes tend to rotate along the grains slip planes. For hole 6 which is located between 2 grains, the shape of the deformed hole is different on each side of the grain boundary. Final failure initiates from hole 6, which is located at the grain boundary between grain 6 which is a soft grain and grain 7 which is a hard grain. By looking at the specimen failure in figure 6.14 d, it can be said that there is a very high possibility of crack initiating at the grain boundary, that further propagates along this grain boundary promoting the final failure of the specimen.

It can be observed that there is no interaction between holes. The specimen microstructure (grain size, shape, orientation and active slip systems) will be most likely the leading cause of hole shape evolution, hole rotation and final fracture of the sample.

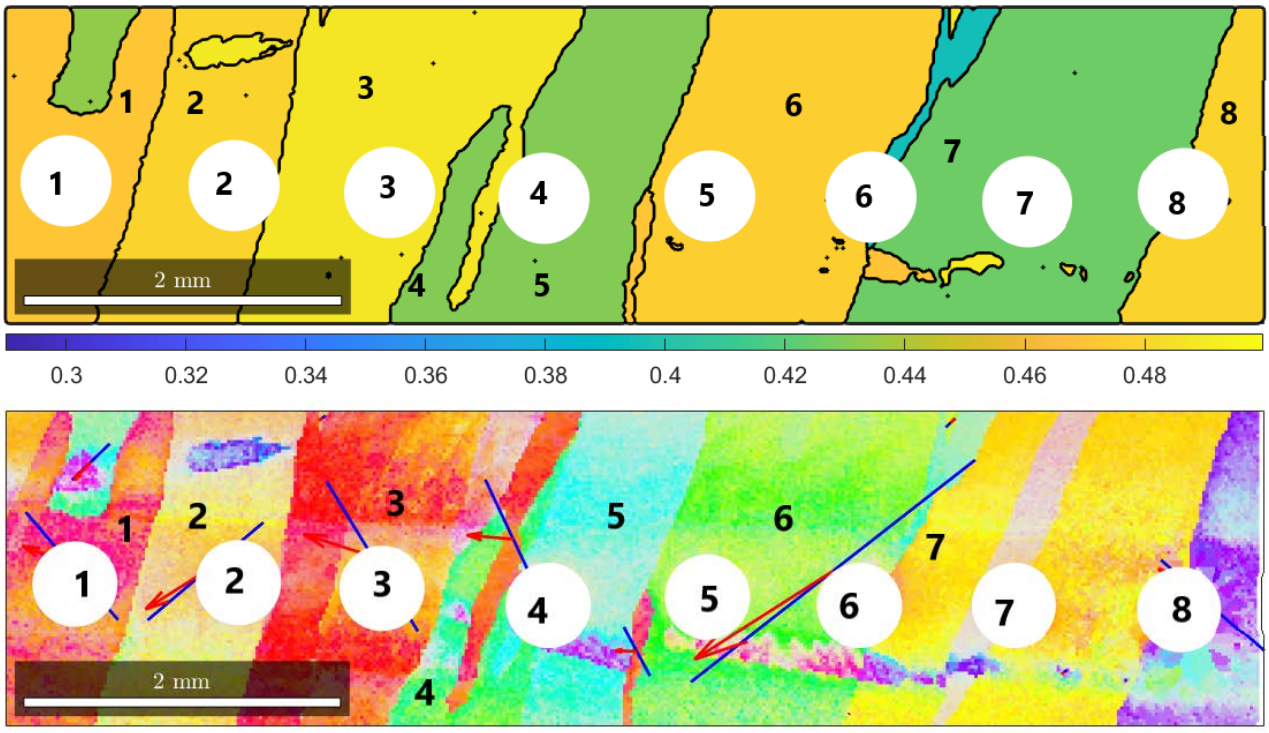

Figure 6.15: *Distribution of the Maximum Schmid factor and active slip system on the front surface of the sample*

6.6.1.3 Digital Image Correlation analysis

Next we will look into the distribution of the local strains in the specimen. The magnitude of local strains also will shed light on the deformation behaviour of the holes and grains around

them. For analyzing the local strains, we will make use of Digital Image Correlation technique. Digital Image Correlation (DIC) is an experimental approach that allows the investigation of the non-uniform distribution of strains at the grain scale in the polycrystals analyzed.

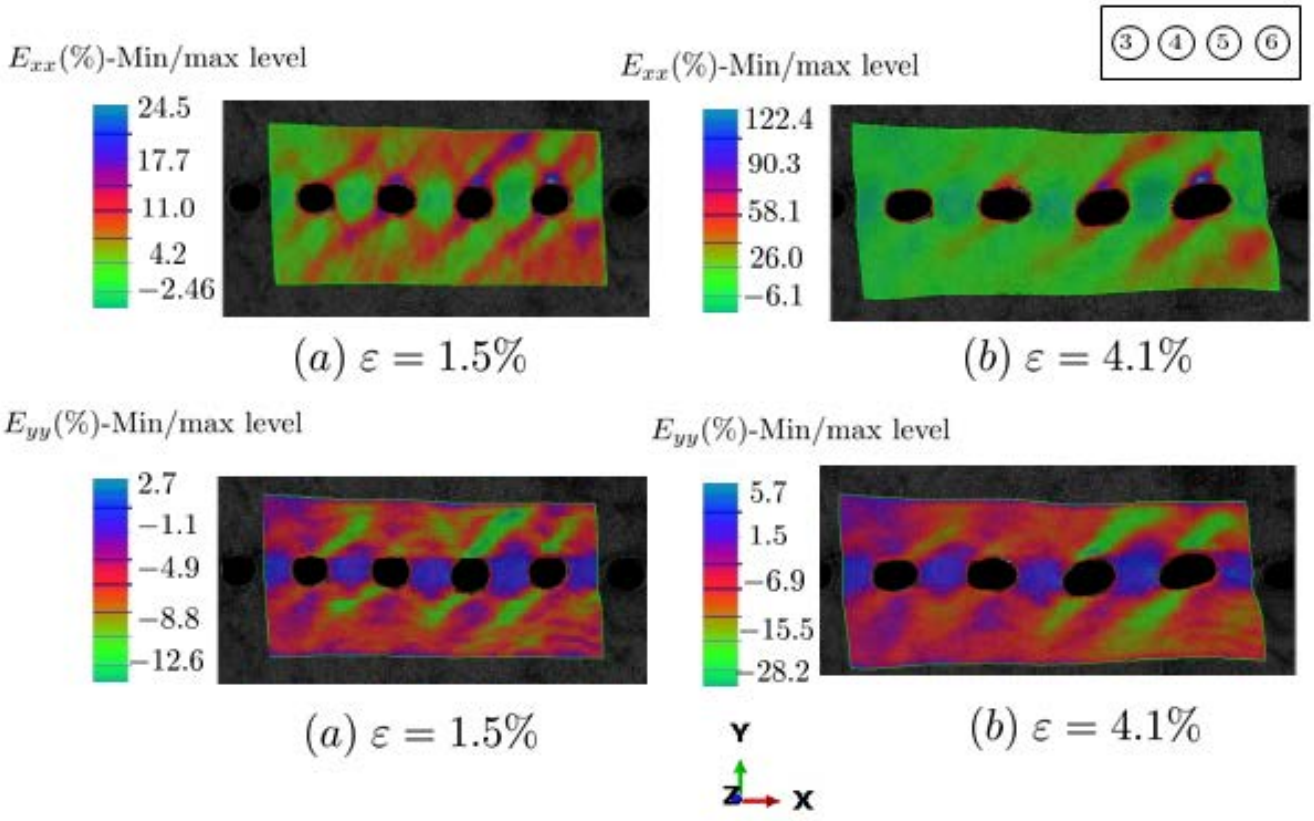

Figure 6.16: *Strain fields E_{xx} and E_{yy} calculated with digital image correlation at different global strains in the area between holes 3 and 6 of the specimen.*

Results pertaining to DIC of the specimen are presented in this section. Experimental measures of local strains in both x (E_{xx}) and y (E_{yy}) directions is as shown in figure 6.16 at different global strain values of ε. Local strains are defined following equations 6.2, 6.3, 6.4. For DIC images, only the area between holes 3 and 6 is taken into account. At global deformation $\varepsilon = 1.5\%$ two bands of larger local axial strain E_{xx} emanate from the holes and travel to top-right and bottom-left corners of the specimen. As the specimen deforms, for $\varepsilon = 4.1\%$, the local axial strain E_{xx} in these two bands increases approximately to values of 58% with strong strain localization ($E_{xx} \approx 122\%$) observed around hole 6. Strain localization is also observed around holes 4 and 5, however, the magnitude of E_{xx} is much lower than the one observed around hole 6.

$$E_{xx} = \frac{1}{2}\left(2\frac{\partial u}{\partial x} + \left(\frac{\partial u}{\partial x}\right)^2 + \left(\frac{\partial v}{\partial x}\right)^2\right) \tag{6.2}$$

$$E_{yy} = \frac{1}{2}\left(2\frac{\partial u}{\partial y} + \left(\frac{\partial u}{\partial y}\right)^2 + \left(\frac{\partial v}{\partial y}\right)^2\right) \tag{6.3}$$

$$E_{xy} = \frac{1}{2}\left(\frac{\partial u}{\partial y} + \frac{\partial v}{\partial x} + \frac{\partial u}{\partial x}\frac{\partial u}{\partial y} + \frac{\partial v}{\partial x}\frac{\partial v}{\partial y}\right) \tag{6.4}$$

Figure 6.16 also shows E_{yy} maps for $\varepsilon = 1.5\%$ and $\varepsilon = 4.1\%$. As expected, E_{yy} values are mainly negative and small in comparison with E_{xx} (compressive deformation in y direction). Localization bands around the holes, arising at an angle close to $\pm 45°$ is also observed for the specimen for E_{yy} . It is interesting to remark that for strain fields E_{xx} and E_{yy} in the ligament region between the holes, local strains are small if compared to the strains in the localization bands. In the region away from the holes, no major strain localization sites are observed, not even close to the boundaries of the grains.

Figure 6.17 shows the profile of magnitude of strain distribution E_{xx} and E_{yy} measured along a straight line (between holes 3 and 6). The high peaks in strains appears close to the location of the holes. As we move away from the holes, the magnitude of strain is not so high for E_{xx}, whereas for E_{yy} the magnitude of strain is low close to the location of the holes and high away from the location of the holes. It can also be observed that E_{xx} is tensile in nature, whereas E_{yy} is compressive. We observe valleys in ligament zones between the holes that makes evident that there is no interaction between holes. Distribution of strain is very high in coordinates close to holes 5 and 6.

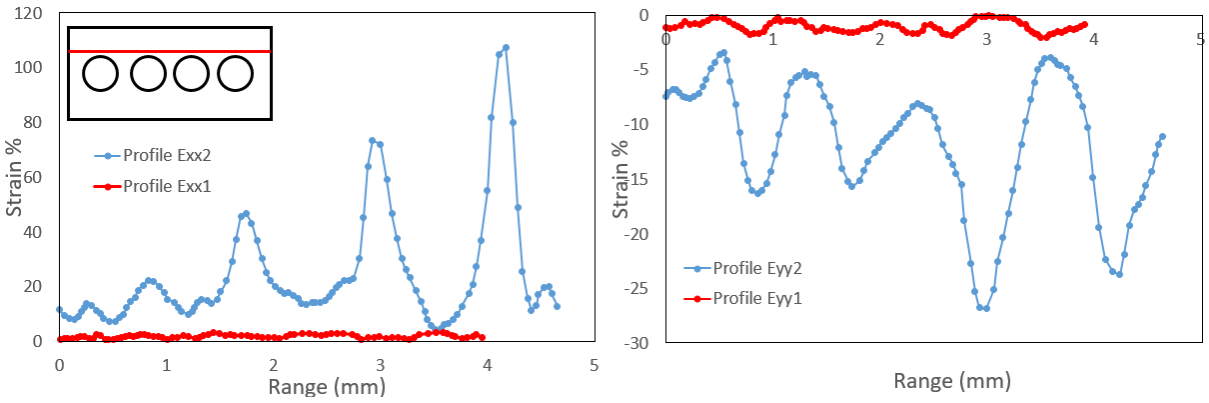

Figure 6.17: *Distribution of local strain (a) E_{xx} and (b) E_{yy} around holes 3 to 6. Red line represents local strain at $\varepsilon_{global} = 1.5\%$ and blue line represents local strain at $\varepsilon_{global} = 4.1\%$. Local strains are calculated along the line just above the holes as shown in the scheme. Peaks in E_{xx} plots refers to location near the holes.*

6.7 Tensile Specimen Pattern 3

Now we will study another specimen (specimen pattern 3), that has the same hole diameter as specimen pattern 2, but the number of holes and spacing between holes are different.

In tensile specimen pattern 3, a total of 7 holes are created within the gauge section, with each hole diameter being $0.5mm$ placed at $\pm 45°$ from the adjacent holes and the loading axis as shown in figure 6.1.

For this specimen pattern, two different samples are analysed, both with different microstructure. For both specimens in-situ tensile test, EDSB and slip trace analysis are performed. Additionally for one of the specimens Digital Image Correlation is also performed.

6.7.1 Sample 1

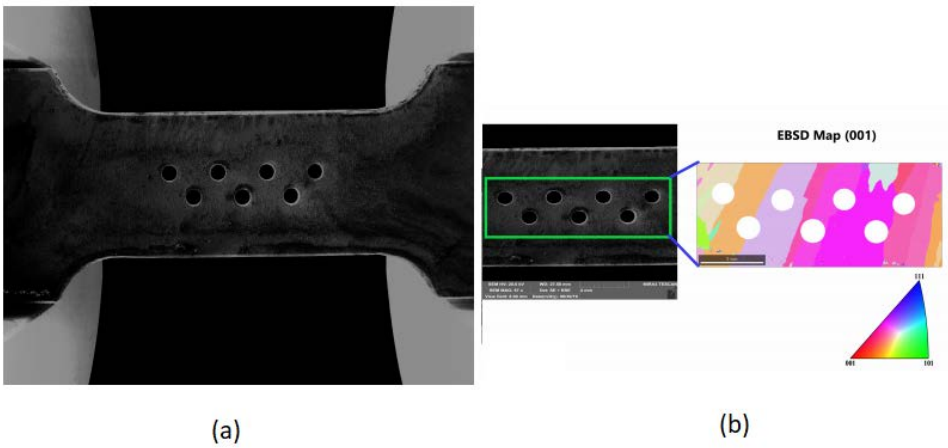

Figure 6.18: *a) Specimen pattern 3 (sample 1) within the SEM chamber covered with particles for DIC. (b) Initial EBSD scan of the front surface of sample 1*

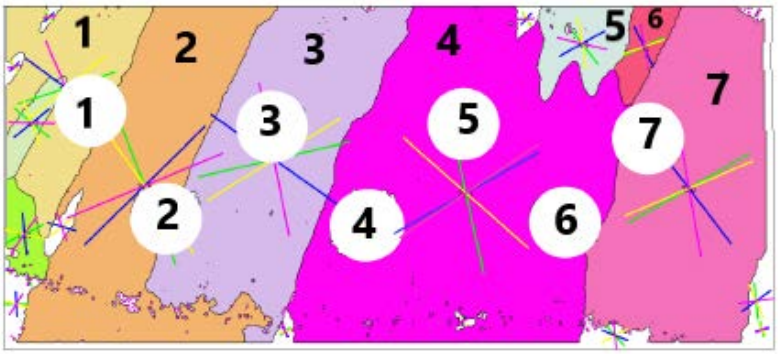

Figure 6.19: *Initial EBSD of the front surface of the sample, with all possible slip planes projection.*

In this section we will study and analyse sample 1 of specimen pattern 3, for which we will perform EBSD, slip trace and digital image correlation analysis.

The initial EBSD scan of the front surface of sample 1 is shown in figure 6.19. This figure shows grain shape, size and orientation and are colored following the inverse pole figure. Both holes and grains are numbered from 1 to 7 for convenience. As seen in figure 6.19, based on the orientation, the grains of the sample have a cube texture predominantly twisted. That is, most of the grain orientations are slightly rotated about [0 0 1] axis. Also most of the grain boundaries are low angle grain boundaries with misorientation angles ranging between $5 - 10°$.

Holes number 3, 4, 5 and 6 are located within a single grain, whereas holes 1, 2 and 7 share boundary with two grains.

6.7.1.1 Hole shape evolution and final failure of the specimen

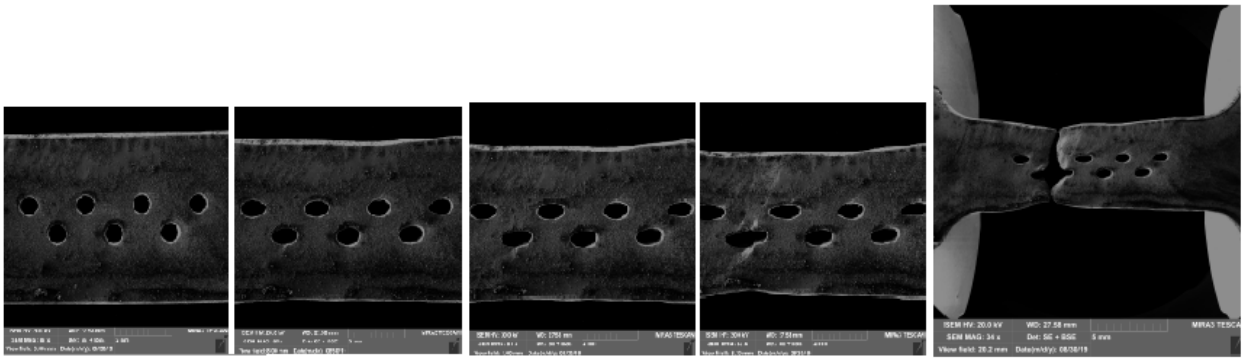

Figure 6.20: *SEM images of specimen showing evolution of slip traces and growth of holes at different global strains* ε_{global}(*Eq.* 6.1).

From high resolution SEM images, the evolution of holes in sample 1 at different global strains are presented in figure 6.20. As is observed from the images, holes start to evolve with different deformation rates and some of them become irregular in shape. Most of them evolve into almost elliptical shapes with major axis of the ellipse being parallel to the horizontal axis of the specimen. Among all the holes, hole number 2 is the most grown/deformed followed by hole number 3. The lowest hole growth/deformation is achieved by hole number 5. At the early stages of global deformation, all the holes start evolving into elliptical shapes, but for global strain level higher ($\varepsilon \geq 4.16\%$), different hole shapes begin to appear. In this way, left and right sides of hole number 2 (between grains 2 and 3) reach very different shapes as loading progresses. As observed in the figure, in the left side of the hole, deformation and growth is much greater than in the right side. For hole number 7 (between grains 4, 6 and 7), the part of the hole on the left side tends to close, whereas the part on the right side still maintains its elliptical shape. Similar trend is observed for hole number 1 (between grains 1 and 2). For hole number 3 (within grain 3), for $\varepsilon = 5.95\%$, we observe higher growth/ deformation on the lower half of the hole if compared with the upper half. The remaining holes number 4, 5 and 6 (within single grains) evolve into fairly regular elliptical shapes during tensile testing. Interaction between neighboring holes does not occur, neither for adjacent holes located at an angle of 0° with respect to the loading axis nor for the case in which they form 45°. Final failure starts around hole 2 and there is no clear indication of failure starting between two holes. Final failure interrupts the plastic growth of the holes and causes rapid fracture of the sample.

6.7.1.2 Maximum Schmid factors and active slip systems

In this sample, high resolution images of slip lines can not be obtained from Scanning Electron Microscopy technique because of the DIC particles covering the surface that obscure images. Due to this, slip line analysis will be performed only with the information calculated

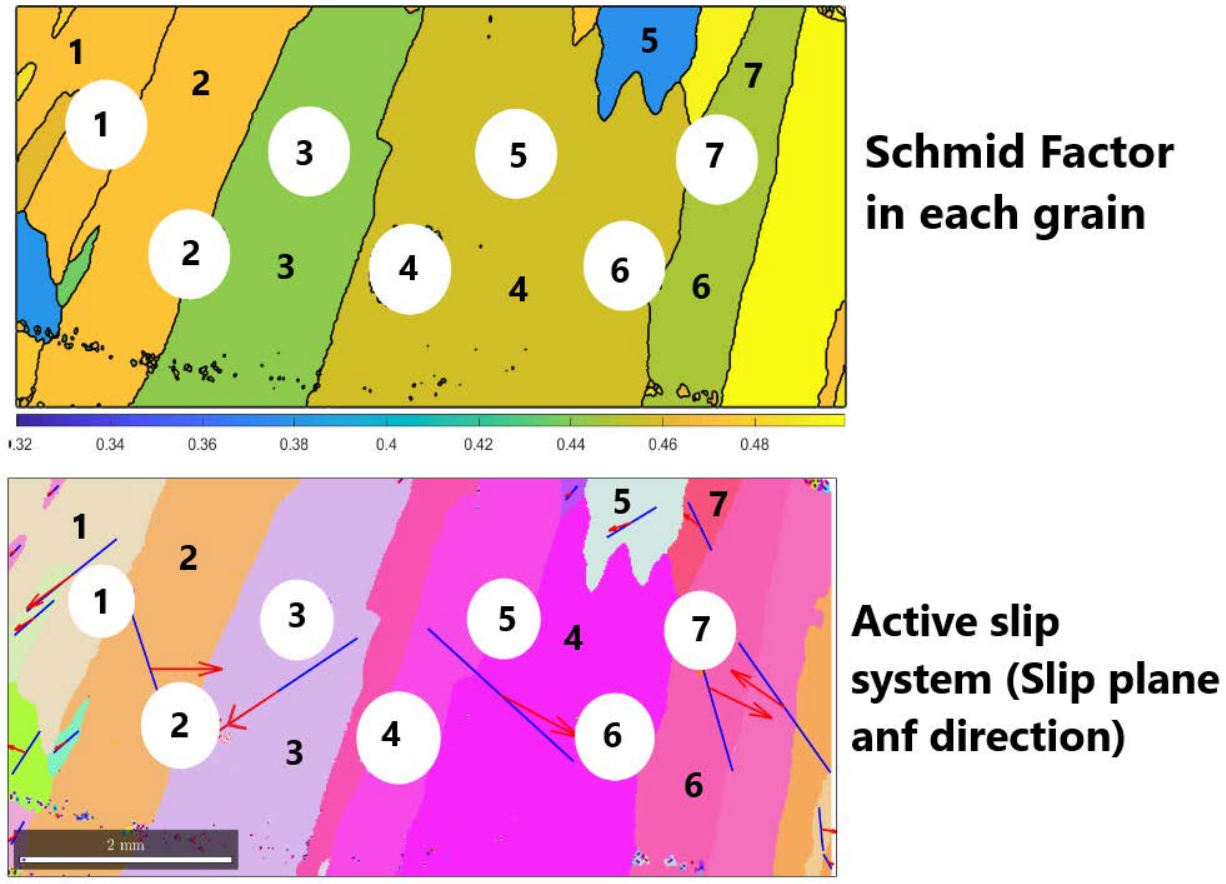

Figure 6.21: *Distribution of the maximum Schmid factor and the active slip system in the front surface of sample 1.*

numerically. From EBSD scans, the slip trace directions and Schmid factors are computed for each grain assuming uniaxial tension along x direction. Figure 6.19 shows all the possible slip planes in the grains of the front surface of the sample. All the 4 slip planes are colored according to the data given in table 6.2. The maximum Schmid factor criterion were used to predict the active slip system from the specimen. Figure 6.21 shows the maximum value of Schmid factor within each grain and the trace of the slip planes in combination with the slip direction for which the Schmid factor is maximum. Slip planes are indicated with blue lines and slip direction with red arrows. By analysing the maximum value of Schmid factor, it is observed that values vary from of 0.32 to 0.5 with most of the grains having maximum Schmid factors in the range $(0.45-0.48)$. The different slip activity for all the grains is significant, indicating that the grains should all have different hardening/softening behaviour. As previously mentioned, hole number 2 is the most deformed hole and final fracture occurred around it. It is therefore interesting to provide a detailed analysis for the grains placed around hole 2 (grains number 2 and 3). Grain 2 and 3 have different values for maximum Schmid factor, 0.47 for grain 2 belonging to slip system 2 and 0.44 in slip system 4 of grain 3. Since both grains have different slip systems, different deformation behaviour is expected in these 2 grains.

In order to have a in-depth look into grains around hole 2, the Schmid factors corresponding to uniaxial stress for all 12 f.c.c slip systems are presented in table 6.4 for grains

number 2 and 3. As we can see, in grain number 2 multiple slip systems (2, 3, 4, 5, 9) are active. For grain 2, the traces of all possible slip planes are marked with different colors as shown in Figure 6.19 and following the criteria given in table 6.2 : green for slip plane (111), yellow for slip plane (11-1), blue for slip plane (-111) and magenta for slip plane (1-11). Slip system number 2 belongs to (111) and has the maximum Schmid factor (0.47). Its trace on the surface corresponds with a straight line marked with green colour. Similarly, for grain number 3, multiple slip systems are active. Slip system number 4 is the one with highest Schmid factor (0.44) belonging to (11-1) plane, closely followed by slip system number 7 (0.41) belonging to (-111) plane. In grain number 3, these two slip systems dominates the deformation process and are marked in Fig.6.19 by the yellow and blue straight lines respectively. Differences in active slip systems can cause differences in deformation behaviour, hence an incompatibility arises between these 2 grains. This incompatibility will have a direct influence on the deformation behaviour of the hole located at the boundary between these 2 grains. The hole evolves with different magnitude and shape on either side of the grain boundary and promotes failure along the grain boundary.

Holes number 4, 5 and 6 are located within the single grain number 4, being grain number 4 the biggest grain in the sample. By analyzing grain 4 it is found to have non-cubic grain orientation with a maximum Schmid factor (0.46). In grain number 4, there exists 3 slip system with Schmid value greater than 0.4 (see table 6.4) in slip systems number 2, 5 and 11 respectively. Grain 4 is also favorable for deformation, that is the reason behind substantial growth and shape of holes 4, 5 and 6. By analysing remaining grains, it is observed that most of them has at least 1 favourable slip system. A more detailed analysis of these remaining grains is not included in the document for the sake of conciseness. Grain number 2 is the most active grain with multiple active slip systems and the highest Schmid factor value. Grain 2 has therefore the most favourable conditions for deformation, acting as a soft grain surrounded by relatively hard grains. This grain will dominate deformation and failure process.

Computational slip bands are observed between holes inclined at 45° in the sample. However, no slip bands formation is shown between the holes located along x axis which means that the holes where placed too far for any interaction to occur. DIC results shown in next section will confirm this sample behavior.

6.7.1.3 Digital Image Correlation analysis

Digital image correlation analysis is also performed for this sample, in order to quantify the heterogeneous strain field of the material and the strain localization near the holes. Results pertaining to DIC of the specimen are presented in this section. Experimental measures of local strains in both x (E_{xx}) and y (E_{yy}) directions is as shown in figure 6.22 at different global strain values $\varepsilon = 1.5\%$ and 3.8%. Local strains are defined following equations 6.2, 6.3, 6.4 and global strain is defined in equation 6.1.

As seen in the figure, at the global strain value $\varepsilon = 1.5\%$ hot spots begin to form around the holes and strain starts localizing within several localized deformation bands, forming angles

Front Surface

Slip System	Grain 2	Grain 3	Grain 4
1	0.166	-0.07	0.02
2	-0.47	-0.002	-0.41
3	0.30	0.07	0.38
4	0.39	-0.44	0.26
5	0.44	-0.26	0.46
6	0.04	0.18	0.21
7	-0.14	0.41	-0.007
8	-0.28	-0.24	-0.2
9	-0.42	0.17	-0.2
10	0.25	0.022	-0.25
11	0.27	-0.33	0.43
12	0.019	-0.31	0.18

Table 6.4: *Schmid factor in each slip system for different grains of sample 1*

of approx. 45° with respect to the loading axis. The magnitude of the local strain in x direction (E_{xx}) is higher if compared to y direction and E_{yy} values are mainly negative (compressive deformation of the sample in y direction). It is important to remark that at $\varepsilon = 1.5\%$, strain values in the ligament region between holes in x direction are low if compared to ±45° direction. As the deformation progresses ($\varepsilon = 3.8\%$) strain localization starts increasing around hole number 2, where the final failure happened. It is interesting to note that, even though there is strain localization between the holes placed in 45° direction, there is no interaction between them.

As shown in Fig 6.22, the area with highest values of local strain (most deformed area) mainly corresponds to grain 2 location. As previously mentioned, a major reason for high values of deformation is attributed to high Schmid factors and multiple active slip systems exhibited by grain number 2. After high local deformations, failure is promoted in the specimen in the vicinity of this area.

6.7.2 Sample 2

In this section, results of specimen sample 2 will be presented. For this sample and as in previous case, holes are arranged at ±45° to each other with the same hole diameter and spacing as in sample 1. Figure 6.23 shows the initial position of the sample in the SEM chamber and the EBSD orientation map. In the EBSD image, holes and grains are numbered for convenience as shown in figure 6.24. From the EBSD images, we can observe that most of the holes are sharing boundary with at least 2 grains. As seen in figure 6.24, hole 1, 5 and 6 are located at the grain boundary and share boundary with 2 grains, whereas holes 2, 3 and 4 share boundary with at least 3 grains. Hole 7 is placed within a single grain.

6.7.2.1 Hole shape evolution and final failure of the specimen

Figure 6.25 shows the evolution of holes at different stages of global deformation. In this specimen, since there are no particles for conducting DIC, we can clearly observe the slip system activity (slip traces) on the surface providing information on the activated slip system and then qualitatively assess the level of strain heterogeneity.

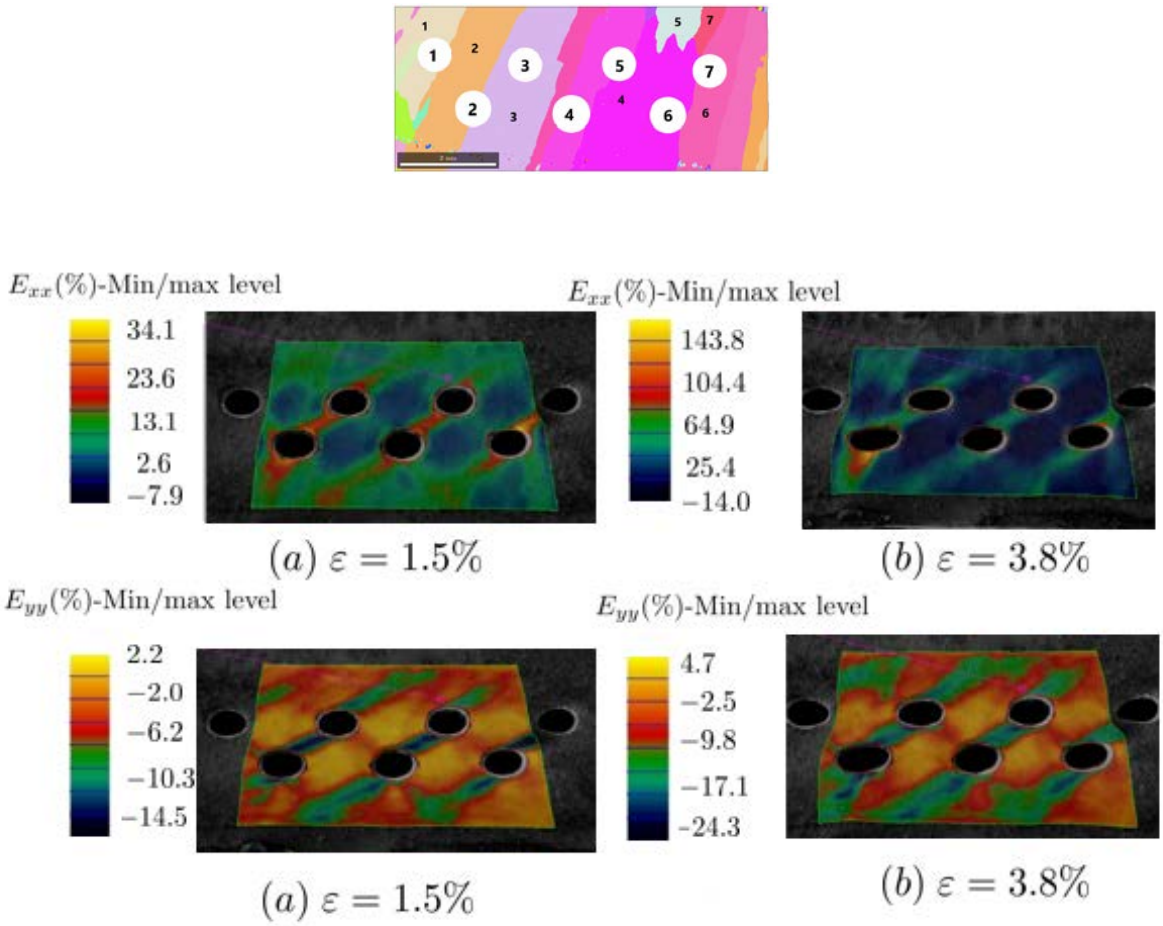

Figure 6.22: *Strain fields E_{xx} and E_{yy} calculated with digital image correlation at different global strains*

As we can see from the SEM images, as deformation proceeds, holes evolve into different shapes and sizes. Before failure, hole 3 expands into an elliptical shape with more hole growth on the left side compared to the right side. As seen in figure 6.24 hole 3 shares boundary with 3 grains. Because of different orientations in each grain, deformation related to each adjacent area is different making the hole deforming with irregular shape. Necking takes place around holes 2 and 3. Final failure occurs at hole 3.

6.7.2.2 Maximum Schmid factors and active slip systems

In order to examine the active slip system activity, visual observations of the slip lines on the specimen surface are compared with the computed distribution of slip traces in the sample. With the help of the computed maximum Schmid factors, the likelihood of the slip system activity is also confirmed.

Figure 6.26 a, shows the maximum Schmid factor value in each grain and figure 6.26 b represents the trace of the slip planes (blue line) in combination with the slip direction (red line) for which the Schmid factor is maximum. The maximum Schmid factor in the grains vary from of $0.34 - 0.48$, with most of the grains having at least one slip system with maximum Schmid factor in the range 0.45-0.48. The analysis of grain numbers 3, 5, 6 and 8 provide an in

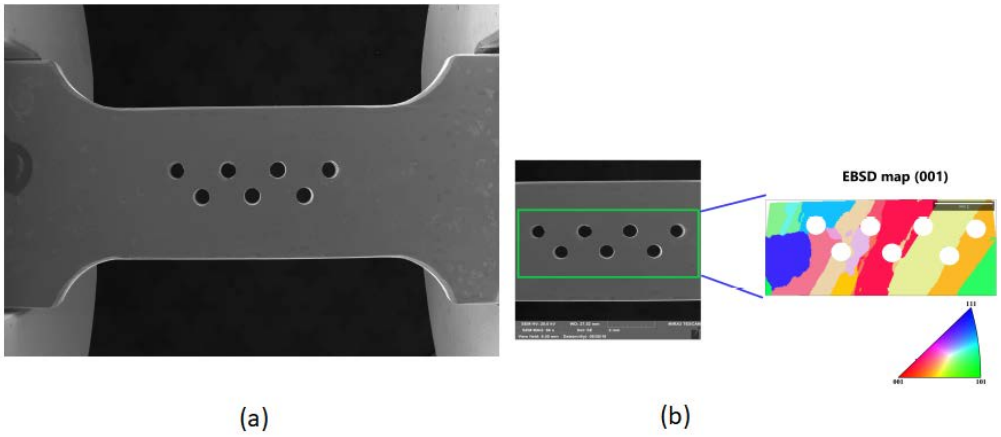

Figure 6.23: *a) Specimen pattern 3 (sample 2) within the SEM chamber. (b) Initial EBSD scan of the front surface of sample 2*

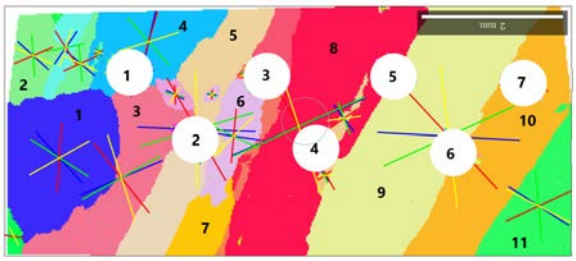

Figure 6.24: *Initial EBSD of the sample with all possible slip planes projections.*

depth look at the region around holes 2 and 3, area where necking and final failure happens. To this end, table 6.5 presents the Schmid factors corresponding to uniaxial stress for all 12 f.c.c slip systems inside grains 3, 5, 6 and 8. Hole 2 is surrounded by grains number 3, 5 and 6 and hole 3 by grains number 5, 6 and 8.

Front Surface

Slip System	**Grain 3**	**Grain 5**	**Grain 6**	**Grain 8**
1	0.19	-0.01	-0.005	0.21
2	0.02	-0.004	-0.04	-0.49
3	-0.22	0.02	0.05	0.28
4	-0.40	-0.25	0.37	0.31
5	-0.16	-0.15	0.15	0.47
6	0.24	0.10	-0.21	0.16
7	0.48	0.46	0.07	-0.11
8	-0.21	-0.36	-0.34	-0.22
9	0.26	0.097	-0.26	-0.33
10	-0.08	-0.20	-0.45	-0.20
11	-0.35	-0.14	0.16	0.26
12	-0.43	-0.34	-0.29	0.06

Table 6.5: *Schmid factor in each slip system for different grains of sample 2*

As previously mentioned, hole 2 is enclosed by grains number 3, 5 and 6. For grain number 3, 3 slip systems have Schmid factor values above 0.4 (4, 7 and 12). Of them all, slip system number 7 is the one with highest Schmid factor (0.48) and acts as the dominating slip system. For grain number 5, 3 slip systems are active (7, 8 and 12), and the highest Schmid factor

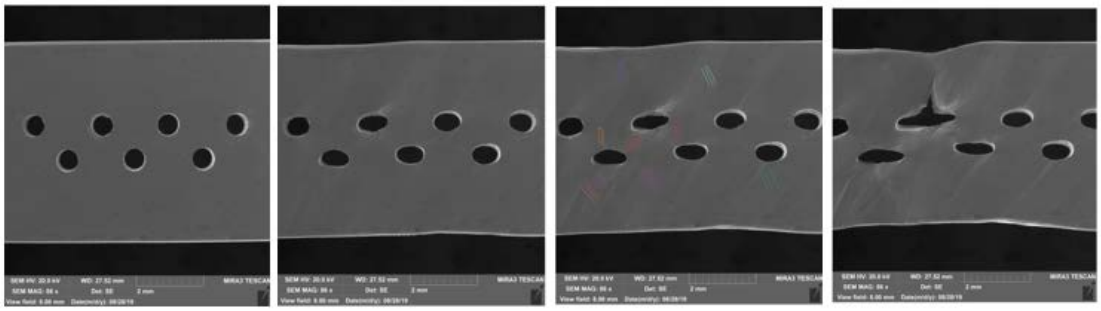

$(a)\ \varepsilon = 0\%$ $(b)\ \varepsilon = 2.6\%$ $(c)\ \varepsilon = 4.16\%$ $(d)\ \varepsilon = 6.19\%$

Figure 6.25: *SEM images of specimen showing evolution of slip traces and growth of holes at different global strains* ε_{global}*(Eq.*6.1*).*

(0.46) corresponds to slip system number 7. For grain number 6, 3 slip systems are active (4, 8 and 10). Slip system number 10 has the highest Schmid value (0.45) and acts as the dominating one.

Hole 3 is in turn surrounded by grain numbers 5, 6 and 8. Grain 5 and 6 were discussed before for hole number 2. For grain number 8 and as seen in the table, multiple slip systems are active (2, 4, 5 and 9). The slip system with the highest Schimd value (0.49) is the slip system number 2.

Slip planes that are visible on the surface of the sample are marked at global strain 4.16% in figure 6.27. As seen in the figure, the experimental and the numerical slip system are fairly consistent in most of the grains and matches well. With different slip orientations controlling the plasticity behaviour in different grains, hole evolving into different shapes on each side of the grain is therefore obvious.

By looking at the slip system activity around hole 3, we see that all 3 grains surrounding the hole have different active slip system. The grain on the top left of hole 3 (grain number 5) has a slip plane which is inclined at an angle close to 45° counter clockwise with respect to the loading axis and a slip direction projecting inwards. For grain that is located at the bottom left of the hole (grain number 6), the trace of the slip plane is inclined by an angle close to 45° counter clockwise with respect to the loading axis and the slip direction is projected outwards. Finally for the grain on the right side of the hole 3 (grain number 8), active slip system is inclined by an angle close to 25° counter clockwise and the slip direction is projected inwards.

Hole 2 also evolves into a irregular shape. Slip planes and slip directions on all the grains surrounding hole 2 are different and leads its heterogeneous evolution. On the specimen surface we observe 2 slip system crossing the region in the lower part of hole 2, with one slip trace matching with the computed one. The additional slip trace is expected to be originated from the hole deformation.

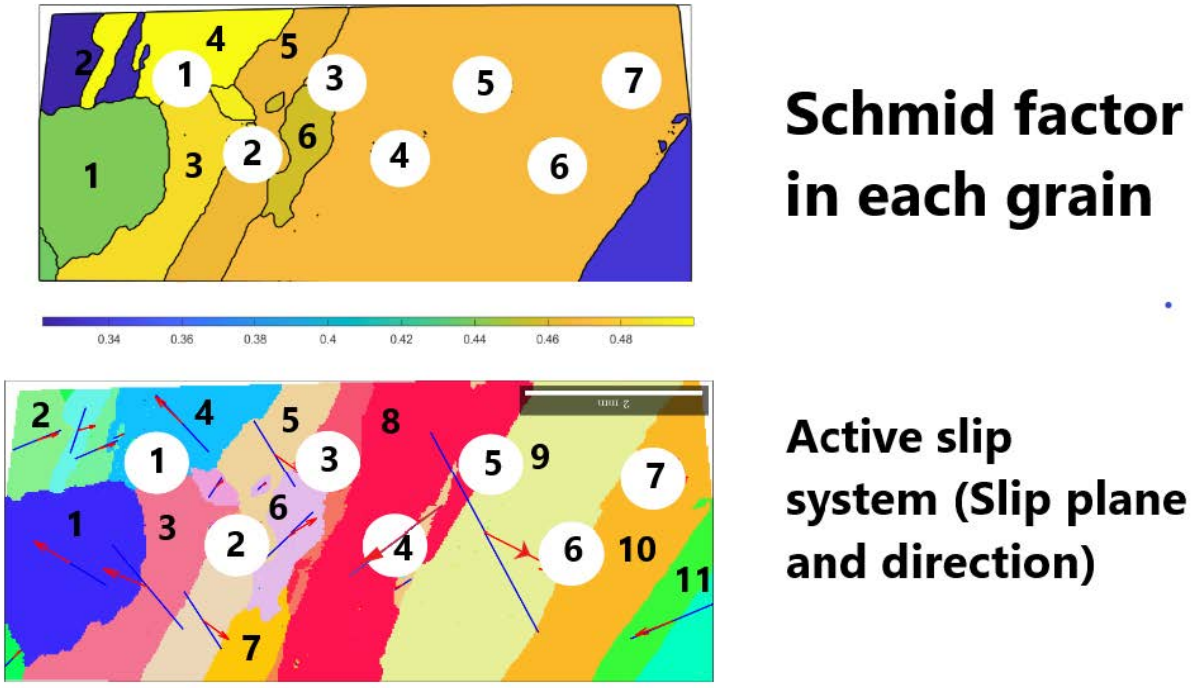

Figure 6.26: *Distribution of the maximum Schmid factor and the active slip system in the front surface of sample 2.*

As in previous cases, even in this specimen it is the local microstructure that dominates the deformation and no coalescence between holes takes place. Even though there is some interaction between holes, it is not the major factor in deciding the final failure of the sample.

6.8 Summary and conclusions

Tensile samples of polycrystalline aluminum, with predrilled holes with different patterns, were analyzed in this work similar to the ones described in Weck and Wilkinson (2008) work. The role of hole size, hole distance and hole position in contrast to microstructural heterogeneity were studied in detail in order to find the most relevant features that causes local deformation and final failure of the specimens. By using EBSD, orientation in terms of Euler Angles in all the grains are obtained in the specimens. Misorientation between crystals, active slip systems and maximum Schmid factors were computed numerically in order to predict which slip system is active and how favourable is the grain to deform. With the help of SEM, specimen images are acquired at high magnifications revealing slip traces and finer details associated with the microstructure of the polycrystal and its evolution during loading. In some specimens, the strain field is also monitored using DIC technique. Qualitative comparisons between experiments and numerical data have been provided in each case. It is clear from results presented in previous sections that microstructure have an important effect on void evolution and final failure. Tensile growth of holes were observed during the experiments, but it was difficult to draw a relationship between rate of growth of holes and its position relative to the notch. For a given sample evolution of holes were not uniform (like in isotropic materials). Some holes expanded, some

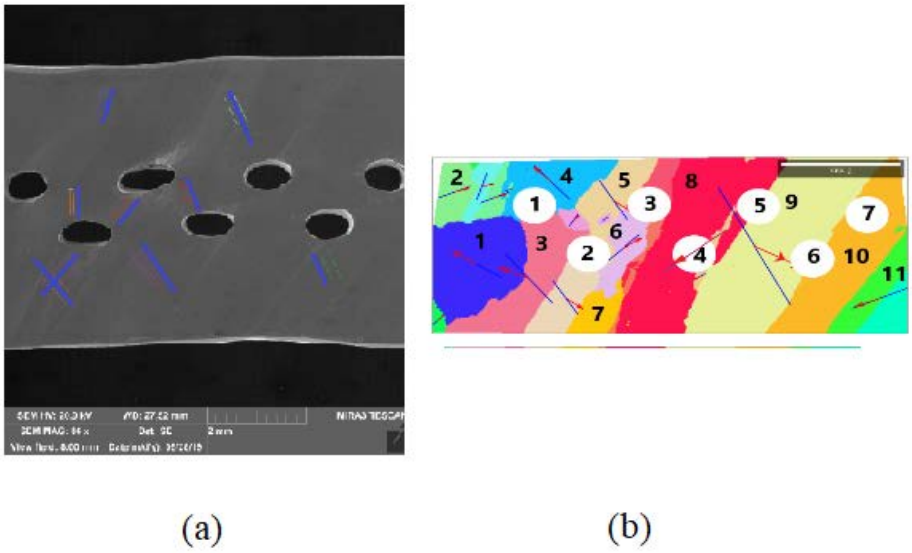

Figure 6.27: *a) Slip planes visible on the surface of the specimen at global strain 4.16%, b) Slip system for which the Schmid factor is maximum*

holes contracted and some holes showed negligible or no growth from the beginning of the deformation. Based on this observation it is very difficult to determine hole interaction or linkage.

By looking at the grains surrounding the hole and analysing the EBSD data, we observe that local crystallographic orientation controls the hole deformation. Hole growth seems easier and higher in soft grains (characterized by high Schmid factor). On the other hand, growth of holes is lesser and difficult in hard grains (characterized by low Schmid factor). For holes located on the grain boundary (between at least two grains), hole growth and shape varied on each side of the grain boundary based on hard or soft grain behavior. Hole growth will be higher on the soft side of grain boundary playing compatibility between grains and slip system activity a mayor role in the shape and size of the hole and final failure of the sample. When there is no compatibility between two grains, we observe that failure occurs at grain boundary, resulting in crack propagation and hence final failure. This trend is also observed in our numerical work (Dakshinamurthy et al., 2021) and previous studies of (Raabe et al., 2001; Zhao et al., 2008), that showed that the initial grain orientation was the major contributor in plastic heterogeneous response in polycrystals.

In this work, interaction between holes were not clearly evident for holes oriented at 90° with respect to loading axis. Even DIC did not show any major strain localization between holes. For holes oriented at 45 °, strain localization was observed between holes. However, there were no hole linkage during the experiments and it was difficult to observe coalescence. In this study, no inter-void ligament failure is observed in any sample and the size of the hole and spacing between holes it would appear not to be sufficient to promote the interaction between adjacent holes. As shown by Weck and Wilkinson (2008), the closer the holes, the higher the possibility of intervoid ligament, the earlier coalescence and the lower failure strain of the whole

sample. If the distance between holes is larger, holes has to deform/ grow more to interact with their neighbours and to promote ligament failure.

The results presented here evidently suggest that initial texture as well as microstructure needs to be considered for modelling deformation and failure in Aluminium. Further work is required to include a parametric study to understand the relation between hole spacing and coalescence, thereby implement these results into a damage model along with crystal plasticity finite element simulations. Further plan needs to be devised for studying holes at grain boundary with emphasis on hard and soft grains on either sides of the holes.

Part IV

Concluding remarks, future works and bibliography

7

Concluding remarks and future works

In this doctoral thesis we have investigated the role of anisotropy, stress triaxiality and Lode parameter on void growth in FCC single crystals, bicrystals and polycrystals. To address these issues we have adopted two approaches: a. we have performed finite element calculations on unit cells containing spherical voids (Part II); b. we have performed in-situ tensile tests on tensile specimens with pre-drilled holes of different diameters (Part III). The key findings of this doctoral thesis are summarized here. Some interesting issues are suggested for future researches.

7.1 Concluding remarks

Part II : Numerical modelling of void growth in single crystals and bi-crystals. In this part we have analysed unit cells with voids under different stress states.

- In chapter 3, we have investigated the effect of crystal orientation on cell deformation and stress-strain behavior of single crystals without voids subjected to different stress states. Using crystal plasticity finite element approach, 3D unit cell calculations for six different crystallographic orientations are performed under controlled stress state (fixed triaxiality and Lode parameter). The effect of Lode parameter is clearly evident for each crystallographic orientation. No effect of triaxiality was observed for all the orientations considered in this study. Symmetric orientations (O1, O2, O3) showed softer response as compared to non-symmetric orientations (O4, O5, O6) irrespective of Lode parameter considered. The results are consistent with all existing literature.

- In chapter 4, we have investigated the effect of crystal orientation on void growth and cell deformation behaviour of porous single crystals subjected to different stress states. Similar to chapter 3, crystal plasticity finite element calculations of a unit cell containing a spherical void at its center is considered. For studying the behaviour of the void, four different orientations are considered: two symmetric orientations (O1, O2) which shows soft response and two non-symmetric orientations (O4, O6) which shows hard response.

Numerical results showed that void growth depends on triaxiality and Lode parameter irrespective of crystal orientation. Void growth is higher and quicker for high triaxialities. Similarly void growth is higher for Lode parameter $L = -1$.

- In chapter 5, we have investigated the response of a void at the grain boundary of FCC bi-crystals subjected to different stress states and different neighbouring grain orientation. Three different cases of unit cells are studied: soft-hard RVE, soft-soft RVE and hard-hard RVE. Crystal plasticity finite element calculations are performed for these three RVEs under four different stress triaxialities and three different Lode parameters. Numerical results showed that the evolution of the void strongly depends on the local triaxiality of a crystal in the bi-crystal. Void growth is higher for higher triaxialities. Significant differences in void growth between the two half cells occurs specially for soft-hard bi-crystal case. In soft-hard bi-crystal RVE, the different behaviour of the void evolution in each half cell can be attributed to the difference in the strength between the two initial orientations and the incompatibility between the two half cells. In the soft-hard bi-crystal case, at high triaxialities, void grows faster in softer crystal compared to harder crystal counter-part, whereas at low triaxialities, void tends to collapse faster in harder half cell compared to neighbouring softer crystal. Void shape evolution is also dependent on triaxiality and Lode parameter values. Slip system activity also depends on triaxiality, Lode parameter and initial crystal orientation and far away from the void becomes similar to a fully dense crystal under the same imposed loading conditions. In soft-hard bi-crystal RVE, the heterogeneity of slip activity, especially within the harder crystal, is significantly higher leading to a non-uniform lattice rotation and consequently grain fragmentation.

Part III : Experimental investigation of void growth in metallic sheets containing holes. In this part we performed uniaxial in-situ tensile test, coupled with scanning electron microscope to study the void growth behaviour in pure Aluminium tensile specimens with pre-drilled holes.

- In chapter 6, by varying the hole diameter, distance between the holes and arrangement of holes, three different types of specimens were analyzed. Results using EBSD, DIC and high resolution SEM images showed that, for a given sample, evolution of holes were not uniform (like in isotropic materials). Some holes expanded, some holes contracted and some holes showed negligible or no growth from the beginning of the deformation. There were no hole linkage during the experiments and it was difficult to observe coalescence. Evolution of holes was significantly influenced by initial orientation of grain embedding the hole. Local microstructure dictated the final failure of the polycrystal.

7.2 Future works

Interesting issues that could be addressed in future research are listed below:

- The crystal plasticity model used in the present study is standard. Observed dependencies can be modified when enhanced strain gradient formulations (Wulfinghoff et al.,

2013; Stupkiewicz and Petryk, 2016; Ling et al., 2018), which introduce size effects, are applied. For example, as recently demonstrated by Ling et al. (2018) using the reduced micromorphic finite strain crystal plasticity model, the void growth is slow down and the void coalescence delayed when the void size is small as compared to the intrinsic length scale of the material. It happens due to the modification of accumulated shear field close to the void. Similarly, the strain gradient formulation may help to account for the grain boundary effect on the resistance to plastic flow, as demonstrated by Wulfinghoff et al. (2013). This may affect the results obtained in the context of bicrystal. Therefore, in the future more advanced crystal plasticity formulations can be considered for the analysis of the grain boundary effect on the void growth.

- In this thesis, focus was laid on cells with spherical voids at its center. This work can be extended to other void shapes (spheroid and ellipsoid). Also in this work spherical axis are always aligned to principal loading axis. Voids that are inclined at some angle to principal loading axis should be analyzed in the future.

- To complement numerical results presented in this work and in order to extract definite conclusions, more numerical simulations should be developed and experimental campaigns focus on studying the evolution of intergranular voids in fcc bi-crystals should be designed and conducted in the future.

Bibliography

ABAQUS/Standard (2019). *Simulia, User's Manual*. ABAQUS Inc., Providence, USA, version 6.19 edition. 26, 143, 147, 149, 151, 153, 160

Andersson, H. (1977). Analysis of a model for void growth and coalescence ahead of a moving crack tip. *Journal of the Mechanics and Physics of Solids*, 25(3):217–233. 4

Asaro, R. J. (1983). Crystal plasticity. *Journal of Applied Mechanics*, 50:921–934. 32

Asaro, R. J. and Needleman, A. (1985). Textured development and strain hardening in rate dependent polycrystals. *Acta metall.*, 33(6):923–953. 25

Asim, U., Siddiq, M. A., and Demiral, M. (2017). Void growth in high strength aluminium alloy single crystals: a CPFEM based study. *Modelling and Simulation in Materials Science and Engineering*, 25(3):035010. 6

Bachmann, F., Hielscher, R., and Schaeben, H. (2010). Texture analysis with mtex–free and open source software toolbox. In *Solid State Phenomena*, volume 160, pages 63–68. Trans Tech Publ. 88

Barlat, F., Aretz, H., Yoon, J. W., Karabin, M., Brem, J., and Dick, R. (2005). Linear transfomation-based anisotropic yield functions. *International journal of plasticity*, 21(5):1009–1039. 41

Basu, S., Dogan, E., Kondori, B., Karaman, I., and Benzerga, A. (2017). Towards designing anisotropy for ductility enhancement: A theory-driven investigation in mg-alloys. *Acta Materialia*, 131:349 – 362. 56

Bauer, R. W. and Wilsdorf, H. G. (1974). Void initiation in ductile fracture. Technical report, Virginia Univ Charlottesville Research Labs for the Engineering Sciences. 4, 5

Beachem, C. (1963). An electron fractographic study of the influence of plastic strain conditions upon ductile rupture processes in metals. *Trans. ASM*, 56(3). 3, 4

Benzerga, A., Besson, J., and Pineau, A. (2004a). Anisotropic ductile fracture: Part I: experiments. *Acta Materialia*, 52(15):4623–4638. 41

Benzerga, A., Besson, J., and Pineau, A. (2004b). Anisotropic ductile fracture: Part II: theory. *Acta Materialia*, 52(15):4639–4650. 41

Benzerga, A. A. and Besson, J. (2001). Plastic potentials for anisotropic porous solids. *European Journal of Mechanics - A/Solids*, 20(3):397 – 434. 56, 59

Besson, J. (2010a). Continuum models of ductile fracture: a review. *International Journal of Damage Mechanics*, 19(1):3–52. 41

Besson, J. (2010b). Continuum models of ductile fracture: A review. *International Journal of Damage Mechanics*, 19(1):3–52. 56

Blaber, J., Adair, B., and Antoniou, A. (2015). Ncorr: open-source 2d digital image correlation matlab software. *Experimental Mechanics*, 55(6):1105–1122. 165

Bourcier, R., Koss, D., Smelser, R., and Richmond, O. (1986). The influence of porosity on the performance and properties of parachutes. *Acta Metall*, 34(12):2443–2453. 4

Bringa, E. M., Traiviratana, S., and Meyers, M. A. (2010). Void initiation in fcc metals: Effect of loading orientation and nanocrystalline effects. *Acta Materialia*, 58(13):4458 – 4477. 56, 57

Buffiere, J.-Y., Maire, E., Cloetens, P., Lormand, G., and Fougeres, R. (1999). Characterization of internal damage in a mmcp using x-ray synchrotron phase contrast microtomography. *Acta materialia*, 47(5):1613–1625. 84

Bunge, H.-J. (1965). Zur darstellung allgemeiner texturen. *International Journal of Materials Research*, 56(12):872–874. 155

Carroll, J., Clark, B., Buchheit, T., Boyce, B., and Weinberger, C. (2013). An experimental statistical analysis of stress projection factors in bcc tantalum. *Materials Science and Engineering: A*, 581:108–118. 5

Cawthorne, C. and Fulton, E. (1967). Voids in irradiated stainless steel. *Nature*, 216(5115):575–576. 5

Chen, G., Ren, C., Yang, X., Jin, X., and Guo, T. (2011). Finite element simulation of high-speed machining of titanium alloy (ti–6al–4v) based on ductile failure model. *The International Journal of Advanced Manufacturing Technology*, 56(9):1027–1038. 41

Chen, L. G. et al. (1983). The sensitivity of the macroscopic consequences of void growth in ductile materials to various mechanical and geometrical micro-parameters. *International journal of solids and structures*, 19(12):1089–1098. 4

Cruzado, A., Llorca, J., and Segurado, J. (2017). Modeling cyclic deformation of inconel 718 superalloy by means of crystal plasticity and computational homogenization. *International Journal of Solids and Structures*, 122:148–161. 143

Dæhli, L. E. B., Faleskog, J., Børvik, T., and Hopperstad, O. S. (2017). Unit cell simulations and porous plasticity modelling for strongly anisotropic fcc metals. *European Journal of Mechanics-A/Solids*, 65:360–383. 41

Dakshinamurthy, M., Kowalczyk-Gajewska, K., and Vadillo, G. (2021). Influence of crystallographic orientation on the void growth at the grain boundaries in bi-crystals. *International Journal of Solids and Structures*, 212:61–79. 7, 111

de Botton, G. and Ponte Castañeda, P. (1995). Variational estimates for the creep behavior of polycrystals. *Proc. R. Soc. London*, A448:121–142. 56

Deshpande, N. U., Gokhale, A. M., Denzer, D. K., and Liu, J. (1998). Relationship between fracture toughness, fracture path, and microstructure of 7050 aluminum alloy: Part I. quantitative characterization. *Metallurgical and Materials Transactions A*, 29(4):1191–1201. 56, 57

Dorward, R. C. and Beerntsen, D. (1995). Grain structure and quench-rate effects on strength and toughness of aa7050 al-zn-mg-cu-zr alloy plate. *Metallurgical and Materials Transactions A*, 26(9):2481–2484. 56

Duva, J. and Hutchinson, J. (1984). Constitutive potentials for dilutely voided nonlinear materials. *Mechanics of materials*, 3(1):41–54. 41

Esling, C., E. B.-F. and Bunge., H. J. (1982). Three-dimensional texture analysis after bunge and roe: correspondence between the respective mathematical techniques. *Texture, Stress, and Microstructure*, 5(12):95–125. 155

Fourmeau, M., Børvik, T., Benallal, A., and Hopperstad, O. S. (2013a). Anisotropic failure modes of high-strength aluminium alloy under various stress states. *International Journal of Plasticity*, 48:34–53. 41

Fourmeau, M., Børvik, T., Benallal, A., and Hopperstad, O. (2013b). Anisotropic failure modes of high-strength aluminium alloy under various stress states. *International Journal of Plasticity*, 48:34 – 53. 56

Furnémont, F. L. Q., Rompaey, T. V., Delannay, F., Jacques, P., and Pardoen, T. (2007). Multiscale mechanics of trip-assisted multiphase steels: II. micromechanical modelling. *Acta Materialia*, Volume 55, Issue 11:3695–3705. 56

Gammage, J., Wilkinson, D., Brechet, Y., and Embury, D. (2004). A model for damage coalescence in heterogeneous multi-phase materials. *Acta Materialia*, 52(18):5255–5263. 84

Gent, A. and Lindley, P. (1959). Internal rupture of bonded rubber cylinders in tension. *Proceedings of the Royal Society of London. Series A. Mathematical and Physical Sciences*, 249(1257):195–205. 3

Gologanu, M., Leblond, J.-B., Perrin, G., and Devaux, J. (1997). Recent extensions of Gurson's model for porous ductile metals. In *Continuum micromechanics*, pages 61–130. Springer. 41

Gologanu, M., Leblond, J.-B., Perrin, G., and Devaux, J. (2001). Theoretical models for void coalescence in porous ductile solids. I. coalescence "in layers". *International journal of solids and structures*, 38(32-33):5581–5594. 41, 84

Goods, S. and Brown, L. (1983). The nucleation of cavities by plastic deformation. In *Perspectives in Creep Fracture*, pages 71–85. Elsevier. 5, 84

Gurland, J. and Plateau, J. (1963). The mechanism of ductile rupture of metals containing inclusions. 3, 4

Gurson, A. L. (1977a). Continuum theory of ductile rupture by void nucleation and growth: Part I—Yield criteria and flow rules for porous ductile media. *Journal of engineering materials and technology*, 99(1):2–15. 41

Gurson, A. L. (1977b). Continuum Theory of Ductile Rupture by Void Nucleation and Growth: Part I—Yield Criteria and Flow Rules for Porous Ductile Media. *Journal of Engineering Materials and Technology*, 99(1):2–15. 56, 84

Han, X., Besson, J., Forest, S., Tanguy, B., and Bugat, S. (2013). A yield function for single crystals containing voids. *International Journal of Solids and Structures*, 50(14):2115 – 2131. 21, 26, 41, 56

Hancock, J. and Mackenzie, A. (1976). On the mechanisms of ductile failure in high-strength steels subjected to multi-axial stress-states. *Journal of the Mechanics and Physics of Solids*, 24(2-3):147–160. 23, 4

Hielscher, R., Silbermann, C. B., Schmidl, E., and Ihlemann, J. (2019). Denoising of crystal orientation maps. *Journal of Applied Crystallography*, 52(5):984–996. 88

Hill, R. (1948). A theory of the yielding and plastic flow of anisotropic metals. *Proceedings of the Royal Society of London A: Mathematical, Physical and Engineering Sciences*, 193(1033):281–297. 41

Hill, R. (1967). The essential structure of constitutive laws for metal composites and polycrystals. *Journal of the Mechanics and Physics of Solids*, 15:79–95. 152

Holzapfel, G. A. (2000). *Nonlinear solid mechanics: a continuum approach for engineering science*, volume 24. John Wiley and Sons. 131

Hom, C. and McMeeking, R. (1989). Void growth in elastic-plastic materials. *Journal of Applied Mechanics*, 56:309–317. 5

Hosokawa, A., Wilkinson, D. S., Kang, J., and Maire, E. (2012). Effect of triaxiality on void growth and coalescence in model materials investigated by x-ray tomography. *Acta Materialia*, 60(6-7):2829–2839. 84

Hosokawa, A., Wilkinson, D. S., Kang, J., and Maire, E. (2013). Onset of void coalescence in uniaxial tension studied by continuous x-ray tomography. *Acta Materialia*, 61(4):1021–1036. 6, 84

Hosseini, N., Nieto-Fuentes, J., Dakshinamurthy, M., Rodríguez-Martínez, J., and Vadillo, G. (2022). The effect of material orientation on void growth. *International Journal of Plasticity*, 148:103149. 42

Huang, M., Li, Z., and Wang, C. (2007). Discrete dislocation dynamics modelling of microvoid growth and its intrinsic mechanism in single crystals. *Acta Materialia*, 55(4):1387–1396. 5

Huang, Y. and Kinloch, A. (1992). The role of plastic void growth in the fracture of rubber-toughened epoxy polymers. *Journal of materials science letters*, 11(8):484–487. 3

Hull, D. and Rimmer, D. (1959). The growth of grain-boundary voids under stress. *Philosophical Magazine*, 4(42):673–687. 5

Hütter, G., Zybell, L., and Kuna, M. (2014). Size effects due to secondary voids during ductile crack propagation. *International Journal of Solids and Structures*, 51(3-4):839–847. 5

Jeong, W., Lee, C.-H., Moon, J., Jang, D., and Lee, M.-G. (2018). Grain scale representative volume element simulation to investigate the effect of crystal orientation on void growth in single and multi-crystals. *Metals*, 8(6). 57

Kadkhodapour, J., Butz, A., and Rad, S. Z. (2011a). Mechanisms of void formation during tensile testing in a commercial, dual-phase steel. *Acta Materialia*, 59(7):2575 – 2588. 56

Kadkhodapour, J., Butz, A., Ziaei-Rad, S., and Schmauder, S. (2011b). A micro mechanical study on failure initiation of dual phase steels under tension using single crystal plasticity model. *International Journal of Plasticity*, 27(7):1103 – 1125. 56

Kalidindi, S. R., Bronkhorst, C. A., and Anand, L. (1992). Crystallographic texture evolution in bulk deformation processing of fcc metals. *J. Mech. Phys. Solids*, 40:537–569. 21, 26, 34, 57

Keralavarma, S. and Benzerga, A. (2010). A constitutive model for plastically anisotropic solids with non-spherical voids. *Journal of the Mechanics and Physics of Solids*, 58(6):874–901. 59, 60

Keralavarma, S., Reddi, D., and Benzerga, A. (2020). Ductile failure as a constitutive instability in porous plastic solids. *Journal of the Mechanics and Physics of Solids*, 139:103917. 59

Khadyko, M., Dumoulin, S., Børvik, T., and Hopperstad, O. S. (2014). An experimental–numerical method to determine the work-hardening of anisotropic ductile materials at large strains. *International Journal of Mechanical Sciences*, 88:25–36. 41

Koplik, J. and Needleman, A. (1988). Void growth and coalescence in porous plastic solids. *International Journal of Solids and Structures*, 24(8):835–853. 4, 41

Kysar, J. W. and Gan, Y. X. (2005). Void growth in fcc and bcc single crystals. *11th International Conference on Fracture 2005, ICF11*, 5:3836–3841. 6

Kysar, J. W., Gan, Y. X., and Mendez-Arzuza, G. (2005). Cylindrical void in a rigid-ideally plastic single crystal. part I: Anisotropic slip line theory solution for face-centered cubic crystals. *International Journal of Plasticity*, 21(8):1481–1520. 5

Landron, C., Bouaziz, O., Maire, E., and Adrien, J. (2013). Experimental investigation of void coalescence in a dual phase steel using x-ray tomography. *Acta Materialia*, 61(18):6821–6829. 6

Lani, F., Furnémont, Q., Rompaey, T. V., Delannay, F., Jacques, P., and Pardoen, T. (2007). Multiscale mechanics of trip-assisted multiphase steels: I. micromechanical modelling. *Acta Materialia*, Volume 55, Issue 11:3681–3693. 56

Lebensohn, R. A. and Cazacu, O. (2012). Effect of single-crystal plastic deformation mechanisms on the dilatational plastic response of porous polycrystals. *International Journal of Solids and Structures*, 49(26):3838–3852. 41

Lhuissier, P., Scheel, M., Salvo, L., Di Michiel, M., and Blandin, J. (2013). Continuous characterization by x-ray microtomography of damage during high-temperature deformation of magnesium alloy. *Scripta Materialia*, 69(1):85–88. 84

Li, G. C. and Howard, I. (1983). The effect of strain softening in the matrix material during void growth. *Journal of the Mechanics and Physics of Solids*, 31(1):85–102. 4

Li, Z. and Guo, W. (2002). The influence of plasticity mismatch on the growth and coalescence of spheroidal voids on the bimaterial interface. *International Journal of Plasticity*, 18(2):249–279. 5

Li, Z. and Steinmann, P. (2006). Rve-based studies on the coupled effects of void size and void shape on yield behavior and void growth at micron scales. *International Journal of Plasticity*, 22(7):1195–1216. 4

Ling, C., Besson, J., Forest, S., Tanguy, B., Latourte, F., and Bosso, E. (2016). An elastoviscoplastic model for porous single crystals at finite strains and its assessment based on unit cell simulations. *International Journal of Plasticity*, 84:58–87. 74

Ling, C., Forest, S., Besson, J., Tanguy, B., and Latourte, F. (2018). A reduced micromorphic single crystal plasticity model at finite deformations. application to strain localization and void growth in ductile metals. *International Journal of Solids and Structures*, 134:43–69. 117

Liu, B., Qiu, X., Huang, Y., Hwang, K., Li, M., and Liu, C. (2003). The size effect on void growth in ductile materials. *Journal of the Mechanics and Physics of Solids*, 51(7):1171–1187. 4

Liu, H., Yang, Y., Yu, Z., Sun, Z., and Wang, Y. (2009). The application of a ductile fracture criterion to the prediction of the forming limit of sheet metals. *Journal of Materials Processing Technology*, 209:5443–5447. 57

Liu, W., He, Z., Tang, J., Hu, Z., and Cui, D. (2012). The effects of load condition on void coalescence in fcc single crystals. *Computational materials science*, 60:66–74. 5

Liu, W., Huang, H., and Tang, J. (2010). Fem simulation of void coalescence in fcc crystals. *Computational Materials Science*, 50(2):411 – 418. 57

Liu, W., Zhang, X., Tang, J., and Du, Y. (2007a). Simulation of void growth and coalescence behavior with 3d crystal plasticity theory. *Computational materials science*, 40(1):130–139. 5

Liu, W., Zhang, X., Tang, J., and Du, Y. (2007b). Simulation of void growth and coalescence behavior with 3d crystal plasticity theory. *Computational Materials Science*, 40(1):130 – 139. 41, 57

Lyles Jr, R. and Wilsdorf, H. (1975). Microcrack nucleation and fracture in silver crystals. *Acta Metallurgica*, 23(2):269–277. 5

Magnusen, P., Dubensky, E., and Koss, D. (1988). The effect of void arrays on void linking during ductile fracture. *Acta Metallurgica*, 36(6):1503–1509. 84, 85

Maire, E., Bouaziz, O., Di Michiel, M., and Verdu, C. (2008). Initiation and growth of damage in a dual-phase steel observed by x-ray microtomography. *Acta Materialia*, 56(18):4954–4964. 84

Maire, E., Zhou, S., Adrien, J., and Dimichiel, M. (2011). Damage quantification in aluminium alloys using in situ tensile tests in x-ray tomography. *Engineering Fracture Mechanics*, 78(15):2679–2690. 41, 84

MATLAB (2010). *version 7.10.0 (R2010a)*. The MathWorks Inc., Natick, Massachusetts. 88, 161

Mbiakop, A., Constantinescu, A., and Danas, K. (2015). A model for porous single crystals with cylindrical voids of elliptical cross-section. *International Journal of Solids and Structures*, 64-65:100 – 119. 56

McClintock, F. A. (1968). A criterion for ductile fracture by the growth of holes. *Journal of Applied Mechanics*, 35:363–371. 3, 4, 84

McDonald, B., Bornstein, H., Ameri, A., Daliri, A., and Orifici, A. C. (2019). Plasticity and ductile fracture behaviour of four armour steels. *International Journal of Solids and Structures*, 176:135–149. 41

Meissonnier, F., Busso, E., and O'Dowd, N. (2001). Finite element implementation of a generalised non-local rate-dependent crystallographic formulation for finite strains. *International Journal of Plasticity*, 17(4):601 – 640. 26, 147, 149

Meyers, M. A., Staudhammer, K. P., and Murr, L. E. (1986). *Metallurgical applications of shock-wave and high-strain-rate phenomena*. Marcel Dekker New York, NY. 23, 4

Monchiet, V., Cazacu, O., Charkaluk, E., and Kondo, D. (2008). Macroscopic yield criteria for plastic anisotropic materials containing spheroidal voids. *International Journal of Plasticity*, 24(7):1158–1189. 41

Morere, B., Ehrström, J. C., Gregson, P. J., and Sinclair, I. (2000). Microstructural effects on fracture toughness in aa7010 plate. *Metallurgical and Materials Transactions A*, 31(10):2503–2515. 56, 57

Morin, L., Leblond, J.-B., and Kondo, D. (2015). A Gurson-type criterion for plastically anisotropic solids containing arbitrary ellipsoidal voids. *International Journal of Solids and Structures*, 77:86–101. 41

Nahshon, K. and Hutchinson, J. (2008). Modification of the Gurson model for shear failure. *European Journal of Mechanics-A/Solids*, 27(1):1–17. 41

Needleman, A. (1972). Void growth in an elastic-plastic medium. *Journal of Applied Mechanics*, 41:964–970. 4

Needleman, A. (1984). The numerical analysis of necking instabilities. In *North-Holland Mathematics Studies*, volume 94, pages 249–273. Elsevier. 84

Nemat-Nasser, S. and Hori, M. (1987). Void collapse and void growth in crystalline solids. *Journal of applied physics*, 62(7):2746–2757. 5

Nemcko, M. J., Qiao, H., Wu, P., and Wilkinson, D. S. (2016). Effects of void fraction on void growth and linkage in commercially pure magnesium. *Acta Materialia*, 113:68–80. 6, 84

Nemcko, M. J. and Wilkinson, D. S. (2016). Impact of microstructure on void growth and linkage in pure magnesium. *International Journal of Fracture*, 200(1):31–47. 84

Ohashi, T. (2005). Crystal plasticity analysis of dislocation emission from micro voids. *International journal of plasticity*, 21(11):2071–2088. 5

O'regan, T., Quinn, D., Howe, M., and McHugh, P. (1997). Void growth simulations in single crystals. *Computational mechanics*, 20(1):115–121. 5

O'Regan, T. L., Quinn, D. F., Howe, M. A., and McHugh, P. E. (1997). Void growth simulations in single crystals. *Computational Mechanics*, 20(1):115–121. 57

Orsini, V. and Zikry, M. (2001). Void growth and interaction in crystalline materials. *International Journal of Plasticity*, 17(10):1393–1417. 5, 41

Pan, B., Qian, K., Xie, H., and Asundi, A. (2009). Two-dimensional digital image correlation for in-plane displacement and strain measurement: a review. *Measurement science and technology*, 20(6):062001. 27, 163, 164

Papaefthymiou, S., Prahl, U., Bleck, W., van der Zwaag, S., and Sietsma, J. (2006). Experimental observations on thecorrelation between microstructure and fracture of multiphase steels: Dedicated to professor eckard macherauch on the occasion of the 80th anniversary of his birth. *Zeitschrift für Metallkunde*, 97(12):1723–1731. 56

Pardoen, T. and Hutchinson, J. (2000). An extended model for void growth and coalescence. *Journal of the Mechanics and Physics of Solids*, 48(12):2467–2512. 6, 84

Paux, J., Morin, L., Brenner, R., and Kondo, D. (2015). An approximate yield criterion for porous single crystals. *European Journal of Mechanics - A/Solids*, 51:1 – 10. 56, 59

Perez-Bergquist, A., Cerreta, E., Trujillo, C., Cao, F., and Gray, G. (2011). Orientation dependence of void formation and substructure deformation in a spalled copper bicrystal. *Scripta Materialia*, 65(12):1069 – 1072. 56

Pishchalnikov, Y. A., Sapozhnikov, O. A., Bailey, M. R., Williams Jr, J. C., Cleveland, R. O., Colonius, T., Crum, L. A., Evan, A. P., and McAteer, J. A. (2003). Cavitation bubble cluster activity in the breakage of kidney stones by lithotripter shockwaves. *Journal of endourology*, 17(7):435–446. 3

Potirniche, G., Hearndon, J., Horstemeyer, M., and Ling, X. (2006a). Lattice orientation effects on void growth and coalescence in fcc single crystals. *International Journal of Plasticity*, 22(5):921–942. 5

Potirniche, G., Hearndon, J., Horstemeyer, M., and Ling, X. (2006b). Lattice orientation effects on void growth and coalescence in fcc single crystals. *International Journal of Plasticity*, 22(5):921–942. 41, 57

Pushkareva, M., Adrien, J., Maire, E., Segurado, J., Llorca, J., and Weck, A. (2016). Three-dimensional investigation of grain orientation effects on void growth in commercially pure titanium. *Materials Science and Engineering: A*, 671:221–232. 6, 84

Puttick, K. (1959). Ductile fracture in metals. *Philosophical magazine*, 4(44):964–969. 5, 84

Python (2021). *version 3.10.4*. Python Software Foundation. 161

Raabe, D., Sachtleber, M., Zhao, Z., Roters, F., and Zaefferer, S. (2001). Micromechanical and macromechanical effects in grain scale polycrystal plasticity experimentation and simulation. *Acta materialia*, 49(17):3433–3441. 111

Rice, J. R. and Tracey, D. M. (1969). On the ductile enlargement of voids in triaxial stress fields. *Journal of the Mechanics and Physics of Solids*, 17(3):201–217. 3, 4, 84

Rogers, H. (1960). The tensile fracture of ductile metals. *Metal. Soc. AIME*, 218:498–506. 3, 4

Roters, F., Eisenlohr, P., Bieler, T. R., and Raabe, D. (2011). *Crystal plasticity finite element methods: in materials science and engineering*. John Wiley & Sons. 23, 6, 11, 12, 13, 15, 16, 20, 21, 22, 24

Segurado, J. and LLorca, J. (2005). A computational micromechanics study of the effect of interface decohesion on the mechanical behavior of composites. *Acta materialia*, 53(18):4931–4942. 41

Segurado, J. and Llorca, J. (2009). An analysis of the size effect on void growth in single crystals using discrete dislocation dynamics. *Acta Materialia*, 57(5):1427–1436. 5, 41

Segurado, J., Llorca, J., and González, C. (2002). On the accuracy of mean-field approaches to simulate the plastic deformation of composites. *Scripta Materialia*, 46(7):525 – 529. 153

Selvarajou, B., Joshi, S. P., and Benzerga, A. A. (2019). Void growth and coalescence in hexagonal close packed crystals. *Journal of the Mechanics and Physics of Solids*, 125:198 – 224. 57

Seo, D., Toda, H., Kobayashi, M., Uesugi, K., Takeuchi, A., and Suzuki, Y. (2015). Three-dimensional investigation of void coalescence in free-cutting steel using x-ray tomography. *isij international*, 55(7):1483–1488. 84

Song, D. and Castañeda, P. P. (2017). Macroscopic response of strongly anisotropic porous viscoplastic single crystals and applications to ice. *Extreme Mechanics Letters*, 10:41 – 49. Filling Gaps in Material Property Space: IUTAM Symposium. 56

Srivastava, A. and Needleman, A. (2013). Void growth versus void collapse in a creeping single crystal. *Journal of the Mechanics and Physics of Solids*, 61(5):1169 – 1184. 6, 41, 54, 61, 75

Srivastava, A. and Needleman, A. (2015a). Effect of crystal orientation on porosity evolution in a creeping single crystal. *Mechanics of Materials*, 90:10 – 29. Proceedings of the IUTAM Symposium on Micromechanics of Defects in Solids. 6

Srivastava, A. and Needleman, A. (2015b). Effect of crystal orientation on porosity evolution in a creeping single crystal. *Mechanics of Materials*, 90:10 – 29. Proceedings of the IUTAM Symposium on Micromechanics of Defects in Solids. 27, 41, 57, 59, 61, 75

Stupkiewicz, S. and Petryk, H. (2016). A minimal gradient-enhancement of the classical continuum theory of crystal plasticity. part II: Size effects. *Archives of Mechanics*, 68:487–513. 117

Thomason, P. (1985). A three-dimensional model for ductile fracture by the growth and coalescence of microvoids. *Acta Metallurgica*, 33(6):1087–1095. 6

Thompson, A. W. (1987). Modeling of local strains in ductile fracture. *Metallurgical Transactions A*, 18(11):1877–1886. 5, 84

Toda, H., Maire, E., Yamauchi, S., Tsuruta, H., Hiramatsu, T., and Kobayashi, M. (2011). In situ observation of ductile fracture using x-ray tomography technique. *Acta Materialia*, 59(5):1995–2008. 84

Tvergaard, V. (1979). Influence of voids on shear band instability under plane strain condition. *The Danish Center for Applied Mathematics and Mechanics, Report No. 159*. 4

Tvergaard, V. (1981). Influence of voids on shear band instabilities under plane strain conditions. *International Journal of Fracture*, 17(4):389–407. 41

Tvergaard, V. (1982). On localization in ductile materials containing spherical voids. *International Journal of Fracture*, 18(4):237–252. 41

Tvergaard, V. (1990). Material failure by void growth to coalescence. *Advances in Applied Mechanics*, 27:83–151. 41

Tvergaard, V. and Hutchinson, J. W. (2002). Two mechanisms of ductile fracture: void by void growth versus multiple void interaction. *International Journal of Solids and Structures*, 39(13-14):3581–3597. 5

Tvergaard, V. and Needleman, A. (1984). Analysis of the cup-cone fracture in a round tensile bar. *Acta Metallurgica*, 32:157–169. 41, 56

Tvergaard, V. and Needleman, A. (1997). Nonlocal effects on localization in a void-sheet. *International Journal of Solids and Structures*, 34(18):2221–2238. 5

Tvergaard, V. and Niordson, C. (2004). Nonlocal plasticity effects on interaction of different size voids. *International Journal of Plasticity*, 20(1):107–120. 5

Vadillo, G., Reboul, J., and Fernández-Sáez, J. (2016). A modified gurson model to account for the influence of the Lode parameter at high triaxialities. *European Journal of Mechanics A/Solids*, 56:31–44. 152

Weck, A. and Wilkinson, D. (2008). Experimental investigation of void coalescence in metallic sheets containing laser drilled holes. *Acta Materialia*, 56(8):1774–1784. 84, 85, 110, 111

Weck, A., Wilkinson, D., Maire, E., and Toda, H. (2008). Visualization by x-ray tomography of void growth and coalescence leading to fracture in model materials. *Acta Materialia*, 56(12):2919–2928. 84

Worswick, M. and Pick, R. (1990). Void growth and constitutive softening in a periodically voided solid. *Journal of the Mechanics and Physics of Solids*, 38(5):601–625. 41

Wulfinghoff, S., Bayerschen, E., and Böhlke, T. (2013). A reduced micromorphic single crystal plasticity model at finite deformations. application to strain localization and void growth in ductile metals. *International Journal of Plasticity*, 51:33–46. 116, 117

Yerra, S., Tekog, C., Scheyvaerts, F., Delannay, L., Van Houtte, P., Pardoen, T., et al. (2010a). Void growth and coalescence in single crystals. *International Journal of Solids and Structures*, 47(7-8):1016–1029. 5, 41, 54

Yerra, S., Tekog~lu, C., Scheyvaerts, F., Delannay, L., Houtte, P. V., and Pardoen, T. (2010b). Void growth and coalescence in single crystals. *International Journal of Solids and Structures*, 47(7):1016 – 1029. 56, 57, 61

Zhao, Z., Ramesh, M., Raabe, D., Cuitino, A., and Radovitzky, R. (2008). Investigation of three-dimensional aspects of grain-scale plastic surface deformation of an aluminum oligocrystal. *International Journal of Plasticity*, 24(12):2278–2297. 111

Zybell, L., Hütter, G., Linse, T., Mühlich, U., and Kuna, M. (2014). Size effects in ductile failure of porous materials containing two populations of voids. *European Journal of Mechanics-A/Solids*, 45:8–19. 5

Part V

Appendices

Mathematical fundamentals

Scalar, vector and tensor fields are the mathematical tools necessary for constituting equations in continuum mechanics. In this appendix we provide essential concepts on basics of tensor algebra and tensor calculus necessary to follow mathematical equations used in this manuscript. Content presented in this appendix are adopted from Holzapfel (2000).

Contents

Following standard notations, scalars are represented by lowercase Greek letters, vectors by lowercase bold-face Latin letters, third-order tensors by uppercase bold-face calligraphic letters and fourth-order tensors by uppercase blackboard Latin letters.

$\alpha, \beta, \gamma, \ldots$ (scalars)
$\mathbf{a}, \mathbf{b}, \mathbf{c}, \ldots$ (vectors)
$\mathbf{A}, \mathbf{B}, \mathbf{C}, \ldots$ (second-order tensors)
$\mathscr{A}, \mathscr{B}, \mathscr{C}, \ldots$ (third-order tensors)
$\mathbb{A}, \mathbb{B}, \mathbb{C}, \ldots$ (fourth-order tensors)

A.1 Index notation

To carry out mathematical operations easily in computational mechanics we need a basis for all tensor and vector quantities. To this end, we introduce a right-handed and orthonormal

system $\{\mathbf{e}_1, \mathbf{e}_2, \mathbf{e}_3\}$ having the properties:

$$\begin{aligned} &\mathbf{e}_1 \cdot \mathbf{e}_2 = \mathbf{e}_2 \cdot \mathbf{e}_3 = \mathbf{e}_1 \cdot \mathbf{e}_3 = 0 \\ &\mathbf{e}_1 \cdot \mathbf{e}_1 = \mathbf{e}_2 \cdot \mathbf{e}_2 = \mathbf{e}_3 \cdot \mathbf{e}_3 = 1 \\ &\mathbf{e}_1 \times \mathbf{e}_2 = \mathbf{e}_3, \quad \mathbf{e}_2 \times \mathbf{e}_3 = \mathbf{e}_1, \quad \mathbf{e}_3 \times \mathbf{e}_1 = \mathbf{e}_2 \end{aligned} \tag{A.1}$$

where $\mathbf{e}_1$, $\mathbf{e}_2$ and $\mathbf{e}_3$ are three unit vectors and $(\cdot)$ denotes the dot product and $(\times)$ refers to the cross product (see section A.2 below).

In the three-dimensional Euclidean space, a vector $\mathbf{u}$ can be written as a linear combination of $\mathbf{e}_1$, $\mathbf{e}_2$ and $\mathbf{e}_3$ as:

$$\mathbf{u} = u_1\mathbf{e}_1 + u_2\mathbf{e}_2 + u_3\mathbf{e}_3 \tag{A.2}$$

where u_1, u_2 and u_3 are the Cartesian components of $\mathbf{u}$ such that:

$$u_1 = \mathbf{u} \cdot \mathbf{e}_1, \quad u_2 = \mathbf{u} \cdot \mathbf{e}_2, \quad u_3 = \mathbf{u} \cdot \mathbf{e}_3 \tag{A.3}$$

By adopting the summation convention, Eq. (A.2) is equivalently written in index notation as:

$$\mathbf{u} = u_i\mathbf{e}_i, \qquad (\text{sum over } i = 1, 2, 3) \tag{A.4}$$

In index notation, Eqs. $(A.1)_1$ and $(A.1)_2$ define the Kronecker delta, δ_{ij}, of the form:

$$\mathbf{e}_i \cdot \mathbf{e}_j = \delta_{ij} \equiv \begin{cases} 1, & \text{if} \quad i = j \\ 0, & \text{if} \quad i \neq j \end{cases} \tag{A.5}$$

A.2 Algebra of vectors

Dot product. Let $\mathbf{u}$ and $\mathbf{v}$ be two nonzero vectors. The dot product of $\mathbf{u}$ and $\mathbf{v}$ also called scalar or inner product produces a scalar. It reads:

$$\mathbf{u} \cdot \mathbf{v} = |\mathbf{u}|\,|\mathbf{v}| \cos(\theta) \tag{A.6}$$

where θ is the angle between $\mathbf{u}$ and $\mathbf{v}$. The quantity $|\mathbf{u}|$ is the magnitude or length of $\mathbf{u}$ defined by:

$$|\mathbf{u}| = \sqrt{\mathbf{u} \cdot \mathbf{u}} \tag{A.7}$$

The previous relations are written in index notation as:

$$\mathbf{u} \cdot \mathbf{v} = u_1v_1 + u_2v_2 + u_3v_3 \tag{A.8}$$

$$|\mathbf{u}|^2 = u_1^2 + u_2^2 + u_3^2 \tag{A.9}$$

The dot product has the following properties:

$$\begin{aligned} &\mathbf{u}\cdot\mathbf{v} = \mathbf{v}\cdot\mathbf{u} \\ &\mathbf{u}\cdot\mathbf{o} = 0 \\ &\mathbf{u}\cdot(\alpha\mathbf{v}+\beta\mathbf{w}) = \alpha(\mathbf{u}\cdot\mathbf{v}) + \beta(\mathbf{u}\cdot\mathbf{w}) \end{aligned} \tag{A.10}$$

where $\mathbf{o}$ stands for the unique zero vector.

Cross product. Also called vector product, the cross product of $\mathbf{u}$ and $\mathbf{v}$ yields a new vector defined by:

$$\mathbf{u}\times\mathbf{v} = |\mathbf{u}|\,|\mathbf{v}|\sin(\theta)\,\mathbf{n} \tag{A.11}$$

where $\mathbf{n}$ is unit vector such that the orthonormal system $\{\mathbf{u},\mathbf{v},\mathbf{n}\}$ is right-handed.

In index notation, the cross product is of the form:

$$\mathbf{u}\times\mathbf{v} = \det\begin{bmatrix} \mathbf{e}_1 & \mathbf{e}_2 & \mathbf{e}_3 \\ u_1 & u_2 & u_3 \\ v_1 & v_2 & v_3 \end{bmatrix} = \varepsilon_{ijk}u_i v_j \mathbf{e}_k \tag{A.12}$$

where ε_{ijk} is the permutation or alternating or Levi-Civita symbol defined by:

$$\varepsilon_{ijk} = \begin{cases} 1, & \text{for even permutations of } (i,j,k) \text{ (i.e. 123, 231, 312)} \\ -1, & \text{for odd permutations of } (i,j,k) \text{ (i.e. 132, 213, 321)} \\ 0, & \text{if there is a repeated index} \end{cases} \tag{A.13}$$

with the properties $\varepsilon_{ijk} = \varepsilon_{jki} = \varepsilon_{kij}$, $\varepsilon_{ijk} = -\varepsilon_{ikj}$ and $\varepsilon_{ijk} = -\varepsilon_{jik}$.

Note that the cross product is not commutative in contrast with the dot product which is commutative. Some properties of the cross product are:

$$\begin{aligned} &\mathbf{u}\times\mathbf{v} = -\mathbf{v}\times\mathbf{u} \\ &\mathbf{u}\times\mathbf{v} = \mathbf{o} \quad \text{means } \mathbf{u} \text{ and } \mathbf{v} \text{ are linearly dependent} \\ &(\alpha\mathbf{u})\times\mathbf{v} = \mathbf{u}\times(\alpha\mathbf{v}) = \alpha(\mathbf{u}\times\mathbf{v}) \end{aligned} \tag{A.14}$$

Triple scalar product. The volume V of a parallelepiped formed by a right-handed triad $\mathbf{u}$, $\mathbf{v}$, $\mathbf{w}$ is called tripled scalar or box product. It is expressed in index notation as:

$$V = (\mathbf{u}\times\mathbf{v})\cdot\mathbf{w} = \varepsilon_{ijk}u_i v_j w_k = \det\begin{bmatrix} u_1 & v_1 & w_1 \\ u_2 & v_2 & w_2 \\ u_3 & v_3 & w_3 \end{bmatrix} \tag{A.15}$$

If the $\mathbf{u}$, $\mathbf{v}$, $\mathbf{w}$ are linearly dependent then V has zero value.

Triple vector product. It is the product $\mathbf{u} \times (\mathbf{v} \times \mathbf{w})$ defined as:

$$\mathbf{u} \times (\mathbf{v} \times \mathbf{w}) = (\mathbf{u} \cdot \mathbf{w})\,\mathbf{v} - (\mathbf{u} \cdot \mathbf{v})\,\mathbf{w} \tag{A.16}$$

Similarly, we have that:

$$(\mathbf{u} \times \mathbf{v}) \times \mathbf{w} = (\mathbf{u} \cdot \mathbf{w})\,\mathbf{v} - (\mathbf{v} \cdot \mathbf{w})\,\mathbf{u} \tag{A.17}$$

Generally, the triple vector is not associative, that is, $\mathbf{u} \times (\mathbf{v} \times \mathbf{w}) \neq (\mathbf{u} \times \mathbf{v}) \times \mathbf{w}$

A.3 Algebra of tensors

A linear operator $\mathbf{A}$ that acts on a vector $\mathbf{u}$ to generate a vector $\mathbf{v}$ can be seen as second-order tensor:

$$\mathbf{v} = \mathbf{A}\mathbf{u} \tag{A.18}$$

Tensor product. Also referred to as direct or matrix product or dyad. The tensor product of $\mathbf{u}$ and $\mathbf{v}$ denoted by $\mathbf{u} \otimes \mathbf{v}$ is a second-order tensor that transforms linearly $\mathbf{w}$ into a vector with the direction of $\mathbf{u}$ as follows:

$$(\mathbf{u} \otimes \mathbf{v})\,\mathbf{w} = (\mathbf{v} \cdot \mathbf{w})\,\mathbf{u} \tag{A.19}$$

The tensor product is, in general, not commutative, that is, $\mathbf{u} \otimes \mathbf{v} \neq \mathbf{v} \otimes \mathbf{u}$. Moreover we have the following properties:

$$\begin{aligned}
&(\mathbf{u} \otimes \mathbf{v})\,(\alpha\mathbf{w} + \mathbf{x}) = \alpha\,(\mathbf{u} \otimes \mathbf{v})\,\mathbf{w} + (\mathbf{u} \otimes \mathbf{v})\,\mathbf{x} \\
&(\alpha\mathbf{u} + \beta\mathbf{v}) \otimes \mathbf{w} = \alpha\,(\mathbf{u} \otimes \mathbf{w}) + \beta\,(\mathbf{v} \otimes \mathbf{w}) \\
&(\mathbf{u} \otimes \mathbf{v})\,(\mathbf{w} \otimes \mathbf{x}) = (\mathbf{v} \cdot \mathbf{w})\,\mathbf{u} \otimes \mathbf{x} = \mathbf{u} \otimes \mathbf{x}\,(\mathbf{v} \cdot \mathbf{w}) \\
&\mathbf{A}\,(\mathbf{u} \otimes \mathbf{v}) = (\mathbf{A}\mathbf{u}) \otimes \mathbf{v}
\end{aligned} \tag{A.20}$$

Any second-order tensor $\mathbf{A}$ can be represented by a linear combination of dyads formed by the basis $\{\mathbf{e}_i\}$ as:

$$\mathbf{A} = A_{ij}\mathbf{e}_i \otimes \mathbf{e}_j \tag{A.21}$$

A_{ij} which represent the Cartesian components of $\mathbf{A}$ with respect to $\{\mathbf{e}_i\}$ are written in matrix notation as:

$$[\mathbf{A}] = \begin{bmatrix} A_{11} & A_{12} & A_{13} \\ A_{21} & A_{22} & A_{23} \\ A_{31} & A_{32} & A_{33} \end{bmatrix} \tag{A.22}$$

For all nonzero vectors $\mathbf{v}$, if $\mathbf{v}\cdot\mathbf{Av}\geqslant 0$ then $\mathbf{A}$ is said to be a positive semi-definite tensor and if $\mathbf{v}\cdot\mathbf{Av}>0$ then $\mathbf{A}$ is said to be a positive definite tensor. In the case where $\mathbf{v}\cdot\mathbf{Av}\leqslant 0$, $\mathbf{A}$ is called negative semi-definite tensor and if $\mathbf{v}\cdot\mathbf{Av}<0$, $\mathbf{A}$ is called negative definite tensor.

The Cartesian components of $\mathbf{u}\otimes\mathbf{v}$ with respect to $\{\mathbf{e}_i\}$ are defined by:

$$(\mathbf{u}\otimes\mathbf{v})_{ij}=u_iv_j=\begin{bmatrix}u_1\\u_2\\u_3\end{bmatrix}\begin{bmatrix}v_1 & v_2 & v_3\end{bmatrix}=\begin{bmatrix}u_1v_1 & u_1v_2 & u_1v_3\\u_2v_1 & u_2v_2 & u_2v_3\\u_3v_1 & u_3v_2 & u_3v_3\end{bmatrix} \tag{A.23}$$

The identity tensor $\mathbf{I}$ is defined by:

$$\mathbf{u}=\mathbf{Iu} \tag{A.24}$$

for all vectors $\mathbf{u}$.

The Cartesian components of the unit tensor $\mathbf{I}$ are:

$$\mathbf{I}=\delta_{ij}\mathbf{e}_i\otimes\mathbf{e}_j=\mathbf{e}_j\otimes\mathbf{e}_j \tag{A.25}$$

Dot product. $\mathbf{AB}$ which denotes the dot product of two second-order tensors $\mathbf{A}$ and $\mathbf{B}$ yields a second-order tensor according to the following relation for all vectors $\mathbf{u}$:

$$(\mathbf{AB})\,\mathbf{u}=\mathbf{A}\,(\mathbf{Bu}) \tag{A.26}$$

Generally, $\mathbf{AB}\neq\mathbf{BA}$ and $\mathbf{Au}\neq\mathbf{uA}$ which are the dot products of second-order tensors are not commutative. The components of $\mathbf{AB}$ with respect to $\{\mathbf{e}_i\}$ are as follows:

$$(\mathbf{AB})_{ij}=A_{ik}B_{kj}=A_{i1}B_{1j}+A_{i2}B_{2j}+A_{i3}B_{3j} \tag{A.27}$$

Transpose of a tensor. For all vectors $\mathbf{u}$ and $\mathbf{v}$, the transpose $\mathbf{A}^{\mathrm{T}}$ of a second-order tensor $\mathbf{A}$ follow the rule:

$$\mathbf{v}\cdot\mathbf{A}^{\mathrm{T}}\mathbf{u}=\mathbf{u}\cdot\mathbf{Av}=\mathbf{Av}\cdot\mathbf{u} \tag{A.28}$$

and has the following properties:

$$\begin{aligned}&\left(\mathbf{A}^{\mathrm{T}}\right)^{\mathrm{T}}=\mathbf{A}\\&(\alpha\mathbf{A}+\beta\mathbf{B})^{\mathrm{T}}=\alpha\mathbf{A}^{\mathrm{T}}+\beta\mathbf{B}^{\mathrm{T}}\\&(\mathbf{AB})^{\mathrm{T}}=\mathbf{B}^{\mathrm{T}}\mathbf{A}^{\mathrm{T}}\\&(\mathbf{u}\otimes\mathbf{v})^{\mathrm{T}}=\mathbf{v}\otimes\mathbf{u}\end{aligned} \tag{A.29}$$

The Cartesian components of $\mathbf{A}^{\mathrm{T}}$ with respect to $\{\mathbf{e}_i\}$ are defined by:

$$\left(\mathbf{A}^{\mathrm{T}}\right)_{ij} = A_{ji} \tag{A.30}$$

Trace and contraction. The trace tr$\mathbf{A}$ which denotes the trace of a tensor $\mathbf{A}$ reads:

$$\mathrm{tr}\mathbf{A} = A_{ii} = A_{11} + A_{22} + A_{33} \tag{A.31}$$

The properties of the trace are:

$$\begin{aligned} &\mathrm{tr}\left(\mathbf{A}^{\mathrm{T}}\right) = \mathrm{tr}\mathbf{A} \\ &\mathrm{tr}\left(\mathbf{AB}\right) = \mathrm{tr}\left(\mathbf{BA}\right) \\ &\mathrm{tr}\left(\mathbf{A}+\mathbf{B}\right) = \mathrm{tr}\mathbf{A} + \mathrm{tr}\mathbf{B} \\ &\mathrm{tr}\left(\alpha\mathbf{A}\right) = \alpha\mathrm{tr}\mathbf{A} \end{aligned} \tag{A.32}$$

A double contraction of two tensors $\mathbf{A}$ and $\mathbf{B}$ is defined by:

$$\mathbf{A} : \mathbf{B} = \mathrm{tr}\left(\mathbf{A}^{\mathrm{T}}\mathbf{B}\right) = \mathrm{tr}\left(\mathbf{B}^{\mathrm{T}}\mathbf{A}\right) \tag{A.33}$$

$$= \mathrm{tr}\left(\mathbf{AB}^{\mathrm{T}}\right) = \mathrm{tr}\left(\mathbf{BA}^{\mathrm{T}}\right) \tag{A.34}$$

The properties of the double contraction are:

$$\begin{aligned} &\mathbf{A} : \mathbf{B} = \mathbf{B} : \mathbf{A} \\ &\mathbf{I} : \mathbf{A} = \mathrm{tr}\mathbf{A} = \mathbf{A} : \mathbf{I} \\ &\mathbf{A} : (\mathbf{BC}) = \left(\mathbf{B}^{\mathrm{T}}\mathbf{A}\right) : \mathbf{C} = \left(\mathbf{AC}^{\mathrm{T}}\right) : \mathbf{B} \\ &\mathbf{A} : (\mathbf{u} \otimes \mathbf{v}) = \mathbf{u} \cdot \mathbf{Av} = (\mathbf{u} \otimes \mathbf{v}) : \mathbf{A} \\ &(\mathbf{u} \otimes \mathbf{v}) : (\mathbf{w} \otimes \mathbf{x}) = (\mathbf{u} \cdot \mathbf{w})\,(\mathbf{v} \cdot \mathbf{x}) \\ &(\mathbf{e}_i \otimes \mathbf{e}_j) : (\mathbf{e}_k \otimes \mathbf{e}_l) = (\mathbf{e}_i \cdot \mathbf{e}_k) : (\mathbf{e}_j \cdot \mathbf{e}_l) = \delta_{ik}\delta_{jl} \end{aligned} \tag{A.35}$$

The norm of a tensor $\mathbf{A}$ is a scalar denoted by $|\mathbf{A}|$ and defined as:

$$|\mathbf{A}| = (\mathbf{A} : \mathbf{A})^{1/2} = (A_{ij}A_{ij})^{1/2} \geqslant 0 \tag{A.36}$$

Determinant and inverse of a tensor. The determinant of a tensor $\mathbf{A}$ is a scalar defined by:

$$\det\mathbf{A} = \det\left[\mathbf{A}\right] = \det\begin{bmatrix} A_{11} & A_{12} & A_{13} \\ A_{21} & A_{22} & A_{23} \\ A_{31} & A_{32} & A_{33} \end{bmatrix} \tag{A.37}$$

with the following properties:

$$\begin{aligned} \det(\mathbf{AB}) &= \det\mathbf{A}\det\mathbf{B} \\ \det\left(\mathbf{A}^{\mathrm{T}}\right) &= \det\mathbf{A} \end{aligned} \tag{A.38}$$

If $\det\mathbf{A} = 0$ then the tensor $\mathbf{A}$ is said to be singular. A nonsingular tensor $\mathbf{A}$, that is, $\det\mathbf{A} \neq 0$, is invertible according to the following rule:

$$\mathbf{A}\mathbf{A}^{-1} = \mathbf{I} = \mathbf{A}^{-1}\mathbf{A} \tag{A.39}$$

where the tensor $\mathbf{A}^{-1}$ is a unique inverse of the tensor $\mathbf{A}$.

For all invertible tensors $\mathbf{A}$ and $\mathbf{B}$, we have the following properties:

$$\begin{aligned} (\mathbf{AB})^{-1} &= \mathbf{B}^{-1}\mathbf{A}^{-1} \\ (\mathbf{A}^{-1})^{-1} &= \mathbf{A} \\ (\mathbf{A}^{-1})^{\mathrm{T}} &= \left(\mathbf{A}^{\mathrm{T}}\right)^{-1} \\ \mathbf{A}^{-2} &= \mathbf{A}^{-1}\mathbf{A}^{-1} \\ \det(\mathbf{A}^{-1}) &= (\det\mathbf{A})^{-1} \end{aligned} \tag{A.40}$$

Orthogonal tensor. For all vectors $\mathbf{u}$ and $\mathbf{v}$, an orthogonal tensor $\mathbf{Q}$ fulfills the following requirement:

$$\mathbf{Q}\mathbf{u}\cdot\mathbf{Q}\mathbf{v} = \mathbf{u}\cdot\mathbf{v} \tag{A.41}$$

If $\mathbf{Q}$ is an orthogonal tensor, we have that $\mathbf{Q}^{\mathrm{T}}\mathbf{Q} = \mathbf{Q}\mathbf{Q}^{\mathrm{T}} = \mathbf{I}$ leading to $\mathbf{Q}^{\mathrm{T}} = \mathbf{Q}^{-1}$. Additionally, we have that $\det\left(\mathbf{Q}^{\mathrm{T}}\mathbf{Q}\right) = (\det\mathbf{Q})^2$ with $\det\mathbf{Q} = \pm 1$. $\mathbf{Q}$ is said to be proper (improper) orthogonal corresponding to rotation (reflection) if $\det\mathbf{Q} = +1(-1)$, respectively.

Symmetric and skew tensors. Every tensor $\mathbf{A}$ can be separated into a symmetric tensor $\mathbf{S}$ and a skew or antisymmetric tensor $\mathbf{W}$ such that:

$$\begin{aligned} \mathbf{S} &= \frac{1}{2}\left(\mathbf{A} + \mathbf{A}^{\mathrm{T}}\right) = \mathbf{S}^{\mathrm{T}} \\ \mathbf{W} &= \frac{1}{2}\left(\mathbf{A} - \mathbf{A}^{\mathrm{T}}\right) = -\mathbf{W}^{\mathrm{T}} \end{aligned} \tag{A.42}$$

In matrix notation, $\mathbf{S}$ and $\mathbf{W}$ read:

$$[\mathbf{S}] = \begin{bmatrix} S_{11} & S_{12} & S_{13} \\ S_{12} & S_{22} & S_{23} \\ S_{13} & S_{23} & S_{33} \end{bmatrix} \tag{A.43}$$

$$[\mathbf{W}] = \begin{bmatrix} 0 & W_{12} & W_{13} \\ -W_{12} & 0 & W_{23} \\ -W_{13} & -W_{23} & 0 \end{bmatrix} \tag{A.44}$$

For all tensors $\mathbf{B}$, we have the following properties:

$$\begin{aligned} &\mathbf{S} : \mathbf{B} = \mathbf{S} : \mathbf{B}^{\mathrm{T}} = \mathbf{S} : \frac{1}{2}\left(\mathbf{B} + \mathbf{B}^{\mathrm{T}}\right) \\ &\mathbf{W} : \mathbf{B} = -\mathbf{W} : \mathbf{B}^{\mathrm{T}} = \mathbf{W} : \frac{1}{2}\left(\mathbf{B} - \mathbf{B}^{\mathrm{T}}\right) \\ &\mathbf{S} : \mathbf{W} = 0 \end{aligned} \tag{A.45}$$

Spherical and deviatoric tensors. Any tensor $\mathbf{A}$ can be separated into its spherical part and its deviatoric part as follows:

$$\mathbf{A} = \alpha\mathbf{I} + \mathrm{dev}\mathbf{A} \tag{A.46}$$

where $\alpha = \frac{1}{3}\mathrm{tr}\mathbf{A} = \frac{1}{3}(\mathbf{I} : \mathbf{A})$. $\alpha\mathbf{I}$ is called spherical tensor and $\mathrm{dev}\mathbf{A}$ is called deviatoric tensor or deviator of $\mathbf{A}$. The trace of $\mathrm{dev}\mathbf{A}$ is always zero, that is, $\mathrm{tr}\,(\mathrm{dev}\mathbf{A}) = 0$.

A.4 High-order tensors

Any tensor of order or rank n is of the form:

$$A_{i_1 i_2 \ldots i_n}\mathbf{e}_{i_1} \otimes \mathbf{e}_{i_2} \otimes \cdots \otimes \mathbf{e}_{i_n} \tag{A.47}$$

with 3^n components $A_{i_1 i_2 \ldots i_n}$. In particular, a tensor of order zero is scalar with $3^0 = 1$ component and a tensor of order one is a vector with $3^1 = 3$ components.

Tensor of order three. According to Eq. (A.47), any tensor of order three is of the form:

$$\mathscr{A} = \mathscr{A}_{ijk}\mathbf{e}_i \otimes \mathbf{e}_j \otimes \mathbf{e}_k \tag{A.48}$$

with $3^3 = 27$ components $\mathscr{A}_{ijk}$ defined by:

$$\mathscr{A}_{ijk} = (\mathbf{e}_i \otimes \mathbf{e}_j) : \mathscr{A}\mathbf{e}_k \tag{A.49}$$

A double contraction of a tensor of order three $\mathscr{A}$ and a tensor of order two $\mathbf{B}$ yields a vector according to the following relation:

$$\mathscr{A} : \mathbf{B} = \mathscr{A}_{ijk}B_{jk}\mathbf{e}_i \tag{A.50}$$

Tensor of order four. According to Eq. (A.47), any tensor of order four is of the form:

$$\mathbb{A} = A_{ijkl}\mathbf{e}_i \otimes \mathbf{e}_j \otimes \mathbf{e}_k \otimes \mathbf{e}_l \tag{A.51}$$

with $3^4 = 81$ components A_{ijkl} defined by:

$$A_{ijkl} = (\mathbf{e}_i \otimes \mathbf{e}_j) : \mathbb{A} : (\mathbf{e}_k \otimes \mathbf{e}_l) \tag{A.52}$$

A double contraction of a fourth-order tensor $\mathbb{A}$ and a second-order tensor $\mathbf{B}$ yields a second-order tensor according to the following relation:

$$\mathbb{A} : \mathbf{B} = A_{ijkl}B_{kl}\mathbf{e}_i \otimes \mathbf{e}_j \tag{A.53}$$

Fourth-order unit tensors $\mathbb{I}$ and $\bar{\mathbb{I}}$ are such that:

$$\mathbf{A} = \mathbb{I} : \mathbf{A} \tag{A.54}$$
$$\mathbf{A}^{\mathrm{T}} = \bar{\mathbb{I}} : \mathbf{A} \tag{A.55}$$
$$\tag{A.56}$$

for any second-order tensor $\mathbf{A}$. $\mathbb{I}$ and $\bar{\mathbb{I}}$ read:

$$\mathbb{I} = \delta_{ik}\delta_{jl}\mathbf{e}_i \otimes \mathbf{e}_j \otimes \mathbf{e}_k \otimes \mathbf{e}_l = \mathbf{e}_i \otimes \mathbf{e}_j \otimes \mathbf{e}_i \otimes \mathbf{e}_j \tag{A.57}$$
$$\bar{\mathbb{I}} = \delta_{il}\delta_{jk}\mathbf{e}_i \otimes \mathbf{e}_j \otimes \mathbf{e}_k \otimes \mathbf{e}_l = \mathbf{e}_i \otimes \mathbf{e}_j \otimes \mathbf{e}_j \otimes \mathbf{e}_i \tag{A.58}$$
$$\tag{A.59}$$

where $(\mathbb{I})_{ijkl} = \delta_{ik}\delta_{jl}$ and $\left(\bar{\mathbb{I}}\right)_{ijkl} = \delta_{il}\delta_{jk}$ represent the Cartesian components.

A.5 Eigenvalues and eigenvectors of second-order tensors

Eigenvalues or principal values λ_i and eigenvectors or principal directions $\hat{\mathbf{n}}_i$ (nonzero vectors) of a second-order tensor $\mathbf{A}$ satisfy the requirement:

$$\mathbf{A}\hat{\mathbf{n}}_i = \lambda_i\hat{\mathbf{n}}_i, \qquad (i = 1, 2, 3; \text{no summation}) \tag{A.60}$$

Note that all eigenvalues λ_i of a positive definite symmetric tensor $\mathbf{A}$ are real and positive. Additionally, the set of eigenvectors of a symmetric tensor $\mathbf{A}$ form an orthonormal basis $\{\hat{\mathbf{n}}_i\}$.

The previous relation can be rewritten as:

$$(\mathbf{A} - \lambda_i\mathbf{I})\,\hat{\mathbf{n}}_i = \mathbf{o}, \qquad (i = 1, 2, 3; \text{no summation}) \tag{A.61}$$

Principal scalar invariants. According to Eq. (A.61), since $\hat{\mathbf{n}}_i \neq \mathbf{o}$, we have the following relation:

$$\det\left(\mathbf{A} - \lambda_i \mathbf{I}\right) = \lambda^3 - I_1\lambda^2 + I_2\lambda - I_3 = 0 \tag{A.62}$$

known as the characteristic polynomial or equation whose solutions are the eigenvalues $\lambda_i, i = 1, 2, 3$.

In Eq. (A.62), $I_i\left(\mathbf{A}\right), i = 1, 2, 3$ are the so-called principal scalar invariants of $\mathbf{A}$ given by:

$$\begin{aligned} I_1\left(\mathbf{A}\right) &= A_{ii} = \mathrm{tr}\mathbf{A} \\ I_2\left(\mathbf{A}\right) &= \frac{1}{2}\left(A_{ii}A_{jj} - A_{ji}A_{ij}\right) = \frac{1}{2}\left[\left(\mathrm{tr}\mathbf{A}\right)^2 - \mathrm{tr}\left(\mathbf{A}^2\right)\right] = \mathrm{tr}\mathbf{A}^{-1}\det\mathbf{A} \\ I_3\left(\mathbf{A}\right) &= \varepsilon_{ijk}A_{1i}A_{2j}A_{3k} = \det\mathbf{A} \end{aligned} \tag{A.63}$$

Spectral decomposition of a tensor. Also referred to as eigendecomposition, the spectral decomposition is the representation of a symmetric tensor $\mathbf{A}$ by its eigenvalues $\lambda_i, i = 1, 2, 3$ and its eigenvectors forming an orthonormal basis $\{\hat{\mathbf{n}}_i\}$ as follows:

$$\mathbf{A} = \sum_{i=1}^{3} \lambda_i \hat{\mathbf{n}}_i \otimes \hat{\mathbf{n}}_i \tag{A.64}$$

The components A_{ij} of $\mathbf{A}$ with respect to the orthonormal basis $\{\hat{\mathbf{n}}_i\}$ are defined by:

$$A_{ij} = \lambda_j \delta_{ij} \tag{A.65}$$

written in matrix notation as:

$$\left[\mathbf{A}\right] = \begin{bmatrix} \lambda_1 & 0 & 0 \\ 0 & \lambda_2 & 0 \\ 0 & 0 & \lambda_3 \end{bmatrix} \tag{A.66}$$

Hence Eq. (A.63) can be rewritten as:

$$\begin{aligned} I_1\left(\mathbf{A}\right) &= \lambda_1 + \lambda_2 + \lambda_3 \\ I_2\left(\mathbf{A}\right) &= \lambda_1\lambda_2 + \lambda_2\lambda_3 + \lambda_3\lambda_1 \\ I_3\left(\mathbf{A}\right) &= \lambda_1\lambda_2\lambda_3 \end{aligned} \tag{A.67}$$

A.6 Gradients and related operators

In the following, we consider a scalar field $\Phi\left(\mathbf{x}\right)$, a vector field $\mathbf{u}\left(\mathbf{x}\right)$ and a tensor field $\mathbf{A}\left(\mathbf{x}\right)$ that assign a scalar, vector and tensor to each material point $\mathbf{x}$ of a body, respectively.

Gradient of a scalar field. The gradient or derivative of a scalar field $\Phi(\mathbf{x})$ is expressed as:

$$\text{grad}\Phi = \boldsymbol{\nabla}\Phi = \frac{\partial \Phi}{\partial x_i}\mathbf{e}_i = \frac{\partial \Phi}{\partial x_1}\mathbf{e}_1 + \frac{\partial \Phi}{\partial x_2}\mathbf{e}_2 + \frac{\partial \Phi}{\partial x_3}\mathbf{e}_3 \tag{A.68}$$

where the operator $\boldsymbol{\nabla} = \dfrac{\partial}{\partial x_i}\mathbf{e}_i$ is called Nabla operator.

The dot product, cross product and tensor product of the Nabla operator with a smooth vector or tensor field $(\bullet)$ are:

$$\begin{aligned} \boldsymbol{\nabla} \cdot (\bullet) &= \frac{\partial (\bullet)}{\partial x_i} \cdot \mathbf{e}_i \\ \boldsymbol{\nabla} \times (\bullet) &= \mathbf{e}_i \times \frac{\partial (\bullet)}{\partial x_i} \\ \boldsymbol{\nabla} \otimes (\bullet) &= \frac{\partial (\bullet)}{\partial x_i} \otimes \mathbf{e}_i \end{aligned} \tag{A.69}$$

Divergence of a vector field. The dot product of the vector operator $\boldsymbol{\nabla}$ with a smooth vector field $\mathbf{u}(\mathbf{x})$ yields a scalar field called divergence of $\mathbf{u}$:

$$\text{div}\mathbf{u} = \boldsymbol{\nabla} \cdot \mathbf{u} = \frac{\partial u_j}{\partial x_i}\mathbf{e}_j \cdot \mathbf{e}_i = \frac{\partial u_1}{\partial x_1} + \frac{\partial u_2}{\partial x_2} + \frac{\partial u_3}{\partial x_3} \tag{A.70}$$

The vector field $\mathbf{u}(\mathbf{x})$ is said to be divergence-free or solenoidal if $\text{div}\mathbf{u} = 0$.

Curl of a vector field. The cross product of the vector operator $\boldsymbol{\nabla}$ with a smooth vector field $\mathbf{u}(\mathbf{x})$ yields a vector field called curl or rotation of $\mathbf{u}$:

$$\text{curl}\mathbf{u} = \boldsymbol{\nabla} \times \mathbf{u} = \frac{\partial u_j}{\partial x_i}\mathbf{e}_i \times \mathbf{e}_j = \varepsilon_{ijk}\frac{\partial u_j}{\partial x_i}\mathbf{e}_k \tag{A.71}$$

or

$$\text{curl}\mathbf{u} = \left(\frac{\partial u_3}{\partial x_2} - \frac{\partial u_2}{\partial x_3}\right)\mathbf{e}_1 + \left(\frac{\partial u_1}{\partial x_3} - \frac{\partial u_3}{\partial x_1}\right)\mathbf{e}_2 + \left(\frac{\partial u_2}{\partial x_1} - \frac{\partial u_1}{\partial x_2}\right)\mathbf{e}_3 \tag{A.72}$$

The vector field $\mathbf{u}(\mathbf{x})$ is said to be curl-free or irrotational or conservative if $\text{curl}\mathbf{u} = 0$. Furthermore, it can be shown that:

$$\begin{aligned} &\text{curl grad}\Phi = \mathbf{o} \\ &\text{div curl}\mathbf{u} = 0 \end{aligned} \tag{A.73}$$

Gradient of a vector field. The tensor product of the vector operator $\boldsymbol{\nabla}$ with a smooth vector field $\mathbf{u}(\mathbf{x})$ yields a second-order tensor field called gradient or derivative of $\mathbf{u}$:

$$\text{grad}\mathbf{u} = \boldsymbol{\nabla} \otimes \mathbf{u} = \frac{\partial u_i}{\partial x_j}\mathbf{e}_i \otimes \mathbf{e}_j \tag{A.74}$$

with Cartesian components $(\text{grad}\mathbf{u})_{ij} = \dfrac{\partial u_i}{\partial x_j}$ written in matrix notation as:

$$[\text{grad}\mathbf{u}] = \begin{bmatrix} \dfrac{\partial u_1}{\partial x_1} & \dfrac{\partial u_1}{\partial x_2} & \dfrac{\partial u_1}{\partial x_3} \\ \dfrac{\partial u_2}{\partial x_1} & \dfrac{\partial u_2}{\partial x_2} & \dfrac{\partial u_2}{\partial x_3} \\ \dfrac{\partial u_3}{\partial x_1} & \dfrac{\partial u_3}{\partial x_2} & \dfrac{\partial u_3}{\partial x_3} \end{bmatrix} \tag{A.75}$$

It can be proved that $\text{tr}(\text{grad}\mathbf{u}) = \text{div}\mathbf{u}$.

Divergence and gradient of a second-order tensor field. The dot product and the tensor product of the vector operator $\boldsymbol{\nabla}$ with a smooth tensor field $\mathbf{A}(\mathbf{x})$ yield the divergence, $\text{div}\mathbf{A}$, and the gradient or derivative, $\text{grad}\mathbf{A}$, of $\mathbf{A}$, respectively:

$$\begin{aligned} \text{div}\mathbf{A} &= \boldsymbol{\nabla} \cdot \mathbf{A} = \frac{\partial A_{ij}}{\partial x_j}\mathbf{e}_i \\ \text{grad}\mathbf{A} &= \boldsymbol{\nabla} \otimes \mathbf{A} = \frac{\partial A_{ij}}{\partial x_k}\mathbf{e}_i \otimes \mathbf{e}_j \otimes \mathbf{e}_k \end{aligned} \tag{A.76}$$

Laplacian and Hessian. The Laplacian operator or simply Laplacian denoted by ∇^2 or Δ is defined as:

$$\nabla^2(\bullet) = \boldsymbol{\nabla} \cdot \boldsymbol{\nabla}(\bullet) = \frac{\partial^2(\bullet)}{\partial x_i^2} = \frac{\partial^2(\bullet)}{\partial x_1^2} + \frac{\partial^2(\bullet)}{\partial x_2^2} + \frac{\partial^2(\bullet)}{\partial x_3^2} \tag{A.77}$$

The Laplacian of a scalar field Φ yields another scalar field.

The Hessian denoted by $\boldsymbol{\nabla}\boldsymbol{\nabla}$ is defined as:

$$\boldsymbol{\nabla}\boldsymbol{\nabla}(\bullet) = \boldsymbol{\nabla} \otimes \boldsymbol{\nabla}(\bullet) = \frac{\partial^2(\bullet)}{\partial x_i \partial x_j}\mathbf{e}_i \otimes \mathbf{e}_j \tag{A.78}$$

A.7 Divergence theorem

Let us consider any smooth vector field $\mathbf{u}(\mathbf{x})$ and tensor field $\mathbf{A}(\mathbf{x})$ defined on a region with volume v and boundary surface s. The divergence theorem also known as Gauss's divergence theorem transform a surface integral into a volume integral as follows:

$$\int_s \mathbf{u} \cdot \mathbf{n}\mathrm{d}s = \int_v \text{div}\mathbf{u}\mathrm{d}v \qquad \text{or} \qquad \int_s u_i n_i \mathrm{d}s = \int_v \frac{\partial u_i}{\partial x_i}\mathrm{d}v \tag{A.79}$$

$$\int_s \mathbf{A}\mathbf{n}\mathrm{d}s = \int_v \text{div}\mathbf{A}\mathrm{d}v \qquad \text{or} \qquad \int_s A_{ij} n_j \mathrm{d}s = \int_v \frac{\partial A_{ij}}{\partial x_j}\mathrm{d}v \tag{A.80}$$

where $\mathbf{n}$ is the outward unit normal field acting along the surface s, $\mathrm{d}v$ and $\mathrm{d}s$ are infinitesimal volume and surface elements at $\mathbf{x}$, respectively.

Numerical integration algorithm

In this appendix, we present the numerical algorithm used to implement the constitutive equations presented in Chapter 2 (see Section 2.2.3.1) into the finite element code ABAQUS/Standard (2019) through a user subroutine UMAT.

In this appendix, time integration of crystal plasticity equations presented in section 2.2.3.1 is performed following the backward Euler implicit integration scheme presented in work of Cruzado et al. (2017) for the computation of $\Delta\gamma^{\alpha}_{t+\Delta t}$:

$$\Delta\gamma^{\alpha}_{t+\Delta t} = \dot{\gamma^{\alpha}}_{t+\Delta t}(\Delta\gamma^{\alpha}_{t+\Delta t})\ \Delta t \tag{B.1}$$

where $\dot{\gamma^{\alpha}}_{t+\Delta t}$ is given by :

$$\dot{\gamma^{\alpha}} = \gamma_0 \left| \frac{\tau^{\alpha}}{\tau^{\alpha}_c} \right|^{1/m} sgn(\tau^{\alpha}) \tag{B.2}$$

By using Newton-Raphson approach, the resolution of the implicit problem for calculation of $\dot{\gamma^{\alpha}}_{t+\Delta t}$ is performed defining:

$$\mathbb{R}^{\alpha} = \Delta\gamma^{\alpha}_{t+\Delta t} - \dot{\gamma}^{\alpha}_{t+\Delta t}(\Delta\gamma^{\alpha}_{t+\Delta t})\Delta t \tag{B.3}$$

where $\mathbb{R}^{\alpha}$ is the residual of shear rate on each slip system α.

By using first order Taylor expansion of above equation, we obtain:

$$\mathbb{R}^{\alpha(k)} + \frac{\partial \mathbb{R}^{\alpha(k)}}{\partial \Delta\gamma^{\alpha(k)}_{t+\Delta t}}\ \delta\Delta\gamma^{\alpha(k)}_{t+\Delta t} = 0 \tag{B.4}$$

A new value of $\delta\Delta\gamma^{\alpha(k)}_{t+\Delta t}$ is calculated as

$$\delta\Delta\gamma^{\alpha(k)}_{t+\Delta t} = -\mathbb{R}^{\alpha(k)} \left(\frac{\partial \mathbb{R}^{\alpha(k)}}{\partial \Delta\gamma^{\alpha(k)}_{t+\Delta t}} \right)^{-1} \tag{B.5}$$

And using this value of $\delta\Delta\gamma^{\alpha(k)}_{t+\Delta t}$, the new value of $\Delta\gamma$ in iteration $k+1$ is given by:

$$\Delta\gamma^{\alpha(k+1)}_{t+\Delta t} = \Delta\gamma^{\alpha(k)}_{t+\Delta t} + \delta\Delta\gamma^{\alpha(k)}_{t+\Delta t} \tag{B.6}$$

This process is carried out until residual $\mathbb{R}^{\alpha}$ becomes less than a given value.

Solving previous equations using Newton-Raphson, requires the derivative of functions $\frac{\partial \mathbb{R}^{\alpha(k)}}{\partial \Delta\gamma^{\beta(k)}_{t+\Delta t}}$, and hence $\frac{\partial \dot{\gamma}^{\alpha(k)}_{t+\Delta t}(\Delta\gamma^{\alpha(k)}_{t+\Delta t})}{\partial \Delta\gamma^{\beta(k)}_{t+\Delta t}}$.

$$\frac{\partial \mathbb{R}^{\alpha(k)}}{\partial \Delta\gamma^{\beta(k)}_{t+\Delta t}} = \delta_{\alpha\beta} - \left(\frac{\partial \dot{\gamma}^{\alpha(k)}_{t+\Delta t}(\Delta\gamma^{\alpha(k)}_{t+\Delta t})}{\partial \Delta\gamma^{\beta(k)}_{t+\Delta t}} \right) \Delta t \; ; \qquad \delta_{\alpha\beta} = \begin{cases} 1 & \text{if } \alpha = \beta \\ 0 & \text{otherwise} \end{cases} \tag{B.7}$$

The derivative of this functions decides the stability and accuracy of the solution.

From now on and in order to simplify the notation, $\Delta\gamma^{\beta(k)}_{t+\Delta t}$ is represented as $\dot{\gamma}^{\alpha}(\Delta\gamma^{\alpha})$.

$\dot{\gamma}^{\alpha}(\Delta\gamma^{\alpha})$ is calculated as shown below:

$$\frac{\partial \dot{\gamma}^{\alpha}(\Delta\gamma^{\alpha})}{\partial \Delta\gamma^{\beta}} = \frac{\partial \dot{\gamma}^{\alpha}}{\partial \tau^{\alpha}} \frac{\partial \tau^{\alpha}}{\partial \Delta\gamma^{\beta}} + \frac{\partial \dot{\gamma}^{\alpha}}{\partial {\tau_c}^{\alpha}} \frac{\partial {\tau_c}^{\alpha}}{\partial \Delta\gamma^{\beta}} \tag{B.8}$$

Since $\dot{\gamma}^{\alpha}$ depends on τ^{α} and τ_c^{α}, each derivative are calculated separately.

The dependence of $\dot{\gamma}^{\alpha}$ on τ^{α} and other terms can be represented as :

$\dot{\gamma}^{\alpha} \Rightarrow \; \tau^{\alpha} \Rightarrow \; \mathbf{S} \Rightarrow \; \mathbf{F}_e \Rightarrow \; \mathbf{L}_p \Rightarrow \; \Delta\gamma^{\alpha}$

by using previous relations, the derivative of $\Delta\gamma^{\alpha}$ can be calculated as explained below:

The first derivative of $\Delta\gamma^{\alpha}$ with respect to τ^{α} and τ_c^{α} is calculated as:

$$\frac{\partial \dot{\gamma}^{\alpha}(\Delta\gamma^{\alpha})}{\partial \Delta\gamma^{\beta}} = \left[\frac{n \; \dot{\gamma}_0}{\tau_c^{\alpha}} \left| \frac{\tau^{\alpha}}{\tau_c^{\alpha}} \right|^{n-1} sgn(\tau^{\alpha}) \right] \left[\left[\frac{\partial \tau^{\alpha}}{\partial \mathbf{S}} : \frac{\partial \mathbf{S}}{\partial \mathbf{E}_e} : \frac{\partial \mathbf{E}_e}{\partial \Delta\gamma^{\beta}} \right] + \left[\frac{-1}{\tau_c^{\alpha}} \right] \left[\frac{\partial \tau_c^{\alpha}}{\partial \Delta\gamma^{\beta}} \right] \right] \tag{B.9}$$

Now each term in the above equation is solved separately. First $\Delta\gamma^{\alpha}$ is given w.r.t to the second Piola stress, later w.r.t to $\mathbf{F}_e$, and finally w.r.t to $\mathbf{L}_p$.

τ^{α} is related to second Piola stress $\mathbf{S}$ by :

$$\tau^{\alpha} = \; \mathbf{S}_{ij} \; (m_i^{\alpha} \otimes n_j^{\alpha}) \qquad\qquad (i,j = 1,2,3) \tag{B.10}$$

$\Delta\gamma^{\alpha}$ is given in terms of second Piola stress as :

$$\dot{\gamma}^{\alpha} = \dot{\gamma}_0 \left| \frac{\mathbf{S} : (m^{\alpha} \otimes n^{\alpha})}{\tau_c^{\alpha}} \right|^{n} sgn(\tau^{\alpha}) \tag{B.11}$$

The second Piola stress $\mathbf{S}$ is written in terms of the green Lagrange strain $\mathbf{E}_e$:

$$\mathbf{S}_{ij} = \mathbb{C}_{ijkl} \; \mathbf{E}_{ejk} \tag{B.12}$$

and the Green Lagrange strain $\mathbf{E}_e$ is given in terms of $\mathbf{F}_e$ as:

$$\mathbf{E}_e = \frac{1}{2}(\mathbf{F}_e^T \mathbf{F}_e - \mathbf{I}) \tag{B.13}$$

$\mathbf{F}_e$ is written in terms of $\mathbf{F}_p$ and $\mathbf{L}_p$ as:

$$\mathbf{F}_e = \mathbf{F}\mathbf{F}_{p_0}^{-1}(\mathbf{I} - \sum_{\alpha=1}^{nslip} \Delta\gamma^\alpha \ (m_i^\alpha \otimes n_j^\alpha) \tag{B.14}$$

$$\mathbf{F}_e = \mathbf{F}_{e_0}(\mathbf{I} - \sum_{\alpha=1}^{\text{nslip}} \Delta\gamma^\alpha \ (m_i^\alpha \otimes n_j^\alpha)) \tag{B.15}$$

$\Delta\gamma^\alpha$ in terms of $\mathbf{F}_e$ is given by :

$$\dot{\gamma}^\alpha = \dot{\gamma}_0 \left| \frac{\left[\mathbb{C} : \frac{1}{2}\left(\mathbf{F}_e^T\mathbf{F}_e - \mathbf{I}\right)\right] : (m^\alpha \otimes n^\alpha)}{\tau_c^\alpha} \right|^n sgn(\tau^\alpha) \tag{B.16}$$

with

$$\mathbf{F}_e^T\mathbf{F}_e = \left[\mathbf{F}^T\mathbf{F}_p^{-T} \left(\mathbf{I} - \sum_{\alpha}^{nslip} \Delta\gamma^\alpha (m^\alpha \otimes n^\alpha)\right)^T \left(\mathbf{I} - \sum_{\alpha}^{nslip} \Delta\gamma^\alpha (m^\alpha \otimes n^\alpha)\right)\mathbf{F}\mathbf{F}_p^{-1}\right] \tag{B.17}$$

The Newton Raphson solution can be obtained by solving and combining each differential separately.

The algorithm for calculating $\frac{\partial\left(\mathbf{F}_e^T\mathbf{F}_e \ (\text{i, j})\right)}{\partial\Delta\gamma^\alpha}$ is presented below:

Algorithm 1:

Result: $\frac{\partial\left(\mathbf{F}_e^T\mathbf{F}_e \ (\text{i, j})\right)}{\partial\Delta\gamma^\alpha}$

while *i = 1, 3 ;* **do**

  while *j = 1, 3 ;* **do**

    initialization $\frac{\partial\left(\mathbf{F}_e^T\mathbf{F}_e \ (\text{i, j})\right)}{\partial\Delta\gamma^\alpha} = 0$

    while *k = 1, 3 ;* **do**

$$\frac{\partial(\mathbf{F}_e^T\mathbf{F}_e(i,j))}{\partial\Delta\gamma^\alpha} \ += \left[\left[\left(\mathbf{F}_{e_0}(k,1:3)\ \mathbf{Smd}^\alpha(k:3,i)\ \mathbf{F}_e(k,j)\right) + \left(\mathbf{F}_{e_0}(k,1:3)\ \mathbf{Smd}^\alpha(1:3,j)\ \mathbf{F}_e(k,i)\right)\right]\right]$$

    end

  end

end

Now the algorithm for calculating $\frac{\partial\mathbf{S}(\text{nslip, i, j})}{\partial\Delta\gamma^\alpha}$ is presented below:

Algorithm 2: $\frac{\partial \mathbf{S}(\text{nslip, i, j})}{\partial \Delta\gamma^{\alpha}}$:

while *is = 1, nslip ;* **do**
  while *i = 1, 3 ;* **do**
    while *j = 1, 3 ;* **do**
      initialization $\frac{\partial\left(\mathbf{F}_e^T\mathbf{F}_e\ (is,i,j)\right)}{\partial\Delta\gamma^{\alpha}} = 0$
      while *k = 1, 3 ;* **do**

$$\frac{\partial(\mathbf{F}_e^T\mathbf{F}_e(is,i,j))}{\partial\Delta\gamma^{\alpha}} \mathrel{+}= \Big[\Big[\Big(\mathbf{F}_{e_0}(k,1:3)\ \mathbf{Smd}^{\alpha}(is,k:3,i)\ \mathbf{F}_e(k,j)\Big) + \Big(\mathbf{F}_{e_0}(k,1:3)\ \mathbf{Smd}^{\alpha}(is,1:3,j)\ \mathbf{F}_e(k,i)\Big)\Big]\Big]$$

      end
    end
  end
  $\frac{\partial(\mathbf{E}_e(is,\ :,\ :))}{\partial\Delta\gamma^{\alpha}} = -\frac{\partial(\mathbf{F}_e^T\mathbf{F}_e(is,\ :,\ :))}{2\partial\Delta\gamma^{\alpha}}$
  $\frac{\partial(\mathbf{S}\ (is,\ :,\ :))}{\partial\Delta\gamma^{\alpha}} = \mathbb{C} : \frac{\partial\mathbf{E}_e\ (is,\ :,\ :)}{\partial\Delta\gamma^{\alpha}}$
end

The algorithm for calculating $\frac{\partial\tau^i}{\partial\Delta\gamma^j}$ is presented below:

Algorithm 3:

Result: $\frac{\partial\tau^i}{\partial\Delta\gamma^j}$
while *is = 1, nslip ;* **do**
  while *js = 1, nslip ;* **do**
    initialization $\frac{\partial\tau(i,\ j)}{\partial\Delta\gamma} = 0$

$$\frac{\partial\tau(is,\ js)}{\partial\Delta\gamma} = \frac{\partial\mathbf{S}\ (js,1:3,1:3)}{\partial\Delta\gamma}\ :\ \mathbf{Smd}(is,1:3,1:3)$$

  end
end

Jacobian Matrix calculation

In this appendix, we present the numerical implementation of the Jacobian matrix necessary to achieve quadratic convergence of the global solution procedure within the finite element solver ABAQUS/Standard (2019). Equations necessary for obtaining Jacobian matrix and its related operations are adopted following the work of Meissonnier et al. (2001).

In order to solve the non-linear behaviour of the material considering an implicit finite element procedure, the Newton-Raphson method has been adopted here. For a successful implementation, the proper Jacobian needs to be established, which should be consistent with the time integration procedure used for the constitutive modelling. For the fully implicit backward Euler integration scheme used in this work, analytical Jacobian in the form of $\frac{d\sigma}{d\varepsilon}$ is presented in the section below.

Starting from the definition of Second-Piola stress, the derivative of σ with respect to ε is obtained. Second Piola stress is split into $\mathbf{S}_{ij}^{tr}$ trial stress and $\mathbf{S}_{cal}$ calculated stress as shown below:

$$\mathbf{S}_{ij} = \mathbf{S}_{ij}^{tr} - \sum_{\alpha=1}^{\text{nslip}} \Delta\gamma^{\alpha}\mathbb{K}_{ij}^{\alpha} \tag{C.1}$$

Trial Second Piola stress $\mathbf{S}_{ij}^{tr}$ is the linear part of the stress with Schmid matrix, given by:

$$\mathbf{S}_{ij}^{tr} = \frac{\mathbb{C}_{ijkl}}{2}(\mathbb{A} - \mathbf{I})_{kl} \tag{C.2}$$

$$\mathbb{K}_{ij}^{\alpha} = \frac{\mathbb{C}_{ijkl}}{2}(\mathbb{A}\ \mathbf{Smd}^{\alpha} + \mathbf{Smd}^{\alpha T}\mathbb{A})_{kl} \tag{C.3}$$

with constant $\mathbb{A}_{ij}$ defined by:

$$\mathbb{A}_{ij} = \mathbf{F}_{p_n}^{-T}\mathbf{F}^{T}\mathbf{F}\mathbf{F}_{p_n}^{-1} \tag{C.4}$$

$$\mathbf{F}_{p} = \mathbf{F}_{p_n}(\mathbf{I} + \sum_{\alpha=1}^{\text{nslip}} \Delta\gamma^{\alpha}\mathbf{Smd}^{\alpha}) \tag{C.5}$$

For solving $\frac{d\sigma}{d\varepsilon}$, first we need to solve $\frac{\partial \mathbf{F}_p}{\partial \mathbf{E}}$ and $\frac{\partial \mathbf{S}}{\partial \mathbf{E}}$. The $\frac{\partial \mathbf{F}_p}{\partial \mathbf{E}}$ term has the form:

$$\frac{\partial \mathbf{F}_p}{\partial \mathbf{E}} = \sum_{\alpha=1}^{\text{nslip}} (\mathbf{F}_{p_n} \mathbf{Smd}^\alpha) \otimes \frac{\partial \Delta\gamma^\alpha}{\partial \mathbf{E}} \tag{C.6}$$

with $\frac{\partial \Delta\gamma^\alpha}{\partial \mathbf{E}}$ given by the equation shown below:

$$\frac{\partial \Delta\gamma^\alpha}{\partial \mathbf{E}} = \frac{\partial \Delta\gamma^\alpha}{\partial \mathbf{S}} : \underbrace{\frac{\partial \mathbf{S}}{\partial \mathbf{E}}}_{\text{calculated}} + \frac{\partial \Delta\gamma^\alpha}{\partial \tau_c^\alpha} : \underbrace{\frac{\partial \tau_c^\alpha}{\partial \mathbf{E}}}_{\text{neglected}} \tag{C.7}$$

For the calculation of $\frac{\partial \Delta\gamma^\alpha}{\partial \mathbf{E}}$, we need to obtain $\frac{\partial \mathbf{S}}{\partial \mathbf{E}}$ and $\underbrace{\frac{\partial \tau_c^\alpha}{\partial \mathbf{E}}}$. Here only the differential of $\mathbf{S}$ w.r.t to $\mathbf{E}$ is calculated and the derivative of τ_c^α w.r.t to $\mathbf{E}$ is neglected in order to simplify the calculations.

Now, by using the definition of $\mathbf{S}$, its derivative w.r.t $\mathbf{E}$ is calculated as shown below:

$$\frac{\partial \mathbf{S}}{\partial \mathbf{E}} = \frac{\partial \mathbf{S}^{tr}}{\partial \mathbf{E}} - \left[\sum_{\alpha=1}^{\text{nslip}} \frac{\partial \Delta\gamma^\alpha}{\partial \mathbf{E}} \mathbb{K}_{ij}^\alpha + \sum_{\alpha=1}^{\text{nslip}} \Delta\gamma^\alpha \frac{\partial \mathbb{K}_{ij}^\alpha}{\partial \mathbf{E}} \right] \tag{C.8}$$

Since the expression of $\mathbf{S}$ depends on the value of $\Delta\gamma^\alpha$, which intern depends on $\mathbf{S}$:

$$\frac{\partial \mathbf{S}}{\partial \mathbf{E}} = \left[\frac{\partial \mathbf{S}^{tr}}{\partial \mathbf{E}} - \sum_{\alpha=1}^{\text{nslip}} \Delta\gamma^\alpha \frac{\partial \mathbb{K}_{ij}^\alpha}{\partial \mathbf{E}} \right] - \sum_{\alpha=1}^{\text{nslip}} \underbrace{\frac{\partial \Delta\gamma^\alpha}{\partial \mathbf{E}}}_{(\frac{\partial \Delta\gamma^\alpha}{\partial \mathbf{S}} : \frac{\partial \mathbf{S}}{\partial \mathbf{E}})} \mathbb{K}_{ij}^\alpha \tag{C.9}$$

we end up with the expression $\frac{\partial \mathbf{S}}{\partial \mathbf{E}}$ on both left hand side and right hand side of the equation:

$$\frac{\partial \mathbf{S}}{\partial \mathbf{E}} = \left[\frac{\partial \mathbf{S}^{tr}}{\partial \mathbf{E}} - \sum_{\alpha=1}^{\text{nslip}} \Delta\gamma^\alpha \frac{\partial \mathbb{K}_{ij}^\alpha}{\partial \mathbf{E}} \right] - \sum_{\alpha=1}^{\text{nslip}} (\frac{\partial \Delta\gamma^\alpha}{\partial \mathbf{S}} : \frac{\partial \mathbf{S}}{\partial \mathbf{E}}) \mathbb{K}_{ij}^\alpha \tag{C.10}$$

Now by rearranging terms, we get:

$$\frac{\partial \mathbf{S}}{\partial \mathbf{E}} = \left[\frac{\partial \mathbf{S}^{tr}}{\partial \mathbf{E}} - \sum_{\alpha=1}^{\text{nslip}} \Delta\gamma^\alpha \frac{\partial \mathbb{K}_{ij}^\alpha}{\partial \mathbf{E}} \right] - \sum_{\alpha=1}^{\text{nslip}} (\frac{\partial \Delta\gamma^\alpha}{\partial \mathbf{S}} \otimes \mathbb{K}_{ij}^\alpha) : \frac{\partial \mathbf{S}}{\partial \mathbf{E}} \tag{C.11}$$

$$\frac{\partial \mathbf{S}}{\partial \mathbf{E}} + \sum_{\alpha=1}^{\text{nslip}} (\frac{\partial \Delta\gamma^\alpha}{\partial \mathbf{S}} \otimes \mathbb{K}_{ij}^\alpha) : \frac{\partial \mathbf{S}}{\partial \mathbf{E}} = \left[\frac{\partial \mathbf{S}^{tr}}{\partial \mathbf{E}} - \sum_{\alpha=1}^{\text{nslip}} \Delta\gamma^\alpha \frac{\partial \mathbb{K}_{ij}^\alpha}{\partial \mathbf{E}} \right] \tag{C.12}$$

$$\left[\mathbf{I} + \sum_{\alpha=1}^{\text{nslip}} (\frac{\partial \Delta\gamma^\alpha}{\partial \mathbf{S}} \otimes \mathbb{K}_{ij}^\alpha) : \mathbf{I} \right] \frac{\partial \mathbf{S}}{\partial \mathbf{E}} = \left[\frac{\partial \mathbf{S}^{tr}}{\partial \mathbf{E}} - \sum_{\alpha=1}^{\text{nslip}} \Delta\gamma^\alpha \frac{\partial \mathbb{K}_{ij}^\alpha}{\partial \mathbf{E}} \right] \tag{C.13}$$

$$\frac{\partial \mathbf{S}}{\partial \mathbf{E}} = \left[\mathbf{I} + \sum_{\alpha=1}^{\text{nslip}} (\frac{\partial \Delta\gamma^\alpha}{\partial \mathbf{S}} \otimes \mathbb{K}_{ij}^\alpha) : \mathbf{I} \right]^{-1} \left[\frac{\partial \mathbf{S}^{tr}}{\partial \mathbf{E}} - \sum_{\alpha=1}^{\text{nslip}} \Delta\gamma^\alpha \frac{\partial \mathbb{K}_{ij}^\alpha}{\partial \mathbf{E}} \right] \tag{C.14}$$

Now to complete the calculations of $\frac{\partial \mathbf{S}}{\partial \mathbf{E}}$, we need to calculate $\frac{\partial \mathbf{S}^{tr}}{\partial \mathbf{E}}$ and $\frac{\partial \mathbb{K}^\alpha}{\partial \mathbf{E}}$.

By using the definition of $\mathbf{S}^{tr}$ we get $\frac{\partial \mathbf{S}^{tr}}{\partial \mathbf{E}}$ as

$$\frac{\partial \mathbf{S}^{tr}}{\partial \mathbf{E}} = \mathbb{C} : (\mathbf{F}_{p_n}^{-1} \underline{\otimes} \mathbf{F}_{p_n}^{-1}) \tag{C.15}$$

Finally $\frac{\partial \mathbb{K}^{\alpha}}{\partial \mathbf{E}}$ can be calculated as:

$$\frac{\partial \mathbb{K}^{\alpha}}{\partial \mathbf{E}} = \mathbb{C} : \left[(\mathbf{F}_{p_n}^{-T} \underline{\otimes} (\mathbf{F}_{p_n}^{-1} \mathbf{Smd}^{\alpha})^T + (\mathbf{F}_{p_n}^{-1} \mathbf{Smd}^{\alpha})^T \underline{\otimes} \mathbf{F}_{p_n}^{-T} \right] \tag{C.16}$$

With equations C.15 and C.16 in equation C.14 we are able to find the final expression for $\frac{\partial \mathbf{S}}{\partial \mathbf{E}}$

For computing the tangent stiffness matrix, ABAQUS/Standard (2019) requires an updated Cauchy stress tensor and an updated material Jacobian using the Jaumann rate of the Cauchy stress. Meissonnier et al. (2001) showed that it is possible to define the Jaumann rate of the Cauchy stress as

$$\boldsymbol{C}^{JC} = \frac{1}{J} \left[\boldsymbol{F} \underline{\otimes} \boldsymbol{F} : \frac{\partial \boldsymbol{S}}{\partial \boldsymbol{E}} : \boldsymbol{F} \underline{\otimes} \boldsymbol{F} \right] + \mathbf{I} \underline{\otimes} \boldsymbol{\sigma}^T + \boldsymbol{\sigma} \overline{\otimes} \mathbf{I} - \frac{1}{J} \boldsymbol{\sigma} \otimes \mathbf{I} \tag{C.17}$$

where $\underline{\otimes}, \overline{\otimes}$ are defined as lower dyadic and upper dyadic products as defined in Meissonnier et al. (2001).

By substituting $\frac{\partial \mathbf{S}}{\partial \mathbf{E}}$ in equation C.17 and following suitable operations we can calculate the consistent tangent matrix required by ABAQUS/Standard (2019).

Prescribed boundary conditions

In this appendix, we present a brief description of the boundary conditions applied for the unit cells. Fully periodic boundary conditions and controlled stress state are applied for all cell calculations in Chapter 3, Chapter 4 and Chapter 5. Multi point constrain (MPC), which is implemented as a subroutine in ABAQUS/Standard (2019) is presented with necessary equations to maintain constant stress triaxiality and Lode parameter in the unit cell. All equations necessary for implementing periodic boundary conditions in the unit cell are also detailed here.

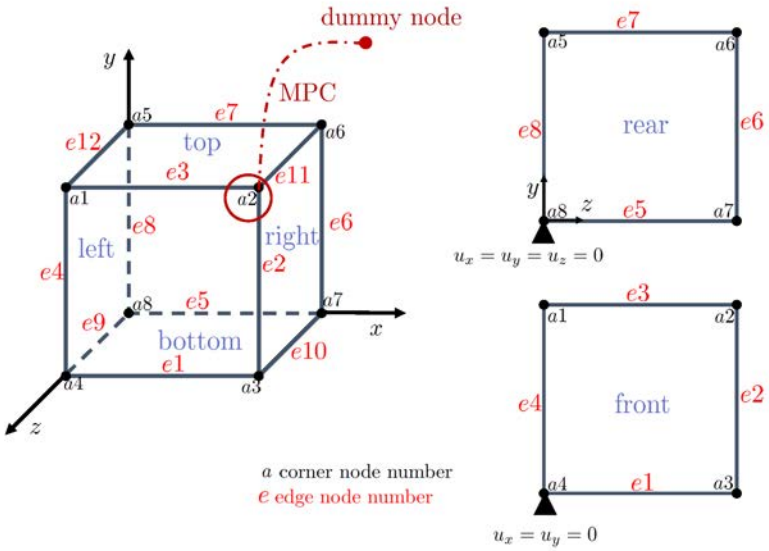

Figure D.1: *Periodic boundary conditions applied to the 3D cell.*

Boundary conditions applied for a representative volume element is described in detail in this appendix. In the undeformed cell, the edges of the cell are aligned along the coordinate axes (X, Y, Z), and the origin of the reference coordinate system corresponds to the node $a6$ (see Figure D.1). The faces of the cell are initially straight and the nodes on the opposite faces are connected in order to obtain a periodic response from the cell. Apart from the periodic response, in the present work, constant values of stress triaxiality and Lode parameter are applied to the cell. The procedure to prescribe loading to keep constant values of macroscopic

stress triaxiality and Lode parameter throughout the deformation history follows the work of Vadillo et al. (2016).

D.1 Defining multipoint constraints

If the ratio of principal macroscopic true stress R and Q are defined in the form:

$$R = \frac{\sigma_2}{\sigma_1}; \qquad Q = \frac{\sigma_3}{\sigma_1}; \tag{D.1}$$

triaxiality T and Lode parameter L (Eq. (2.43)) can be written as:

$$T = \frac{\sqrt{2}(R+Q+1)}{3\sqrt{(1-R^2)+(1-Q^2)+(R^2-Q^2)}}; \quad L = \frac{2R-Q-1}{1-Q} \tag{D.2}$$

Since the macroscopic principal true stresses (σ_1, σ_2, σ_3) and the normal components of macroscopic strain rate in the basis of stress principal directions ($\dot{\varepsilon}_{11}$, $\dot{\varepsilon}_{22}$, $\dot{\varepsilon}_{33}$) are equal to the volume average values in a cell (Hill (1967)), the total rate of deformation work in the whole cell $\dot{W}$ can be written as:

$$\dot{W} = V\sigma_1\dot{\varepsilon}_{11} + V\sigma_2\dot{\varepsilon}_{22} + V\sigma_3\dot{\varepsilon}_{33} \tag{D.3}$$

$\dot{W}$ can be also expressed in terms of the transformed rates of deformation and forces, as:

$$\dot{W} = V\sigma_{(I)}\dot{\varepsilon}_{(I)} + V\sigma_{(II)}\dot{\varepsilon}_{(II)} + V\sigma_{(III)}\dot{\varepsilon}_{(III)} \tag{D.4}$$

considering the transformation

$$\begin{pmatrix} \dot{\varepsilon}_{(I)} \\ \dot{\varepsilon}_{(II)} \\ \dot{\varepsilon}_{(III)} \end{pmatrix} = \mathbf{N} \begin{pmatrix} \dot{\varepsilon}_{11} \\ \dot{\varepsilon}_{22} \\ \dot{\varepsilon}_{33} \end{pmatrix}; \quad \begin{pmatrix} \sigma_{(I)} \\ \sigma_{(II)} \\ \sigma_{(III)} \end{pmatrix} = \mathbf{N} \begin{pmatrix} \sigma_1 \\ \sigma_2 \\ \sigma_3 \end{pmatrix}; \quad \text{with } \mathbf{N} = \begin{pmatrix} A_{11} & A_{12} & A_{13} \\ A_{21} & A_{22} & A_{23} \\ A_{31} & A_{32} & A_{33} \end{pmatrix}; \tag{D.5}$$

and:

$$\begin{aligned} A_{11} &= \frac{1}{\sqrt{1+R^2+Q^2}}; \quad A_{12} = \frac{R}{\sqrt{1+R^2+Q^2}}; \quad A_{13} = \frac{Q}{\sqrt{1+R^2+Q^2}} \\ A_{21} &= -\frac{R}{\sqrt{1+R^2}}; \quad A_{22} = \frac{1}{\sqrt{1+R^2}}; \quad A_{23} = 0. \\ A_{31} &= \frac{Q}{\sqrt{(1+R^2)(1+R^2+Q^2)}}; \quad A_{32} = \frac{RQ}{\sqrt{(1+R^2)(1+R^2+Q^2)}} \\ A_{33} &= -\frac{(1+R^2)}{\sqrt{(1+R^2)(1+R^2+Q^2)}} \end{aligned} \tag{D.6}$$

If in the transformed coordinate system, the three imposed incremental boundary conditions are prescribed as stress uniaxial:

$$\sigma_{(II)} = 0; \quad \sigma_{(III)} = 0; \quad \dot{\varepsilon}_{(I)} = \dot{\varepsilon}_{dummy} \tag{D.7}$$

the three prescribed boundary conditions in 1,2,3 directions, using $\mathbf{N}^{-1}$ relations are therefore:

$$R\sigma_1 - \sigma_2 = 0; \qquad Q\sigma_1 - \sigma_3 = 0; \qquad \dot{\varepsilon}_{11} + R\dot{\varepsilon}_{22} + Q\dot{\varepsilon}_{33} = \dot{\varepsilon}_{dummy}\sqrt{1 + R^2 + Q^2} \tag{D.8}$$

Values of $\dot{\varepsilon}_{11}$, $\dot{\varepsilon}_{22}$, $\dot{\varepsilon}_{33}$ and hence stress states (T and L) can be controlled in the cell by fixing properly values R and Q and prescribing incremental strain on an added dummy node. The multi-point constraints given in equations D.6, D.8 are implemented into ABAQUS/Standard (2019) via a user defined subroutine MPC.

D.2 Defining periodic boundary conditions

Due to the anisotropy of the problem, and in order to determine a proper deformation behavior of the cell, periodic boundary conditions should be adopted in the external surfaces of the cell in all three directions. In this work, the general ideas of the implementation of periodic boundary conditions into a Finite Element solver as given in Segurado et al. (2002) is adopted. For the implementation of periodic boundary conditions, it is necessary to couple the displacements of opposite external nodes, on which an average macroscopic strain is allowed.

For simplicity and easy implementation, nodes on the surfaces of the cell are categorized into 3 different groups: corner nodes, edge nodes and surface nodes (see figure D.1 for nomenclature details).

The node $a2$ is connected to the dummy node by the MPC subroutine, through which the average strains are applied to the system. This means that any deformation that is applied to the cell through the MPC has to be applied only connecting $a2$ to the added dummy node. In order to prescribe displacements in the outer surfaces which ensure periodicity:

$$u_i^{k+} - u_i^{k-} = E_{ij}\Delta x_j; \quad i,j = 1,2,3; \quad \Delta x_j = x_j^{k+} - x_j^{k-}; \quad \mathbf{t}^+ - \mathbf{t}^- = 0; \quad \mathbf{t} = \sigma.\mathbf{n} \tag{D.9}$$

being E_{ij} the macroscopic strain tensor and x_j the position vector, the following set of relations should be applied to the external nodes of the cell in order to avoid constraint linkages. These conditions are implemented in ABAQUS/Standard (2019) by the use of the command *Equation .

1. *For nodes on the faces of the cell:*

$$u^{Top}(x,y,z) - u^{Bottom}(x,y,z) = u^{a_5}(x,y,z) - u^{a_8}(x,y,z)$$
$$u^{Rear}(x,y,z) - u^{Front}(x,y,z) = u^{a_8}(x,y,z) - u^{a_4}(x,y,z)$$
$$u^{Left}(x,y,z) - u^{Right}(x,y,z) = u^{a_8}(x,y,z) - u^{a_7}(x,y,z)$$

2. *For nodes on the edges of the cell:*

$$
\begin{aligned}
u^{e_7}(x,y,z) - u^{e_3}(x,y,z) &= u^{a_8}(x,y,z) - u^{a_4}(x,y,z) \\
u^{e_3}(x,y,z) - u^{e_1}(x,y,z) &= u^{a_5}(x,y,z) - u^{a_8}(x,y,z) \\
u^{e_1}(x,y,z) - u^{e_5}(x,y,z) &= u^{a_4}(x,y,z) - u^{a_8}(x,y,z)
\end{aligned}
$$

$$
\begin{aligned}
u^{e_{12}}(x,y,z) - u^{e_{11}}(x,y,z) &= u^{a_8}(x,y,z) - u^{a_7}(x,y,z) \\
u^{e_{11}}(x,y,z) - u^{e_{10}}(x,y,z) &= u^{a_5}(x,y,z) - u^{a_8}(x,y,z) \\
u^{e_{10}}(x,y,z) - u^{e_9}(x,y,z) &= u^{a_7}(x,y,z) - u^{a_8}(x,y,z)
\end{aligned}
$$

$$
\begin{aligned}
u^{e_8}(x,y,z) - u^{e_4}(x,y,z) &= u^{a_8}(x,y,z) - u^{a_4}(x,y,z) \\
u^{e_4}(x,y,z) - u^{e_2}(x,y,z) &= u^{a_8}(x,y,z) - u^{a_7}(x,y,z) \\
u^{e_2}(x,y,z) - u^{e_6}(x,y,z) &= u^{a_4}(x,y,z) - u^{a_8}(x,y,z)
\end{aligned}
$$

3. *For nodes on the corner of the cell:*

$$
\begin{aligned}
&u_x^{a_6} = u_x^{a_7}; \quad u_x^{a_3} = u_x^{a_2}; \quad u_x^{a_7} = u_x^{a_3}; \quad u_x^{a_1} = u_x^{a_4}; \\
&u_y^{a_3} = u_y^{a_4}; \quad u_y^{a_1} = u_y^{a_2}; \quad u_y^{a_5} = u_y^{a_1}; \quad u_y^{a_6} = u_y^{a_5}; \\
&u_z^{a_1} = u_z^{a_4}; \quad u_z^{a_4} = u_z^{a_2}; \quad u_z^{a_7} = u_z^{a_6}; \quad u_z^{a_3} = u_z^{a_2}; \\
&u_{x,y,z}^{a_8} = 0; \quad u_{x,y}^{a_4} = 0;
\end{aligned}
$$

Euler angles and Orientation matrix

In this appendix, we discuss a simple technique to find all possible Euler angles from a rotation matrix. Euler angles with Bunge convention are commonly used for describing the orientations of each crystal.

E.1 Introduction

Crystallographic orientation can be referred as the position of a grain/ crystal with respect to a reference position. In three-dimension we require three independent variables or a crystallographic plane which comprises two independent variables.

E.2 Euler angle

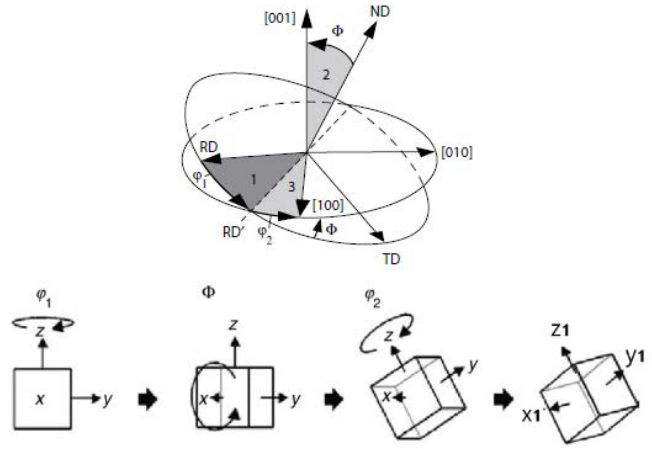

Figure E.1: *Diagram showing rotation through the Euler angles* ϕ_1, Φ, ϕ_2, *describing the rotation between the specimen and crystal axes*

A well known method for expressing crystallographic orientation is by using Euler angles. The Euler angles refer to three rotations that, when performed in the correct sequence, transform the specimen coordinate system onto the crystal coordinate system as shown in figure E.1. The most common notation for expressing Euler angles was formulated by Bunge (Bunge, 1965; Esling and Bunge., 1982) .

For example, going from a sample reference basis (x, y, z) to a sample rotated basis (x_1, y_1, z_1) three subsequent rotations are necessary, and are referred by notation ϕ_1, Φ, ϕ_2 respectively. The rotations can be summed up as follows:

$$(x, y, z) \xrightarrow[\phi_1]{\text{z axis}} (u, v, w) \xrightarrow[\Phi]{\text{u axis}} (u, w, z_1) \xrightarrow[\phi_1]{\text{z}_1\text{axis}} (x_1, y_1, z_1)$$

Where the range of $\phi_1 \in (0, 2\pi)$, $\Phi \in (0, \pi)$, $\phi_2 \in (0, 2\pi)$.
Having specified the three rotations, now we can build the rotation matrix $\mathbf{g}$ with respect to the three Euler angles:

$$\mathbf{g}(\phi_1, \Phi, \phi_2) = g_3(\phi_2) g_2(\Phi) g_1(\phi_1)$$

$$g_1(\phi_1) = \begin{bmatrix} \cos(\phi_1) & \sin(\phi_1) & 0 \\ \text{-sin}(\phi_1) & \cos(\phi_1) & 0 \\ 0 & 0 & 1 \end{bmatrix}$$

$$g_2(\Phi) = \begin{bmatrix} 1 & 0 & 0 \\ 0 & \cos(\Phi) & \sin(\Phi) \\ 0 & \text{-sin}(\Phi) & \cos(\Phi) \end{bmatrix}$$

$$g_3(\phi_2) = \begin{bmatrix} \cos(\phi_2) & \sin(\phi_2) & 0 \\ \text{-sin}(\phi_2) & \cos(\phi_2) & 0 \\ 0 & 0 & 1 \end{bmatrix}$$

$$\mathbf{g}(\phi_1, \Phi, \phi_2) =$$
$$\begin{bmatrix} \cos(\phi_1)\cos(\phi_2) - \sin(\phi_1)\sin(\phi_2)\cos(\Phi) & \sin(\phi_1)\cos(\phi_2) + \cos(\phi_1)\sin(\phi_2)\cos(\Phi) & \sin(\phi_2)\sin(\Phi) \\ -\cos(\phi_1)\sin(\phi_2) - \sin(\phi_1)\cos(\phi_2)\cos(\Phi) & -\sin(\phi_1)\sin(\phi_2) + \cos(\phi_1)\cos(\phi_2)\cos(\Phi) & \cos(\phi_2)\sin(\Phi) \\ \sin(\phi_1)\sin(\Phi) & -\cos(\phi_1)\sin(\Phi) & \cos(\Phi) \end{bmatrix}$$

By using orientation matrix $\mathbf{g}$, we can calculate Euler angles if we know direction cosine (crystal plane normal (hkl) and direction $[uvw]$) or vice versa.

E.3 Calculating Euler angles from Orientation matrix

For calculating Euler angles from direction cosines, first we have to build orientation matrix $\mathbf{g}$ following the procedure mentioned below:

$$\hat{\mathbf{n}} = \frac{(h,k,l)}{\sqrt{h^2+k^2+l^2}}$$

$$\hat{\mathbf{b}} = \frac{(u,v,w)}{\sqrt{u^2+v^2+w^2}}$$

$$\hat{\mathbf{t}} = \frac{\hat{\mathbf{n}} \times \hat{\mathbf{b}}}{| \hat{\mathbf{n}} \times \hat{\mathbf{b}} |}$$

$$\mathbf{g}_{ij} = \text{Crystal} \begin{bmatrix} b_1 & t_1 & n_1 \\ b_2 & t_2 & n_2 \\ b_3 & t_3 & n_3 \end{bmatrix}^{\text{Sample}}$$

$$\mathbf{g}_{ij} = \text{Crystal} \begin{bmatrix} b_1 & t_1 & n_1 \\ b_2 & t_2 & n_2 \\ b_3 & t_3 & n_3 \end{bmatrix}^{\text{RD TD ND}} \tag{E.1}$$

once the **g** matrix is constructed, we can calculate the Euler angles by two ways: First one is by directly using miller indices:

$$cos\Phi = \frac{\text{l}}{\sqrt{h^2 + k^2 + l^2}} \tag{E.2}$$

$$\text{sin}\phi_1 = \frac{\text{w}}{\sqrt{u^2 + v^2 + w^2}} \frac{\sqrt{h^2 + k^2 + l^2}}{\sqrt{h^2 + k^2}} \tag{E.3}$$

$$\text{cos}\phi_2 = \frac{\text{k}}{\sqrt{h^2 + k^2}} \tag{E.4}$$

Another way of calculating Euler angles from **g** matrix is by using the formulation:

$$cos\Phi = g_{33} \tag{E.5}$$

$$tan\phi_1 = \frac{-g_{31}}{g_{32}} \tag{E.6}$$

$$tan\phi_2 = \frac{g_{13}}{g_{23}} \tag{E.7}$$

E.3.1 Sample1 : Euler angle calculation from direction cosines

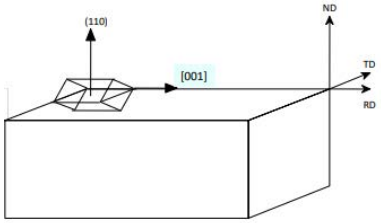

Figure E.2: *Diagram showing crystal in global reference plane with ND, TD, RD.*

In this section, an example is presented of how to calculate Euler angles from direction cosines. Figure E.2 shows an example of Crystal orientation in which (011) plane is oriented towards the ND and the [001] inside the (011) plane is along the RD.

Now we will first construct **g** matrix as shown in equation E.1 with miller indices. The **g** matrix for the above case is :

$$g = \begin{bmatrix} 1 & 0 & b \\ 0 & \frac{1}{\sqrt{2}} & \frac{1}{\sqrt{2}} \\ 0 & -\frac{1}{\sqrt{2}} & \frac{1}{\sqrt{2}} \end{bmatrix}$$

Following equations E.5, E.6 ,E.7, we find that Euler angles are : $\Phi = 45°;\ \phi_1 = 0°;\ \phi_2 = 0°$.

Calculating void volume in RVE

In this appendix, we present convex hull algorithm in order to calculate void volume during deformation of the representative unit cell. Void volume calculation will be used for both single crystals and bi-crystals analysis.

F.1 Void volume calculation for symmetric/isotropic orientations

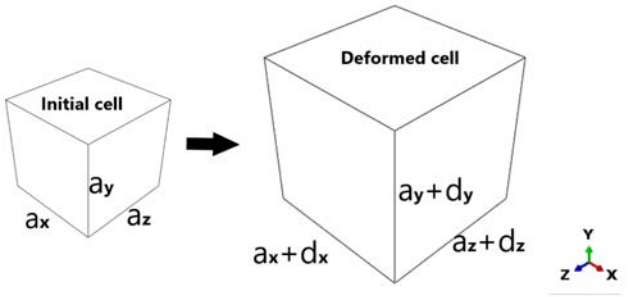

Figure F.1: *Representation of cell volume before and after deformation in isotropic orientations*

In symmetric/isotropic orientations, void volume is calculated as the difference between the volume of the cell and the volume of the matrix, i.e., $V_v = V_{cell} - V_{matrix}$, where V_{cell} is the current volume of the cell and V_{matrix} is the current volume of the matrix (current sum of the volume of all the elements in the cell). V_{cell} is calculated as $(a_x + d_x) \cdot (a_y + d_y) \cdot (a_z + d_z)$, where a_x, a_y, a_z are the initial width of the cell in x, y, z directions and d_x, d_y, d_z are the displacements applied at each increment in respective directions as shown in figure F.1. For symmetric orientations (O1, O2) there exist a crystal reflection symmetry about coordinate planes normal to <100> and <110> and also cell faces remain straight through out the deformation, hence calculating void volume fraction evolution is straight forward using the method mentioned above.

F.2 Void volume calculation for non-symmetric/ anisotropic orientation

For non symmetric orientations (O4, O6), the initially straight sides of the unit cell (along which fully periodic conditions are applied) becomes curved during loading. The cell faces will not be straight during deformation that makes void volume calculation difficult. To overcome the problem of calculating void volume, the convex-hull algorithm approach has been adopted in this work.

F.2.1 Convex-hull algorithm

In this work, the 3D (x, y, z) coordinates of all the nodes on the surface of the void (initially spherical) are extracted from the finite element calculations for all the time steps using ABAQUS/Standard (2019). By using these coordinates, void volume is calculated at each time increment with the help of convex hull algorithm. With this approach, we can directly calculate the volume of the void at any given time in the simulations.

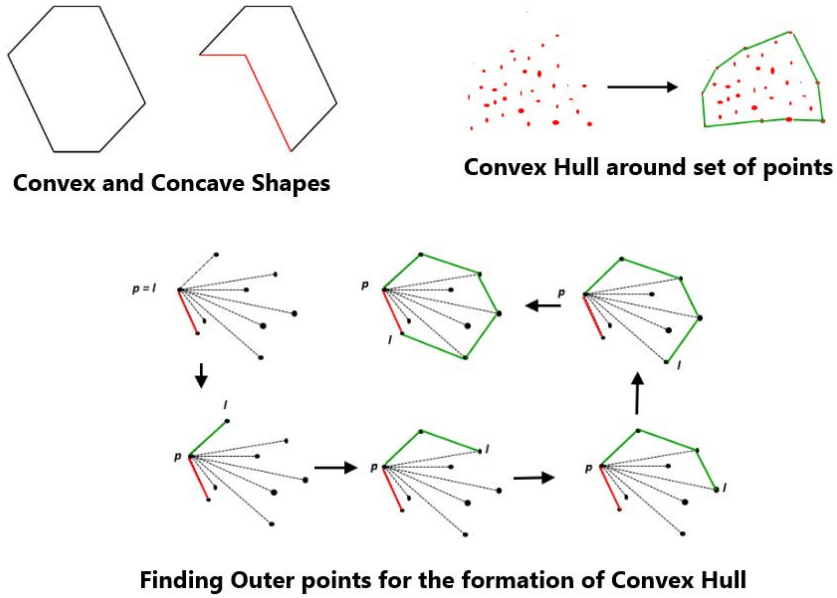

Figure F.2: *Representation of convex hull formation around a given set of points.*

The convex hull of a set of points is defined as the smallest convex polygon that encloses all of the points in the set. Here convex means that the polygon has no corner that is bent inwards. Figure F.2 shows an illustration of convex and non convex edges. Left side figure shows convex corners and right side figure shows a non convex side (coloured red). Given a set of points, finding a convex polygon that encloses all the points is not straight forward.

Any algorithm used to find the convex hull of a set of points, basically should find the subset of points that lie on the convex hull, along with the order in which these points are encountered when going around the convex hull.

The basic principle behind working of algorithm is to go around the sorted array consisting of coordinates of all the points and determining if the points lie on the surface/convex hull. For every 3 set of points we encounter, we check if they form a convex or a concave corner.We ignore the corners that are concave, as the middle point of this set cannot lie on the convex hull. By this way we remove the points that does not belong to the convex hull. The measurement of whether corner bending can be calculated by the cross product and if the product turns out to be positive then the corner is bending inwards and if its negative then the bending is outwards. Looking at figure F.2, which shows set of points having a convex corner, we keep the middle point out of these three points and by following same procedure for all the points we can find the convex hull of given set of points.

Once the outer surface of the points is calculated with convex hull, we can calculate its volume (3D) or area (2D) by integration of the small regions. MATLAB (2010) and Python (2021) have existing libraries for finding convex hull of a set of points and also to calculate area (2D) or volume (3D). In this work python libraries are used extensively for calculating the convex hull and hence the volume of a set of points. With the help of convex hull, we can directly calculate the volume of a void at any given point in the simulations even when cell faces get irregular shapes.

Digital Image Correlation technique

In this appendix, we present a brief description of Digital Image Correlation technique (DIC) extensively used in chapter 6. DIC is used for measuring strains on the surface of the specimen. Definition of strains and how strains are calculated are presented in this appendix.

G.1 Introduction

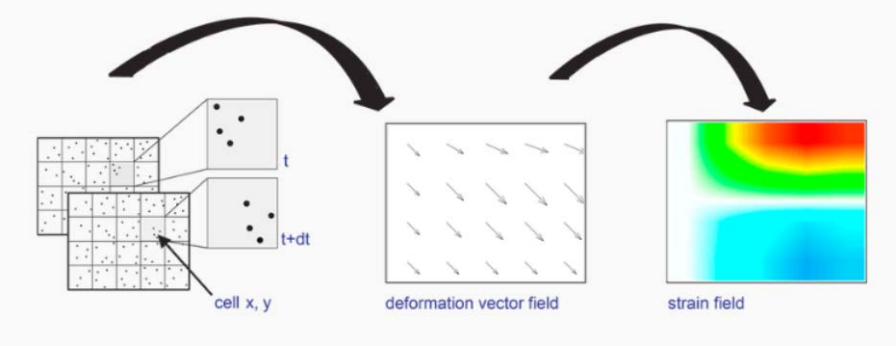

Figure G.1: *Representation of digital image correlation process*[0]

Measurement of surface deformation and strains of specimens during testing is an important part of the experimental study made in this work. Non-interferometric optical techniques such as grid method and DIC have grown in the current days in order to extract this information. Digital image correlation (often referred as "DIC") is a powerful flexible tool for measuring surface deformation in solid mechanics and extracting displacement and strain fields as shown in figure G.1. Because of its simplicity in experimental setup, specimen preparation, wide range of measurement sensitivity and resolution, DIC is widely used these days (Pan et al., 2009). Apart from these advantages DIC can be easily coupled with optical microscopy, Scanning electron microscope (SEM) and Scanning tunneling microscope (STM). In the present study DIC is coupled with SEM to realize micro-scale deformation measurements.

G.2 Principle of DIC

The basic concept of measurement in DIC is tracking a group of pixels (called subsets) in initial and deformed image, through temporal matching and correlation functions. A subset

[0]Picture taken from https://www.smart-piv.com/en/products/strainmaster/2d-stereo-dic/index.php, accessed 10th june 2022.

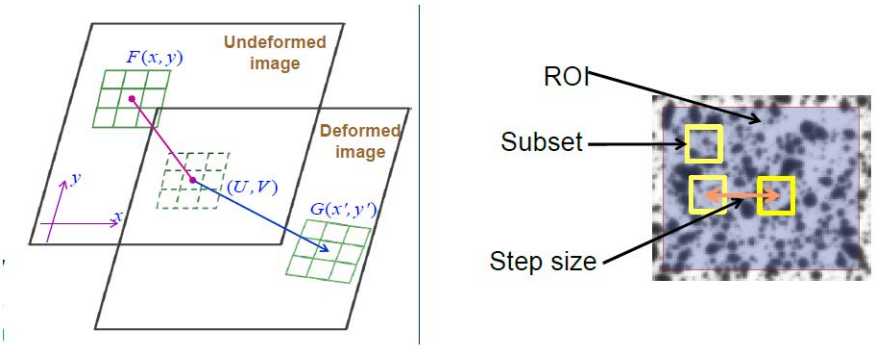

Figure G.2: *Pictorial representation of principle and basic terminologies of DIC. Figure recreated from (Pan et al., 2009)*

is a collection of group of pixels carrying a unique gray value information for deformation measurement. The distance between two subset centers are called step size. The representation of subsets and step size are shown in figure G.2. The shape functions of subset are superimposed to the reference subset for deformed shape of the subset in the deformed image. Interpolation functions are used for the deformed position of subset that are not at the integer location, therefore a proper interpolation function is necessary to obtain grey intensity value at non integer location. Subset interpolation functions transforms data from pixel coordinate of subset to the coordinates of deformed image. A first order interpolation function sample is given by equation:

$$\begin{bmatrix} U(x,y) \\ V(x,y) \end{bmatrix} = \begin{bmatrix} u \\ v \end{bmatrix} + \begin{bmatrix} \frac{\partial u}{\partial x} & \frac{\partial u}{\partial y} \\ \frac{\partial v}{\partial x} & \frac{\partial v}{\partial y} \end{bmatrix} \begin{bmatrix} \triangle x \\ \triangle y \end{bmatrix} \tag{G.1}$$

where u and v are displacements in 2D plane, and U, V represents the amount of change in displacement of the pixel in x and y directions respectively. Based on these displacements we can calculate strains (E_{xx},E_{yy}, E_{xy}) using the equations below:

$$E_{xx} = \frac{1}{2}\left(2\frac{\partial u}{\partial x} + \left(\frac{\partial u}{\partial x}\right)^2 + \left(\frac{\partial v}{\partial x}\right)^2\right) \tag{G.2}$$

$$E_{yy} = \frac{1}{2}\left(2\frac{\partial u}{\partial y} + \left(\frac{\partial u}{\partial y}\right)^2 + \left(\frac{\partial v}{\partial y}\right)^2\right) \tag{G.3}$$

$$E_{xy} = \frac{1}{2}\left(\frac{\partial u}{\partial y} + \frac{\partial v}{\partial x} + \frac{\partial u}{\partial x}\frac{\partial u}{\partial y} + \frac{\partial v}{\partial x}\frac{\partial v}{\partial y}\right) \tag{G.4}$$

The definition for correlation function $\mathbf{C}$ should match the similarity between the subset in the undeformed and deformed images.

$$\mathbf{C} = \frac{\int_{\triangle A}(F(x,y))(G(x'+U,y'+V))dA}{\left[\int_{\triangle A}[F(x,y)]^2 dA \int_{\triangle A}[G(x'+U,y'+V)]^2 dA\right]^{\frac{1}{2}}} \tag{G.5}$$

Where $F(x, y)$ is the pixel intensity or grey scale value at a point (x, y) in undeformed configuration, $G(x' + U, y' + v)$ is the grey scale value at point (x', y') in the deformed image. A represents the outer surface of the selected Subset

Finally unknown displacement and strain parameters $\left(u, v, \frac{\partial u}{\partial x}, \frac{\partial u}{\partial y}, \frac{\partial v}{\partial x}, \frac{\partial v}{\partial y} \right)$ are determined by minimizing the correlation function using Newton-Raphson method.

G.2.1 Major steps involved in DIC

1. Preparation of specimen
2. Capturing images of planar specimen surface at different stages of loading
3. Post-processing of acquired images using scripts/softwares to obtain strain field

The specimen surface should have grey intensity distribution, that deforms along with specimen surface. Normally speckle pattern can be natural texture of specimen or artificially made black and white paint. In this work we have used diamond colloidal particles (made of synthetic diamond) of different size (3mm to 9μm) for creating grey white scale. The particles are sprayed uniformly on the surface of the specimen to create speckle pattern. Images of the specimen are taken during tensile testing and these high resolution images are used for post-processing. In this work strain measurements are obtained by performing post-processing in **Ncorr** (Blaber et al., 2015) tool, which is a open-source 2D DIC **MATLAB** software.